Numerical analysis of magneto-mechanically coupled mesostructures

Von der Fakultät für Ingenieurwissenschaften,
Abteilung Bauwissenschaften
der Universität Duisburg-Essen
zur Erlangung des akademischen Grades

Doktor-Ingenieur

genehmigte Dissertation

von

Maximilian Reichel, M.Sc.

Hauptberichter:	Prof. Dr.-Ing. habil. J. Schröder
Korreferentin:	Prof. Dr.-Ing. B.-X. Xu

Tag der Einreichung:	04. Oktober 2023
Tag der mündlichen Prüfung:	08. Januar 2024

Fakultät für Ingenieurwissenschaften,
Abteilung Bauwissenschaften
der Universität Duisburg-Essen
Institut für Mechanik
Prof. Dr.-Ing. habil. J. Schröder

Berichte des Instituts für Mechanik, Universität Duisburg-Essen

Nr. 31

Herausgeber:

Prof. Dr.-Ing. habil. J. Schröder

Organisation und Verwaltung:

Prof. Dr.-Ing. habil. J. Schröder
Institut für Mechanik
Fakultät für Ingenieurwissenschaften
Abteilung Bauwissenschaften
Universität Duisburg-Essen
Universitätsstraße 12
45141 Essen
Tel.: 0201 / 183 - 2682
Fax.: 0201 / 183 - 2680

ISBN 978-3-9821811-7-2

Im Jahresmittel muss es Spaß machen!

DOI: 10.17185/duepublico/81735
URN: urn:nbn:de:hbz:465-20240314-062212-5

Vorwort

Die vorliegende Arbeit entstand während meiner Tätigkeit als Wissenschaftlicher Mitarbeiter am Institut für Mechanik (Abteilung Bauwissenschaften, Fakultät für Ingenieurswissenschaften) an der Universität Duisburg-Essen im Rahmen des durch die Deutsche Forschungsgemeinschaft (DFG) finanzierten Sonderforschungsbereiches SFB TRR 270 "Hysterese-Design magnetischer Materialien für effiziente Energieumwandlung - HoMMage" (Projektnummer 405553726). An dieser Stelle möchte ich mich bei der DFG für die finanzielle Unterstützung bedanken und meinen persönlichen Dank meinen Wegbegleitern aussprechen, die zum Erfolg dieser Arbeit beigetragen haben.

An erster Stelle möchte ich mich aufrichtig bei meinem sehr geschätzten Doktorvater Professor Jörg Schröder bedanken, der mir die Möglichkeit gab unter seiner Leitung zu promovieren. Dabei liegt mein größter Dank auf seiner Förderung und Forderung sowie seinem mir entgegengebrachtem Vertrauen eigene Idee einzubringen und umsetzen zu können. Mein besonderer Dank gilt Frau Professorin Bai-Xiang Xu, sowohl für die Übernahme des Korreferates als auch für die sehr angenehme und erfolgreiche Zusammenarbeit im Rahmen des SFB.
Mein weiterer Dank gilt Professor Joachim Bluhm für seine fachliche Expertise auf dem Gebiet der Kontinuumsmechanik sowie seine offene und herzliche Art. Meinen aufrichtigen Dank möchte ich Alexander Schwarz und Sascha Maassen gegenüber ausdrücken, die mir zu jeder Zeit mit Rat und Tat zur Seite standen. Ebenfalls herzlich bedanken möchte ich mich bei Marvin Koßler für den Druck meiner Dissertationsschrift, während ich in den USA war. Des Weiteren gilt mein Dank Thomas Feggeler, Rainer Niekamp und Maximilian Scheunemann für kleinere und größere Impulse zwischendurch. Ebenfalls danke ich meinen aktuellen und ehemaligen Kolleginnen und Kollegen Solveigh Averweg, Marcos Margalho de Barros, Dominik Brands, Philipp Hartwig, Sonja Hellebrand, Yasemin von Hoegen, Simon Maike, Matthias Labusch, Mangesh Pise, Markus Prangs, Sabine Ressel, Mohammad Sarhil, Lisa Scheunemann, Carina Schwarz, Serdar Serdas und Julia Sunten.

Meiner Familie, insbesondere meinen Eltern, Petra Reichel und Andreas Schmitz, sowie meinen Freunden, besonders Lucas Schlaak, möchte ich für ihre Unterstützung und Ratschläge in jeglicher Situation von Herzen danken.

Abschließend gilt mein größter Dank meiner Verlobten Alexandra Vorwerk für ihre stetige Unterstützung sowie ihre Geduld, ihr Verständnis und ihre liebevolle Art. Vor allem in den schwierigen Phasen dieser Arbeit hat sie mir Rückhalt und Zuversicht gegeben. Danke für alles.

Essen, im März 2024 Maximilian Reichel

Abstract

The present work is devoted to the numerical analysis of magneto-mechanically coupled mesostructures in the framework of the finite element method. Magnetic materials are used in many industrial applications, thus the demand for environmentally friendly magnets with improved efficiency is continuously increasing. To meet this demand, alternative methods and more environmentally friendly chemical compositions need to be investigated in addition to current process routes. The objective in this work is the numerical analysis of magnetic materials based on a continuum mechanical formulation. On the one hand, the focus is on the development of new algorithms for the efficient treatment of open boundary problems in magnetostatics and their numerical implementation. On the other hand, the implementation of the micromagnetic equations in the framework of the finite element method and the validation of this numerical model is forced. After completion of the validation, polycrystalline magnetic microstructures are numerically analyzed.

Zusammenfassung

Die vorliegende Arbeit widmet sich der numerischen Analyse von magneto-mechanisch gekoppelten Mesostrukturen im Rahmen der Finite-Elemente-Methode. Magnetische Materialien finden in vielen industriellen Bereichen Anwendung, sodass der Bedarf an umweltfreundlichen Magneten mit gesteigerter Effizienz kontinuierlich zu nimmt. Um diesen Bedarf decken zu können, müssen neben den aktuellen Prozessrouten auch alternative Methoden und umweltverträglichere chemische Zusammensetzungen untersucht werden. Das Ziel in dieser Arbeit ist die numerische Analyse von magnetischen Materialien basierend auf einer kontinuumsmechanischen Formulierung. Der Fokus liegt zum einen auf der Entwicklung von neuen Algorithmen zur effizienten Behandlung von offenen Randproblemen in der Magnetostatik sowie deren numerischer Umsetzung. Zum anderen wird die Implementierung der mikromagnetischen Gleichungen im Rahmen der Finite-Elemente-Methode und die Validierung dieses numerischen Modells forciert. Nach Abschluss der Validierung werden polykristalline magnetische Mikrostrukturen numerisch analysiert.

Contents

1 Introduction and Motivation

Important challenges as the "green" energy transition, the mobility transformation as well as the ongoing digitization require particularly powerful and efficient magnetic materials. To address the resulting growing demand for efficient magnetic materials, researchers from engineering sciences, mathematics, physics, and materials sciences have formed an interdisciplinary consortium in terms of the collaborative research center Hysteresis Design of Magnetic Materials for Efficient Energy Conversion (CRC TRR 270 HoMMage). This work shows the results of the subproject A07 "Scale-bridging of magneto-mechanical mesostructures of additive manufactured and severe plastically deformed materials" in HoMMage after almost four years of research work. The focus of this project is on the numerical characterization of magnetic materials with the goal of providing simulation-based material compositions and microstructure textures that will eventually lead to improved magnetic properties.

What types of magnetic materials exist?
In general, magnetic materials can be subdivided into two classes, the so-called hard and soft magnetic materials. Both types of magnetic materials exhibit different properties and thus also different fields of application. The hard or permanent magnetic materials generate intrinsically strong magnetic fields and posses high resistance to external magnetic fields. On the one hand, particularly powerful permanent magnets have fields of applications in hard disk drives, hybrid and electrical vehicles (Fig. 1.1a)) as well as wind power plants (Fig. 1.1b)), among others, cf. Constantinides [2016] and Kovacs et al. [2020]. Especially the last two applications play a crucial role in the "green" energy transition, as efficient transportation in electric cars or energy conversion by means of wind generators/turbines can contribute to the reduction of climate-damaging greenhouse gases.

a) b) c)

Figure 1.1: Strong and efficient permanent magnets can be used to enhance a) the electric transportation (Kemp [2021]) and b) the energy conversion (Vorwerk [2023]), since they are c) important components of electric motors (one magnet highlighted in blue circle) (Baumeister [2020]).

Soft magnetic materials on the other hand, generate very low magnetic fields on their own and are, unlike permanent magnets, not particularly resistant to external magnetic fields. These properties make soft magnetic materials to ideal components in transformers (Gutfleisch et al. [2011]), where they are used for the low-loss transformation of energy, and in the write heads of hard disk drives (Comstock [2002]).

Why is there research interest in magnets?
The current gold standard in the field of permanent magnets, in terms of performance, are Neodym-Iron-Boron (NdFeB) magnets. Due to many industrial applications, the demand for NdFeB permanent magnets has increased enormously within the recent years. Fig. 1.2 shows the current consumption of NdFeB-based permanent magnets as well as the estimated future demand. Accordingly, the increasing consumption is likely to be continued within the coming years.

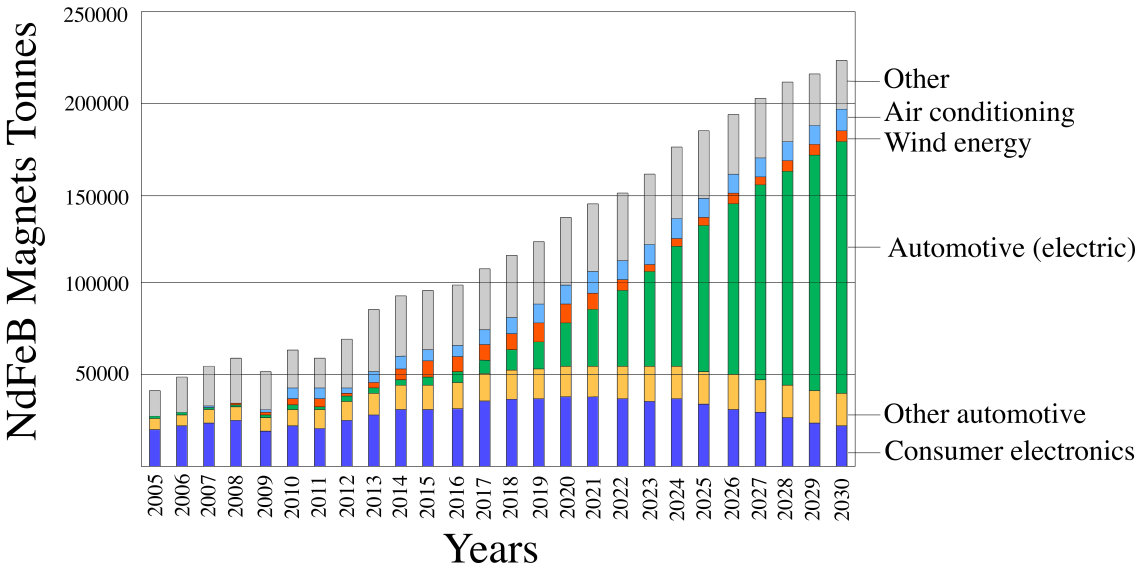

Figure 1.2: The world wide consumption of NdFeB permanent magnets. The automotive sector is expected to be the fastest growing consumer market. This chart is adapted from Ara [2019].

To meet this growing demand, the efficiency of currently available permanent magnets must be significantly improved. Potential for improving magnetic performance can be derived from the so-called Brown's paradox, cf. Brown [1945]. Brown's paradox identifies a difference between the theoretically possible and the practically available efficiency of hard magnets. Reasons for the gap between theoretical and practical values are numerous. These can include impurities or non-magnetic inclusions, as well as misoriented grains in the grain structure, which can lead to drastic losses in performance, as stated in Kronmüller [1987]. Hence, the underlying microstructure has a decisive influence on the magnetic behavior. New process routes, such as severe plastic deformation (SPD) or additive manufacturing (AM), are intended to better control the production and targeted influence of these microstructures in the future. Besides the microstructural influence, the stoichiometric composition of the materials is also of great importance. NdFeB magnets currently deliver the highest energy product, but are prone to corrosion and higher temperatures, at which they quickly suffer high performance degradation, see Gutfleisch et al. [2011]. The material properties can be enhanced by supplementary added heavy rare earths (HRE) elements, such as Dysprosium (Dy) or Terbium (Tb), cf. Soderžnik et al. [2017]. These HRE additions improve the behavior of the NdFeB magnets in terms of coercivity as well as temperature resistance, cf. Soderžnik et al. [2016] and Herbst and Croat [1991]. However, they give rise to new problems. The extraction of HRE is usually carried out under highly invasive interventions in nature with serious consequences for the environment. In addition to

these environmental disadvantages, the market price of HRE is subject to strong fluctuations due to the availability on the world market, see Mcguiness et al. [2015]. A global distribution of HRE production and its resources is shown a Fig. 1.3. According to this, China currently accounts for the largest share of HRE on the world market and also has the most HRE reserves, followed by Russia. To minimize the environmental footprint of permanent magnets as well as dependencies on individual countries, one goal is to reduce the proportions of these critical components or replace them with other earth abundant elements. Substitute materials should be harmlessly degradable to humans and the environment and be sourced from countries with guaranteed continuous accessibility to prevent dependencies that can be used as political leverage.

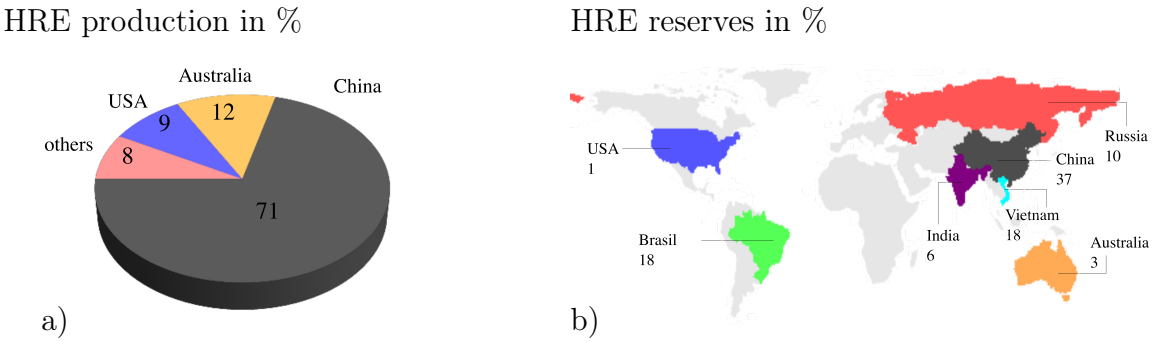

Figure 1.3: World wide heavy rear earth a) production and b) resources in percent. The graphics are adapted from Rostek-Buetti [2019].

How can simulations support?
Mathematical equations can be used to represent physical processes. Hence, it is possible to observe local phenomena such as nucleations, domain wall motions or grain interactions on very fine time scales and with high resolution. Experiments can be time consuming, but the actual reaction might pass quickly and occur on very fine scales. However, simulations can be used to better focus and/or time experiments (where and/or when can crucial processes happen?), to get to the core of certain mechanisms in detail (e.g. finer spatial and/or time discretization as in experiment) and thus to optimize the entire experimental process. In this context, finite-element-based simulations may help to analyze the properties and the performance of the considered magnets. The theoretical framework is provided by the micromagnetic theory, that models the behavior of the magnetization vectors in the context of the phase field theory. It allows to study local domain wall motions and pinning mechanisms, based on competing energy contributions.

The present work deals with the numerical characterization of magnetic materials in the framework of the finite element method (FEM). A special interest is thereby set on the efficient simulation of magnetic stray fields emitted by magnets and the modeling of the non-linear magnetization behavior within magnetic solids, also considering mechanical interactions. Hence, this contribution is structured as follows:

Chapter 2 explores the origin of effectively measurable magnetism. Starting at the atomistic scale with quantum mechanical fundamentals, through the continuum description of the single magnetic moments, up to domain motions at the micrometer level, the mechanisms and properties of magnetic materials are reviewed. On the continuum level, Maxwell's equations are introduced, which are of central importance in this work, since they define the fundamental basis for electro-magnetic relations.

Chapter 3 introduces the continuum mechanical foundations, restricting the concept on the limitations of the linear elastic theory. After the definition of selected fundamental kinematical relations as well as the introduction of the strain tensor, the mechanical balance equations are derived. Subsequently, the evaluation of the second law of thermodynamics enables the formulation of a thermo-magneto-mechanical material law.

Chapter 4 explains the procedure of the finit element method for the magnetic Gauss law, starting with the initially defined magnetostatic boundary value problem to eventually obtain the required local and global systems of equations for an isoparametric finite element as well as a fully discretized magnet. Since magnetic materials emit magnetic fields in their direct proximity, numerical simulations must be capable to represent them in order to avoid errors. These fields decrease rapidly with increasing distance from the magnet, but it is not obvious when they exactly vanish. Therefore, two numerical methods are introduced to efficiently handle open boundary problems. The first is based on a static condensation and the second on the scaled boundary finite element method (SBFEM).

Chapter 5 presents the micromagnetic theory stating with the micromagnetic energy functional, followed by the derivation of Browns equations and the derivation of the Landau-Lifshitz-Gilbert equation. Based on the previous preparations, the finite element formulation is derived, focusing on the numerical implementation of different methods to constrain the length of the magnetization vectors on the unit sphere and their subsequent evaluation.

Chapter 6 shows the results of micromagnetic simulations of polycrystalline hard magnetic $Nd_2Fe_{14}B$ materials. The first simulations are devoted to the investigation of defect structures within severe plastically deformed specimens, while the last example investigates the magnetization reversal of a three dimensional heterogeneous microstructure.

Chapter 7 concludes the work and gives an outlook to future investigations in the field of magnetic simulations.

2 Magnetic foundations

This work addresses primarily the description and characterization of magnetic materials in the context of a continuum theory. Since magnetism in general happens on different size scales, which are all interrelated, some basic phenomena, terminology and definitions are discussed in this section to give a general overview of the subject. This includes the origin of the magnetic moment and its contributions (spin and orbit magnetic moment), the properties and laws of magnetic fields, different types of magnetism as well as the nature of magnetic domains. For a more comprehensive introduction to the basics of magnetism, compare to Bertotti [1998], Chikazumi and Charap [1978], Hubert and Schäfer [1998], Coey [2010], Cullity and Graham [2009], Getzlaff [2008] and Coey and Parkin [2021].

2.1 Origin of magnetism

The macroscopically measurable magnetism in ferromagnetic materials results from the sum of all atomic magnetic moments. This in turn means that the individual components (atoms) of the macroscopic body must already have an independent magnetic moment to contribute to the collective magnetic moment. A magnetization within these atoms is caused by the unpaired electron magnetic moment. Unpaired, in this context, implies that there exists an electron on an outer shell, generating a magnetic moment that is not compensated by an other electron moment within the same shell. If the atoms under consideration have magnetic moments, their macroscopic sum must not be zero. Unless this is the case, a macroscopically measurable collective magnetization arises. However, before macroscopic effects are considered, their origin must be examined in more detail. In general, the origin of magnetization can be described in a clearly simplified way. In each atom several electrons move in their orbits and rotate around their own axis generating a vector valued magnetic moment. These motions give rise to magnetic moments of which the sum (spin and orbital moment) represents the moment of the atom as a vector quantity. Pauli's exclusion principle states that two electrons within an orbital generate magnetic moments of identical amount but with opposite orientation, such that they cancel each other out. Hence, the magnetization within an atom results of an unpaired electron magnetic moment. This oversimplified description of the origin of a net magnetic moment undergoes indeed some restrictions. Hence, the classical model of the electronic magnetic moments is shortly described, followed by an excursus into the quantum mechanical approach.

Classical model In the classical model, a relation is established between the angular momentum (orbital and spin) of an electron and the magnetic moment. The total electronic magnetic moment

$$\boldsymbol{m}_{\mathrm{tot}} = \boldsymbol{m}_0 + \boldsymbol{m}_{\mathrm{s}} \tag{2.1}$$

consists of two contributions, i.e. the magnetic moment due to the orbital angular moment $\boldsymbol{m}_0$ as well as the spin magnetic moment $\boldsymbol{m}_{\mathrm{s}}$. The orbital magnetic moment is caused by the motion of an electron within its orbitals that can be stated as

$$\boldsymbol{m}_0 = -\frac{e}{2\,m_e}\,\boldsymbol{p}_0, \tag{2.2}$$

where $\boldsymbol{p}_0$ indicates the orbital angular momentum, while e and m_e denote the charge and the mass of an electron. The spin magnetic moment caused by the spin angular momentum

$\boldsymbol{p}_s$ follows the similar relation

$$\boldsymbol{m}_\mathrm{s} = -\frac{e}{m_e}\,\boldsymbol{p}_\mathrm{s}, \tag{2.3}$$

but appears, compared to Eq. 2.2, twice as large as the orbital magnetic moment.

Quantum mechanical approach The classical approach presented above allows arbitrary values for the orbital and spin angular moments $\boldsymbol{p}_0$ and $\boldsymbol{p}_\mathrm{s}$. This assumption does not match reality, since angular momentum contributions are constrained by quantum mechanics. The exact contribution of the angular moments depends on the configuration of the electrons within the atom. For the full description of the electron states, the so-called quantum numbers are used. This is the principal quantum number n[1.)], the orbital angular momentum number l[2.)], the magnetic moment quantum number m_l and the magnetic spin quantum number m_s. The principal quantum number $n = 1, 2, 3, ...$ indicates on which electron shell the electron is located and thus the corresponding energy level. The orbital quantum number $l = 0, 1, 2, ..., (n-1)$ describes the geometry of the orbital [3.)] in which the electron is located. Due to Pauli's exclusion principle electrons cannot posses the same values for all four quantum numbers. Assuming two electrons posses same values for the first three numbers (principal- (n), orbital angular- (l) and magnetic quantum number (m_l)) the spin quantum number ($m_s = \pm\frac{1}{2}$) must differ for both electrons, indicating antiparallel orientations of the resulting electron magnetic moment. Hence, these paired electrons posses magnetic moments that cancel each other out and do not contribute to the collective magnetic moment. Only unpaired electrons contribute to this effect. The orbital angular momentum can be defined as

$$\boldsymbol{p}_0 = \left(\frac{h}{2\pi}\right) l. \tag{2.4}$$

To describe the electron spin, the spin quantum number s is defined. This always corresponds to $s = 1/2$ and can thus be used to define the spin angular momentum as

$$\boldsymbol{p}_\mathrm{s} = \left(\frac{h}{2\pi}\right) s. \tag{2.5}$$

The magnetic orbital moment quantum number $m_l = -l, -(l-1), ..., l-1, l$ describes the orientation of the orbital angular momentum vector. Strictly speaking, this is a projection of the orbital angular momentum onto a quantization axis depending on the Planck constant h. The quantization axis in the case considered here is the z-axis, which also corresponds to the direction of an externally applied magnetic field. Thus, for the orbital angular momentum along the z-component the following is obtained

$$p_{0\,\mathrm{z}} = \left(\frac{h}{2\pi}\right) l_z, \quad \text{with} \quad l_z = \frac{h}{2\pi} m_l. \tag{2.6}$$

Analogously, the magnetic spin quantum number m_s can be the projection of the electron spin on a quantization axis. Electron spin moments can occur exclusively parallel (spin-up,

[1.)] Defined by the danish physicist Niels Bohr.

[2.)] Defined by the german physicist Arnold Sommerfeld.

[3.)] In quantum mechanics, orbitals indicate a probability of where the electron can be found at a location $\boldsymbol{r} = \hat{\boldsymbol{r}}(x, y, z)$. Orbitals of different shapes accordingly indicate a different probability of residence.

i.e. 1/2) or antiparallel (spin-down, i.e. -1/2) to a magnetic field. This gives the following quantization

$$p_{\mathrm{s\,z}} = \left(\frac{h}{2\pi}\right) s_z, \quad \text{with} \quad s_z = \frac{h}{2\pi} m_s \quad \text{and} \quad m_s = \pm 1/2. \tag{2.7}$$

The quantities introduced above can now be used to fit Eq. 2.2 and Eq. 2.3. Hence, the orbital angular momentum results in

$$\boldsymbol{m}_0 = \frac{-e}{2m_e}\,\boldsymbol{p}_0 = \frac{-e}{2m_e}\frac{h}{2\pi}\,l = \frac{-e}{4\pi m_e}\,l = -\mu_{\mathrm{B}}\,l, \tag{2.8}$$

where $\mu_{\mathrm{B}} = \frac{-e}{4\pi m_e} \approx 9.27 \cdot 10^{-24}\mathrm{Am}^2$ is known as the Bohr magneton. Analogously the spin angular momentum yields

$$\boldsymbol{m}_{\mathrm{s}} = \frac{-e}{m_e}\,\boldsymbol{p}_{\mathrm{s}} = \frac{-e}{m_e}\frac{h}{2\pi}\,s = \frac{-2\,e}{4\pi m_e}\,s = -2\,\mu_{\mathrm{B}}\,s. \tag{2.9}$$

Taking quantum mechanics (Eq. 2.8 and Eq. 2.9) into account, Eq. 2.1 leads to the total magnetic moment

$$\boldsymbol{m}_{\mathrm{tot}} = \boldsymbol{m}_0 + \boldsymbol{m}_{\mathrm{s}} = -(\mu_{\mathrm{B}}\,l + 2\,\mu_{\mathrm{B}}\,s). \tag{2.10}$$

However, the macroscopic description of magnetic materials within the framework of a continuum theory requires to consider the magnetization of a body per unit volume as

$$\boldsymbol{M} = \sum_i \frac{1}{V_i} \int_{\mathrm{V_i}} \boldsymbol{m}_{\mathrm{tot}}\,\mathrm{dV}. \tag{2.11}$$

The parallel alignment of many magnetic moments into one direction leads to the formation of so-called magnetic domains (cf. Sec. 2.5). Nevertheless, the net magnetization of the magnetic material is zero, since all domains pointing in different directions cancel each other out. The application of an external magnetic field leads to an increase in the net magnetization in the material, since the field aligns the magnetization parallel to itself until all domains are reversed and aligned. This state corresponds to the upper limit of the magnetization within the considered material that is given by the material-specific magnetization saturation $M_{\mathrm{s}} = \|\boldsymbol{M}\|$. This process of domain shifting leads to the magnetic hysteresis loop described in more detail in section 2.5.

2.2 Properties of magnetic fields and Maxwell's equations

A magnetic field $\boldsymbol{H}$ is generated whenever electrically charged particles move, changing the energy within a reference volume and consequently creating an energy gradient. Ampère[4.)] came to this conclusion when he read about Oersted's[5.)] discovery that compass needles can be influenced by electrical currents. Thereby, it is not important what kind of charged particles are involved; it can be an electrical current flowing through a coil, but also electrically charged particles moving inside a permanent magnet (orbital and spin motion). Hence, the unit of the magnetic field is defined in amperes per meter (A/m).

[4.)] André-Marie Ampère was a french physicist.

[5.)] Hans Christian Ørsted was a danish physicist.

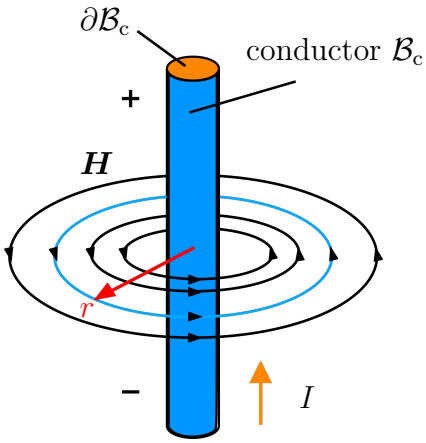

Figure 2.1: Magnetic field pattern obtained from an infinitely long current carrying conductor.

For simplified cases the strength of the magnetic field $\boldsymbol{H}$ can be analytically calculated. Starting from an infinitely long electric conductor $\mathcal{B}_c$ carrying a current I, a magnetic field $\boldsymbol{H}$ is generated in the form of closed loops around the conductor, cf. Fig. 2.1. This current I can be obtained by integrating the current density $\boldsymbol{j}$ over the cross-sectional area $\partial\mathcal{B}_c$ of the conductor as $I = \int_{\partial\mathcal{B}_c} \boldsymbol{j}\, \mathrm{d}\boldsymbol{a}$. The current within this conductor is found to be proportional to the sum of the components of the magnetic field along a defined closed curve. The relation between the current and the magnetic field can be mathematically expressed in terms of

$$\oint_{\mathcal{S}} \boldsymbol{H}\, d\boldsymbol{x} = I, \tag{2.12}$$

which requires the evaluation of a line integral along the magnetic field lines. Since the magnetic field lines shown in Fig. 2.1 follow circular paths, the line integral can be calculated over the circumference of a circle with radius r as

$$2\pi r \boldsymbol{H} = I \quad \rightsquigarrow \quad \boldsymbol{H} = \frac{I}{2\pi r}. \tag{2.13}$$

The magnetic induction $\boldsymbol{B}$ in free space is closely related to the magnetic field and can be obtained via the linear relation

$$\boldsymbol{B} = \mu_0\, \boldsymbol{H}, \tag{2.14}$$

where $\mu_0 = 4\pi \times 10^{-7}$ H/m indicates the magnetic permeability of vacuum. Since μ_0 is a constant valued parameter, Eq. 2.12 can be modified to

$$\oint_{\mathcal{S}} \boldsymbol{B}\, d\boldsymbol{x} = \mu_0\, I. \tag{2.15}$$

Applying Stokes theorem, the line integral in Eq. 2.15 can be transferred into a surface integral. This enables to give both, the equation in integral form as well as in its local form as

$$\int_{\partial\mathcal{B}} \mathrm{curl}\boldsymbol{B}\, \mathrm{d}\boldsymbol{a} = \mu_0 \int_{\partial\mathcal{B}} \boldsymbol{j}\, \mathrm{d}\boldsymbol{a} \quad \text{or} \quad \mathrm{curl}\boldsymbol{B} = \mu_0 \boldsymbol{j}. \tag{2.16}$$

Commonly, both expressions in Eq. 2.16 are known as Ampère's circuital law. However, Eq. 2.16 can be extended to also consider the change in time of the dielectric displacement $\partial\boldsymbol{D}/\partial t$, leading to

$$\mathrm{curl}\boldsymbol{B} = \mu_0\, \boldsymbol{j} + \frac{\partial \boldsymbol{D}}{\partial t} \tag{2.17}$$

as one of Maxwell's equations. Another Maxwell equation, also referred to as magnetic Gauss law, states that the magnetic field must have no sources or sinks, as illustrated exemplarily in Fig. 2.1. Here, the magnetic field forms circular trajectories around the electrical conductor without an origin or end. Mathematically, this property can be expressed by

$$\operatorname{div} \boldsymbol{B} = 0. \tag{2.18}$$

As repeatedly shown in this section (e.g. in Eq. 2.17), a clear connection between the electrically charged particles and the origin of magnetic fields exists. Therefore, the last two of Maxwell's equations, which deal with the behavior of electric fields, are briefly introduced in the following. These involve Faraday's law of induction

$$\operatorname{curl} \boldsymbol{E} = -\frac{\partial \boldsymbol{B}}{\partial t}, \tag{2.19}$$

which relates the time change of magnetic induction to the resulting electric field $\boldsymbol{E}$ and the electric Gauss law

$$\operatorname{div} \boldsymbol{D} = \rho_\mathrm{f}, \tag{2.20}$$

which states that the electric field lines diverge in the presence of electric charges. Thus, the electric charge is a source of the electric field.

2.3 Magnetism in matter

In Sec. 2.1 and Sec. 2.2 the magnetization $\boldsymbol{M}$ and the magnetic field $\boldsymbol{H}$ have been considered separately. However, the connection of the two quantities can be established via the magnetic induction

$$\boldsymbol{B} = \mu_0(\boldsymbol{H} + \boldsymbol{M}), \tag{2.21}$$

that is composed of the magnetic field $\boldsymbol{H}$ and the magnetization $\boldsymbol{M}$. Fig. 2.2 presents exemplarily the relation between the magnetic field and the magnetic induction for different types of magnetic materials.

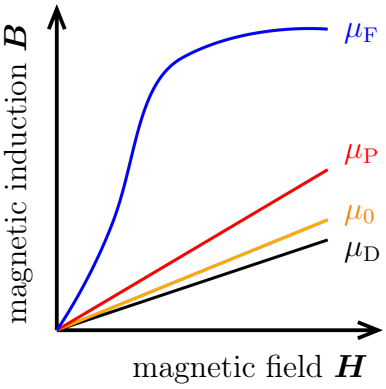

Figure 2.2: The magnetic induction $\boldsymbol{B}$ within different magnetic materials as a response of an externally applied magnetic field $\boldsymbol{H}$. Adopted from Labusch [2018].

In different materials, the magnetization may be present to different extents, so that in some cases no macroscopic magnetization is available. In paramagnetic or diamagnetic materials, a connection between the induction and the magnetic field is formed by the corresponding permeabilities μ_P and μ_D (red and black curve in Fig. 2.2). For magnetic

fields in vacuum the linear relation introduced in Eq. 2.14 is valid, because there is no magnetization attainable. Ferromagnetic materials in general posses a non-linear relation μ_F between the magnetic field and the induction as indicated in Fig. 2.2 as the blue curve.

2.4 Different types of magnetism

The different properties of the most important magnetic materials are briefly introduced in this section. Here, this includes diamagnetic, paramagnetic, ferromagnetic, and antiferromagnetic materials.

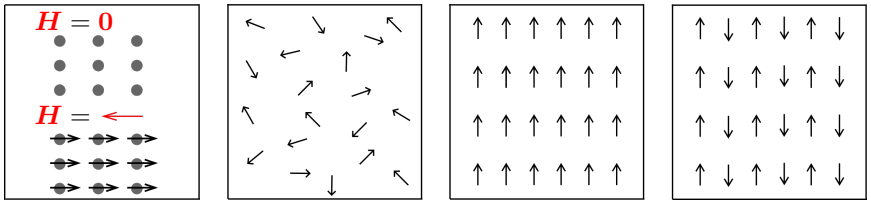

Figure 2.3: A rough sketch of four types of magnetism: a) diamagnetism, b) paramagnetism, c) ferromagnetism, d) antiferromagnetism. Adopted from Lacovacci et al. [2016] and Labusch [2018].

Diamagnetism

Diamagnetic materials have the property to generate a magnetization opposed to the externally applied field. The reason for this phenomenon can be explained as follows: The external field causes an orbital motion of electrons around the nuclei and thus generates a current. These electrically charged particles in motion, generate their own magnetic field, which opposes the externally applied magnetic field. However, in the absence of an external magnetic field no magnetization can be measured.

Paramagnetism

Paramagnetic materials usually consist of atoms or molecules with odd numbers of electrons. Hence, the net magnetic moment arises from an unpaired electron spin. However, the absence of exchange interactions (compare to Sec. 5.2) leads to random orientations of the magnetic moments (Fig. 2.3b)) and no effective magnetization, since they cancel each other out. This unstructured orientation becomes aligned parallel to externally applied magnetic fields. Thermal influences on a paramagnet cause the magnetic moments to remain unstructured and further complicate the parallel alignment induced by an external magnetic field. Paramagnetic materials are e.g. Platinum, Aluminium and Oxigen, among others.

Ferromagnetism

In *ferromagnetic* materials the magnetic spin moments are aligned parallel to each other (Fig. 2.3c)). This results of the strong exchange interactions between those spins. A parallel spin orientation minimizes the exchange energy introduced in Sec. 5.2. Even minor deviations from this orientation lead to an additional energy contribution and an unfavored state. Ferromagnetic materials also exhibit strong temperature dependencies. Above the so-called Curie temperature T_c they behave paramagnetic, below they posses their typical ferromagnetic characteristics. However, their effective magnetization equals zero in the unmagnetized state, since ferromagnetic materials form so-called magnetic domains.

These domains are regions of equally oriented magnetization, but cancel each other out macroscopically. Magnetic domains are discussed in more detail in Sec. 2.5.

Antiferromagnetism

In analogy to ferromagnetic materials, *antiferromagnetic* materials are paramagnetic above a critical temperature, the so-called Néel temperature T_N. Below this temperature point the material behaves antiferromagnetic, with an antiparallel orientation of the magnetic moments as given in Fig. 2.3d). This alignment is caused by the magnetic exchange interactions and the negative exchange coefficient J_{ij}, that favors the antiparallel orientated state of the spins. While ferromagnetic materials posses domains with distinct orientations, that can be summed up to an effective magnetization of this particular domain, antiferromagnetic materials also posses magnetic domains, but their magnetization sums up to zero due to the antiparallel alignment.

2.5 Magnetic domains and domain walls

Magnetic domains are fundamental properties of materials exhibiting collective magnetic order. Thus, they are important components of sensors as well as other engineering applications. The domains consist of areas with the same magnetization patterns possessing the same magnetization orientation, caused by the magnetic exchange energy. They can be stimulated by internal (e.g. demagnetizing fields) as well as external influences (e.g. magnetic fields, mechanical loads or electrical currents) always striving for an energetically appropriate and stable state. Such a stable state can be obtained by the minimization of various competing energies, that form the magnetic energy functional of the system, including contributions to magnetostatics, exchange interactions and the underlying anisotropic lattice. The magnetostatic contribution with the external magnetic field and the demagnetization/stray field exhibits a dominant influence. This sensitivity to magnetic fields (comp. Fig. 2.6), in this case especially to external fields, is one of the origins of the hysteresis properties. External magnetic fields may shift the energetic minima and thus cause a rearrangement of the domains, eventually leading to the magnetic hysteretic behavior.

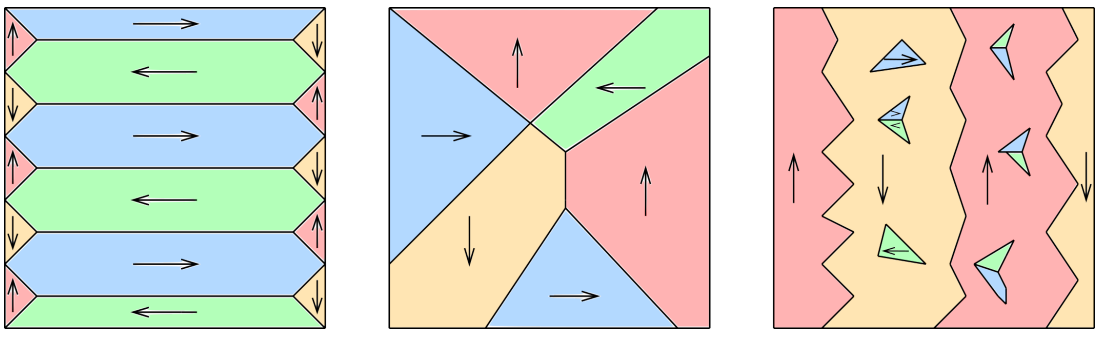

Figure 2.4: Possible domain patterns of different magnetic materials: a) NiFe, b) Fe-film and c) FeSi-sheet. Compare Hubert and Schäfer [1998] and Coey and Parkin [2021] for images obtained by Kerr microscopy.

In general, domains are defined as regions of equal magnetization, that spontaneously appear in unstructured ferro- or ferrimagnetic media Hubert and Schäfer [1998]. Their

arrangement within a sample strongly dependents on the material, the predominant magneto-crystalline anisotropy, defect structures, and external stimuli such as voltages, stresses and external fields. In general, the arrangements of domains can vary widely from material to material, as illustrated exemplarily in Fig. 2.4. These magnetic domains are separated by transition zones, called domain walls. In general, two types of domain walls are possible, that can be distinguished as Bloch and Neél walls, depending on the thickness of the considered material. Bloch walls can occur in any bulk material, whereas Neél walls can only occur in thin film materials with thickness below the domain wall thickness, cf. Coey [2010]. The magnetization orientation within Bloch domain walls changes parallel to the wall plane (assuming here the yz-plane) leading to divergence free magnetization patterns. Since no component of the magnetization vectors points into the x-direction (rotation only takes place within the yz-plane), the equation $\operatorname{div} \boldsymbol{M} = \partial_x M_x + \partial_y M_y + \partial_z M_z = 0$ holds. This circumstance prohibits the evolution of magnetic stray fields, since there are no interference sources, which could cause them. An illustration of the spatial change in orientation of the magnetization within a Bloch wall is given in Fig. 2.5a). In contrast to Bloch walls, where the magnetization vectors are always parallel to the domain wall, the entire reorientation of the vectors within Neél walls takes place in a plane, as presented in Fig. 2.5b). As a result, at least components of the magnetization vectors are orthogonal to the plane of the domain wall, resulting in a source of interference and maximizing the stray field energy. Thus, Neél walls present themselves as energetically inferior to Bloch walls.

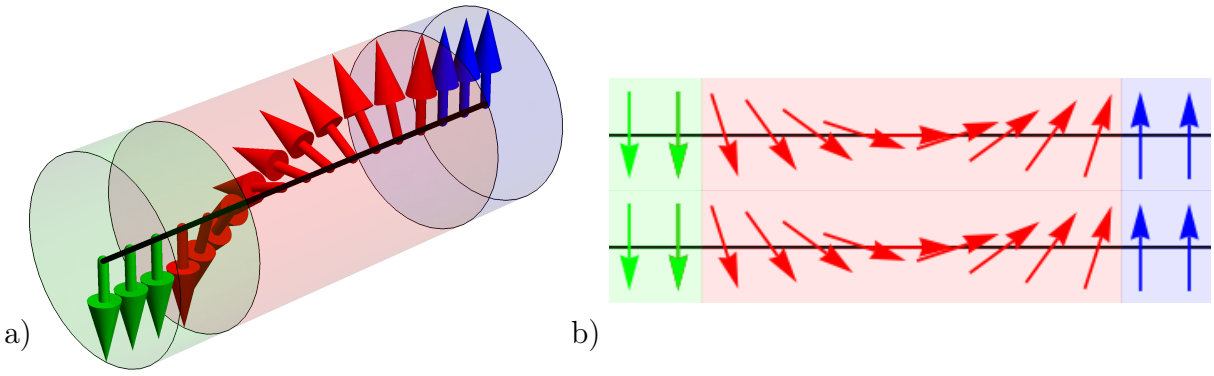

Figure 2.5: Two different types of domain walls exist. a) the Bloch domain wall is a full 3D rotation around a certain axis, while b) the Neél type domain wall is a pure 2D rotation.

If an external magnetic field $\boldsymbol{H}$ is applied to a domain formation as shown in Fig. 2.6a), the domains pointing approximately in the same direction of the $\boldsymbol{H}$-field begin to grow, whereas the contrarily oriented domains shrink. This process is illustrated in Fig. 2.6b). The domain, grows until the domain wall vanishes, which means the unification of the two domains. The resulting domain is magnetized to its saturation M_s and completely aligned parallel to its magneto-crystalline easy-axis, but not parallel to the external field (comp. Fig. 2.6c)). For higher intensities of $\boldsymbol{H}$, the magnetization will eventually align parallel to the external field, as illustrated in Fig. 2.6c).

2.6 Soft and hard magnetic materials

In general, magnetic materials can be roughly classified into soft and hard magnetic materials. Both types have different properties and thus fundamentally different fields of

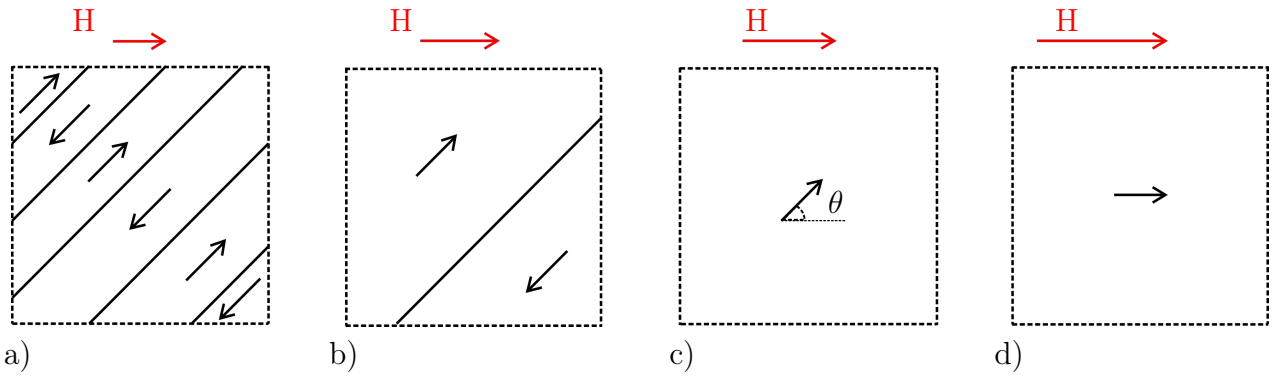

Figure 2.6: Process of magnetization of a specimen with six exemplary domains: a) $\boldsymbol{M} = 0$, b) $\boldsymbol{M} > 0$, c) $\boldsymbol{M} = M_S \cos\theta$, and d) $\boldsymbol{M} = \boldsymbol{M}_S$.

application. Soft magnetic materials are often associated with electrical circuits, because they are able to amplify the magnetic flux induced by electrical currents. Thus, it is reasonable for soft magnetic materials to have intensive use in applications such as electrical power generators, inductors or relays. Contrarily, hard or permanent magnetic materials are passive tools, that generate magnetic fields without electrical currents flowing in a coil. The property of hard magnetic materials to emit magnetic fields is utilized within electric motors, wind turbines or other power conversion equipment.

Saturation magnetization

The upper limit of the magnetization of a magnetic material is described by the so-called saturation magnetization M_s. While the net magnetization of the considered ferromagnet is zero in its initial state, it increases with growing external magnetic fields. Once a material specific field strength is reached, all magnetic moments within the magnet are aligned parallel to the applied field and the magnetization is maximized or saturated.

Remanence

If the magnetic field is successively reduced in intensity, measurable magnetization may also decrease. To determine the remanence R_r of a material, the field must be reduced to zero. The remaining magnetization corresponds to the remanence, which is qualitatively indicated in Fig. 2.7 for a hard magnetic material.

Coercivity or coercive field strength

The magnetization can be reduced to zero if reversed magnetic fields are applied to the magnetic material. The field strength that is necessary to reduce the magnetization of a saturated magnet exactly to zero is denoted as coercive field strength or coercivity H_c. The coercivity can be strongly affected by the condition of the sample, like internal distortions or external heat influences. A qualitative location of H_c is given in Fig. 2.7 for a hard magnetic material. A distinction between hard and soft magnetic materials can be made by means of the coercivity introduced above. Magnetically soft materials are in general easy to demagnetize and posses a coercivity below $H_\mathrm{c} \leq 1000$ A/m. In contrast to that, a magnet is considered to be magnetically hard, if the coercivity is greater or equal than $H_\mathrm{c} \geq 10,000$ A/m, indicating greater resistance against externally applied magnetic fields, cf. Jiles [2015]. To highlight the differences between both types of magnetic materials Fig. 2.7 shows the sketch of a soft (red) and a hard (blue) magnetic hysteresis loop. Hard magnetic materials are supposed to be a stable permanent source of magnetic fields, that do not become demagnetized easily. Contrarily, soft magnetic materials are supposed to be easy to demagnetize.

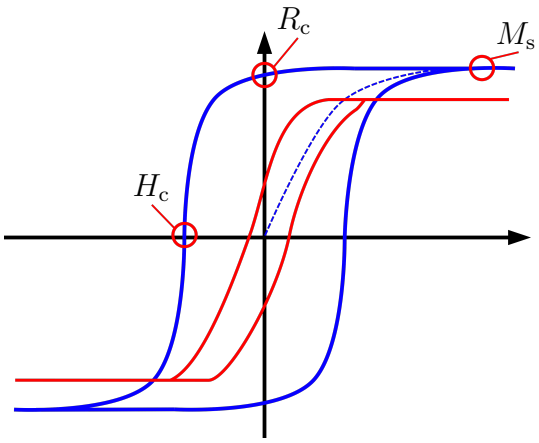

Figure 2.7: A hard (blue) and a soft (red) magnetic hysteresis loop are plotted within the same coordinate system. Characteristic values for the description of a magnetic material are indicated for the hard magnetic hysteresis, starting from left to right: Coercivity H_c, remanence R_c and magnetic saturation M_s.

3 Continuum mechanical foundations

A close analysis of the materials, i.e. even more precise than visible with a microscope, shows that every material consists of atomistic particles. These particles can individually exhibit a different behavior than a cluster consisting of innumerable atoms. Therefore, both length scales are described by different theories: the atomistic and the continuum theory. The atomistic theory thus describes the behavior of single to very few atoms, while the continuum theory always assumes a certain volume average. In the context of this work, however, only continuum theories are considered. Hence, this chapter addresses continuum mechanical basic features as kinematics of solids, the concept of stress and balance principles. While kinematics describe the motion and deformation of bodies, the concept of stress and the balance equations form the basis of the fundamental physical laws. Detailed treatments of continuum mechanics are available in standard textbooks such as Holzapfel [2000], Wriggers [2008], Stein and Barthold [1996], Schröder et al. [2023] or Trusdell and Noll [2004].

3.1 Kinematics, deformations, and stresses

An arbitrary body $\mathcal{B} \subseteq \mathbb{R}^3$ can be considered as the summation of infinite material points. These points can be described by the position vector $\boldsymbol{X}$ in their initial position (reference configuration) and $\boldsymbol{x}$ in their actual position (current configuration). If $\mathcal{B}$ undergoes a deformation, the mapping of the reference configuration into the current configuration can be described by $\boldsymbol{x} = \boldsymbol{\varphi}(\boldsymbol{X}, t)$. Based on these two configurations, the displacements $\boldsymbol{u}$ can be calculated as $\boldsymbol{u} = \boldsymbol{x} - \boldsymbol{X}$. The so-called deformation gradient

$$\boldsymbol{F} = \frac{\partial \boldsymbol{x}}{\partial \boldsymbol{X}} = \frac{\partial \boldsymbol{X}}{\partial \boldsymbol{X}} + \frac{\partial \boldsymbol{u}}{\partial \boldsymbol{X}} = \boldsymbol{I} + \partial_{\boldsymbol{X}} \boldsymbol{u} = \boldsymbol{I} + \operatorname{Grad} \boldsymbol{u} \tag{3.1}$$

represents the starting point of most deformation measures. It is thus an essential quantity for the mapping of infinitesimal line elements $\mathrm{d}\boldsymbol{X}$, area elements $\mathrm{d}\boldsymbol{A}$ as well as volume elements dV of the reference configuration into their corresponding actual configuration. These different elements can be converted between the configurations as follows

$$\mathrm{d}\boldsymbol{x} = \boldsymbol{F} \cdot \mathrm{d}\boldsymbol{X}, \quad \mathrm{d}\boldsymbol{a} = J \boldsymbol{F}^{-\mathrm{T}} \, \mathrm{d}\boldsymbol{A}, \quad \text{and} \quad \mathrm{dv} = J \, \mathrm{dV}, \tag{3.2}$$

where $J = \det \boldsymbol{F} > 0$ denotes the so-called Jacobi determinant. For later use, the time derivative of the Jacobi determinant is introduced at this point as

$$\dot{J} = J \operatorname{div} \dot{\boldsymbol{x}}. \tag{3.3}$$

In the context of this work only very small mechanical deformations and rotations are considered. Therefore, it is sufficient to introduce the linear strain tensor as

$$\boldsymbol{\varepsilon} = \frac{1}{2} \left(\nabla \boldsymbol{u} + (\nabla \boldsymbol{u})^{\mathrm{T}} \right), \tag{3.4}$$

that results of a linearization of non-linear strain measurements, like the Green-Lagrange strain tensor. For a deeper insight into the topic of non-linear strain measures the reader is referred to standard works as Wriggers [2008] and Korelc and Wriggers [2016] among others. If a statically supported body $\mathcal{B}$ is subjected to external traction vectors $\boldsymbol{t}$

on its surface $\partial\mathcal{B}$, the existence of a Cauchy stress tensor $\boldsymbol{\sigma}$ can be postulated by the Cauchy theorem via the relation $\boldsymbol{t} = \boldsymbol{\sigma} \cdot \boldsymbol{n}$. In this case, $\boldsymbol{n}$ represents the outward surface vector normal to $\partial\mathcal{B}$. Since the Cauchy stress tensor is related to the current configuration, it is often referred to as true stress. Since this work deals strictly with small deformations and stress analyses plays a rather subordinate role, further stress measures are omitted.

3.2 Balance principles

The balance equations of continuum mechanics are axioms which apply independently to individual properties of a material under consideration and are therefore independent of materials or material laws. In the following, the properties of the balance of mass, the balance of linear momentum, and the balance of moment of momentum are described and their equations are derived.

Balance of mass: The present work only considers mass-conserving processes. Hence, the mass

$$m = \int_{\mathcal{B}} \rho \, \mathrm{dv} \tag{3.5}$$

of a considered continuum $\mathcal{B}$ must remain constant over time, while evolving from initial to current configuration. ρ indicates the density of the considered material. Consequently,

$$\dot{m} = \frac{\mathrm{d}}{\mathrm{dt}} \int_{\mathcal{B}} \rho \, \mathrm{dv} \; = \; 0 \tag{3.6}$$

holds for the time derivative of the mass. As described in Eq. 3.2 the mapping of any volume from its initial to its current configuration is described by $\mathrm{dv} = J \, \mathrm{dV}$. Applying the volume mapping and Eq. 3.3 to the rate of m, the balance of mass can be stated as

$$\int_{\mathcal{B}} \dot{\rho} + \rho \; \mathrm{div} \; \dot{\boldsymbol{x}} \, \mathrm{dv} = 0 \quad \text{and} \quad \dot{\rho} + \rho \; \mathrm{div} \; \dot{\boldsymbol{x}} = 0 \tag{3.7}$$

in its global and local formulation. The local representation of the balance of mass is reasonable, since it applies not only to a total body, but also to any (local) material point.

Balance of linear momentum: The balance of momentum relates the change in time of a linear momentum $\boldsymbol{l}$ to the sum of all external forces $\boldsymbol{k}$ as

$$\dot{\boldsymbol{l}} = \boldsymbol{k}. \tag{3.8}$$

Thereby, the linear momentum and the external force contributions are defined as

$$\boldsymbol{l} = \int_{\mathcal{B}} \rho \, \dot{\boldsymbol{x}} \, \mathrm{dv} \quad \text{and} \quad \boldsymbol{k} = \int_{\mathcal{B}} \underbrace{\rho \, \boldsymbol{b}}_{\boldsymbol{f}} \, \mathrm{dv} + \int_{\partial\mathcal{B}} \boldsymbol{t} \, \mathrm{da}, \tag{3.9}$$

where $\dot{\boldsymbol{x}}$ denotes the velocity of a material point, $\boldsymbol{f}$ refers to the body force vector resulting from the integral of the local external force $\rho \, \boldsymbol{b}$ over the current volume of $\mathcal{B}$ and $\boldsymbol{t} = \boldsymbol{\sigma} \cdot \boldsymbol{n}$ indicates the stress or traction vector acting on the surface $\partial\mathcal{B}$. The divergence theorem

$$\int_{\partial\mathcal{B}} \boldsymbol{\sigma} \cdot \boldsymbol{n} \, \mathrm{da} = \int_{\mathcal{B}} \mathrm{div} \, \boldsymbol{\sigma} \, \mathrm{dv} \tag{3.10}$$

allows to rewrite the external contribution of the forces in terms of volume integrals as

$$\boldsymbol{k} = \int_{\mathcal{B}} (\boldsymbol{f} + \operatorname{div} \boldsymbol{\sigma}) \, \mathrm{dv}. \tag{3.11}$$

With the help of the balance of mass, the material time derivative of the linear momentum appears as

$$\dot{\boldsymbol{l}} = \int_{\mathcal{B}} \rho \, \ddot{\boldsymbol{x}} \, \mathrm{dv}, \tag{3.12}$$

where $\ddot{\boldsymbol{x}}$ indicates the acceleration of a specific material point. Inserting both, Eq. 3.11 and Eq. 3.12, into Eq. 3.8 yields the strong form of the balance of linear momentum as

$$\rho \, \ddot{\boldsymbol{x}} = \boldsymbol{f} + \operatorname{div} \boldsymbol{\sigma}. \tag{3.13}$$

However, in the context of this work only mechanically static processes, i.e. $\ddot{\boldsymbol{x}} = 0$ as well as zero body force will be considered, what simplifies Eq. 3.13 to

$$\operatorname{div} \boldsymbol{\sigma} = \boldsymbol{0}. \tag{3.14}$$

Balance of angular momentum: The balance of angular momentum

$$\dot{\boldsymbol{h}}_0 = \boldsymbol{i}_0 \tag{3.15}$$

relates the angular momentum $\boldsymbol{h}_0$ to the net moment of all forces $\boldsymbol{i}_0$ that are acting on the body $\mathcal{B}$ with respect to a spatially defined point 0. Both can be expressed in terms of

$$\boldsymbol{h}_0 = \int_{\mathcal{B}} \boldsymbol{x} \times \rho \, \dot{\boldsymbol{x}} \, \mathrm{dv} \quad \text{and} \quad \boldsymbol{i}_0 = \int_{\mathcal{B}} \boldsymbol{x} \times \boldsymbol{f} \, \mathrm{dv} + \int_{\partial\mathcal{B}} \boldsymbol{x} \times \boldsymbol{t} \, \mathrm{da}. \tag{3.16}$$

Taking the time derivative of Eq. 3.16_1 and recalling the local statement of the balance of mass (Eq. 3.7), the time rate of the angular momentum appears as

$$\dot{\boldsymbol{h}}_0 = \int_{\mathcal{B}} \boldsymbol{x} \times \rho \, \ddot{\boldsymbol{x}} \, \mathrm{dv}. \tag{3.17}$$

Applying Cauchy's theorem $\boldsymbol{t} = \boldsymbol{\sigma} \cdot \boldsymbol{n}$ and the divergence theorem $\int_{\mathcal{B}} \boldsymbol{x} \times \boldsymbol{\sigma} \cdot \boldsymbol{n} \, \mathrm{da} = \int_{\mathcal{B}} \boldsymbol{x} \times \operatorname{div} \boldsymbol{\sigma} + \nabla_{\boldsymbol{x}} \boldsymbol{x} \times \boldsymbol{\sigma}^{\mathrm{T}} \, \mathrm{dv}$ with $\nabla_{\boldsymbol{x}} \boldsymbol{x} = \boldsymbol{I}$ to Eq. 3.16_2 yields

$$\boldsymbol{i}_0 = \int_{\mathcal{B}} \{\boldsymbol{x} \times (\boldsymbol{f} + \operatorname{div} \boldsymbol{\sigma}) + \boldsymbol{I} \times \boldsymbol{\sigma}\} \, \mathrm{dv}. \tag{3.18}$$

Insertion of Eq. 3.18 and Eq. 3.17 into Eq. 3.15 gives the balance of angular momentum

$$\int_{\mathcal{B}} \boldsymbol{x} \times \underbrace{(\boldsymbol{f} + \operatorname{div} \boldsymbol{\sigma} - \rho \ddot{\boldsymbol{x}})}_{=\boldsymbol{0} \text{ with Eq.3.13}} \, \mathrm{dv} + \int_{\mathcal{B}} \boldsymbol{I} \times \boldsymbol{\sigma} \, \mathrm{dv} = \boldsymbol{0} \quad \rightsquigarrow \quad \boldsymbol{I} \times \boldsymbol{\sigma} = \boldsymbol{0}. \tag{3.19}$$

The local statement in Eq. 3.19 postulates the symmetry of the Cauchy stress tensor, i.e.

$$\boldsymbol{\sigma} = \boldsymbol{\sigma}^{\mathrm{T}}. \tag{3.20}$$

3.3 Balance of energy/first law of thermodynamics

The energy balance, also referred to as the first law of thermodynamics, equates the time rates of the kinetic $\mathcal{K}$ as well as the internal energy $\mathcal{U}$ with the sum of all internal and external energy contributions (mechanical, thermal, magnetic, etc.) acting on the body $\mathcal{B}$. In the context of this work only mechanical, magnetic and, thermal processes are considered. Hence, the balance of energy reads as

$$\dot{\mathcal{K}} + \dot{\mathcal{U}} = \mathcal{W}_{\text{mec}} + \mathcal{W}_{\text{mag}} + \mathcal{Q}, \tag{3.21}$$

with the kinetic and the internal energies

$$\mathcal{K} = \frac{1}{2}\int_{\mathcal{B}} \rho\, \dot{\boldsymbol{x}} \cdot \dot{\boldsymbol{x}}\, \mathrm{dv} \quad \text{and} \quad \mathcal{U} = \int_{\mathcal{B}} \rho\, U\, \mathrm{dv} \tag{3.22}$$

as well as the specific internal energy density U. Their corresponding time rates appear as

$$\dot{\mathcal{K}} = \int_{\mathcal{B}} (\rho\, \dot{\boldsymbol{x}} \cdot \dot{\boldsymbol{x}}\, \mathrm{dv})^{\cdot} = \int_{\mathcal{B}} \rho\, \dot{\boldsymbol{x}} \cdot \ddot{\boldsymbol{x}}\, \mathrm{dv} \quad \text{and} \quad \dot{\mathcal{U}} = \int_{\mathcal{B}} \left(\rho \dot{U}\, \mathrm{dv}\right)^{\cdot} = \int_{\mathcal{B}} \rho \dot{U}\, \mathrm{dv} \tag{3.23}$$

by recalling Eq. 3.3 and the balance of mass. The energy entering or leaving the system can be of mechanical, magnetic or thermal nature. These contributions can be stated as

$$\begin{aligned} \mathcal{W}_{\text{mec}} &= \int_{\mathcal{B}} \dot{\boldsymbol{x}} \cdot \boldsymbol{f}\, \mathrm{dv} + \int_{\partial\mathcal{B}} \dot{\boldsymbol{x}} \cdot \boldsymbol{t}\, \mathrm{da}, \\ \mathcal{W}_{\text{mag}} &= \int_{\mathcal{B}} \dot{\boldsymbol{B}} \cdot \boldsymbol{H}\, \mathrm{dv}, \\ \text{and} \qquad \mathcal{Q} &= \int_{\mathcal{B}} \rho\, r\, \mathrm{dv} - \int_{\partial\mathcal{B}} \boldsymbol{q} \cdot \boldsymbol{n}\, \mathrm{da}, \end{aligned} \tag{3.24}$$

with the internal heat source r and the heat influx $\boldsymbol{q}$. The relation $\boldsymbol{t} = \boldsymbol{\sigma} \cdot \boldsymbol{n}$ as well as the divergence theorem allow to convert the surface integral in Eq. 3.24_1 into a volume integral as

$$\int_{\partial\mathcal{B}} \dot{\boldsymbol{x}} \cdot (\boldsymbol{\sigma} \cdot \boldsymbol{n})\, \mathrm{da} = \int_{\partial\mathcal{B}} (\boldsymbol{\sigma}^{\mathrm{T}} \cdot \dot{\boldsymbol{x}}) \cdot \boldsymbol{n}\, \mathrm{da} = \int_{\mathcal{B}} \mathrm{div}(\boldsymbol{\sigma}^{\mathrm{T}} \cdot \dot{\boldsymbol{x}})\, \mathrm{dv}. \tag{3.25}$$

The divergence theorem is also applied to Eq. 3.24_3. Hence, the reformulation of Eq. 3.24_1 and Eq. 3.24_3 yield

$$\mathcal{W}_{\text{mec}} = \int_{\mathcal{B}} (\boldsymbol{f} + \mathrm{div}\, \boldsymbol{\sigma}) \cdot \dot{\boldsymbol{x}}\, \mathrm{dv} + \int_{\mathcal{B}} \boldsymbol{\sigma} : \boldsymbol{L}\, \mathrm{dv} \quad \text{and} \quad \mathcal{Q} = \int_{\mathcal{B}} (\rho\, r\, - \mathrm{div}\, \boldsymbol{q})\, \mathrm{dv}, \tag{3.26}$$

where $\boldsymbol{L} = \nabla \dot{\boldsymbol{x}} = \boldsymbol{D} + \boldsymbol{W}$ denotes the spacial velocity gradient, that can be additively decomposed into a symmetric $\boldsymbol{D} = \frac{1}{2}(\boldsymbol{L} + \boldsymbol{L}^{\mathrm{T}})$ and a non-symmetric part $\boldsymbol{W} = \frac{1}{2}(\boldsymbol{L} - \boldsymbol{L}^{\mathrm{T}})$. Since $\boldsymbol{\sigma} : \boldsymbol{W} = 0$, only the symmetric part contributes to the following. Inserting Eq. 3.23, Eq. 3.24, and Eq. 3.26 into Eq. 3.21 yields the total balance of energy as

$$\begin{aligned} \int_{\mathcal{B}} \rho \dot{U}\, \mathrm{dv} = \int_{\mathcal{B}} (\underbrace{\boldsymbol{f} - \rho\, \ddot{\boldsymbol{x}} + \mathrm{div}\, \boldsymbol{\sigma}}_{=\boldsymbol{0}\ \text{with Eq.3.13}}) \cdot \dot{\boldsymbol{x}}\, \mathrm{dv} + \int_{\mathcal{B}} \boldsymbol{\sigma} : \boldsymbol{D}\, \mathrm{dv} \\ + \int_{\mathcal{B}} \dot{\boldsymbol{B}} \cdot \boldsymbol{H}\, \mathrm{dv} + \int_{\mathcal{B}} (\rho\, r\, - \mathrm{div}\, \boldsymbol{q})\, \mathrm{dv}. \end{aligned} \tag{3.27}$$

Since only small deformations are considered, the relation $\dot{\boldsymbol{\varepsilon}} = \boldsymbol{D}$ holds and the balance of energy can be stated in its local form as

$$\rho \dot{U} = \boldsymbol{\sigma} : \dot{\boldsymbol{\varepsilon}} + \dot{\boldsymbol{B}} \cdot \boldsymbol{H} + \rho r - \operatorname{div} \boldsymbol{q}. \tag{3.28}$$

3.4 Entropy inequality/second law of thermodynamics

The second law of thermodynamics is not a conservation law, but an inequality that determines a physically driven process direction. While the first law of thermodynamics describes the lossless transformation of energy from one state to another, the second law of thermodynamics gives a direction for this conversion. These conditions are strongly related to the thermal energy within a body $\mathcal{B}$ and can be expressed by the physical concept of entropy $\mathcal{S}$ defined by

$$\mathcal{S} = \int_{\mathcal{B}} \rho \eta \, \mathrm{dv}, \tag{3.29}$$

where η is the entropy density. Energetically non-dissipative processes are generally referred to as reversible and accompanied by a constant amount of entropy. This contrasts with energetically dissipative processes. These are referred to as irreversible processes and characterized by the generation of entropy. An annihilation of entropy is physically impossible, thus entropy within a system can either remain constant or increase. This can be summarized as: The change in entropy over time is always greater than or equal to the contribution added to the system by an internal heat source or heat influx across the surface $\partial\mathcal{B}$. Mathematically follows

$$\dot{\mathcal{S}} \geq \int_{\mathcal{B}} \frac{\rho r}{\vartheta} \, \mathrm{dv} - \int_{\partial\mathcal{B}} \frac{\boldsymbol{q} \cdot \boldsymbol{n}}{\vartheta} \, \mathrm{da}, \tag{3.30}$$

where ϑ represents the absolute temperature of the body. Application of the divergence theorem enables the representation of the local form

$$\rho \dot{\eta} \geq \frac{\rho r}{\vartheta} - \operatorname{div}\left(\frac{\boldsymbol{q}}{\vartheta}\right). \tag{3.31}$$

Utilizing the product rule $\operatorname{div}\left(\frac{\boldsymbol{q}}{\vartheta}\right) = \frac{1}{\vartheta} \operatorname{div} \boldsymbol{q} - \boldsymbol{q} \cdot \frac{1}{\vartheta^2} \nabla\vartheta$ the divergence term can be reformulated so that the entropy inequality yields

$$\vartheta \rho \dot{\eta} \geq \rho r - \operatorname{div} \boldsymbol{q} + \boldsymbol{q} \cdot \frac{1}{\vartheta} \nabla\theta. \tag{3.32}$$

Reformulating and inserting the local form of the balance of energy Eq. 3.28 in Eq. 3.32 and assuming isothermal processes yields

$$\rho \left(\vartheta \dot{\eta} - \dot{U}\right) + \boldsymbol{\sigma} : \dot{\boldsymbol{\varepsilon}} + \boldsymbol{B} \cdot \dot{\boldsymbol{H}} \geq 0. \tag{3.33}$$

3.5 Constitutive relations

In the following, magneto-mechanical constitutive relations are derived. For this purpose, thermodynamic potentials are analyzed and examined for their consistency according to the second law of thermodynamics. Thereby, the internal energy U is taken as a starting point. In general, there exist other thermodynamic potentials. A selection of these can be

taken from Tab. 3.1. It has to be noted, that these can be derived in terms of the internal energy. The internal energy is formulated in terms of extensive variables. These extensive variables depend on the size of the system under consideration (e.g. the volume V, strains $\boldsymbol{\varepsilon}$, ...) and thus contrast with intensive variables, which are independent of size (e.g. temperature ϑ, density ρ, ...). A pairing of an extensive and an intensive variable is called a work conjugate pair. For magneto-mechanical materials the internal energy $U := U(\boldsymbol{\varepsilon}, \boldsymbol{B}, \eta)$ is based on the mechanical strains $\boldsymbol{\varepsilon}$, the magnetic induction $\boldsymbol{B}$ as well as the entropy η. Its time rate yields

$$\dot{U} = \frac{\partial U}{\partial \boldsymbol{\varepsilon}} : \dot{\boldsymbol{\varepsilon}} + \frac{\partial U}{\partial \boldsymbol{B}} \cdot \dot{\boldsymbol{B}} + \frac{\partial U}{\partial \eta}\, \dot{\eta}. \tag{3.34}$$

Insertion of Eq. 3.34 into Eq. 3.32 allows the reformulation into

$$\left(\boldsymbol{\sigma} - \frac{\partial U}{\partial \boldsymbol{\varepsilon}}\right) : \dot{\boldsymbol{\varepsilon}} + \left(\boldsymbol{H} - \frac{\partial U}{\partial \boldsymbol{B}}\right) \cdot \dot{\boldsymbol{B}} + \left(\vartheta - \frac{\partial U}{\partial \eta}\right) \dot{\eta} \geq 0. \tag{3.35}$$

Evaluation of Eq. 3.35 indicates the stresses, the magnetic field, and the entropy

$$\boldsymbol{\sigma} = \frac{\partial U}{\partial \boldsymbol{\varepsilon}}, \quad \boldsymbol{H} = \frac{\partial U}{\partial \boldsymbol{B}}, \quad \text{and} \quad \vartheta = \frac{\partial U}{\partial \eta} \tag{3.36}$$

as partial derivatives of the internal energy. These quantities can be identified as the intensive counterparts to the extensive expressions. A reinsertion of these relations into the rate of the internal energy Eq. 3.34 yields

$$\dot{U} = \boldsymbol{\sigma} : \dot{\boldsymbol{\varepsilon}} + \boldsymbol{H} \cdot \dot{\boldsymbol{B}} + \vartheta\, \dot{\eta}. \tag{3.37}$$

However, in the analysis of magneto-mechanical processes it is reasonable to formulate the thermodynamic potential in terms of the process variables $\boldsymbol{\varepsilon}$ and $\boldsymbol{H}$, since it is more convenient to derive the equilibrium conditions in terms of the displacements $\boldsymbol{u}$ and the magnetic scalar potential φ. Therefore, a Legendre transformation based on the product rule $\boldsymbol{H} \cdot \dot{\boldsymbol{B}} = \overline{\boldsymbol{H} \cdot \boldsymbol{B}} - \boldsymbol{B} \cdot \dot{\boldsymbol{H}}$ is applied, so that the reformulation of Eq. 3.37 yields

$$\dot{U} = \boldsymbol{\sigma} : \dot{\boldsymbol{\varepsilon}} + \overline{\boldsymbol{H} \cdot \boldsymbol{B}} - \boldsymbol{B} \cdot \dot{\boldsymbol{H}} + \vartheta\, \dot{\eta} \quad \rightsquigarrow \quad \underbrace{\overline{U - \boldsymbol{H} \cdot \boldsymbol{B}}}_{:= \dot{H}_2(\boldsymbol{\varepsilon}, \boldsymbol{H}, \eta)} = \boldsymbol{\sigma} : \dot{\boldsymbol{\varepsilon}} - \boldsymbol{B} \cdot \dot{\boldsymbol{H}} + \vartheta\, \dot{\eta}, \tag{3.38}$$

what can be given as the magnetic enthalpy potential as

$$H_2 = U - \boldsymbol{H} \cdot \boldsymbol{B}. \tag{3.39}$$

Hence, the constitutive relations of the thermodynamically consistent, magneto-mechanically coupled material model appear as

$$\boldsymbol{\sigma} = \frac{\partial H_2}{\partial \boldsymbol{\varepsilon}}, \quad \boldsymbol{B} = \frac{\partial H_2}{\partial \boldsymbol{H}}, \quad \text{and} \quad \vartheta = \frac{\partial H_2}{\partial \eta}. \tag{3.40}$$

Since only isothermal processes are considered, Eq. 3.40 is already sufficient for the purposes of this work. For completeness, the material model is subsequently subjected to a further reformulation of Eq. 3.40_3, again using a Legendre transformation as $\vartheta\, \dot{\eta} = \overline{\vartheta\, \eta} - \dot{\vartheta}\, \eta$, yielding

$$\dot{H}_2 = \boldsymbol{\sigma} : \dot{\boldsymbol{\varepsilon}} - \boldsymbol{B} \cdot \dot{\boldsymbol{H}} + \overline{\vartheta\, \eta} - \dot{\vartheta}\, \eta \quad \rightsquigarrow \quad \underbrace{\overline{H_2 - \vartheta\, \eta}}_{:= \dot{G}_2(\boldsymbol{\varepsilon}, \boldsymbol{H}, \vartheta)} = \boldsymbol{\sigma} : \dot{\boldsymbol{\varepsilon}} - \boldsymbol{B} \cdot \dot{\boldsymbol{H}} + \eta\, \dot{\vartheta}. \tag{3.41}$$

Based on Eq. 3.41 the magnetic Gibbs energy can be introduced as

$$G_2 = U - \boldsymbol{H} \cdot \boldsymbol{B} - \vartheta\,\eta. \tag{3.42}$$

Thus, the entropy can be represented as a function of temperature as

$$\eta = \frac{\partial\, G_2}{\partial\, \vartheta}, \tag{3.43}$$

defining the whole set of constitutive relations based on Eq. 3.40 as

$$\boldsymbol{\sigma} = \frac{\partial\, G_2}{\partial\, \boldsymbol{\varepsilon}}, \quad \boldsymbol{B} = \frac{\partial\, G_2}{\partial\, \boldsymbol{H}}, \quad \text{and} \quad \eta = \frac{\partial\, G_2}{\partial\, \vartheta}. \tag{3.44}$$

In direct analogy to the potentials derived above, many other potentials and their associated rate equations can be given. An overview of the basic thermodynamic potentials is given in Tab. 3.1, cf. Lupascu et al. [2018] and Labusch [2018].

Table 3.1: Thermodynamic potentials and corresponding rate equations. Adopted from Labusch [2018].

Thermodynamic potential	Natural variables	Rate of thermodynamic potential
Internal energy U	$\boldsymbol{\varepsilon}$, $\boldsymbol{B}$, η	$\dot{U} = \boldsymbol{\sigma} : \dot{\boldsymbol{\varepsilon}} + \boldsymbol{H} \cdot \dot{\boldsymbol{B}} + \vartheta\,\dot{\eta}$
Free enegry $\psi = U - \vartheta\,\eta$	$\boldsymbol{\varepsilon}$, $\boldsymbol{B}$, θ	$\dot{\psi} = \boldsymbol{\sigma} : \dot{\boldsymbol{\varepsilon}} + \boldsymbol{H} \cdot \dot{\boldsymbol{B}} - \eta\,\dot{\vartheta}$
Enthalpy $H = U - \boldsymbol{\sigma} : \boldsymbol{\varepsilon} - \boldsymbol{H} \cdot \boldsymbol{B}$	$\boldsymbol{\sigma}$, $\boldsymbol{H}$, η	$\dot{H} = -\boldsymbol{\varepsilon} : \dot{\boldsymbol{\sigma}} - \boldsymbol{B} \cdot \dot{\boldsymbol{H}} + \vartheta\,\dot{\eta}$
Elastic enthalpy $H_1 = U - \boldsymbol{\sigma} : \boldsymbol{\varepsilon}$	$\boldsymbol{\sigma}$, $\boldsymbol{B}$, η	$\dot{H}_1 = -\boldsymbol{\varepsilon} : \dot{\boldsymbol{\sigma}} + \boldsymbol{H} \cdot \dot{\boldsymbol{B}} + \vartheta\,\dot{\eta}$
Magnetic enthalpy $H_2 = U - \boldsymbol{H} \cdot \boldsymbol{B}$	$\boldsymbol{\varepsilon}$, $\boldsymbol{H}$, η	$\dot{H}_2 = \boldsymbol{\sigma} : \dot{\boldsymbol{\varepsilon}} - \boldsymbol{B} \cdot \dot{\boldsymbol{H}} + \vartheta\,\dot{\eta}$
Magnetic energy $G = U - \boldsymbol{\sigma} : \boldsymbol{\varepsilon} - \boldsymbol{H} \cdot \boldsymbol{B} - \vartheta\,\eta$	$\boldsymbol{\sigma}$, $\boldsymbol{H}$, θ	$\dot{G} = -\boldsymbol{\varepsilon} : \dot{\boldsymbol{\sigma}} - \boldsymbol{B} \cdot \dot{\boldsymbol{H}} - \eta\,\dot{\vartheta}$
Elastic Gibbs energy $G_1 = U - \boldsymbol{\sigma} : \boldsymbol{\varepsilon} - \vartheta\,\eta$	$\boldsymbol{\sigma}$, $\boldsymbol{D}$, θ	$\dot{G}_1 = -\boldsymbol{\varepsilon} : \dot{\boldsymbol{\sigma}} + \boldsymbol{H} \cdot \dot{\boldsymbol{B}} - \eta\,\dot{\vartheta}$
Magnetic Gibbs energy $G_2 = U - \boldsymbol{H} \cdot \boldsymbol{B} - \vartheta\,\eta$	$\boldsymbol{\varepsilon}$, $\boldsymbol{H}$, θ	$\dot{G}_2 = \boldsymbol{\sigma} : \dot{\boldsymbol{\varepsilon}} - \boldsymbol{B} \cdot \dot{\boldsymbol{H}} - \eta\,\dot{\vartheta}$

4 Magnetostatic problems

In many scientific fields, physical phenomena and their underlying mechanisms are studied. To obtain an in-depth understanding of those phenomena, mathematical models can be applied in a supportive way. These models are generally based on differential equations depending on the considered variables. Within the context of magnetostatic problems the magnetic Gauss law is applied to describe the evolution of magnetic fields. In magnetism the interaction between the magnetic solid and its surrounding free space is of crucial importance for the correct description of the most important magnetic mechanisms. The so-called demagnetization fields inside a magnet and the stray fields outside the magnet are directly affected by the magnetic solid. Stray fields evolve in the immediate surrounding of a magnet but loose intensity with increasing distance. Here, the question of the required distance between the magnet and the vanishing of the stray field sets the prerequisites for an open boundary value problem. Besides the introduction into magnetism and magnetic materials given in Sec. 2 a general overview can be found in standard literature as Bertotti [1998], Jiles [2015], and Coey [2010]. For simple geometries analytical solutions of the differential equations are often available, but as soon as these geometries become complex, a numerical approximation of the solution is required. A particularly flexible approximation scheme for differential equations on complex but finite geometries is provided by the finite element method (FEM). Over the last decades, the FEM has become a reliable tool that can be found in pure research codes but also in commercially distributed programs. A fundamental overview on the FEM is given in standard literature such as Wriggers [2001], Bathe [1986], Zienkiewicz and Taylor [2005], and Korelc and Wriggers [2016].
This chapter starts with an introduction to the FEM fundamentals for the governing field equation in magnetostatics, which is the Gauss law. Subsequently, an overview on numerical methods that are able to treat the magnetostatic open boundary value problem is given. Afterwards, an FE-based method for the treatment of open boundary value problems is presented, which utilizes the Schur complement. Finally, a hybrid FEM-SBFEM formulation is proposed.

Parts of this chapter are published in:
J. Schröder, M. Reichel and C. Birk, An efficient numerical scheme for the FE-approximation of magnetic stray fields in infinite domains, *Computational Mechanics*, 70:141-153, (2022).

C. Birk, M. Reichel and J. Schröder, Magnetostatic simulations with consideration of exterior domains using the scaled boundary finite element method, *Computer Methods in Applied Mechanics and Engineering*, 399:115362, (2022), Copyright Elsevier.

4.1 Finite element method for magnetostatic problems

In this section the general procedure of solving differential equations using the finite element method based on the example of the magnetic Gauss law is described. Initially, the complete boundary value problem is defined, including the magnetic Gauss law as well as the corresponding essential (Dirichlet) and natural (Neumann) boundary conditions for an arbitrarily shaped body $\mathcal{B}$. Subsequently, the introduced boundary value problem is transferred into its discrete analog using the FEM. This leads to an algebraic expression, that can be solved using, e.g. Newton-like iteration methods.

4.1.1 Magnetostatic boundary value problem

The governing field equation within the considered boundary value problem is the magnetic Gauss law

$$\operatorname{div} \boldsymbol{B} = \boldsymbol{0} \quad \text{with} \quad \boldsymbol{B} = \boldsymbol{\mu} \cdot (\boldsymbol{H} + \boldsymbol{M}) \quad \text{on} \quad \mathcal{B}, \tag{4.1}$$

where $\boldsymbol{B}$ indicates the magnetic induction, $\boldsymbol{M}$ the magnetization and $\boldsymbol{\mu}$ the magnetic material tensor. Eq. 4.1 is also referred to as strong form of the magnetic Gauss law. Let φ denote a magnetic scalar potential then the magnetic field can be derived via its negative gradient

$$\boldsymbol{H} := -\nabla\varphi. \tag{4.2}$$

A full description of the boundary value problem requires the definition of suited boundary conditions on $\partial\mathcal{B} = \partial\mathcal{B}_\varphi \cup \partial\mathcal{B}_B$, with $\partial\mathcal{B}_\varphi \cap \partial\mathcal{B}_B = \emptyset$ corresponding to the scalar potential

$$\varphi = \varphi_0 \quad \text{on} \quad \partial\mathcal{B}_\varphi \quad \text{and} \quad \boldsymbol{B} \cdot \boldsymbol{n} = \zeta_0 \quad \text{on} \quad \partial\mathcal{B}_B \tag{4.3}$$

as essential (Dirichlet) or natural (Neumann) boundary conditions.

Weak formulation of the magnetostatic boundary value problem

The strong form of the magnetic Gauss law (Eq. 4.1) is transferred into its weak form by applying the standard Galerkin method, being a weighted residual approach. This requires the preliminary definition of the function spaces and their associated norms to fully describe the unknown field variable φ and its corresponding virtual counterpart φ. Let $a \in \mathbb{R}$ denote a scalar-valued function, $\boldsymbol{a} \in \mathbb{R}^3$ a vector-valued function, and $\boldsymbol{A} \in \mathbb{R}^{3\times3}$ a matrix-valued function. The $L^2(\mathcal{B})$-space can be formally expressed as

$$L^2 \;:=\; \left\{ a : \|a\|_{L^2(\mathcal{B})} < \infty \right\}, \quad \text{with} \quad \|a\|_{L^2(\mathcal{B})} = \sqrt{\int_{\mathcal{B}} |a|^2 \,\mathrm{dv}} \tag{4.4}$$

being the corresponding $L^2(\mathcal{B})$-norm for scalar valued functions a on the domain $\mathcal{B} \in \mathbb{R}^3$. Vector- and matrix-valued functions $\boldsymbol{a} \in [L^2(\mathcal{B})]^3$ and $\boldsymbol{A} \in [L^2(\mathcal{B})]^{3\times3}$ require the norms

$$\|\boldsymbol{a}\|_{L^2(\mathcal{B})} = \sqrt{\int_{\mathcal{B}} \boldsymbol{a} \cdot \boldsymbol{a} \,\mathrm{dv}} \quad \text{and} \quad \|\boldsymbol{A}\|_{L^2(\mathcal{B})} = \sqrt{\int_{\mathcal{B}} \boldsymbol{A} : \boldsymbol{A} \,\mathrm{dv}} \tag{4.5}$$

on the domain $\mathcal{B} \subseteq \mathbb{R}^3$. With the definition of Eq. 4.5 the $L^2(\mathcal{B})$-space of the vector-valued function $\boldsymbol{a}$ as well as matrix-valued function $\boldsymbol{A}$ the can be defined as

$$L^2 \;:=\; \{\boldsymbol{a} : \|\boldsymbol{a}\|_{L^2} < \infty\} \quad \text{and} \quad L^2 \;:=\; \{\boldsymbol{A} : \|\boldsymbol{A}\|_{L^2} < \infty\}. \tag{4.6}$$

The definition of the $L^2(\mathcal{B})$-space allows to express the function space H^1 for scalar functions a, vectorial functions $\boldsymbol{a}$, and matrix functions $\boldsymbol{A}$ as

$$\begin{aligned} H^1_a(\mathcal{B}) \;&:=\; \left\{ a \in L^2(\mathcal{B}) \;:\; \nabla a \in L^2(\mathcal{B}) \right\}, \\ H^1_{\boldsymbol{a}}(\mathcal{B}) \;&:=\; \left\{ \boldsymbol{a} \in L^2(\mathcal{B}) \;:\; \nabla \boldsymbol{a} \in L^2(\mathcal{B}) \right\}, \\ \text{and} \quad H^1_{\boldsymbol{A}}(\mathcal{B}) \;&:=\; \left\{ \boldsymbol{A} \in L^2(\mathcal{B}) \;:\; \nabla \boldsymbol{A} \in L^2(\mathcal{B}) \right\}. \end{aligned} \tag{4.7}$$

Subsequently, the functions of the solution $\varphi \in H^1$ and their virtual counter parts $\delta\varphi \in H^1$ (also called test functions) can be specified as

$$\begin{aligned} \Phi &= \{\varphi : \mathcal{B} \to \mathbb{R} \,|\, \varphi \in H^1(\mathcal{B});\;\; \varphi|_{\partial\mathcal{B}_\varphi} = \varphi_0\} \\ \text{and} \quad \delta\Phi &= \{\delta\varphi : \mathcal{B} \to \mathbb{R} \,|\, \delta\varphi \in H^1(\mathcal{B});\;\; \delta\varphi|_{\partial\mathcal{B}_\varphi} = 0\}. \end{aligned} \tag{4.8}$$

Eq. 4.1 is multiplied by the test functions $\delta\varphi$ and integrated over the volume $\mathcal{B}$ of the considered body, resulting in

$$G_\varphi = \int_{\mathcal{B}} \operatorname{div} \boldsymbol{B}\ \delta\varphi \,\mathrm{dv} = 0. \tag{4.9}$$

Since the induction depends on the magnetic field, which is obtained by taking the derivative of the scalar potential φ, Eq. 4.9 requires the double derivative of φ. Applying the product rule $\operatorname{div}(\boldsymbol{B}\delta\varphi) = \operatorname{div}\boldsymbol{B}\delta\varphi + \boldsymbol{B}\cdot\nabla\varphi$, rearranging it to $\operatorname{div}\boldsymbol{B}\delta\varphi = \operatorname{div}(\boldsymbol{B}\delta\varphi) - \boldsymbol{B}\cdot\nabla\varphi$ and considering the virtual magnetic field to be defined as $\delta\boldsymbol{H} := -\nabla\delta\varphi$ the weak form yields

$$G_\varphi = \int_{\mathcal{B}} \boldsymbol{B}\cdot\delta\boldsymbol{H}\,\mathrm{dv} + \int_{\mathcal{B}} \operatorname{div}(\boldsymbol{B}\delta\varphi)\,\mathrm{dv} = 0. \tag{4.10}$$

Finally, the volume integral in Eq. 4.10 can be transferred into a surface integral by using Gauss's theorem $\int_{\mathcal{B}} \operatorname{div}(\boldsymbol{B}\delta\varphi)\,\mathrm{dv} = \int_{\partial\mathcal{B}} \delta\varphi(\boldsymbol{B}\cdot\boldsymbol{n})\,\mathrm{da}$ and Cauchy's theorem $\boldsymbol{B}\cdot\boldsymbol{n} = \zeta$ as

$$G_\varphi = G_\varphi(\varphi,\delta\varphi) = \underbrace{\int_{\mathcal{B}} \boldsymbol{B}\cdot\delta\boldsymbol{H}\,\mathrm{dv}}_{G_\varphi^{\mathrm{int}}} + \underbrace{\int_{\partial\mathcal{B}} \zeta_0\delta\varphi\,\mathrm{da}}_{G_\varphi^{\mathrm{ext}}} = 0, \tag{4.11}$$

where G_φ^{int} and G_φ^{ext} represent the internal and external magnetic work, respectively.

Linearization of the weak formulation

Arbitrary non-linear problems often depend on iterative solution procedures like Newton's method, which requires the linearization of Eq. 4.11 for a given point $\varphi = \hat{\varphi}$ following

$$Lin\, G_\varphi(\hat{\varphi},\,\delta\varphi,\,\Delta\varphi) := G_\varphi(\hat{\varphi},\,\delta\varphi) + \Delta G_\varphi(\hat{\varphi},\,\delta\varphi,\,\Delta\varphi). \tag{4.12}$$

Using the directional derivative of $G_\varphi(\varphi,\,\delta\varphi)$ at $\hat{\varphi}$ into the direction of $\Delta\varphi$ the linear increment yields

$$\Delta G_\varphi(\hat{\varphi},\,\delta\varphi,\,\Delta\varphi) = \frac{\mathrm{d}}{\mathrm{d}\epsilon}\left[G_\varphi(\hat{\varphi}+\epsilon\,\Delta\varphi,\,\delta\varphi)\right]\Big|_{\epsilon=0} = DG_\varphi(\hat{\varphi},\,\delta\varphi)\cdot\Delta\varphi, \tag{4.13}$$

where $\Delta\varphi$ denotes the incremental scalar potential and $\epsilon\in\mathbb{R}$ a scalar parameter. Conservative behavior of the external loading ζ_0 is assumed, i.e. the directional derivative yields $\Delta G_\varphi^{\mathrm{ext}} = 0$. Hence, the linear increment of Eq. 4.11 can be given as

$$\Delta G_\varphi = \int_{\mathcal{B}} \delta\boldsymbol{H}\cdot\Delta\boldsymbol{B}\,\mathrm{dv} = \int_{\mathcal{B}} \delta\boldsymbol{H}\cdot\frac{\partial\boldsymbol{B}}{\partial\boldsymbol{H}}\cdot\Delta\boldsymbol{H}\,\mathrm{dv} = \int_{\mathcal{B}} \delta\boldsymbol{H}\cdot\boldsymbol{\mu}\cdot\Delta\boldsymbol{H}\,\mathrm{dv}, \tag{4.14}$$

with $\Delta\boldsymbol{H}$ and $\boldsymbol{\mu}$ indicating the incremental magnetic field and the magnetic material tensor.

4.1.2 Discretization and assembly procedure

Discretization of the variables, weak formulations, and increments

A numerical approximation of the weak form in an arbitrarily formed continuum $\mathcal{B}$ requires the transformation of $\mathcal{B}$ into a discrete counterpart $\mathcal{B}^{\mathrm{h}}$. This discrete continuum consists of $\mathrm{num}_{\mathrm{ele}}$ sub-domains the so-called finit elements, i.e.

$$\mathcal{B} \approx \mathcal{B}^{\mathrm{h}} = \bigcup_{\mathrm{e}=1}^{\mathrm{num}_{\mathrm{ele}}} \mathcal{B}^{\mathrm{e}}, \tag{4.15}$$

where $\mathcal{B}^{\mathrm{e}}$ denotes the individual finite elements. This discretization step, from a continuous to a discrete continuum, is sketched in Fig. 4.1.

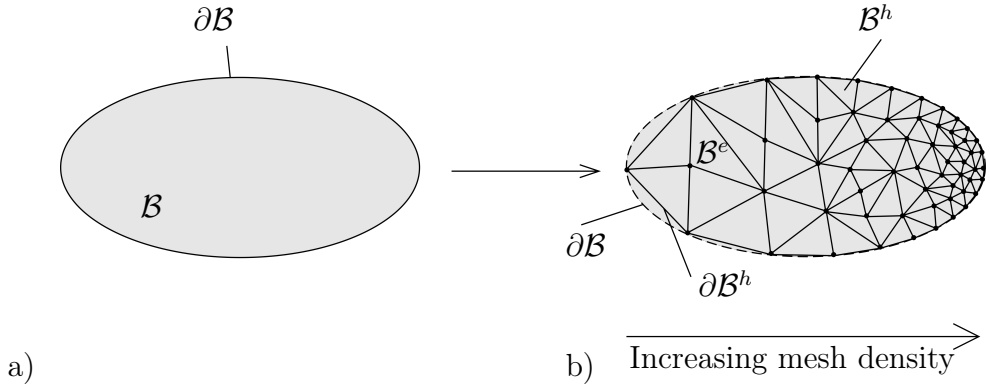

Figure 4.1: a) a continuum $\mathcal{B}$ is transferred into b) its discrete counterpart $\mathcal{B}^{\mathrm{h}}$, which is a composition of finite elements $\mathcal{B}^{\mathrm{e}}$.

The discrete FEM formulation is presented in matrix-vector notation. In detail both first- and second-order tensors are structured in vectors $\in \mathbb{R}^{1\times n}$, whereas higher-order tensors are structured in matrices $\in \mathbb{R}^{n\times m}$. In contrast to tensors, matrices and vectors are indicated by an underline $\underline{\bullet}$. The domain $\mathcal{B}$, the associated position vector $\boldsymbol{x}$, and the unknown variable φ are approximated by the same interpolation functions N^{I}. In this case, $\mathrm{n}_{\mathrm{nodes}}$ indicates the number of existing nodes in the element and I indicates the current node. This approach, known as the isoparametric concept, leads to the approximated quantities by multiplying the interpolation functions node-wise by the corresponding nodal position vector $\underline{\boldsymbol{x}}^{\mathrm{I}}$ or the degree of freedom d^{I} as

$$\underline{\boldsymbol{x}} = \sum_{\mathrm{I}=1}^{\mathrm{n}_{\mathrm{nodes}}} \mathrm{N}^{\mathrm{I}}(\underline{\boldsymbol{\xi}})\underline{\boldsymbol{x}}^{\mathrm{I}} \quad \text{and} \quad \varphi = \sum_{\mathrm{I}=1}^{\mathrm{n}_{\mathrm{nodes}}} \mathrm{N}^{\mathrm{I}}(\underline{\boldsymbol{\xi}})d^{\mathrm{I}}_{\varphi}. \tag{4.16}$$

The interpolation functions are defined within the so-called isoparametric space described by the natural coordinates $\underline{\boldsymbol{\xi}} := \{\xi, \eta, \zeta\}$. Hence, a transformation from the isoparametric to the physical space needs to be executed. This is achieved by applying the chain rule

$$\frac{\partial \mathrm{N}^{\mathrm{I}}(\underline{\boldsymbol{\xi}})}{\partial \underline{\boldsymbol{x}}} = \frac{\partial \mathrm{N}^{\mathrm{I}}(\underline{\boldsymbol{\xi}})}{\partial \underline{\boldsymbol{\xi}}} \frac{\partial \underline{\boldsymbol{\xi}}}{\partial \underline{\boldsymbol{x}}} = \underline{\boldsymbol{J}}^{-T} \frac{\partial \underline{\boldsymbol{\xi}}}{\partial \underline{\boldsymbol{x}}}, \tag{4.17}$$

with $\underline{\boldsymbol{J}}$ denoting the Jacobian matrix.

By applying the isoparametric concept to the virtual δd^{I} and incremental Δd^{I} degrees of freedom, the interpolations yield

$$\delta\varphi = \sum_{\mathrm{I}=1}^{\mathrm{n}_{\mathrm{nodes}}} \mathrm{N}^{\mathrm{I}}(\underline{\boldsymbol{\xi}})\delta d^{\mathrm{I}}_{\varphi} \quad \text{and} \quad \Delta\varphi = \sum_{\mathrm{I}=1}^{\mathrm{n}_{\mathrm{nodes}}} \mathrm{N}^{\mathrm{I}}(\underline{\boldsymbol{\xi}})\Delta d^{\mathrm{I}}_{\varphi}. \tag{4.18}$$

Analogously to Eq. 4.18 the approximation of the corresponding gradients results in

$$-\underline{\boldsymbol{H}} = \sum_{\mathrm{I}=1}^{\mathrm{n}_{\mathrm{nodes}}} \underline{\mathrm{B}}^{\mathrm{I}}_{\varphi}(\underline{\boldsymbol{\xi}})d^{\mathrm{I}}_{\varphi}, \quad -\delta\underline{\boldsymbol{H}} = \sum_{\mathrm{I}=1}^{\mathrm{n}_{\mathrm{nodes}}} \underline{\mathrm{B}}^{\mathrm{I}}_{\varphi}(\underline{\boldsymbol{\xi}})\delta d^{\mathrm{I}}_{\varphi}, \quad \text{and} \quad -\Delta\underline{\boldsymbol{H}} = \sum_{\mathrm{I}=1}^{\mathrm{n}_{\mathrm{nodes}}} \underline{\mathrm{B}}^{\mathrm{I}}_{\varphi}(\underline{\boldsymbol{\xi}})\Delta d^{\mathrm{I}}_{\varphi}, \tag{4.19}$$

with $\underline{\mathbb{B}}^{\mathrm{I}}_{\varphi}$ indicating a vector that contains the spatial derivatives of the interpolation functions as

$$\underline{\mathbb{B}}^{\mathrm{I}}_{\varphi} = \begin{bmatrix} \mathbb{N}^{\mathrm{I}}_{,1} \\ \mathbb{N}^{\mathrm{I}}_{,2} \\ \mathbb{N}^{\mathrm{I}}_{,3} \end{bmatrix} . \tag{4.20}$$

With all these definitions at hand, the discrete counterparts of Eq. 4.11 and Eq. 4.14 can be expressed as

$$G^{\mathrm{h}}_{\varphi} = \sum_{\mathrm{I}=1}^{\mathrm{n_{nodes}}} \delta d^{\mathrm{I}}_{\varphi} \underbrace{\int_{\mathcal{B}} (\underline{\mathbb{B}}^{\mathrm{I}}_{\varphi})^{\mathrm{T}} \underline{\boldsymbol{B}} \, \mathrm{dv} + \int_{\partial\mathcal{B}} \mathbb{N}^{\mathrm{I}}_{\varphi} \zeta_0 \, \mathrm{da}}_{\mathrm{R}^{\mathrm{I}}_{\varphi}} = (\delta \underline{d}^{\mathrm{e}}_{\varphi})^{\mathrm{T}} \, \underline{\mathbb{R}}^{\mathrm{e}}_{\varphi} \tag{4.21}$$

and

$$\Delta G^{\mathrm{h}}_{\varphi} = \sum_{\mathrm{I}=1}^{\mathrm{n_{nodes}}} \sum_{\mathrm{J}=1}^{\mathrm{n_{nodes}}} \delta d^{\mathrm{I}}_{\varphi} \underbrace{\int_{\mathcal{B}} (\underline{\mathbb{B}}^{\mathrm{I}}_{\varphi})^{\mathrm{T}} \underline{\boldsymbol{\mu}} \, \underline{\mathbb{B}}^{\mathrm{J}}_{\varphi} \, \mathrm{dv}}_{\mathrm{K}^{\mathrm{IJ}}_{\varphi\varphi}} \Delta d^{\mathrm{I}}_{\varphi} = (\delta \underline{d}^{\mathrm{e}}_{\varphi})^{\mathrm{T}} \, \underline{\mathbb{K}}^{\mathrm{e}}_{\varphi\varphi} \, \Delta \underline{d}^{\mathrm{e}}_{\varphi}, \tag{4.22}$$

where $\underline{\mathbb{R}}^{\mathrm{e}}_{\varphi}$ and $\underline{\mathbb{K}}^{\mathrm{e}}_{\varphi\varphi}$ indicate the element residual and system matrix associated to the virtual and incremental element degree of freedom vectors $\delta \underline{d}^{\mathrm{e}}_{\varphi}$ and $\Delta \underline{d}^{\mathrm{e}}_{\varphi}$.
The evaluation of the integrals, appearing in this formulation, is obtained by a numerical approximation, i.e. in the context of this work a five-point Gaussian quadrature. For more information on quadrature rules the reader is referred to Korelc and Wriggers [2016].

Assembling procedure of the global system of equations
The global boundary value problem is defined by the global counterparts of the residual vector $\underline{\mathbb{R}}$ and the system matrix $\underline{\mathbb{K}}$. These can be formed by assembling Eq. 4.21 and Eq. 4.22 over all elements as

$$\underline{\mathbb{K}} = \mathop{\mathsf{A}}_{\mathrm{e}=1}^{num_{ele}} \underline{\mathbb{K}}^{\mathrm{e}}_{\varphi\varphi} \quad \text{and} \quad \underline{\mathbb{R}} = \mathop{\mathsf{A}}_{\mathrm{e}=1}^{num_{ele}} \underline{\mathbb{R}}^{\mathrm{e}}_{\varphi}. \tag{4.23}$$

Together with the global counter parts of the virtual and incremental degree of freedom vectors $\delta \underline{\boldsymbol{D}} \neq \mathbf{0}$ and $\Delta \underline{\boldsymbol{D}}$ the global system of equations

$$\delta \underline{\boldsymbol{D}}^{\mathrm{T}} \, (\underline{\mathbb{K}} \, \Delta \underline{\boldsymbol{D}} + \underline{\mathbb{R}}) = 0 \quad \rightsquigarrow \quad \underline{\mathbb{K}} \, \Delta \underline{\boldsymbol{D}} = -\underline{\mathbb{R}} \tag{4.24}$$

yields the global degree of freedom vector $\underline{\boldsymbol{D}}$ by solving Eq. 4.24 using Newton's method and applying the update procedure $\underline{\boldsymbol{D}} \leftarrow \underline{\boldsymbol{D}} + \Delta \underline{\boldsymbol{D}}$. This procedure is repeated until the norm of the residual vector $||\underline{\mathbb{R}}||$ fulfills a predefined error criterion.

4.2 Motivation of magnetostatic open boundary problems

Ferromagnetic materials emit the so-called stray field in proximity to the magnetic solid. Within the magnet, this field is denoted as demagnetizing field, since it opposes the magnetization. Both contributions to the field, i.e. stray and demagnetizing field, are denoted as the magnetstatic field $\widetilde{\boldsymbol{H}}$ in the following and strongly depend on the geometry of the magnet under investigation. Therefore, certain effects which can be assigned to this field are called shape anisotropy. These magnetostatic fields and thus the magnetosatic energy can be minimized by the formation of magnetic domains. A selection of possible formations is shown in Fig. 4.2 together with the magnetostatic field in the outer space.

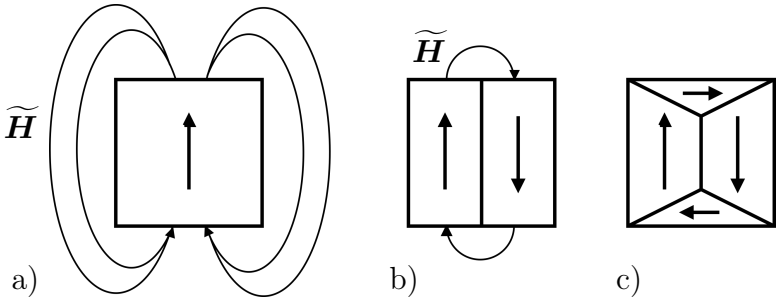

Figure 4.2: Subdivision of a magnet into magnetic domains such that the magnetostatic field $\widetilde{\boldsymbol{H}}$ can form closed loops and minimize the magnetostatic energy, with a) a single domain, b) double domains, and c) a closure domain, also known as Landau pattern.

Since the field contributes significantly to the magnetic behavior, the correct numerical representation of a magnet requires the consideration of the surrounding external space, as illustrated exemplarily in Fig. 4.3 for an Ni-thin film in terms of a finite element discretization.

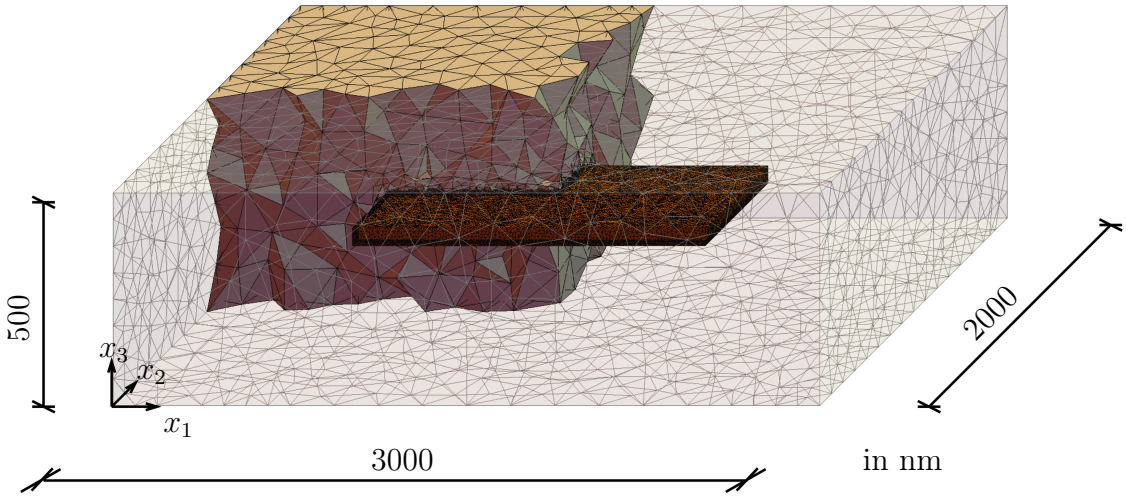

Ni-thin film: 1000 nm×500 nm×50 nm

Figure 4.3: An Ni-thin film of the dimensions 1000 nm×500 nm×50 nm is embedded within a free space matrix (3000 nm×2000 nm×500 nm). The dimensions of the free space are not true to scale for presentation purpose.

The Ni-thin film (Fig. 4.3) is fully magnetized by an external magnetic field along the x_1-axis. The resulting magnetization configuration is superimposed with the corresponding

stray field distribution in Fig. 4.4. This stray field distribution within the free space shows the typical cloud-like patterns, that originates from the magnetization distribution within the magnet. Removing the external magnetic field initiates a rearrangement of the magnetization into the so-called closure domain configuration presented in Fig. 4.5, which is also known as Landau pattern. This closure domain configuration indicates that the domain formation allows for a self-contained (divergence-free) representation of the magnetostatic field and thus there is no stray field around the magnet, cf. Cullity and Graham [2009] and Jiles [2015]. However, in order to find this configuration, the stray and demagnetizing fields must be correctly represented.

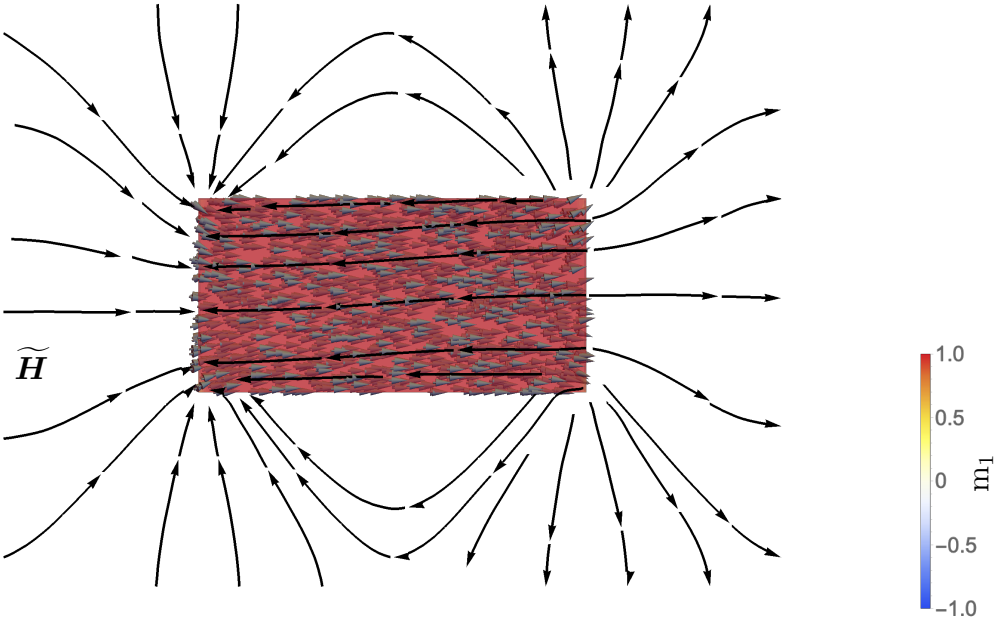

Figure 4.4: The magnetic single domain configuration of an Ni-thin film superimposed with the stream lines of the magnetostatic field $\widetilde{\boldsymbol{H}}$ within the surrounding free space.

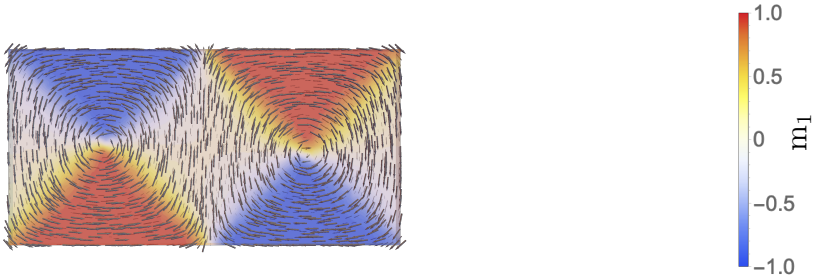

Figure 4.5: A closure domain pattern of an Ni-thin film that does not emit stray fields.

The $\widetilde{\boldsymbol{H}}$ field is derived from the negative derivative of a scalar potential $\widetilde{\varphi}$ with boundary conditions $\widetilde{\varphi}_0 = 0$ prescribed on a boundary $\partial\mathcal{B}_{\widetilde{\varphi}}$ located at infinity[6.]. Although the intensity of the stray field decreases with increasing distance from the magnetic solid, its vanishing distance cannot be predicted. This circumstance describes the general situation of a so-called open boundary problem, which makes the discrete representation of such an outer space difficult, since numerical methods like finite elements are only suitable for finite domains. Therefore, in each of the following two sections, a novel method for the efficient treatment of the magnetostatic open boundary problem is presented.

[6.] More information on the exact prescription of the boundary conditions and the derivation of the stray/demagnetizing field as well as the external magnetic field are provided in the following sections.

4.3 Overview on numerical methods for open boundary problems

A simple way to approximate the stray fields can be realized by defining a sufficiently large but finite exterior space around the magnetic solid and discretize it with finite elements. Since this technique cuts a "box" out of the infinite space and therefore introduces artificial boundaries, it is also known as *truncation method* and has been applied in the context of micromagnetic-mechanical simulations by Miehe and Ethiraj [2012], Reichel et al. [2022; 2023c] and Keip and Rambausek [2016; 2017]. A comprehensive overview of finite element open boundary techniques can also be found in Chen and Konrad [1997]. Here, the authors divide the various techniques into 12 subgroups, such as *truncation of outer boundaries*, *ballooning*, *infinite elements*, *infinitesimal scaling*, *absorbing boundary conditions*, and others. Chen and Konrad [1997] also introduce a useful rule of thumb for the domian of the truncation method to be at least five times larger than the interior domain. To ensure well-posedness of the problem, the Gaussian law requires for the considered case the boundary condition prescribed at infinity. Hence, error estimates have been developed by Bayliss et al. [1982] for several applications. Since a finite-element-based approach requires the replacement of the infinity condition by a boundary condition on a finite surface, they refer to those but also to higher-order boundary conditions. An electromagnetic wave absorbing layer based on a finite-difference time-domain free-space simulation method has been developed by Berenger [1994] for unbounded electromagnetic problems. Givoli [1991] reviewed local and non–local boundary conditions to solve wave problems numerically.

The *Boundary Element Method* (BEM) has proven to be well suited for the numerical treatment of linear magnetostatic problems consisting of homogeneous magnets surrounded by a free space. It requires only the discretization of the solid magnetic surfaces to accurately capture the influence of the surrounding free space as well. To consider nonlinear material behavior within the magnetic solid a hybrid FEM-BEM coupling can be applied, cf. Buchau et al. [2003]. Other hybrid methods based on FEM-BEM couplings have been developed by Aiello et al. [2003] to simulate time-harmonic eddy current problems in three-dimensional unbounded domains. However, due to large numbers of degrees of freedom, standard hybrid FEM-BEM couplings often lead unacceptable numerical costs. To lower the required memory demand and thus the computational effort Hertel et al. [2019] and Knittel et al. [2009] applied special hierarchical matrices. In a comparative study on numerical stray field computations Abert et al. [2013] analyzed finite-difference-based fast Fourier transform methods, tensor-grid methods, and a shell transformation-based finite element method with respect to their complexity, storage requirements, and accuracy. Depending on the task, the different methods have their advantages and disadvantages.

Another method that is well suited for modeling open boundary value problems is the so-called scaled boundary finite element method (SBFEM), which goes back to Wolf and Song [1994], Song and Wolf [1997] and Wolf and Song [2000]. For a comprehensive and up-to-date introduction into the theory of the SBFEM the reader is referred to Song [2018]. The SBFEM unifies the advantages of the FEM and the BEM. Its semi-analytical representation makes it particularly suited for modeling radiation damping in acoustics or dynamic problems in unbounded domains compare e.g. Birk et al. [2016], and Chen et al. [2015]. Electrostatic fields were calculated in 2D using the SBFEM by Liu and Lin [2012], where a special focus was placed on modeling prescribed potentials along side faces of bounded domains. Static and dynamic analyses

of magneto-electro-elastic plates and cylindrical shells within the context of the SBFEM have been published by e.g. Liu et al. [2016] and Ye et al. [2020]. Further applications of the SBFEM are the determination of effective properties in voided structures (Sladek et al. [2016]) as well as the crack analysis of magneto-electro-mechanically coupled materials (Nguyen et al. [2022]).

4.4 An efficient numerical scheme for the FE-approximation of magnetic stray fields in infinite domains

In this section, a simple and efficient method for the stray field approximation is derived and its functionality is demonstrated by numerical examples. The presented method formally belongs to the group of truncation methods and has been published in Schröder et al. [2022].

4.4.1 Magnetostatic open boundary problem

The domain of interest, already introduced in Eq. 4.15 as a continuum $\mathcal{B}$, is subdivided into an interior domain $\mathcal{B}^{\text{int}}$ and an exterior domain $\mathcal{B}^{\text{ext}}$. This subdivision is sketched in Fig. 4.6. Here, the light grey circular body depicts the outer domain, while the inner domain is a composition of the yellow circular body $\mathcal{B}^{\text{int}}_{\text{vac}}$ and the orange ellipse $\mathcal{B}^{\text{int}}_{\text{sol}}$. This implies that the internal domain is allowed to be inhomogeneous. The boundary between the inner and outer regions is denoted as $\partial\mathcal{B}^{\text{b}}$ and the boundary of the outer region as $\partial\mathcal{B}^{\text{ext}}$. The discrete boundary of the interior domain $\partial\mathcal{B}^{\text{int}}$ is associated to $\boldsymbol{n}^{\text{int}}$ describing the outward normal vector. Analogous to the internal domain $\mathcal{B}^{\text{int}}$, a normal vector $\boldsymbol{n}^{\text{ext}} := \boldsymbol{n}$ can also be defined for the inner surface $\partial\mathcal{B}^{\text{ext,i}}$ of the external domain. For both normal vectors on the joint surface $\partial\mathcal{B}^{\text{b}}$ the convention $\boldsymbol{n}^{\text{int}} = -\boldsymbol{n}^{\text{ext}}$ emerges.

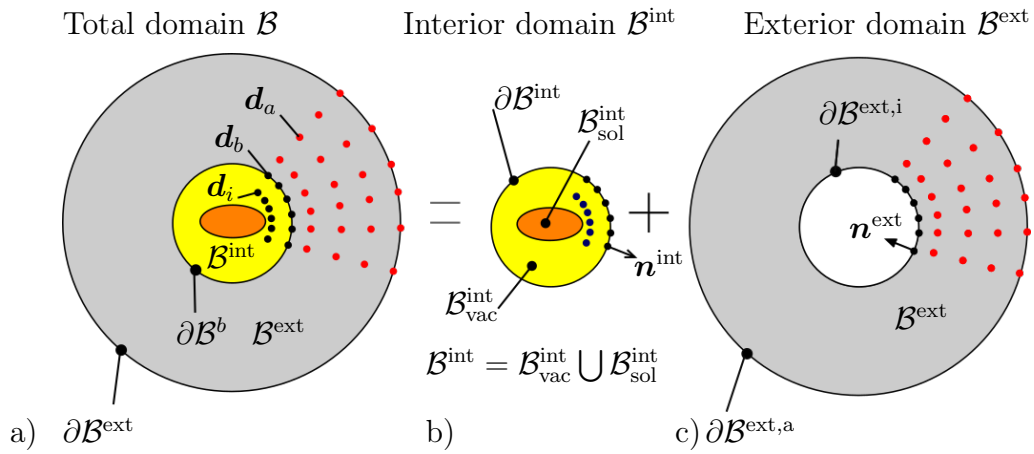

Figure 4.6: Visualization of the discrete subdivided domains and the definitions of the inner and outer boundaries. a) shows the total domain of interest $\mathcal{B}$ containing the interior and exterior subdomains, while b) defines the interior domain $\mathcal{B}^{\text{int}} = \mathcal{B}^{\text{int}}_{\text{vac}} \bigcup \mathcal{B}^{\text{int}}_{\text{sol}}$ and c) the exterior domain $\mathcal{B}^{\text{ext}}$. Taken from Schröder et al. [2022].

Recalling Eq. 4.1, Eq. 4.2, and Eq. 4.3, the here considered magnetostatic boundary value problem must be adapted to the subdivided continuum at this point. The definition of

the Gauss law with the induction and the magnetic field

$$\operatorname{div} \boldsymbol{B} = 0 \quad \text{with} \quad \boldsymbol{B} = \hat{\boldsymbol{B}}(\boldsymbol{H}) \quad \text{and} \quad \boldsymbol{H} = -\nabla\varphi \tag{4.25}$$

remains unaltered, whereas the definition of the surface of the boundary conditions is slightly modified to $\partial\mathcal{B}^{\text{ext,a}} = \partial\mathcal{B}_{\varphi}^{\text{ext,a}} \cup \partial\mathcal{B}_{B}^{\text{ext,a}}$ with $\partial\mathcal{B}_{\varphi}^{\text{ext,a}} \cap \partial\mathcal{B}_{B}^{\text{ext,a}} = \emptyset$. Hence, the corresponding boundary conditions can be specified as

$$\varphi = \varphi_0 \quad \text{on} \quad \partial\mathcal{B}_{\varphi}^{\text{ext,a}} \quad \text{and} \quad \boldsymbol{B} \cdot \boldsymbol{n} = \zeta_0 \quad \text{on} \quad \partial\mathcal{B}_{B}^{\text{ext,a}}. \tag{4.26}$$

Thus, the volume integral of the weak form must also be adjusted to

$$G_{\varphi} = \int_{\mathcal{B}^{\text{int}} \cup \mathcal{B}^{\text{ext}}} \delta\boldsymbol{H} \cdot \boldsymbol{B} \,\mathrm{dv} + \int_{\partial\mathcal{B}_{B}^{\text{ext}}} \zeta_0 \delta\varphi \,\mathrm{da}. \tag{4.27}$$

In the exterior domain a linear material behavior is assumed with the constitutive relation

$$\boldsymbol{B} = \boldsymbol{\mu} \cdot \boldsymbol{H} \quad \text{with} \quad \boldsymbol{\mu} = \mu_0 \boldsymbol{I}, \tag{4.28}$$

where $\boldsymbol{\mu}$, μ_0, and $\boldsymbol{I}$ denote the magnetic free space material tensor, the constant vacuum permeability, and the identity tensor. Thus, Eq. 4.27 and Eq. 4.28 allow to formulate a weak form for each of the internal and external domains as

$$\begin{aligned} G_{\varphi}^{\text{int}} &= \int_{\mathcal{B}^{\text{int}}} \delta\boldsymbol{H} \cdot \hat{\boldsymbol{B}}(\boldsymbol{H}) \,\mathrm{dv} \\ G_{\varphi}^{\text{ext}} &= \int_{\mathcal{B}^{\text{ext}}} \delta\boldsymbol{H} \cdot \boldsymbol{\mu} \cdot \boldsymbol{H} \,\mathrm{dv} + \int_{\partial\mathcal{B}_{B}^{\text{ext,a}}} \zeta_0 \delta\varphi \,\mathrm{da}. \end{aligned} \tag{4.29}$$

At this point some general considerations about the behavior of magnetic fields in homogeneous and heterogeneous continua are given, cf. Schmitz-Antoniak [2012/2013] and Coey [2010]. A constant magnetic field $\overline{\boldsymbol{H}}$ is applied over the entire domain $\mathcal{B}$ with vacuum permeability μ_0. If there are no other bodies with different magnetic permeability μ in the considered domain, the magnetic field remains undisturbed. Thus, no interference fields arise and the resulting induction yields $\overline{\boldsymbol{B}} = \mu_0 \overline{\boldsymbol{H}}$. Additionally, it holds $\operatorname{div} \overline{\boldsymbol{H}} = 0$. If a magnetic body $\mathcal{B}_{\text{sol}}$ with deviating magnetic permeability is positioned in the domain $\mathcal{B}$ and exposed to the external field $\overline{\boldsymbol{H}}$, a magnetization $\boldsymbol{M}$ occurs inside $\mathcal{B}_{\text{sol}}$. This causes sources and sinks on the surface of $\mathcal{B}_{\text{sol}}$. However, according to Maxwell's equations, these must not exist, since the magnetic induction must be divergence-free, as requested in $\operatorname{div} \boldsymbol{B} = 0$. Thus, the sources (sinks) of magnetization must be interpreted as sinks (sources) of a magnetic field $\widetilde{\boldsymbol{H}}$ (which is caused by the magnetization $\boldsymbol{M}$). Mathematically this condition can be expressed by

$$\operatorname{div} \boldsymbol{M} = -\operatorname{div} \widetilde{\boldsymbol{H}} \quad \rightsquigarrow \quad \operatorname{div} \left(\widetilde{\boldsymbol{H}} + \boldsymbol{M} \right) = 0. \tag{4.30}$$

Apparently, this leads to a magnetic field $\widetilde{\boldsymbol{H}}$ which opposes the magnetization within the magnetic solid under consideration. Thanks to the linearity of Maxwell's equations, the total magnetic field $\boldsymbol{H}$ can be expressed as the sum

$$\boldsymbol{H} = \widetilde{\boldsymbol{H}} + \overline{\boldsymbol{H}} \tag{4.31}$$

of the external and interference field. This interference field is better known as demagnetization field (inside the magnet) or stray field (outside the magnet). Hence, the total magnetic induction yields

$$\operatorname{div} \boldsymbol{B} = \mu_0 \operatorname{div}(\boldsymbol{H} + \boldsymbol{M}) = \mu_0 \operatorname{div}(\widetilde{\boldsymbol{H}} + \overline{\boldsymbol{H}} + \boldsymbol{M}) = 0. \tag{4.32}$$

From the above requirements, the following general considerations can be derived. The magnetic potential can be subdivided into a constant and external field related part as well as a fluctuation or demagnetizing part as

$$\varphi = \widetilde{\varphi} + \overline{\varphi} = \widetilde{\varphi}(\boldsymbol{x}) - \lambda \overline{\boldsymbol{H}} \cdot \boldsymbol{x} \tag{4.33}$$

where $\lambda \in [-1, 1]$ indicates a load parameter that can be used e.g. for cycling fields over time. Hence, an analogous split of the magnetic field into the external magnetic field as well as the demagnetization field follows as

$$\boldsymbol{H}(\boldsymbol{x}) := -\nabla \widetilde{\varphi}(\boldsymbol{x}) + \lambda \overline{\boldsymbol{H}} = \widetilde{\boldsymbol{H}}(\boldsymbol{x}) + \lambda \overline{\boldsymbol{H}}. \tag{4.34}$$

These assumptions lead to the substitutions

$$\delta\varphi(\boldsymbol{x}) \;\rightarrow\; \delta\widetilde{\varphi}(\boldsymbol{x}) \quad \text{and} \quad \delta\boldsymbol{H}(\boldsymbol{x}) \;\rightarrow\; -\nabla\, \delta\widetilde{\varphi}(\boldsymbol{x}) =: \delta\widetilde{\boldsymbol{H}}(\boldsymbol{x}) \tag{4.35}$$

of the virtual magnetic potential and magnetic field. With these modifications, the weak forms result in

$$\begin{aligned} G^{\text{int}}_{\widetilde{\varphi}} &= \int_{\mathcal{B}^{\text{int}}} \delta\widetilde{\boldsymbol{H}} \cdot \hat{\boldsymbol{B}}(\lambda\overline{\boldsymbol{H}} + \widetilde{\boldsymbol{H}})\, \mathrm{dv} \\ G^{\text{ext}}_{\widetilde{\varphi}} &= \int_{\mathcal{B}^{\text{ext}}} \delta\widetilde{\boldsymbol{H}} \cdot \boldsymbol{\mu} \cdot (\lambda\overline{\boldsymbol{H}} + \widetilde{\boldsymbol{H}})\, \mathrm{dv} + \int_{\partial\mathcal{B}^{\text{ext,a}}_{B}} \delta\widetilde{\varphi}\, \zeta_0\, \mathrm{da}\,. \end{aligned} \tag{4.36}$$

The external magnetic field $\overline{\boldsymbol{H}}$ is considered as a constant quantity in the simulations, while the fluctuation field $\widetilde{\boldsymbol{H}}$ depends on it. Hence, the corresponding degree of freedom is the magnetic fluctuation field with the boundary conditions

$$\widetilde{\varphi} = 0 \quad \text{on } \partial\mathcal{B}^{\text{ext,a}}_{\varphi} \tag{4.37}$$

prescribed on the complete outer boundary $\partial\mathcal{B}^{\text{ext,a}}$; thus $\partial\mathcal{B}^{\text{ext,a}} = \partial\mathcal{B}^{\text{ext,a}}_{\varphi}$ and $\partial\mathcal{B}^{\text{ext,a}}_{B} = \emptyset$. Before the discrete formulations are introduced, the linearization of Eq. 4.36 is given as

$$\begin{aligned} \Delta G^{\text{int}}_{\widetilde{\varphi}} &= \int_{\mathcal{B}^{\text{int}}} \delta\widetilde{\boldsymbol{H}} \cdot \boldsymbol{\mu}^{\tan}(\boldsymbol{H}) \cdot \Delta\widetilde{\boldsymbol{H}}\, \mathrm{dv} \quad \text{with} \quad \boldsymbol{\mu}^{\tan} = \partial_{\boldsymbol{H}} \hat{\boldsymbol{B}}(\lambda\overline{\boldsymbol{H}} + \widetilde{\boldsymbol{H}}) \\ \Delta G^{\text{ext}}_{\widetilde{\varphi}} &= \int_{\mathcal{B}^{\text{ext}}} \delta\widetilde{\boldsymbol{H}} \cdot \boldsymbol{\mu} \cdot \Delta\widetilde{\boldsymbol{H}}\, \mathrm{dv} \end{aligned} \tag{4.38}$$

following the procedure already described in Eq. 4.12.

4.4.2 Discrete variables

The discretization procedure of a continuum $\mathcal{B}$ can be considered analogue to the standard discretization with finite elements $\mathcal{B}^{\mathrm{e}}$ described in Eq. 4.15. However, additional subdivisions are introduced as

$$\begin{aligned} \mathcal{B} &= \mathcal{B}^{\mathrm{h,int}} \bigcup \mathcal{B}^{\mathrm{h,ext}} \\ \text{with} \quad \mathcal{B}^{\mathrm{int}} \approx \mathcal{B}^{\mathrm{h,int}} &= \bigcup_{e=1}^{\mathrm{num}_{\mathrm{ele}}^{\mathrm{int}}} \mathcal{B}^{\mathrm{e,int}} \quad \text{and} \quad \mathcal{B}^{\mathrm{ext}} \approx \mathcal{B}^{\mathrm{h,ext}} = \bigcup_{e=1}^{\mathrm{num}_{\mathrm{ele}}^{\mathrm{ext}}} \mathcal{B}^{\mathrm{e,ext}} \end{aligned} \tag{4.39}$$

for the internal and external domains $\mathcal{B}^{\mathrm{int}}$ and $\mathcal{B}^{\mathrm{ext}}$. The number of elements in the exterior and in the interior domain are denoted by $\mathrm{num}_{\mathrm{ele}}^{\mathrm{ext}}$ and $\mathrm{num}_{\mathrm{ele}}^{\mathrm{int}}$, respectively; thus, the total number of elements is $\mathrm{num}_{\mathrm{ele}} = \mathrm{num}_{\mathrm{ele}}^{\mathrm{int}} + \mathrm{num}_{\mathrm{ele}}^{\mathrm{ext}}$. Due to the substitution of the magnetic potential by the sum of a basic affine component and a fluctuation field, only the real and the virtual fluctuation field need to be discretized for a typical finite element $\mathcal{B}^{\mathrm{e}}$ as

$$\widetilde{\varphi} \approx \sum_{I=1}^{n_{node}} \mathbb{N}^I \widetilde{d}^I = \underline{\mathbb{N}}^e \underline{\widetilde{\boldsymbol{d}}}^e \quad \text{and} \quad \delta\widetilde{\varphi} \approx \sum_{I=1}^{n_{node}} \mathbb{N}^I \delta\widetilde{d}^I = \underline{\mathbb{N}}^e \delta\underline{\widetilde{\boldsymbol{d}}}^e \,, \tag{4.40}$$

where n_{node} are the number of nodes per element, $\mathbb{N}^I$ are the interpolation functions, $\underline{\mathbb{N}}^e$ denotes a matrix of interpolation functions, $\widetilde{d}^I$ the degrees of freedom, $\delta\widetilde{d}^I$ the virtual degrees of freedom, and $(\underline{\widetilde{\boldsymbol{d}}}^e, \delta\underline{\widetilde{\boldsymbol{d}}}^e)$ are the associated element vectors of unknowns. The following approximations are introduced for the magnetic fields

$$\underline{\widetilde{\boldsymbol{H}}} \approx -\sum_{I=1}^{n_{node}} \underline{\mathbb{B}}^I \widetilde{d}^I = \underline{\mathbb{B}}^e \underline{\widetilde{\boldsymbol{d}}}^e \quad \text{and} \quad \delta\underline{\widetilde{\boldsymbol{H}}} \approx -\sum_{I=1}^{n_{node}} \underline{\mathbb{B}}^I \delta\widetilde{d}^I = \underline{\mathbb{B}}^e \delta\underline{\widetilde{\boldsymbol{d}}}^e \tag{4.41}$$

where $\underline{\mathbb{B}}^I$ and $\underline{\mathbb{B}}^e$ respectively denote the node-wise and element-wise B-matrices, containing the Cartesian derivatives of the interpolation functions.

Discrete interior domain $\mathcal{B}^{\mathrm{int}}$

Substituting Eq. 4.41 into the weak form and its linear increment the discrete counter parts yield

$$\begin{aligned} G_{\varphi}^{\mathrm{h,int}} &= \sum_{\mathrm{e} \in \mathcal{B}^{\mathrm{h,int}}} \delta\underline{\widetilde{\boldsymbol{d}}}^{eT} \int_{\mathcal{B}^{\mathrm{e,int}}} \underline{\mathbb{B}}^{eT} \underline{\hat{\boldsymbol{B}}}(\underline{\boldsymbol{H}}) \,\mathrm{dv} = \sum_{\mathrm{e} \in \mathcal{B}^{\mathrm{h,int}}} \delta\underline{\widetilde{\boldsymbol{d}}}^{eT} \underline{\mathbb{R}}^{\mathrm{e,int}} \quad \text{and} \\ \Delta G_{\varphi}^{\mathrm{h,int}} &= \sum_{\mathrm{e} \in \mathcal{B}^{\mathrm{h,int}}} \delta\underline{\widetilde{\boldsymbol{d}}}^{eT} \int_{\mathcal{B}^{\mathrm{e,int}}} \underline{\mathbb{B}}^{eT} \underline{\boldsymbol{\mu}}^{\tan}(\underline{\boldsymbol{H}}) \underline{\mathbb{B}}^e \,\mathrm{dv}\, \Delta\underline{\widetilde{\boldsymbol{d}}}^e = \sum_{\mathrm{e} \in \mathcal{B}^{\mathrm{h,int}}} \delta\underline{\widetilde{\boldsymbol{d}}}^{eT} \underline{\mathbb{K}}^{\mathrm{e,int}} \Delta\underline{\widetilde{\boldsymbol{d}}}^e \,, \end{aligned} \tag{4.42}$$

with the element right-hand side $\underline{\mathbb{R}}^{\mathrm{e,int}}$ and the element stiffness matrix $\underline{\mathbb{K}}^{\mathrm{e,int}}$. Applying the following assembling procedure leads to the algebraic system of the inner domain

$$\underline{\mathbb{K}}^{\mathrm{int}} = \mathop{\mathsf{A}}_{\mathrm{e} \in \mathcal{B}^{\mathrm{h,int}}} \underline{\mathbb{K}}^{\mathrm{e,int}} \quad \text{and} \quad \underline{\mathbb{R}}^{\mathrm{int}} = -\mathop{\mathsf{A}}_{\mathrm{e} \in \mathcal{B}^{\mathrm{h,int}}} \underline{\mathbb{R}}^{\mathrm{e,int}} \,, \tag{4.43}$$

with the stiffness matrix $\underline{\mathbb{K}}^{\mathrm{int}}$ and the right-hand side $\underline{\mathbb{R}}^{\mathrm{int}}$ associated with the interior domain. To prepare the total system for its subsequent reduction, the partition of the

system proceeds subdividing the degrees of freedom into $\widetilde{\underline{\boldsymbol{d}}}_i$ inside the interior domain $\mathcal{B}^{\text{int}} \setminus \partial\mathcal{B}^{\text{int}}$ and $\widetilde{\underline{\boldsymbol{d}}}_b$ on the interphase $\partial\mathcal{B}^{\text{int}}$ between both domains (compare Fig. 4.6) as

$$\begin{bmatrix} \underline{\mathbb{K}}_{ii}^{\text{int}} & \underline{\mathbb{K}}_{ib}^{\text{int}} \\ \underline{\mathbb{K}}_{bi}^{\text{int}} & \underline{\mathbb{K}}_{bb}^{\text{int}} \end{bmatrix} \begin{bmatrix} \Delta\widetilde{\underline{\boldsymbol{D}}}_i \\ \Delta\widetilde{\underline{\boldsymbol{D}}}_b \end{bmatrix} = \begin{bmatrix} \underline{\mathbb{R}}_i^{\text{int}} \\ \underline{\mathbb{R}}_b^{\text{int}} \end{bmatrix}, \tag{4.44}$$

with $\Delta\widetilde{\underline{\boldsymbol{D}}}^T = (\Delta\widetilde{\underline{\boldsymbol{D}}}_i^T, \Delta\widetilde{\underline{\boldsymbol{D}}}_b^T)$ indicating the incremental global vector of unknowns.

Discrete external domain $\mathcal{B}^{\text{ext}}$

Substituting the constant and a fluctuation component of the magnetic field into the linear constitutive relation defined in Eq. 4.28, it can be reformulated as

$$\boldsymbol{B} = \boldsymbol{\mu}\,(\lambda\overline{\boldsymbol{H}} + \widetilde{\boldsymbol{H}}) =: \lambda\overline{\boldsymbol{B}} + \widetilde{\boldsymbol{B}}\,. \tag{4.45}$$

For the exterior system $\mathcal{B}^{\text{ext}}$ the weak formulation yields

$$\begin{aligned} G_{\varphi}^{\text{h,ext}} &= \sum_{\text{e}\,\in\,\mathcal{B}^{\text{h,ext}}} \delta\widetilde{\underline{\boldsymbol{d}}}^{e^T} \int_{\mathcal{B}^{\text{e,ext}}} \underline{\mathbb{B}}^{e^T} \left(\lambda\overline{\underline{\boldsymbol{B}}} + \widetilde{\underline{\boldsymbol{B}}}\right) \text{dv} \\ &= \sum_{\text{e}\,\in\,\mathcal{B}^{\text{h,ext}}} \delta\widetilde{\underline{\boldsymbol{d}}}^{e^T} \left\{ \underbrace{\lambda \int_{\mathcal{B}^{\text{e,ext}}} \underline{\mathbb{B}}_{\varphi}^{e^T}\overline{\boldsymbol{B}}\,\text{dv}}_{\lambda\,\underline{\mathrm{R}}^{\text{e,ext}}} + \underbrace{\int_{\mathcal{B}^{\text{e,ext}}} \underline{\mathbb{B}}^{e^T}\boldsymbol{\mu}\,\underline{\mathbb{B}}^{e}\,\text{dv}}_{\underline{\mathrm{K}}^{\text{e,ext}}}\,\widetilde{\boldsymbol{d}}^{\text{e}} \right\}. \end{aligned} \tag{4.46}$$

Since the load parameter λ and the given $\underline{\boldsymbol{H}}$-field ($\overline{\underline{\boldsymbol{H}}}$ and therefore $\overline{\underline{\boldsymbol{B}}}$) are constant in an incremental step, the linear increment results in

$$\Delta G_{\varphi}^{\text{h,ext}} = \sum_{\text{e}\,\in\,\mathcal{B}^{\text{h,ext}}} \delta\widetilde{\underline{\boldsymbol{d}}}^{e^T}\,\underline{\mathbb{K}}^{e,ext}\,\Delta\widetilde{\underline{\boldsymbol{d}}}^{e}. \tag{4.47}$$

Hence, the algebraic system of equations rendering the external domain $\mathcal{B}^{\text{ext}}$ appears as

$$\underline{\mathbb{K}}^{\text{ext}}\,\Delta\widetilde{\underline{\boldsymbol{D}}} = \underline{\mathbb{R}}^{\text{ext}}\,, \tag{4.48}$$

with the corresponding global matrices $\underline{\mathbb{K}}^{\text{ext}}$ and $\underline{\mathbb{R}}^{\text{ext}}$, after carrying out the classical assembly procedure for $\mathcal{B}^{\text{ext}}$ as

$$\begin{aligned} \underline{\mathbb{K}}^{\text{ext}} = \mathop{\mathsf{A}}_{\text{e}\,\in\,\mathcal{B}^{\text{e,ext}}} \underline{\mathbb{K}}^{\text{e,ext}} \quad \text{and} \quad \underline{\mathbb{R}}^{\text{ext}} &= -\mathop{\mathsf{A}}_{\text{e}\,\in\,\mathcal{B}^{\text{e,ext}}} \left\{\lambda\,\underline{\mathbb{R}}^{\text{e,ext}} + \underline{\mathbb{K}}^{\text{e,ext}}\,\widetilde{\boldsymbol{d}}^{e}\right\} \\ &= \lambda\,\overline{\underline{\mathbb{R}}}^{\text{ext}} + \underline{\mathbb{K}}^{\text{ext}}\,\widetilde{\underline{\boldsymbol{D}}}\,. \end{aligned} \tag{4.49}$$

To shrink the total size of the system of equations, its degrees of freedoms are partitioned analogously to the inner domain (cf. Eq. 4.44), i.e. the degrees of freedom on the interface between $\mathcal{B}^{\text{ext}}$ and $\mathcal{B}^{\text{int}}$ are denoted as $\widetilde{\underline{\boldsymbol{d}}}_b$ and the degrees of freedom within the outer domain $\mathcal{B}^{\text{ext}} \setminus \partial\mathcal{B}^{\text{int}}$ are denoted as $\widetilde{\underline{\boldsymbol{d}}}_a$ leading to the system of equations of the external domain as

$$\begin{bmatrix} \underline{\mathbb{K}}_{bb}^{\text{ext}} & \underline{\mathbb{K}}_{ba}^{\text{ext}} \\ \underline{\mathbb{K}}_{ab}^{\text{ext}} & \underline{\mathbb{K}}_{aa}^{\text{ext}} \end{bmatrix} \begin{bmatrix} \Delta\widetilde{\underline{\boldsymbol{D}}}_b \\ \Delta\widetilde{\underline{\boldsymbol{D}}}_a \end{bmatrix} = \begin{bmatrix} \underline{\mathbb{R}}_b^{\text{ext}} \\ \underline{\mathbb{R}}_a^{\text{ext}} \end{bmatrix}, \tag{4.50}$$

with $\Delta\underline{\widetilde{\boldsymbol{D}}}$ representing the global solution vector. To keep the formulations as general as possible, non-linear material behavior within the interior domain is assumed. This requires the use of an iterative solution procedure like Newton's method to solve the system of equations. It should also be noted that the field intensity can be increased by a load parameter λ that is included within the right-hand side $\underline{\mathbb{R}}^{\text{ext}}(\lambda, \underline{\widetilde{\boldsymbol{D}}})$, which is a function of the current fluctuation degrees of freedom.

Static condensation of the exterior domain

The next steps deal with the elimination of the degrees of freedom $\widetilde{\boldsymbol{D}}_a$ of Eq. 4.50, which have to be taken explicitly into account for the right-hand side. With the partition of the system of equations into degrees of freedom of the exterior domain $\underline{\widetilde{\boldsymbol{d}}}_a$ as well as the degrees of freedom of the surface between interior and exterior domain $\underline{\widetilde{\boldsymbol{d}}}_b$ (Eq. 4.50) the contributions of the right-hand side vector (Eq. 4.49) require the partition

$$\begin{bmatrix} \underline{\mathbb{R}}_b^{\text{ext}} \\ \underline{\mathbb{R}}_a^{\text{ext}} \end{bmatrix} = \lambda \begin{bmatrix} \underline{\overline{\mathbb{R}}}_b^{\text{ext}} \\ \underline{\overline{\mathbb{R}}}_a^{\text{ext}} \end{bmatrix} + \begin{bmatrix} \underline{\mathbb{K}}_{bb}^{\text{ext}} & \underline{\mathbb{K}}_{ba}^{\text{ext}} \\ \underline{\mathbb{K}}_{ab}^{\text{ext}} & \underline{\mathbb{K}}_{aa}^{\text{ext}} \end{bmatrix} \begin{bmatrix} \underline{\widetilde{\boldsymbol{D}}}_b \\ \underline{\widetilde{\boldsymbol{D}}}_a \end{bmatrix} . \tag{4.51}$$

Insertion of Eq. 4.51 into Eq. 4.50 leads to the system of equations

$$\begin{bmatrix} \underline{\mathbb{K}}_{bb}^{\text{ext}} & \underline{\mathbb{K}}_{ba}^{\text{ext}} \\ \underline{\mathbb{K}}_{ab}^{\text{ext}} & \underline{\mathbb{K}}_{aa}^{\text{ext}} \end{bmatrix} \begin{bmatrix} \Delta\underline{\widetilde{\boldsymbol{D}}}_b \\ \Delta\underline{\widetilde{\boldsymbol{D}}}_a \end{bmatrix} = \begin{bmatrix} \lambda\underline{\overline{\mathbb{R}}}_b^{\text{ext}} + \underline{\mathbb{K}}_{bb}^{\text{ext}}\,\underline{\widetilde{\boldsymbol{D}}}_b + \underline{\mathbb{K}}_{ba}^{\text{ext}}\,\underline{\widetilde{\boldsymbol{D}}}_a \\ \lambda\underline{\overline{\mathbb{R}}}_a^{\text{ext}} + \underline{\mathbb{K}}_{ab}^{\text{ext}}\,\underline{\widetilde{\boldsymbol{D}}}_b + \underline{\mathbb{K}}_{aa}^{\text{ext}}\,\underline{\widetilde{\boldsymbol{D}}}_a \end{bmatrix} . \tag{4.52}$$

Taking the last part of Eq. 4.52 in its full expression yields

$$\underline{\mathbb{K}}_{ab}^{\text{ext}}\,\Delta\underline{\widetilde{\boldsymbol{D}}}_b + \underline{\mathbb{K}}_{aa}^{\text{ext}}\,\Delta\underline{\widetilde{\boldsymbol{D}}}_a = \lambda\,\underline{\overline{\mathbb{R}}}_a^{\text{ext}} + \underline{\mathbb{K}}_{ab}^{\text{ext}}\,\underline{\widetilde{\boldsymbol{D}}}_b + \underline{\mathbb{K}}_{aa}^{\text{ext}}\,\underline{\widetilde{\boldsymbol{D}}}_a . \tag{4.53}$$

The external degrees of freedom $\underline{\widetilde{\boldsymbol{D}}}_a$ are eliminated from Eq. 4.52 by rearranging Eq. 4.53 to $\underline{\widetilde{\boldsymbol{D}}}_a$ and following the prescription

$$\begin{aligned} \underline{\widetilde{\boldsymbol{D}}}_a &= \underline{\mathbb{K}}_{aa}^{\text{ext}\,-1} \left(\underline{\mathbb{K}}_{ab}^{\text{ext}}\,\Delta\underline{\widetilde{\boldsymbol{D}}}_b + \underline{\mathbb{K}}_{aa}^{\text{ext}}\,\Delta\underline{\widetilde{\boldsymbol{D}}}_a - \lambda\,\underline{\overline{\mathbb{R}}}_a^{\text{ext}} - \underline{\mathbb{K}}_{ab}^{\text{ext}}\,\underline{\widetilde{\boldsymbol{D}}}_b \right) \\ &= \underline{\mathbb{L}}_{ab}(\Delta\underline{\widetilde{\boldsymbol{D}}}_b - \underline{\widetilde{\boldsymbol{D}}}_b) + \Delta\underline{\widetilde{\boldsymbol{D}}}_a - \lambda\,\underline{\mathbb{K}}_{aa}^{\text{ext}\,-1}\underline{\overline{\mathbb{R}}}_a^{\text{ext}} . \end{aligned} \tag{4.54}$$

Since the symmetric matrices $\underline{\mathbb{K}}_{aa}^{\text{ext}}, \underline{\mathbb{K}}_{bb}^{\text{ext}}$, and the matrices $\underline{\mathbb{K}}_{ab}^{\text{ext}} = (\underline{\mathbb{K}}_{ab}^{\text{ext}})^T$ are constant, the algorithmic auxiliary matrices

$$\underline{\mathbb{L}}_{ab} := \underline{\mathbb{K}}_{aa}^{\text{ext}\,-1}\,\underline{\mathbb{K}}_{ab}^{\text{ext}} \quad \text{and} \quad \underline{\mathbb{L}}_{ba}^{T} := \underline{\mathbb{K}}_{ba}^{\text{ext}}\,\underline{\mathbb{K}}_{aa}^{\text{ext}\,-1} \tag{4.55}$$

can be defined. Substituting Eq. 4.54_2 into Eq. 4.52_1 yields

$$\begin{aligned} &\underline{\mathbb{K}}_{bb}^{\text{ext}}\,\Delta\underline{\widetilde{\boldsymbol{D}}}_b + \underline{\mathbb{K}}_{ba}^{\text{ext}}\,\Delta\underline{\widetilde{\boldsymbol{D}}}_a = \lambda\,\underline{\overline{\mathbb{R}}}_b^{\text{ext}} + \underline{\mathbb{K}}_{bb}^{\text{ext}}\,\underline{\widetilde{\boldsymbol{D}}}_b + \underline{\mathbb{K}}_{ba}^{\text{ext}}\,\underline{\widetilde{\boldsymbol{D}}}_a \\ &\left[\underline{\mathbb{K}}_{bb}^{\text{ext}} - \underline{\mathbb{K}}_{ba}^{\text{ext}}\,\underline{\mathbb{L}}_{ab}\right]\,\Delta\underline{\widetilde{\boldsymbol{D}}}_b = \lambda\,\left[\underline{\overline{\mathbb{R}}}_b^{\text{ext}} - \underline{\mathbb{L}}_{ba}^{T}\,\underline{\overline{\mathbb{R}}}_a^{\text{ext}}\right] + \left[\underline{\mathbb{K}}_{bb}^{\text{ext}} - \underline{\mathbb{K}}_{ba}^{\text{ext}}\,\underline{\mathbb{L}}_{ab}\right]\,\underline{\widetilde{\boldsymbol{D}}}_b . \end{aligned} \tag{4.56}$$

With the constant matrices $\underline{\mathbb{K}}_{bb}^{\infty}$ and $\underline{\mathbb{R}}_b^{\infty}$, Eq. 4.56_2 is further simplified to

$$\underbrace{\left[\underline{\mathbb{K}}_{bb}^{\text{ext}} - \underline{\mathbb{K}}_{ba}^{\text{ext}}\,\underline{\mathbb{L}}_{ab}\right]}_{=:\underline{\mathbb{K}}_{bb}^{\infty}}\,\Delta\underline{\widetilde{\boldsymbol{D}}}_b = \overbrace{\lambda\,\underbrace{\left[\underline{\overline{\mathbb{R}}}_b^{\text{ext}} - \underline{\mathbb{L}}_{ba}^{T}\,\underline{\overline{\mathbb{R}}}_a^{\text{ext}}\right]}_{=:\underline{\overline{\mathbb{R}}}_b^{\infty}} + \underline{\mathbb{K}}_{bb}^{\infty}\,\underline{\widetilde{\boldsymbol{D}}}_b}^{\underline{\mathbb{R}}_b^{\infty}} . \tag{4.57}$$

Finally, the algebraic system of equations is assembled using the discrete inner and outer domains described in Eq. 4.57 and Eq. 4.44. This yields the final representation

$$\begin{bmatrix} \underline{\mathbb{K}}_{ii}^{\mathrm{int}} & \underline{\mathbb{K}}_{ib}^{\mathrm{int}} \\ \underline{\mathbb{K}}_{bi}^{\mathrm{int}} & \underline{\mathbb{K}}_{bb}^{\mathrm{int}} + \underline{\mathbb{K}}_{bb}^{\infty} \end{bmatrix} \begin{bmatrix} \Delta\underline{\widetilde{\boldsymbol{D}}}_i \\ \Delta\underline{\widetilde{\boldsymbol{D}}}_b \end{bmatrix} = \begin{bmatrix} \underline{\mathbb{R}}_i^{\mathrm{int}} \\ \underline{\mathbb{R}}_b^{\mathrm{int}} + \underline{\mathbb{R}}_b^{\infty} \end{bmatrix} . \tag{4.58}$$

The computational steps defining the whole procedure are summarized in Table 4.1.

Table 4.1: Computational steps. Taken from Schröder et al. [2022].

a) initialize $\widetilde{\boldsymbol{D}}$, $\overline{\boldsymbol{H}}$ and load factor λ

b) discretization of interior and exterior domain: $\mathcal{B}^{\mathrm{h,ext}}$ and $\mathcal{B}^{\mathrm{h,int}}$
computation of matrices $\underline{\mathbb{K}}_{aa}^{\mathrm{ext}}$, $\underline{\mathbb{K}}_{ab}^{\mathrm{ext}}$, $\underline{\mathbb{K}}_{bb}^{\mathrm{ext}}$, $\overline{\mathbb{R}}_a^{\mathrm{ext}}$, $\overline{\mathbb{R}}_b^{\mathrm{ext}}$, and

$$\underline{\mathbb{L}}_{ab} := \underline{\mathbb{K}}_{aa}^{\mathrm{ext}\,-1}\, \underline{\mathbb{K}}_{ab}^{\mathrm{ext}},\ \underline{\mathbb{K}}_{bb}^{\infty} = \underline{\mathbb{K}}_{bb}^{\mathrm{ext}} - \underline{\mathbb{K}}_{ba}^{\mathrm{ext}}\, \underline{\mathbb{L}}_{ab},\ \overline{\mathbb{R}}_b^{\infty} = \overline{\mathbb{R}}_b^{\mathrm{ext}} - \underline{\mathbb{L}}_{ba}^{T}\, \overline{\mathbb{R}}_a^{\mathrm{ext}}$$

store $\underline{\mathbb{K}}_{bb}^{\infty}$ and $\overline{\mathbb{R}}_b^{\infty}$

c) increase load factor $\lambda \leftarrow \lambda + \Delta\lambda$

c1) compute right-hand side

$$\underline{\mathbb{R}}_b^{\infty} = \lambda\, \overline{\mathbb{R}}_b^{\infty} + \underline{\mathbb{K}}_{bb}^{\infty}\, \widetilde{\boldsymbol{D}}_b$$

c2) assemble condensed stiffness matrix using $\underline{\mathbb{R}}^{\mathrm{int}}$ and $\underline{\mathbb{K}}^{\mathrm{int}}$ from Eq. 4.43

$$\begin{bmatrix} \underline{\mathbb{K}}_{ii}^{\mathrm{int}} & \underline{\mathbb{K}}_{ib}^{\mathrm{int}} \\ \underline{\mathbb{K}}_{bi}^{\mathrm{int}} & \underline{\mathbb{K}}_{bb}^{\mathrm{int}} + \underline{\mathbb{K}}_{bb}^{\infty} \end{bmatrix} \begin{bmatrix} \Delta\underline{\widetilde{\boldsymbol{D}}}_i \\ \Delta\underline{\widetilde{\boldsymbol{D}}}_b \end{bmatrix} = \begin{bmatrix} \underline{\mathbb{R}}_i^{\mathrm{int}} \\ \underline{\mathbb{R}}_b^{\mathrm{int}} + \underline{\mathbb{R}}_b^{\infty} \end{bmatrix}$$

c3) solve system of equations w.r.t. $\Delta\underline{\widetilde{\boldsymbol{D}}}$ and update solution vector $\underline{\widetilde{\boldsymbol{D}}} \leftarrow \underline{\widetilde{\boldsymbol{D}}} + \Delta\underline{\widetilde{\boldsymbol{D}}}$

c4) go to c1) until convergence

c5) go to c) until final load step is reached

4.4.3 A simplified non-linear magnetic model

To verify the performance of the proposed numerical scheme, a simplified non-linear constitutive law for the solid magnet inside the domain $\mathcal{B}^{\text{int}}$ is applied. Here, the non-linearity enters the induction $\boldsymbol{B} = \hat{\boldsymbol{B}}(\boldsymbol{H})$, which is a function of $\boldsymbol{H}$. In general, this relation can be expressed via the magnetic permeability $\boldsymbol{\mu}$ and thus via the magnetic susceptibility $\boldsymbol{\chi}$ in

$$\boldsymbol{B} = \boldsymbol{\mu} \cdot \boldsymbol{H} = \mu_0(\boldsymbol{H} + \boldsymbol{\chi} \cdot \boldsymbol{H}) = \mu_0(\boldsymbol{H} + \boldsymbol{M}), \tag{4.59}$$

where $\boldsymbol{M}$ denotes the magnetization. The magnetic susceptibility is not constant in ferromagnets, but a non-linear function of the applied magnetic field strength and of the history of the material, i.e. $\boldsymbol{\chi} = \hat{\boldsymbol{\chi}}(\boldsymbol{M}, ...)$. In ferromagnetic materials, a so-called saturation magnetization is generally observed, i.e. a material-dependent maximum value for the magnetization is reached. If $\boldsymbol{\chi}$ is considered as differential susceptibility, i.e. $\boldsymbol{\chi} = \partial_{\boldsymbol{H}} \boldsymbol{M}$, this becomes zero when the saturation magnetization is reached. Here, for the sake of simplicity, only magnetization curves without hystertic behavior are assumed, i.e. a characteristic of soft magnetic materials. However, the proposed condensation procedure is also valid for the simulation of hard magnets with distinct hysteresis properties. Of course, this model also shows saturation. As a prototype for this, the function

$$\boldsymbol{B} = \mu_0(\boldsymbol{H} + \hat{\boldsymbol{M}}(\boldsymbol{H})) \quad \text{with} \quad \boldsymbol{M} = M_S \tanh\left(\beta \, \|\boldsymbol{H}\|\right) \boldsymbol{n}_H \tag{4.60}$$

is used, where M_S denotes the saturation magnetization, β a slope parameter and $\boldsymbol{n}_H := \boldsymbol{H}/\|\boldsymbol{H}\|$ for $\|\boldsymbol{H}\| \neq 0$ otherwise $\boldsymbol{n}_H = \boldsymbol{0}$. For the linearization of the weak form, cf. Eq. 4.42, $\boldsymbol{\mu}^{\tan}(\boldsymbol{H}) = \partial_{\boldsymbol{H}} \hat{\boldsymbol{B}}(\lambda \overline{\boldsymbol{H}} + \widetilde{\boldsymbol{H}}) = \partial_{\boldsymbol{H}} \hat{\boldsymbol{B}}(\boldsymbol{H})$ is needed; this appears for $\|\boldsymbol{H}\| > 0$ in the explicit form

$$\boldsymbol{\mu}^{\tan}(\boldsymbol{H}) = \mu_0 \, \boldsymbol{1} + \mu_0 \, M_S \, \left((\hat{f}_1(\boldsymbol{H}) - \hat{f}_2(\boldsymbol{H})) \, \boldsymbol{n}_H \otimes \boldsymbol{n}_H + \hat{f}_2(\boldsymbol{H}) \, \boldsymbol{1} \right), \tag{4.61}$$

with

$$\hat{f}_1(\boldsymbol{H}) = \beta \, \left(1 - \tanh^2\left(\beta \, \|\boldsymbol{H}\|\right)\right) \quad \text{and} \quad \hat{f}_2(\boldsymbol{H}) = \frac{\tanh\left(\beta \, \|\boldsymbol{H}\|\right)}{\|\boldsymbol{H}\|} \, , \tag{4.62}$$

otherwise

$$\boldsymbol{\mu}^{\tan}(\boldsymbol{H}) = \mu_0 \, (1 + M_S \, \beta) \, \boldsymbol{1} \tag{4.63}$$

is obtained. Note: This is a very simplified model to describe the magnetization in a solid. Classically, the existence of a free energy function $U(m_1, m_2, m_3)$ is assumed, which is formulated in series expansion of the direction cosines $(m_i | i = 1, 2, 3)$ of the magnetization relative to the crystal axes. This consideration starts from the enthalpy function $\mathcal{H}(\boldsymbol{H}) = U(\boldsymbol{m}) - \mu_0 \, M_S \, \boldsymbol{m} \cdot \boldsymbol{H}$. For the chosen model the enthalpy function for the magnetization part is

$$\mathcal{H}(\boldsymbol{H}) = \frac{1}{2} \mu_0 \, \|\boldsymbol{H}\|^2 + \mu_0 \, \frac{M_S}{\beta} \, \ln(\cosh(\beta \, \|\boldsymbol{H}\|)) \, . \tag{4.64}$$

For the discussion of phenomenological models of hysteresis it is referred to Takács [2001] and Szewczyk [2016]. To demonstrate the feasibility of the model presented above a homogeneous boundary value problem is considered. The domain of interest corresponds to a square with dimensions of 4 μm $\times$ 4 μm and the material parameters as defined in Table 4.2. In order to generate a magnetic response, the area is subjected to the external magnetic field $\overline{\boldsymbol{H}} = \lambda \, 0.07 \, [1, 0]^T$ A/ μm, where λ is a load factor alternating between minus one and one. The corresponding response function can be found in Fig. 4.7, where $\| \cdot \|$ denotes the Euclidean norm.

Table 4.2: Material parameters. Taken from SCHRÖDER ET AL. [2022].

Vacuum permeability μ_0	Saturation magnetization M_s	Slope parameter β
0.4 π (ng μm)/ A^2 μs^2	1.41 A/ μm	50 μm/ A

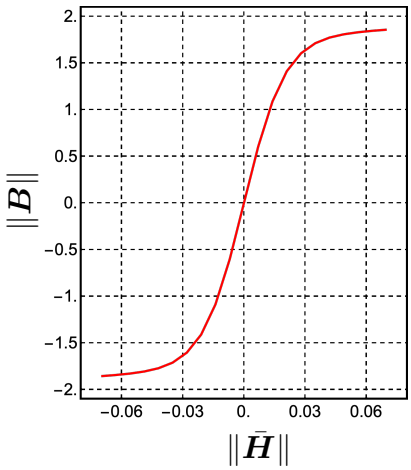

Figure 4.7: The normalized response curve. Taken from SCHRÖDER ET AL. [2022].

4.4.4 Stray field calculation with heterogeneous exterior domain

The method presented above is well suited for approximating large outer domains, while other well-established methods such as the BEM or the SBFEM provide solutions for infinite domains. While the established methods can only provide solutions for outer domains with a certain regularity, the proposed method has the crucial advantage of being able to consider heterogeneous outer domains. This implies in detail that interference fields from neighboring or nearby magnetic bodies can also be taken into account by the presented method, which is further demonstrated in the following example. Three magnetic inclusions, identified as $\mathcal{B}_1^{\text{ext}}$ (green), $\mathcal{B}_2^{\text{ext}}$ (blue), and $\mathcal{B}_2^{\text{int}}$ (red), are considered in direct proximity to one another. In the following, all distances are related to the coordinate system shown in Fig. 4.8. The green inclusion $\mathcal{B}_1^{\text{ext}}$ is described by the center point P_1 (-80 / -110) μm and the radius $\text{r}_1 = 35$ μm. The blue inclusion $\mathcal{B}_2^{\text{ext}}$ is also characterized by a centre point P_2 (80 / -130) μm and the radii $\text{r}_2 = 70$ μm and $\text{r}_3 = 30$ μm. The dimensions of the remaining colored domains can be found in the graphic in Fig. 4.8. All three inclusions are surrounded by free space, here indicated by $\mathcal{B}_3^{\text{ext}}$ (light blue) and $\mathcal{B}_1^{\text{int}}$ (orange). To generate a magnetic response the whole domain is treated with an external magnetic field $\overline{H}_2 = 6.3 \cdot 10^{-3}$ A/ μm. Since the magnetic particles are very closely located, their magnetic fields will influence each other. Due to the fact that the magnetic stray field flattens out towards zero for large distances to the magnetic particles, a huge airspace must be considered. In this contribution, the airspace is taken into account in two different ways. Firstly, a reference solution was generated using the truncation method. Therefore, the FEM is applied to approximate the whole boundary value problem as sketched in Fig. 4.8, i.e. the airspace and the magnetic inclusions. Secondly, the static condensation is applied to the outer domain $\mathcal{B}^{\text{ext}} = \mathcal{B}_1^{\text{ext}} \cup \mathcal{B}_2^{\text{ext}} \cup \mathcal{B}_3^{\text{ext}}$ of the boundary value problem given in Fig. 4.8. This means that the outer domain is reduced onto the border of the interior domain $\mathcal{B}^{\text{int}} = \mathcal{B}_1^{\text{int}} \cup \mathcal{B}_2^{\text{int}}$, so that no further discretization of $\mathcal{B}^{\text{ext}}$ is required. Hence, the area to simulate is reduced to $\mathcal{B}^{\text{int}}$.

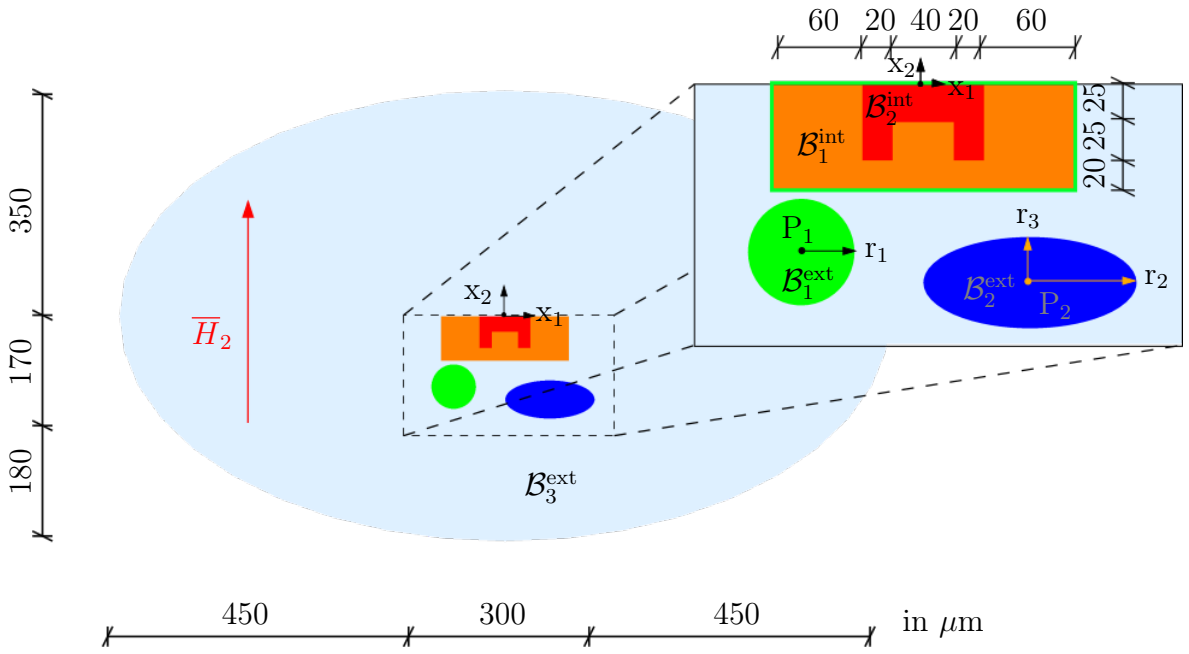

Figure 4.8: The test setup for the analysis of the reduction method. Three differently shaped inclusions $\mathcal{B}_{1-2}^{\text{ext}}$ and $\mathcal{B}_2^{\text{int}}$ are embedded within a free space $\mathcal{B}_3^{\text{ext}}$ and $\mathcal{B}_1^{\text{int}}$. The external magnetic field $\overline{H}_2$ is applied in y direction. The green line framing $\mathcal{B}_1^{\text{int}}$ and $\mathcal{B}_2^{\text{int}}$ indicates the area that is graphically presented during post-processing. Taken from Schröder et al. [2022].

The aim is to verify that both results match and to evaluate the performance of both methods. For the following calculations, identical magnetic properties are assigned to the magnetic inclusions, i.e. $\mu^{\text{mat}} = 1.25 \cdot 10^5$ (ng μm)/ (A^2 μs^2). The free space is considered to be vacuum with $\mu^{\text{air}} = \mu_0$ being the magnetic vacuum permeability.

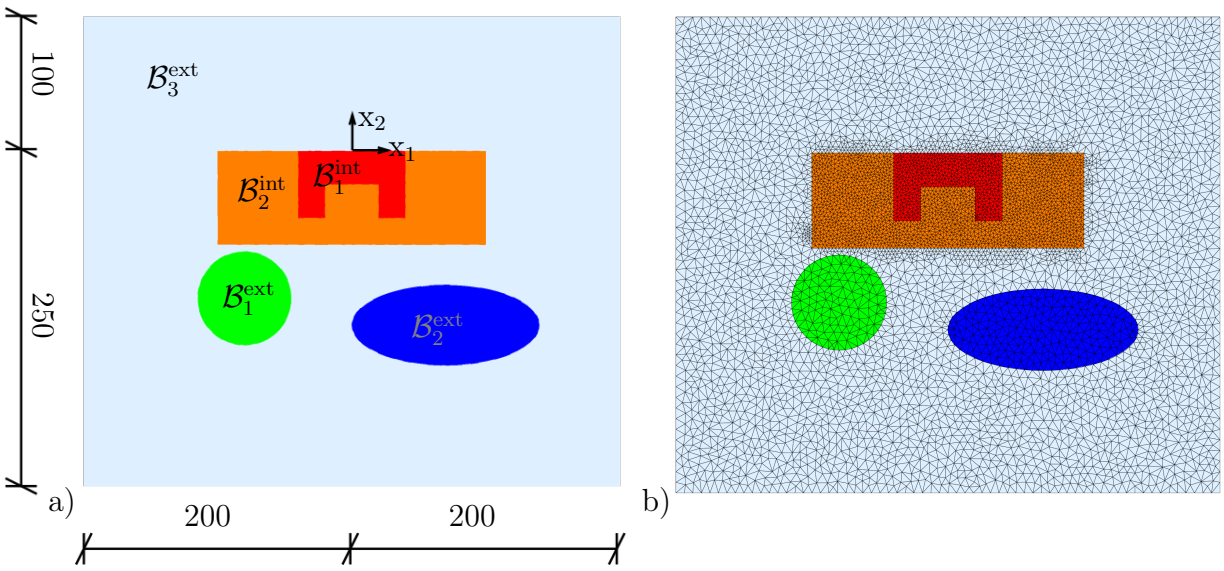

Figure 4.9: Cut out of the boundary value problem given in Fig. 4.8 for the graphic representation of the results, with a) the dimensions and b) the corresponding mesh density. Taken from Schröder et al. [2022].

The material behavior is approximated by a linear material model. Different numbers of degrees of freedom are assigned to the inner and outer domain. The much smaller inner domain has almost 9,000 degrees of freedom, while the outer domain has over 70,000 degrees of freedom. This corresponds to a total number of approximately 80,000 degrees of freedom in the overall system. Of course, the reference simulation provides results for the entire area, but since the outer space is very large, only a fraction of the boundary value problem is used for graphical representation. The cut out used for graphic processing includes the magnetic inhomogeneities and is shown below in Fig. 4.9.

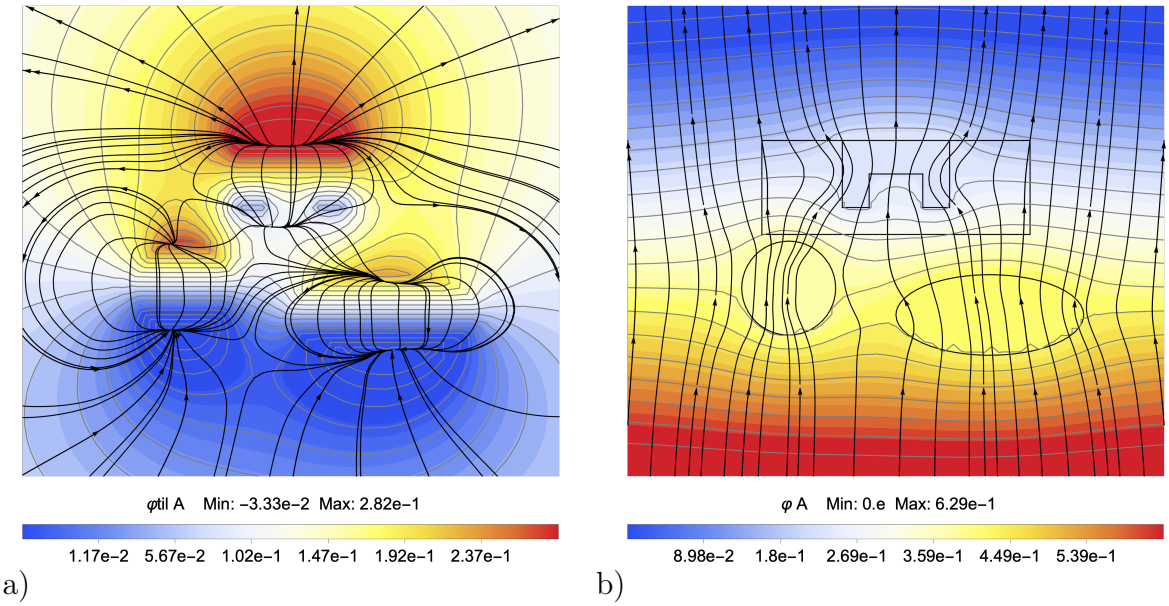

Figure 4.10: Contour plot of a) the fluctuation potential $\widetilde{\varphi}$ and the streamline plot of $\widetilde{\boldsymbol{H}}$ and b) the bulk potential $\varphi = \overline{\varphi} + \widetilde{\varphi}$ and the streamline plot of $\boldsymbol{B}$ on the domain depicted in Fig. 4.9. Taken from Schröder et al. [2022].

Due to the close position of the inclusions to each other, the field lines corresponding to $\widetilde{\boldsymbol{H}}$ show a strong swirling of the fluctuation field around the inclusions as shown in Fig. 4.10a). In contrast to the fluctuation field $\widetilde{\boldsymbol{H}}$, the external magnetic field $\overline{\boldsymbol{H}}$ is a spatially constant distributed quantity. It has the same amplitude in every spatial point of the observed area $\mathcal{B} = \mathcal{B}^{\text{ext}} \cup \mathcal{B}^{\text{int}}$. The external magnetic potential $\overline{\varphi}$ delivers a linear distribution over $\mathcal{B}$. For this reason, the external magnetic field is not shown graphically. Since the fluctuation field evolves cloud-like and the external field is constant, the entire magnetic field $\boldsymbol{H} = \widetilde{\boldsymbol{H}} + \overline{\boldsymbol{H}}$ also changes spatially. The magnetic field $\boldsymbol{H}$ is derived from the entire potential $\varphi = \widetilde{\varphi} + \overline{\varphi}$. Hence, Fig. 4.10b) presents the potential φ as a colored contour plot and the derived magnetic field $\boldsymbol{H}$ as streamlines.
The results of the reduced simulation must be identical to those of the reference solution within the internal domain $\mathcal{B}^{\text{int}}$. Since the outer space $\mathcal{B}^{\text{ext}}$ has already been taken into account in the preliminary static condensation, the domain to discretize with finite elements reduces to $\mathcal{B}^{\text{int}}$, compare Fig. 4.11. Therefore, the plots in Fig. 4.12a) and b) only show the evolution of the magnetic potentials ($\widetilde{\varphi}$ and φ) and the corresponding fields ($\widetilde{\boldsymbol{H}}$ and $\boldsymbol{H}$) for the inner domain $\mathcal{B}^{\text{int}}$.

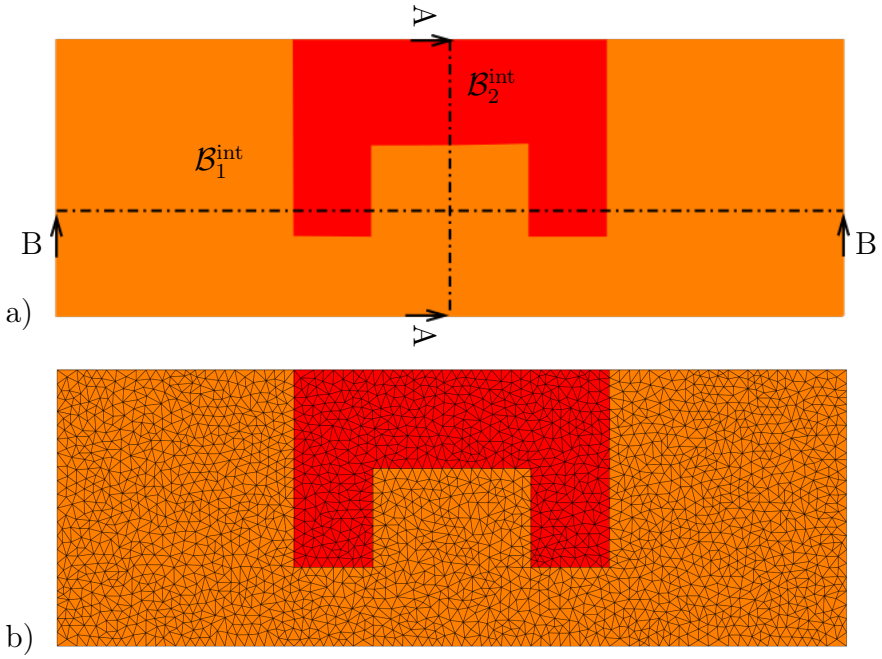

Figure 4.11: Reduced boundary value problem with a) the considered area $\mathcal{B}^{\text{int}}$ where the lines indicate the intersections A-A and B-B and b) the corresponding mesh density. Taken from Schröder et al. [2022].

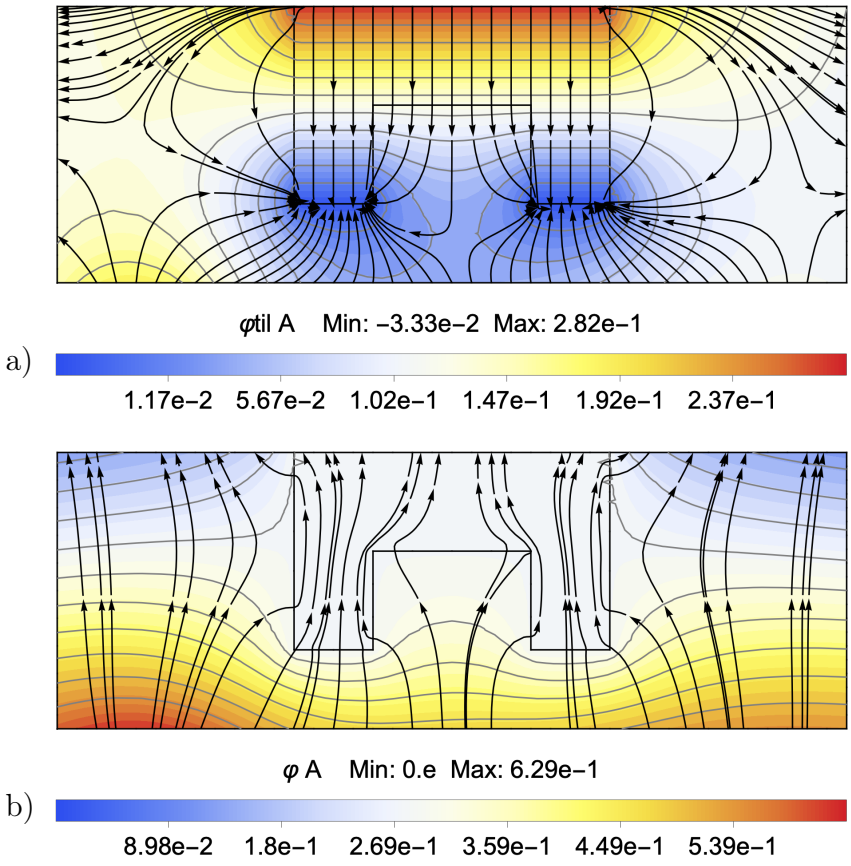

Figure 4.12: Contour plots of the reduced domain of c) the fluctuation field $\widetilde{\varphi}$ and the streamline plot of $\widetilde{\boldsymbol{H}}$ and d) the bulk field $\varphi = \overline{\varphi} + \widetilde{\varphi}$ and the streamline plot of $\boldsymbol{B}$. Taken from Schröder et al. [2022].

Similar to Fig. 4.10, the corresponding potentials are shown as colored contour plots and the derived magnetic fields are superimposed as stream plots. It is obvious that these variables behave analogously to those from the simulation that was calculated previously (reference simulation). The magnetic inclusion $\mathcal{B}_2^{\text{int}}$ colored in red in Fig. 4.11a) and b) is responsible for most of the turbulence in the illustrations. However, the influences of the adjacent inclusions ($\mathcal{B}_2^{\text{ext}}$ and $\mathcal{B}_3^{\text{ext}}$) are also clearly visible, since they were previously taken into account by the static condensation.

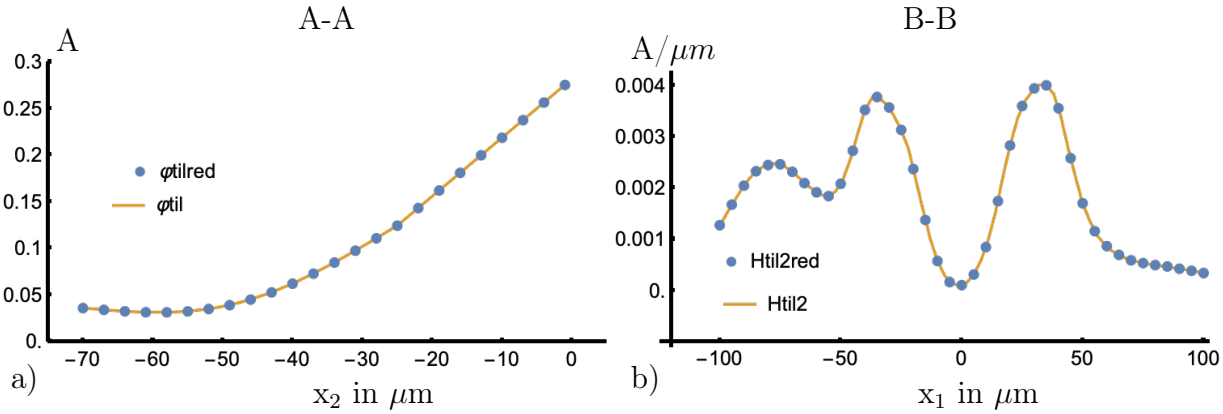

Figure 4.13: a) Shows the discrete values of the fluctuation potential $\widetilde{\varphi}$ along the intersection A-A, while b) presents the discrete values of the fluctuation field $\widetilde{H}_2$ along the intersection B-B. Solutions obtained by calculations over the whole domain (see Fig. 4.8) are presented as solid lines and the solutions of the reduced domain (Fig. 4.11) are given as circular points. Taken from Schröder et al. [2022].

The comparison of the potentials and fields presented in Fig. 4.10 and Fig. 4.12 already confirms a very good agreement of the observed quantities within the reduced domain. In order to emphasize the accuracy of the proposed method, discrete values of the reference solution (whole domain) and the solution obtained on the boundary value problem defined by only the interior domain, are taken along the marked intersection lines A-A and B-B (compare Fig. 4.11a)), see Fig. 4.13. The plots of the discrete values (Fig. 4.13) are congruent and confirm the accuracy of the proposed scheme. A characteristic of classic FEM stiffness matrices is a sparsely populated band structure. This is in complete contrast to the stiffness matrices of the reduced systems, which are typically fully or very densely populated matrices. In Fig. 4.14 both types of matrices are shown. In order to emphasize the differences between these two matrix types, the sparsely populated matrix of the pure FEM calculation is shown together with the significantly smaller, but dense, reduced matrix in Fig. 4.14a). This reduced matrix can also be seen in scaled size in Fig. 4.14b).
In order to evaluate the performance of the presented method against the reference simulation, the times required for solving the system of equations are compared. All following calculations are done using a standard laptop with an i5 processor and 16 GB of RAM. The full system of equations described above (Fig. 4.14a)) was condensed in less than ten seconds to the reduced system of equations (Fig. 4.14b)). Since this reduction of the outer space was carried out as a preliminary calculation, it does not affect the actual solution procedure of the finite element simulation. Hence, the time needed for the reduction procedure is not included in the timings carried out subsequently. Time savings are particularly noticeable in dynamic calculations, therefore the magnetic field applied to the boundary value problem described above is increased from zero to $\overline{H}_2$ within 100 load steps. Since the system of equations is solved repeatedly, the time difference adds up.

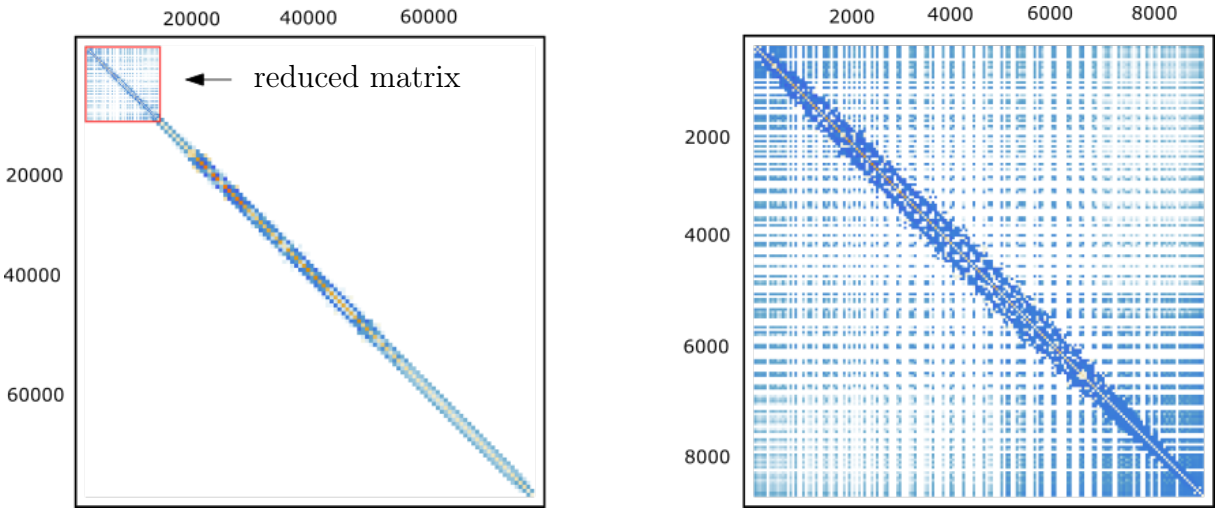

Figure 4.14: The population of the stiffness matrix corresponding to the full FEM solution is presented in a) together with the stiffness matrix corresponding to the reduced calculation marked by a red frame. The population of the reduced stiffness matrix is presented in b) as a scaled plot. Taken from Schröder et al. [2022].

The results obtained for both the reduced and the full FEM simulation are presented in Table 4.3. A large difference in time and therefore a significant gain of efficiency is obtained.

Table 4.3: Required times for solving the linear system of equations. Taken from Schröder et al. [2022].

Steps	Reduced	Reference	Factor
100	10.0523 s	35.2083 s	3.5

Although the performance advantage can already be seen for the linear simulations, the reduction will probably be of even greater advantage, especially for non-linear and time-dependent calculations that require the consideration of an external area. In the case of a non-linear simulation, several Newton iterations are usually required to solve the existing system of equations. Since each individual iteration takes longer for large systems of equations compared to reduced ones, the time savings for serial evaluations of systems of equations, as it is the case with time-dependent problems, are obvious. At this point, the same boundary value problem as utilized for the linear case is used, but the non-linear material behavior, which is introduced in Sec. 4.4.3, is considered in $\mathcal{B}_3^{\text{int}}$. Similar to the previous simulations, a reference solution is created with the truncation method, which is compared to the reduced method afterwards. For this purpose, the external magnetic field $\overline{H}_2$ is increased within 100 load steps in the y direction. The required times of the truncation and the reduced method for solving the systems of equations serially are given in Table 4.4.

4.4.5 3D stray field calculation with homogeneous exterior domain

The method presented above cannot only be applied to two-dimensional boundary value problems, but also to three-dimensional problems. Since large extended domains in three

Table 4.4: Required times for solving the non-linear system of equations. Taken from Schröder et al. [2022].

Steps	Reduced	Reference	Factor
100	12.4677 s	42.1152 s	3.3

dimensions can lead to extremely large systems of equations, their reduction is particularly useful. In this example, a magnetic dodecahedron-shaped grain is treated with three externally applied magnetic fields of the strength $\|\overline{\boldsymbol{H}}\| = 795.78 \cdot 10^{-3}$ A/ μm within a free space. The directions of the three fields correspond to the Cartesian coordinate axes. The considered outer domain $\mathcal{B}^{\text{ext}}$ possesses a radius of 1000 μm, while the radius of the inner domain $\mathcal{B}^{\text{int}} = \mathcal{B}_1^{\text{int}} \cup \mathcal{B}_2^{\text{int}}$ is 150 μm. The magnetic inclusion $\mathcal{B}_2^{\text{int}}$ has an approximated radius of 70 μm. In this example, the domains $\mathcal{B}^{\text{ext}}$ and $\mathcal{B}_1^{\text{int}}$ are considered to represent vacuum, while a permeability of $\mu^{\text{mat}} = 1.25 \cdot 10^5$ (ng μm)/ (A^2 μs^2) is assigned to the magnetic inclusion. The exact geometry, including the dimensions, can be found in Fig. 4.15. The radii of the extended outer domain $\mathcal{B}^{\text{ext}}$, and the inner domain $\mathcal{B}^{\text{int}}$ are presented in Table 4.5 with the corresponding numbers of degrees of freedom within the domains and on the surfaces. By means of this comparison, the size difference between the two systems is emphasized.

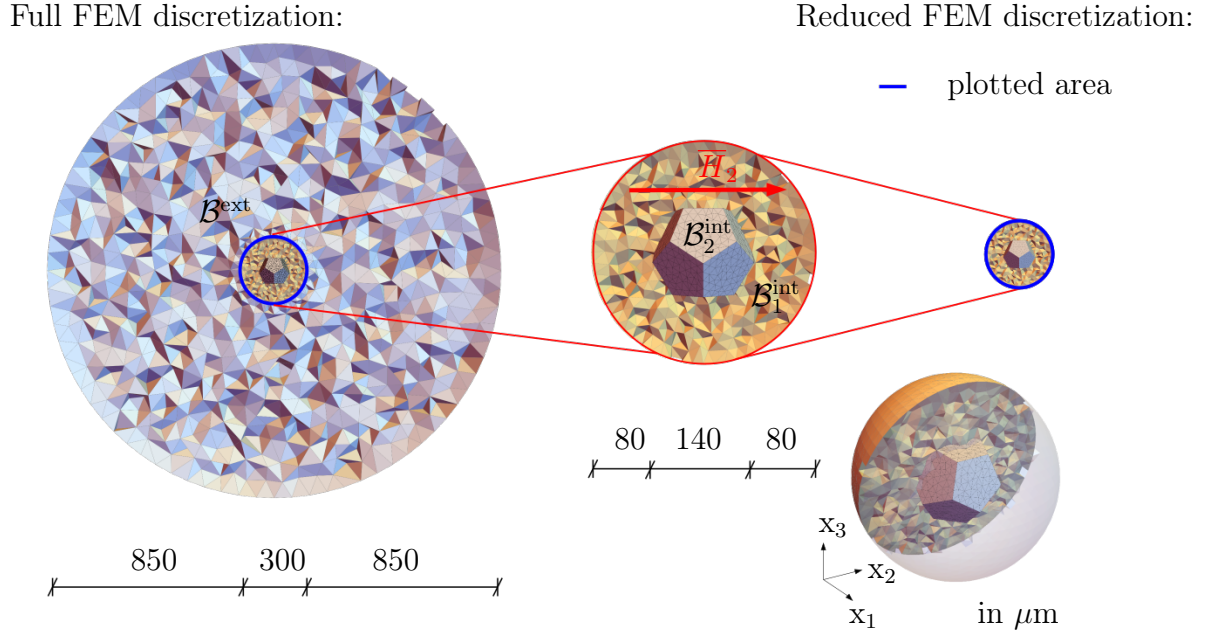

Figure 4.15: The test setup for the analysis of the reduction method in three dimensions. A magnetic, dodecahedral inclusion $\mathcal{B}_2^{\text{int}}$ is surrounded by free space $\mathcal{B}_1^{\text{int}}$. The full FEM discretization also considers an extended exterior domain $\mathcal{B}^{\text{ext}}$. The results are plotted for the volume framed by the blue line. Taken from Schröder et al. [2022].

Because a single inclusion is considered to be placed within a free space of vacuum, no adjacent sources of interference are obtained. Therefore, the externally applied field $\overline{\boldsymbol{H}}$ only generates a reaction within the magnetic inclusion $\mathcal{B}_2^{\text{int}}$, so that the magnetic potentials ($\widetilde{\varphi}$ and φ) and fields ($\widetilde{\boldsymbol{H}}$ and $\boldsymbol{H}$) can propagate without being disturbed. Since the results of the static condensation show good agreement with those of the truncation method, only the field curves in the reduced area $\mathcal{B}^{\text{int}}$ are shown below.

Table 4.5: Comparison of radii and degrees of freedom. Taken from Schröder et al. [2022].

	Rad $\mathcal{B}^{\text{ext}}$	Rad $\mathcal{B}_1^{\text{int}}$	DOF $\mathcal{B}^{\text{ext}}$	DOF $\mathcal{B}_1^{\text{int}} \cup \mathcal{B}_2^{\text{int}}$	DOF on $\partial\mathcal{B}_1^{\text{int}}$
Full FEM	1000 nm	150 nm	160,787	34,973	1538
Reduced FEM	0	150 nm	0	34,973	1538

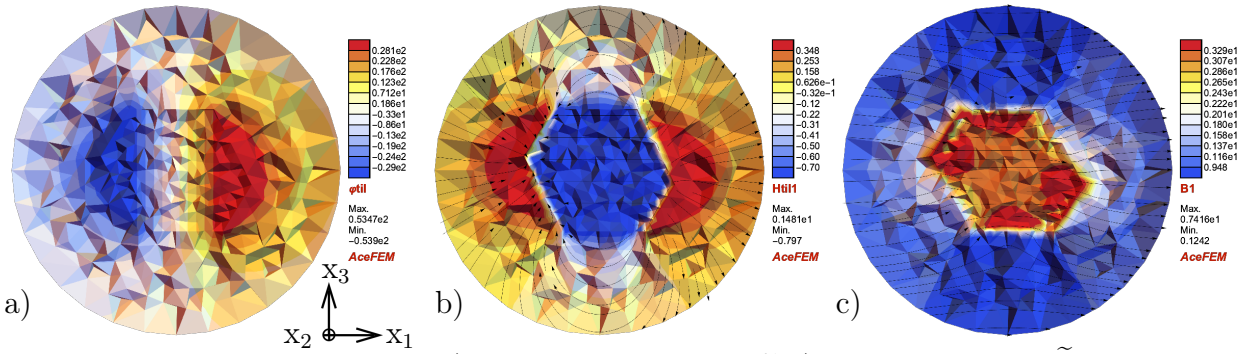

Figure 4.16: Contour plots of a) the fluctuation potential $\widetilde{\varphi}$, b) the fluctuation field $\widetilde{H}_1$ with streamlines, and c) the magnetic induction B_1 with streamlines resulting from an external magnetic field $\overline{H}_1$.

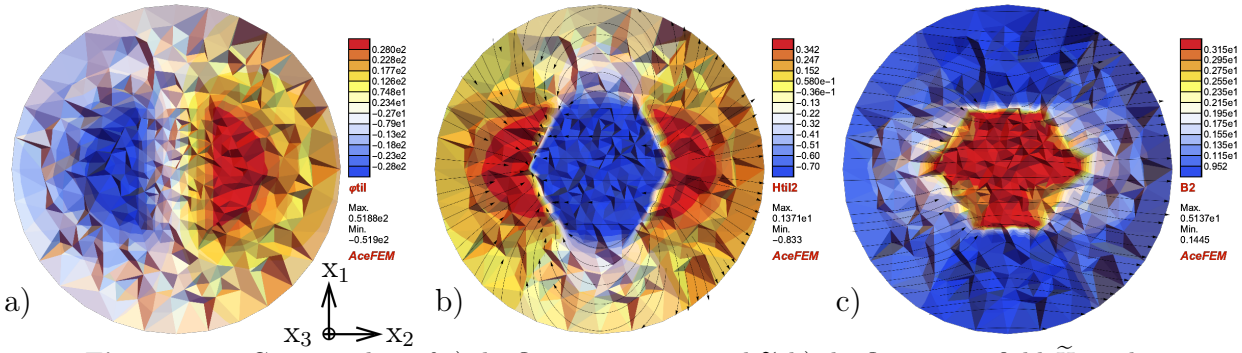

Figure 4.17: Contour plots of a) the fluctuation potential $\widetilde{\varphi}$, b) the fluctuation field $\widetilde{H}_2$ with streamlines, and c) the magnetic induction B_2 with streamlines resulting from an external magnetic field $\overline{H}_2$. Taken from Schröder et al. [2022].

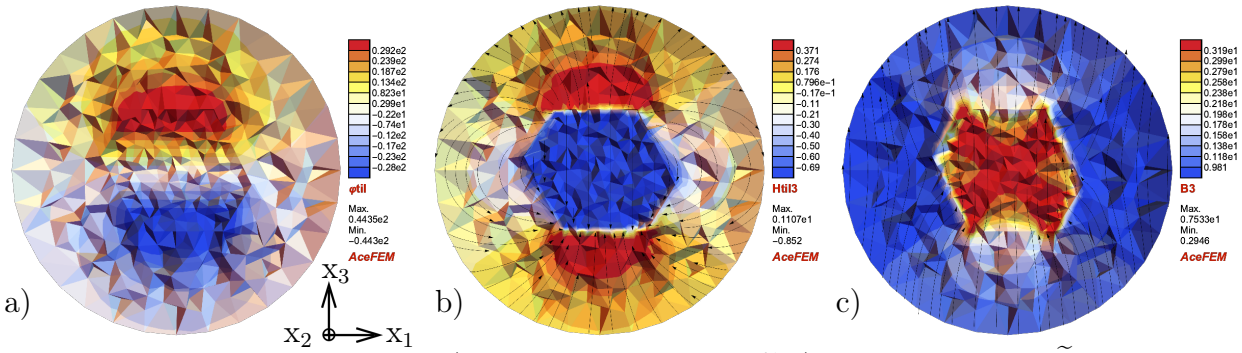

Figure 4.18: Contour plots of a) the fluctuation potential $\widetilde{\varphi}$, b) the fluctuation field $\widetilde{H}_3$ with streamlines, and c) the magnetic induction B_3 with streamlines resulting from an external magnetic field $\overline{H}_3$.

The fluctuation potential shown in Fig. 4.16a) results of an externally applied magnetic field in x_1-direction and shows the typical cloud-like curves. Hence, the fluctuation field $\widetilde{\boldsymbol{H}}$ in Fig. 4.16b) results in a spatially non-linear distribution. Thus, the overall magnetic field $\boldsymbol{H}$ in Fig. 4.16c) also results in a spatially non-linear distribution, which is particularly pronounced within the area of the inhomogeneity. The presented illustrations in Fig. 4.17 and Fig. 4.18 show the respective interaction of the magnetic grain with the external magnetic field in x_2 and x_3 directions. To determine the time gain of a dynamic simulation through static condensation, the magnetic field is increased within 100 load steps, from zero to the maximum field strength of $\overline{H}_2$. Both simulations are timed and the results are compared in Table 4.6. The time advantage of the reduced simulation with a factor of 4.66 compared to the full FEM calculation is obvious. For larger systems an increase in time for the static condensation can be seen. However, the time spent for this calculation can be made up quickly, especially with dynamic simulations. That means, a reduction in three dimensions can also be worthwhile, if results in the outer space are not necessarily required.

Table 4.6: Required times for solving the system of equations. Taken from Schröder et al. [2022].

Steps	Reduced	Reference	Factor
100	557.9 s	2598.8 s	4.66

Analogously to the two-dimensional FEM, the three-dimensional FEM also results in sparsely populated stiffness matrices. Since the reduced matrix is very densely populated, the advantage of sparse matrices is lost through the static condensation of the outer domain $\mathcal{B}^{\text{ext}}$ onto the boundary of the interior domain $\partial\mathcal{B}^{\text{int}}$ as in the two-dimensional case. However, this resulting disadvantage will be counterbalanced by the advantage of a significantly smaller reduced stiffness matrix. To illustrate the size differences, a comparison of the two matrices can be found in Fig. 4.19.

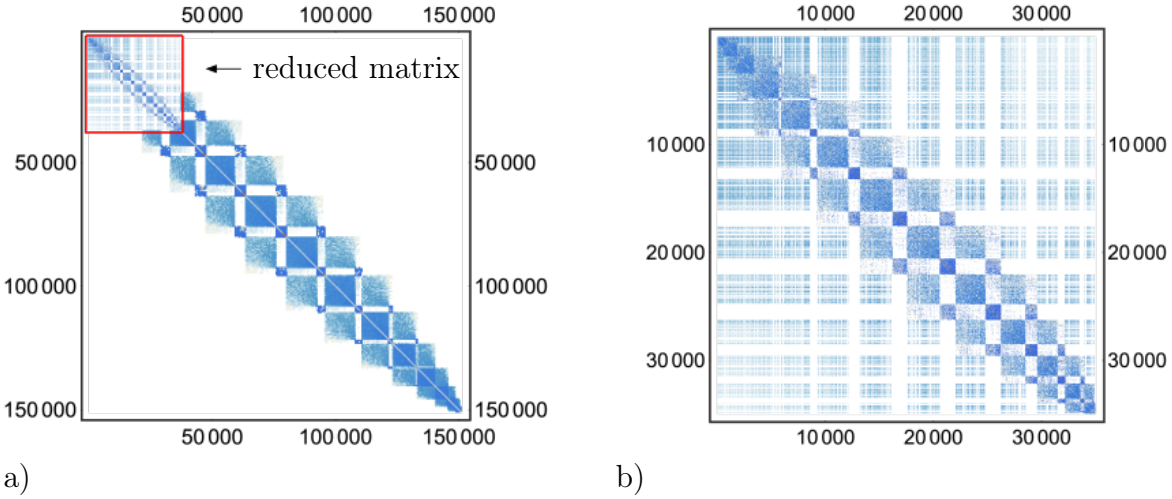

Figure 4.19: The population of the stiffness matrix corresponding to the full FEM solution is presented in a) together with the stiffness matrix corresponding to the reduced calculation marked by a red frame. The population of the reduced stiffness matrix is presented in b) as a scaled plot. Taken from Schröder et al. [2022].

4.5 An SBFEM-based approach for magnetostatic open boundary problems

In this section, another numerical method, the scaled boundary finite element method (SBFEM), is addressed. This method was initially developed and applied to investigate the dynamic behavior of unbounded domains with radiation condition at infinity. The radiation condition states that no energy may be reflected from the boundary located at infinity. Hence, the SBFEM allows to numerically consider the influence of an infinitely large external space, while the static condensation of the external space presented in Sec. 4.4 is limited to very large but finite areas. An overview of the efficient treatment of so-called open boundary problems was discussed in Sec. 4.3. More precisely, the method of interest is a hybrid SBFEM-FEM formulation. Consider, similar to Sec. 4.4, an interior domain (near field) $\mathcal{B}^{\text{int}} = \mathcal{B}^{\text{int}}_{\text{vac}} \bigcup \mathcal{B}^{\text{int}}_{\text{sol}}$ that consists of a magnetic solid $\mathcal{B}^{\text{int}}_{\text{sol}}$ and a finite portion of free space $\mathcal{B}^{\text{int}}_{\text{vac}}$ (Fig. 4.20b)). The material behavior of the solid $\mathcal{B}^{\text{int}}_{\text{sol}}$ as well as the finite part of the free space $\mathcal{B}^{\text{int}}_{\text{vac}}$ are captured using the finite element method. The behavior of the exterior/unbounded domain (far field) $\mathcal{B}^{\text{ext}}$ of the free space, sketched in Fig. 4.20c), is captured utilizing the SBFEM. The influence of the far field on the near field can be considered via the coupling of the SBFEM to the FEM, as depicted in Fig. 4.20a). Strictly speaking, the theory from Sec. 4.4.1 and partially from Sec. 4.4.2 can be applied in this chapter as well. The discretization of $\mathcal{B}^{\text{int}}$ follows the procedure described in Sec. 4.4.2 analogously. However, the hybrid SBFEM-FEM formulation is derived in detail in Birk et al. [2022] and the results within this section have already been published therein.

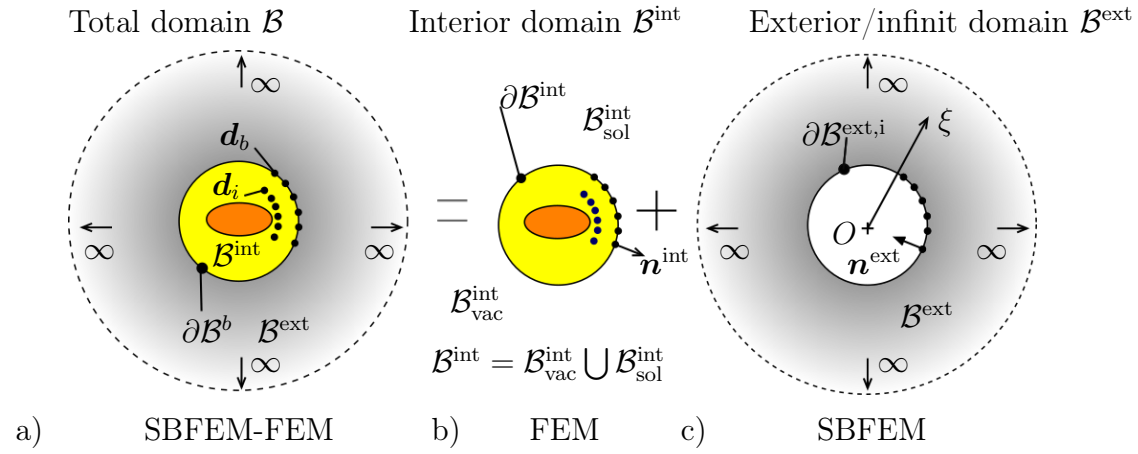

Figure 4.20: The discrete subdivided domains and the definitions of the inner and outer boundaries of a) the total domain of interest $\mathcal{B}$, definition of the interior and exterior subdomains, b) the interior domain $\mathcal{B}^{\text{int}} = \mathcal{B}^{\text{int}}_{\text{vac}} \bigcup \mathcal{B}^{\text{int}}_{\text{sol}}$ (full FEM approximation), and c) the exterior domain $\mathcal{B}^{\text{ext}}$ (full SBFEM approximation).

As mentioned above, the SBFEM is used here to solve Eq. 4.25 semi-analytically in the far field to include the influence of the magnetostatic fields. For this purpose, the circumferential coordinates (η, ζ) as well as the radial coordinate ξ are introduced by means of a coordinate transformation. This facilitates decoupling of the governing field equation (Eq. 4.25) in the circumferential and radial directions. The SBFEM requires the discretization of the surface $\partial\mathcal{B}^{\text{ext,i}}$ by means of finite elements. In general, this surface must satisfy a necessary criterion, the so-called scaling requirement, cf. Song [2018]. The scaling criterion states that a position O, the so-called scaling center, must exist from

which the entire surface $\partial\mathcal{B}^{\mathrm{ext,i}}$ can be seen. Accordingly, 1D line elements are used in a 2D boundary value problem and 2D surface elements are used in a 3D boundary value problem. The positions of the element nodes (based on a Cartesian coordinate system) are stored in the vectors $\boldsymbol{x}_{\mathrm{b}}, \boldsymbol{y}_{\mathrm{b}}$, and $\boldsymbol{z}_{\mathrm{b}}$. Based on the isoparametric concept, these quantities can be obtained by

$$\begin{aligned} x(\xi,\eta,\zeta) &= \xi\, \underline{\mathbb{N}}^s(\eta,\zeta)\underline{\boldsymbol{x}}_b, \\ y(\xi,\eta,\zeta) &= \xi\, \underline{\mathbb{N}}^s(\eta,\zeta)\underline{\boldsymbol{y}}_b, \\ \text{and}\quad z(\xi,\eta,\zeta) &= \xi\, \underline{\mathbb{N}}^s(\eta,\zeta)\underline{\boldsymbol{z}}_b, \end{aligned} \tag{4.65}$$

where $\underline{\mathbb{N}}^s(\eta,\zeta)$ are the interpolation functions of the surface elements and ξ, η, and ζ represent the scaled boundary coordinates. For a more in-depth introduction to the fundamentals of the SBFEM, the monograph Song [2018] is recommended. Analogous to Sec. 4.4, the constant $\overline{\boldsymbol{H}}$ and fluctuation $\widetilde{\boldsymbol{H}}$ part of the magnetic field are inserted into the linear constitutive relation Eq. 4.28, leading to a magnetic induction $\boldsymbol{B} = \lambda\overline{\boldsymbol{B}} + \widetilde{\boldsymbol{B}}$, with a constant and a fluctuation contribution. For the resulting system of equations, the structure of the global system of equations of the hybrid SBFEM-FEM formulation is identical to that already introduced in Eq. 4.58[7.)]. Starting from Eq. 4.58 this system of equations can be divided into a near field and a far field part as follows:

$$\underbrace{\begin{bmatrix} \underline{\mathbb{K}}_{ii}^{\mathrm{int}} & \underline{\mathbb{K}}_{ib}^{\mathrm{int}} \\ \underline{\mathbb{K}}_{bi}^{\mathrm{int}} & \underline{\mathbb{K}}_{bb}^{\mathrm{int}} \end{bmatrix} \begin{bmatrix} \Delta\underline{\widetilde{\boldsymbol{D}}}_i \\ \Delta\underline{\widetilde{\boldsymbol{D}}}_b \end{bmatrix} = \begin{bmatrix} \underline{\mathbb{R}}_i^{\mathrm{int}} \\ \underline{\mathbb{R}}_b^{\mathrm{int}} - \underline{\mathbb{R}}_b^{\mathrm{SB}} \end{bmatrix}}_{\text{Near field}} \quad \text{and} \quad \underbrace{\underline{\mathbb{R}}_b^{\mathrm{SB}} = \underline{\mathbb{K}}_{bb}^{\infty}\, \Delta\underline{\widetilde{\boldsymbol{D}}}_b + \underline{\mathbb{R}}_b^{\infty}}_{\text{Far field}}. \tag{4.66}$$

Here, the system of equations of the near field is represented in the first part of Eq. 4.66. The subindex i refers to the degrees of freedom within the internal domain $\mathcal{B}^{\mathrm{int}} \setminus \partial\mathcal{B}^{\mathrm{int}}$ and the subindex b indicates the degrees of freedom on the boundary $\partial\mathcal{B}^{\mathrm{int}}$. The contribution $\underline{\mathbb{R}}_b^{\mathrm{SB}}$ within the right-hand side represents the influence of the far field on the near field. The second part of Eq. 4.66 can be identified as the system of equations describing the far field. Since the near field is already known and the far field is to be described by means of the SBFEM, the focus is placed here. In the SBFEM formulation that is considered here, the boundary conditions are defined on the interface between the near field and the far field, thus $\xi = 1$ holds. Considering $\xi = 1$, Eq. 4.66b) can be reformulated as follows:

$$\underline{\mathbb{R}}^{\mathrm{SB}}(\xi=1) = \underline{\mathbb{K}}_{bb}^{\infty}\, \Delta\underline{\widetilde{\boldsymbol{D}}}_b(\xi=1) + \underline{\mathbb{R}}_b^{\infty}. \tag{4.67}$$

The vector $\underline{\mathbb{R}}_b^{\infty}$ corresponds to the nodal-flux due to the prescribed constant magnetic field $\overline{\boldsymbol{H}}$ (non-homogeneous term), while $\underline{\mathbb{K}}_{bb}^{\infty}\, \Delta\underline{\widetilde{\boldsymbol{D}}}_b(\xi = 1)$ is the nodal-flux due to the magnetic stray fields. In the framework of the SBFEM, the constant nodal-flux and the system matrix of the unbounded domain are calculated by

$$\underline{\mathbb{R}}_b^{\infty} = -\underline{\boldsymbol{Q}}_0(\xi=1) - (\underline{\boldsymbol{\Psi}}_{21} + \underline{\mathbb{K}}_{bb}^{\infty}) \cdot \underline{\overline{\boldsymbol{w}}}_1 \quad \text{and} \quad \underline{\mathbb{K}}_{bb}^{\infty} = -\underline{\boldsymbol{\Psi}}_{22}\left[\underline{\boldsymbol{\Psi}}_{12}\right]^{-1}, \tag{4.68}$$

[7.)] In fact, the final global system of equations in the publications Schröder et al. [2022] Eq. 31 and Birk et al. [2022] Eq. 87 differ by the sign of the superimposed external right-hand side $\underline{\mathbb{R}}_b^{\infty}$. This is because the system of equations of the far field that has to be condensed (in Schröder et al. [2022]) is already assembled negative beforehand. Thus, the negative sign is already accounted for in the formulation. However, in the following the minus is explicitly taken into account, based on the formulations in Birk et al. [2022].

where $\boldsymbol{Q}_0(\xi = 1)$ represents the contribution of the externally applied magnetic field on the interface for $\xi = 1$ and

$$\underline{\boldsymbol{\Psi}} = \begin{bmatrix} \underline{\boldsymbol{\Psi}}_{11} & \underline{\boldsymbol{\Psi}}_{12} \\ \underline{\boldsymbol{\Psi}}_{21} & \underline{\boldsymbol{\Psi}}_{22} \end{bmatrix} \tag{4.69}$$

indicates a transformation matrix. $\overline{\underline{\boldsymbol{w}}}_1$ corresponds to the amplitudes of a particular solution as derived in Birk et al. [2022]. The hybrid SBFEM-FEM formulation results from a collaboration. Therefore, the computation of the stiffness matrix $\underline{K}_{bb}^{\infty}$ of the unbounded domain is addressed in Appendix A, but for a complete derivation, the reader is referred to the original paper Birk et al. [2022].

4.5.1 Numerical examples

When simulating magnetic materials, it is of crucial importance to consider their surrounding free space as precise as possible to capture the evolving magnetic fields correctly. Poor approximations using the truncation method or related procedures, e.g. due to the selection of outer spaces that are chosen too small, can massively degrade accuracy of the simulated results. In contrast to the latter methods, the hybrid SBFEM-FEM coupling discussed above is very well suited for the approximation of infinite outer domains. To verify the functionality of this method, numerical examples are given below. To this end, the near field is approximated using the FEM while the influence of the surrounding free space (far-field) is approximated using the SBFEM. The hybrid SBFEM-FEM coupling is implemented into the finite element framework of AceGen/AceFEM, compare Korelc [1997], Korelc and Wriggers [2016], and Korelc [2002]. The following numerical examples have been carried out on a 2020 M1 MacBook Pro with 16 GB of RAM.

4.5.2 T-shaped inclusion

In this example, a principle study to validate the hybrid SBFEM-FEM coupling presented above is performed using a magnetic T-shaped inclusion $\mathcal{B}^{\text{sol}}$ as depicted in Fig. 4.21.

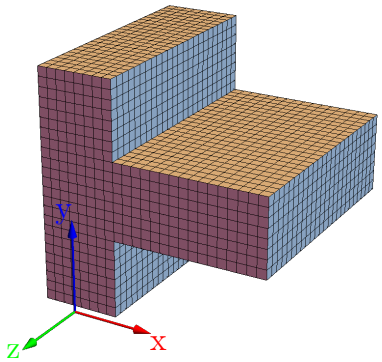

Figure 4.21: The T-shaped magnet $\mathcal{B}^{\text{sol}}$. Taken from Birk et al. [2022].

This T-shaped inclusion

- is computed with a fully FE-discretized outer space $\mathcal{B}^{\text{vac}}$ with a radius of 500 nm. This is necessary to generate a fully FE-based reference solution. Magnetic fields can be plotted all over the free space.

- is surrounded by an FE-discretized outer space $\mathcal{B}^{\text{vac}}$ with 200 nm radius. The coupling to the SBFEM is done on $\partial\mathcal{B}^{\text{vac}}$. The boundary value problem corresponds to Fig. 4.22. Here, the free space $\mathcal{B}^{\text{vac}}$ is only used to depict the magnetic fields in the immediate vicinity of the magnet.
- is coupled directly on the edge $\partial\mathcal{B}^{\text{sol}}$ to the SBFEM to illustrate the advantages of the SBFEM. The size of the boundary value problem reduces to the domain presented in Fig. 4.21. Consequently, magnetic fields can only be represented within the magnetic solid.

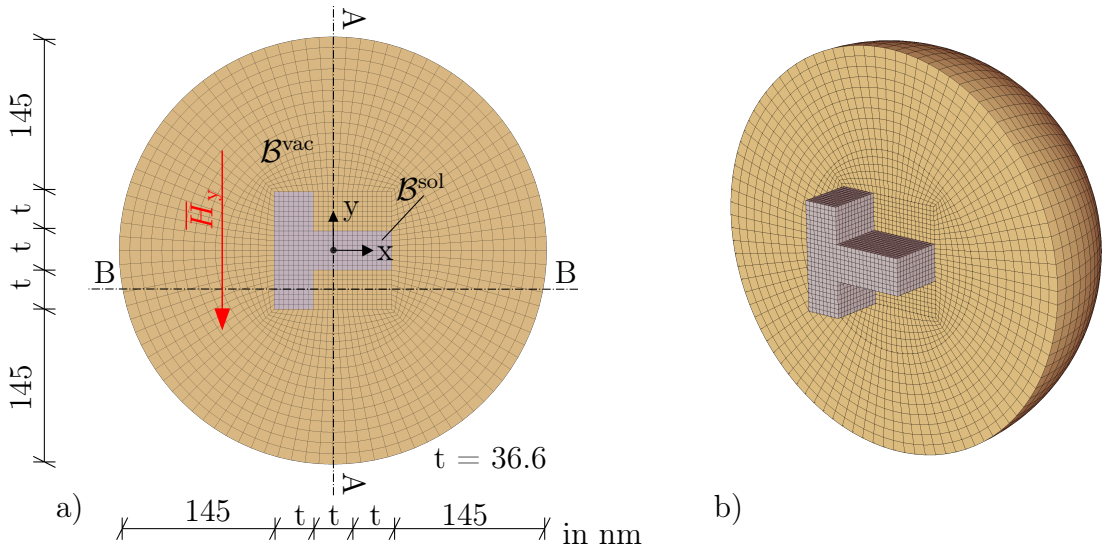

Figure 4.22: A T-shaped permalloy inclusion $\mathcal{B}^{\text{sol}}$ embedded within a vacuum space $\mathcal{B}^{\text{vac}}$ and treated with an externally applied magnetic field $\overline{H}_{\text{y}}$, with a) all relevant geometrical dimensions and b) an overview of the 3D discretized sample. Taken from Birk et al. [2022].

The material permeability of permalloy $\mu_1 = 1.25 \cdot 10^{-1}$ H/m is assigned to the magnetic inclusion $\mathcal{B}^{\text{sol}}$ while the surrounding free space $\mathcal{B}^{\text{vac}}$ is considered to be vacuum with $\mu_0 = 4\pi \cdot 10^{-7}$ H/m, compare Coey [2010]. Since the SBFEM provides a solution for the infinite space, that mimics vacuum, the material parameter μ_0 is also used in the calculations based on the SBFEM. To generate a material response, the boundary value problem described above is treated sequentially with two externally applied magnetic fields $\overline{\boldsymbol{H}} = \frac{1}{4\pi}\,[-1, 0, 0]^T$ A/nm and $\overline{\boldsymbol{H}} = \frac{1}{4\pi}\,[0, -1, 0]^T$ A/nm. The reaction of the magnetic solid to the first external field is given by the fluctuation potential $\widetilde{\varphi}$, that is shown as a contour plot in Fig. 4.23a) and the magnetic fluctuation field shown in Fig. 4.23b). To highlight the orientation of the fluctuation field, the contour plot of $\widetilde{H}_{\text{x}}$ is depicted in Fig. 4.23c) with superimposed stream lines of $\widetilde{\boldsymbol{H}}$. Since the magnetic induction $\boldsymbol{B}$ can be derived from the total magnetic potential φ, B_{x} is illustrated in Fig. 4.23d). The contour plot is superimposed with stream lines of $\boldsymbol{B}$ to highlight the orientation of the induction.
The applied magnetic field $\overline{\boldsymbol{H}}$ generates the fluctuation field $\widetilde{\boldsymbol{H}}$ shown in Fig. 4.23c), which has the opposite orientation in the magnetic solid (compared to the applied field). This fluctuation field is generated by the associated fluctuation potential $\widetilde{\varphi}$, which is shown in Fig. 4.23a). A similar response of the magnet results for a magnetic field parallel to the y-direction. These responses are shown in Fig. 4.24 and demonstrate the ability of this method to apply external fields in arbitrary directions.

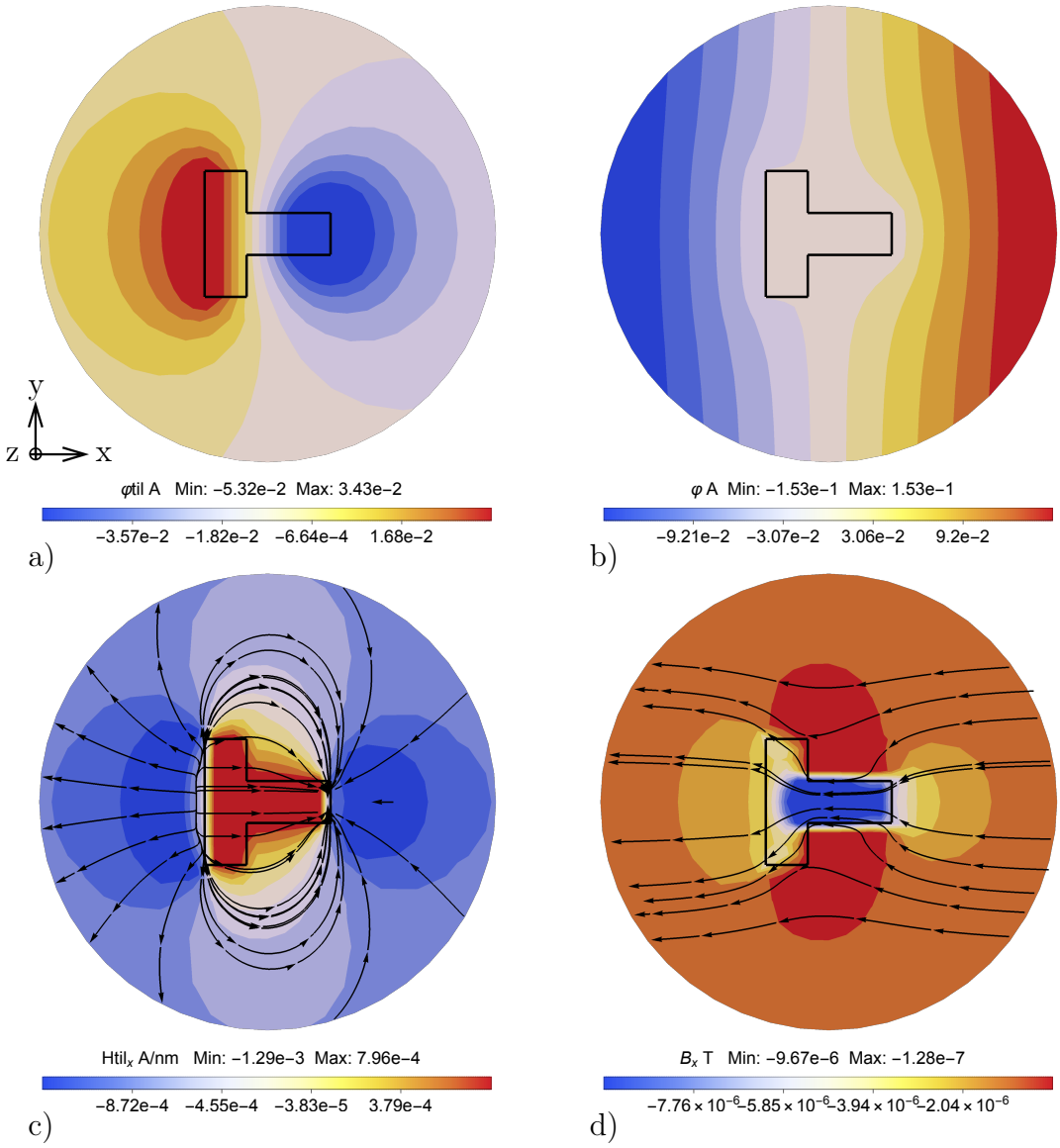

Figure 4.23: Contour plots of a) the magnetic fluctuation potential $\widetilde{\varphi}$ and b) the total magnetic potential φ. The corresponding contour plots of c) the fluctuation field $\widetilde{H}_\mathrm{x}$ with streamlines of $\widetilde{\boldsymbol{H}}$ and d) the magnetic induction B_x with streamlines of $\boldsymbol{B}$.

Since the necessary boundary condition $\widetilde{\varphi} = 0$ of the fluctuation has to be prescribed on a boundary existing at infinity (compare Bayliss et al. [1982]), an implementation with the FEM is not possible. The SBFEM provides a semi-analytical solution, so that the boundary conditions can be considered in advance. Hence, the hybrid SBFEM-FEM coupling, can provide good approximations for so-called open boundary problems. The magnetic induction $\boldsymbol{B}$ shown in Fig. 4.23d) is deflected by the fluctuations around the inclusion and is therefore not unimpeded. To validate the results of the calculation, a comparison with a pure FE reference simulation is carried out at this point. For this purpose, the boundary value problem described in Fig. 4.22 is not coupled to the SBFEM, but enclosed within a large but finite free space Ω discretized by finite elements. The free space is chosen large enough so that truncation errors are negligibly small. Subsequently, discrete values of the magnetic potentials φ, $\widetilde{\varphi}$, and $\overline{\varphi}$ are evaluated along the intersection

line A–A (compare Fig. 4.22), while the intersection line B–B provides the discrete values of the magnetic fields H_y, $\widetilde{H}_y$, and $\overline{H}_y$. These discrete values are plotted in Fig. 4.25 for both, the hybrid SBFEM–FEM coupling and the pure FEM discretization. Since perfect agreement can be observed, this example can be considered as a numerical proof that the presented method delivers very good approximations without direct discretization of the exterior space.

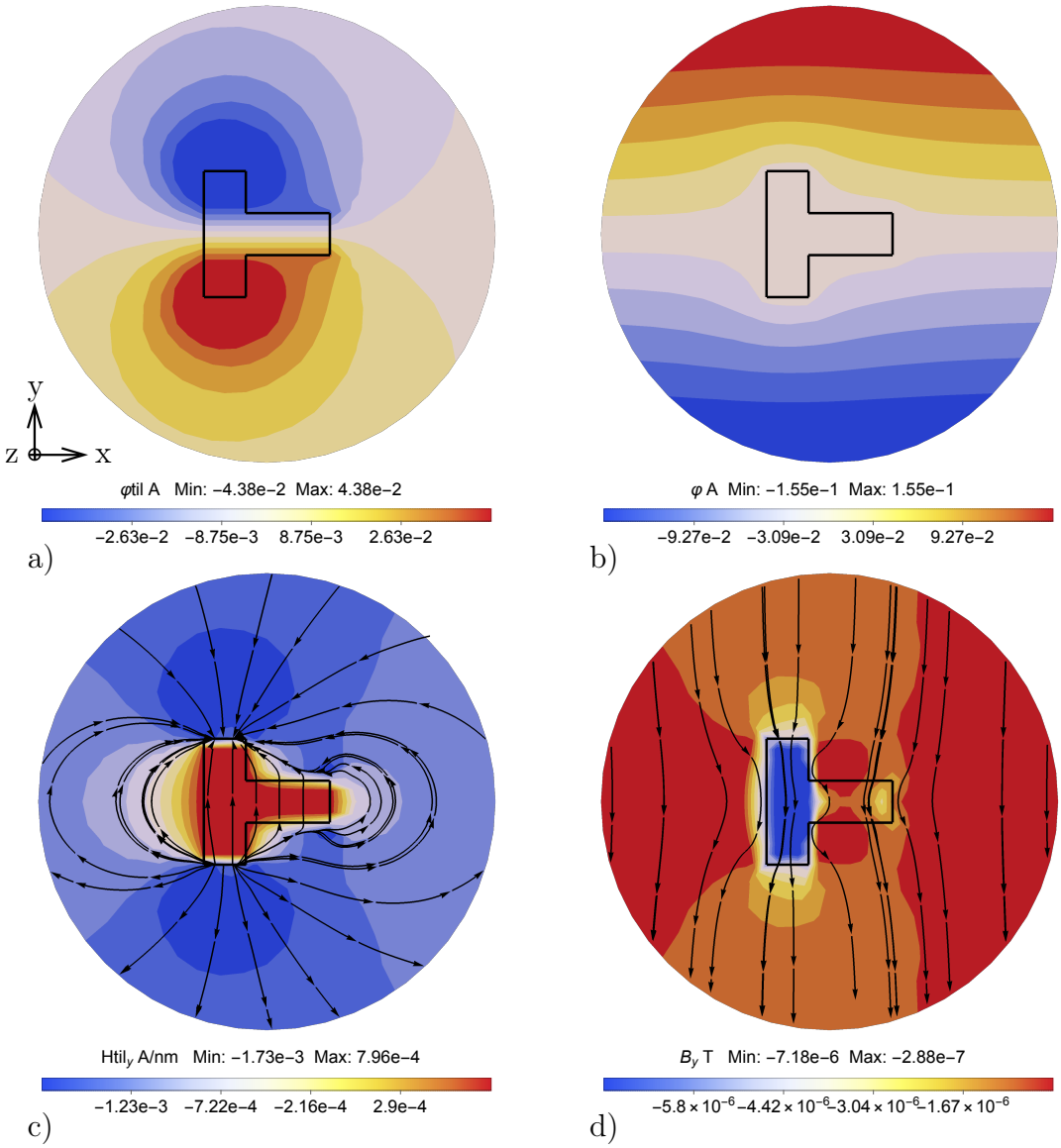

Figure 4.24: Contour plots of a) the magnetic fluctuation potential $\widetilde{\varphi}$ and b) the total magnetic potential φ. The corresponding contour plots of c) the fluctuation field $\widetilde{H}_y$ with streamlines of $\widetilde{\boldsymbol{H}}$ and d) the magnetic induction B_y with streamlines of $\boldsymbol{B}$. Taken from Birk et al. [2022].

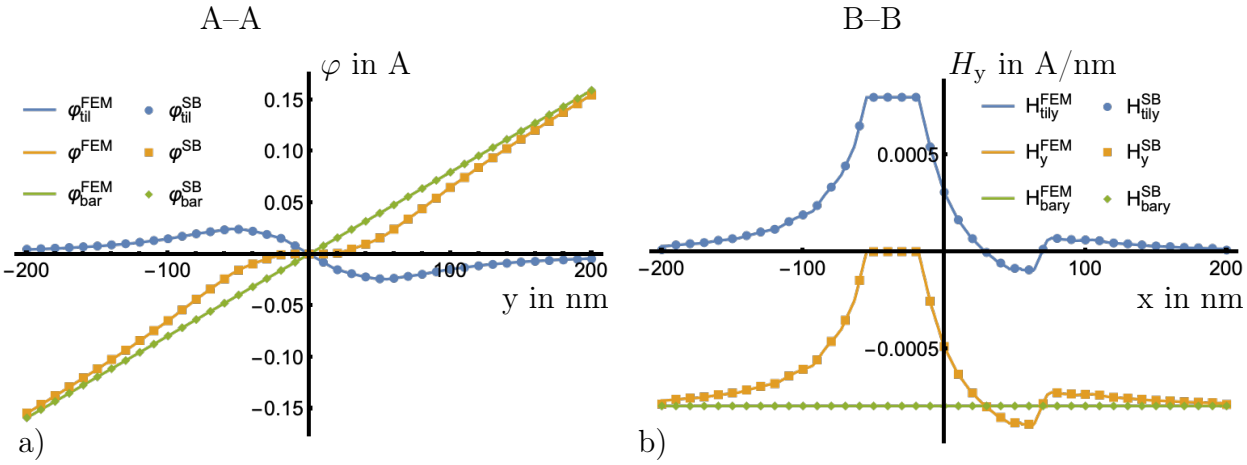

Figure 4.25: The comparison of discrete values of a) the magnetic potentials φ, $\widetilde{\varphi}$, and $\overline{\varphi}$ evaluated along the intersection line A–A, and b) the fields H_y, $\widetilde{H}_\mathrm{y}$, and $\overline{H}_\mathrm{y}$ along B–B. Taken from Birk et al. [2022].

To demonstrate the full potential of the hybrid SBFEM-FEM coupling, the free space discretization with finite elements around the T-shaped inclusion is completely omitted. The SBFEM couples directly to the magnetic material so that no surrounding magnetic fields is visible. The hybrid SBFEM-FEM coupling is compared with a full FEM calculation to subsequently evaluate the presented method with respect to a reduction in computational time. The advantage of classical FEM stiffness matrices is a mostly sparse populated band structure, which can have very large dimensions due to the outer space. In contrast to the typical FEM matrices, those of the SBFEM-FEM coupling are very densely occupied, but by a multiple smaller in dimension, compare to the matrix plots shown in Fig. 4.26. Fig. 4.26a) shows the full FEM matrix superimposed with the SBFEM-FEM coupled matrix.

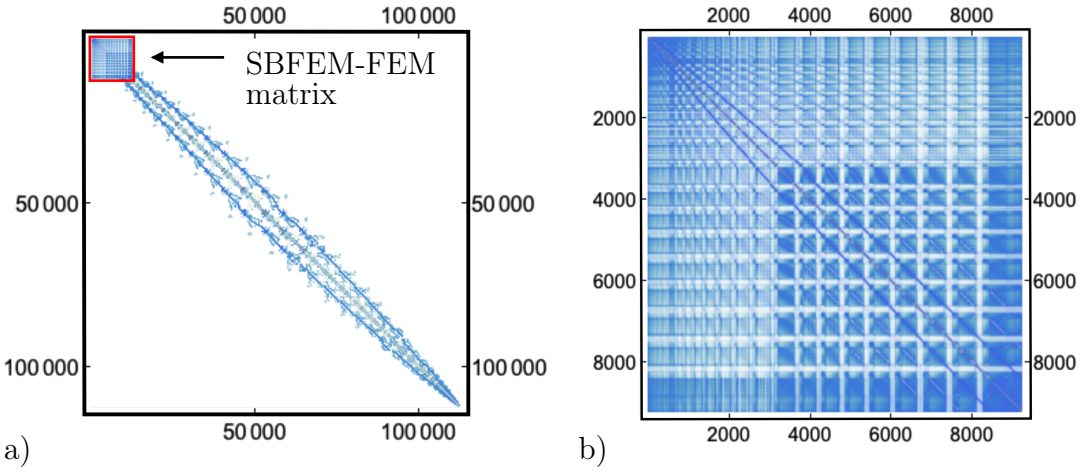

Figure 4.26: The stiffness matrices of the described boundary value problems as matrix plots. The system matrix of a) the fully FE-discretized boundary value problem and b) the SBFEM-FEM coupled matrix. Taken from Birk et al. [2022].

The FEM reference system has a total of 115,907 DOF, of which the magnetic inclusion claims 9,225 DOF. In the SBFEM-FEM coupling considered here, only the T-shaped inclusion exists and thus a total of only 9,225 DOF. The number of degrees of freedom on the edge of the T-shaped inclusion is 2,946 DOF which, also corresponds to the number of DOF considered by the SBFEM. The calculation of the SBFEM stiffness matrix took

201,27 s. The SBFEM-FEM coupling has advantages especially in time-dependent calculations, which require a serial solution of the considered equation system. Therefore, in this example the external magnetic field is increased within 10 steps to the maximum value of $\overline{\boldsymbol{H}} = \frac{1}{4\pi}\,[0,-1,0]^T$ A/nm. The required time is measured for both the FEM reference problem and the reduced SBFEM-FEM problem to subsequently allow a direct comparison of the two methods. The entire solution process requires 101,30 s computational time for the full FEM solution, while it takes 21,62 s for the hybrid formulation, as presented in Table 4.7. Thus, the reduced boundary value problem considered here can be solved about five times faster than the fully discretized FEM reference solution.

Table 4.7: Comparison of the degrees of freedom, the run-times for setting up the SBFE stiffness matrix and the solution procedure of both methods. Taken from Birk et al. [2022].

	FEM reference	Hybrid SBFEM-FEM
Degrees of freedom	115,907	9,225
Build up SBFE matrix in s	not required	207.76
Solution time in s	101.30	21.62

The direct coupling of the SBFEM with the FEM on the boundary $\partial\mathcal{B}^{\text{sol}}$ generates for the magnetic field applied in x-direction ($\overline{\boldsymbol{H}} = \frac{1}{4\pi}\,[-1,0,0]^T$ A/nm) and subsequently in y-direction ($\overline{\boldsymbol{H}} = \frac{1}{4\pi}\,[0,-1,0]^T$ A/nm) only reactions within the magnetic solid, since no free space is available that allows post processing therein. Hence, the distributions of the magnetic potential φ and the induction B_x at field strength $\overline{\boldsymbol{H}} = \frac{1}{4\pi}\,[-1,0,0]^T$ A/nm is depicted in Fig. 4.27 and for a field strength $\overline{\boldsymbol{H}} = \frac{1}{4\pi}\,[0,-1,0]^T$ A/nm in Fig. 4.28. Since the agreement between the FEM reference solution and the SBFEM-FEM coupling is exact, only the contour plots of the latter are presented below.

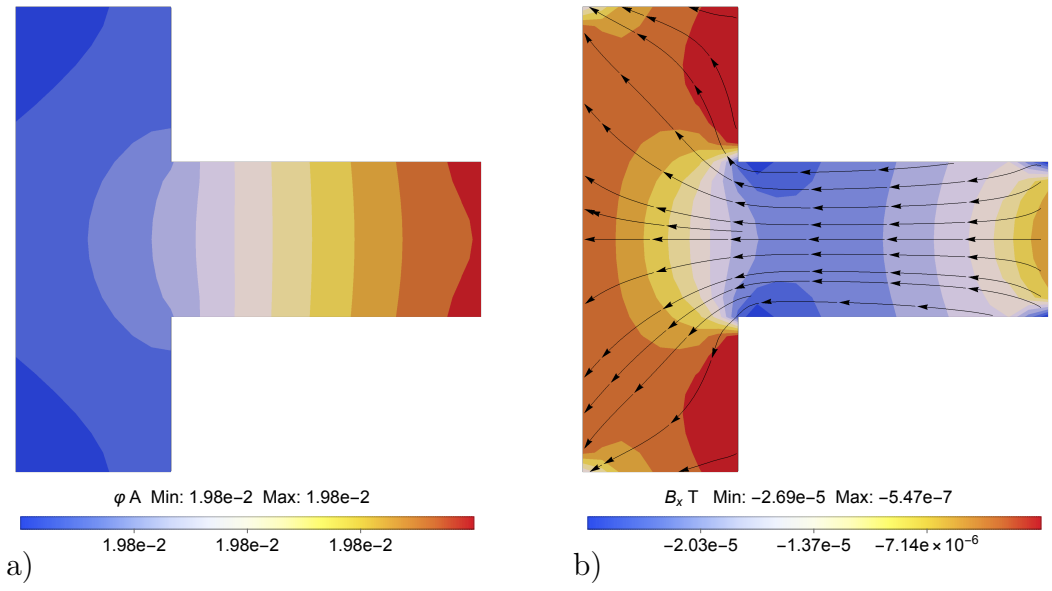

Figure 4.27: Contour plots of a) the magnetic potential φ and b) magnetic induction B_{x}. To highlight the orientation of the induction it is superimposed with the corresponding stream lines of $\boldsymbol{B}$.

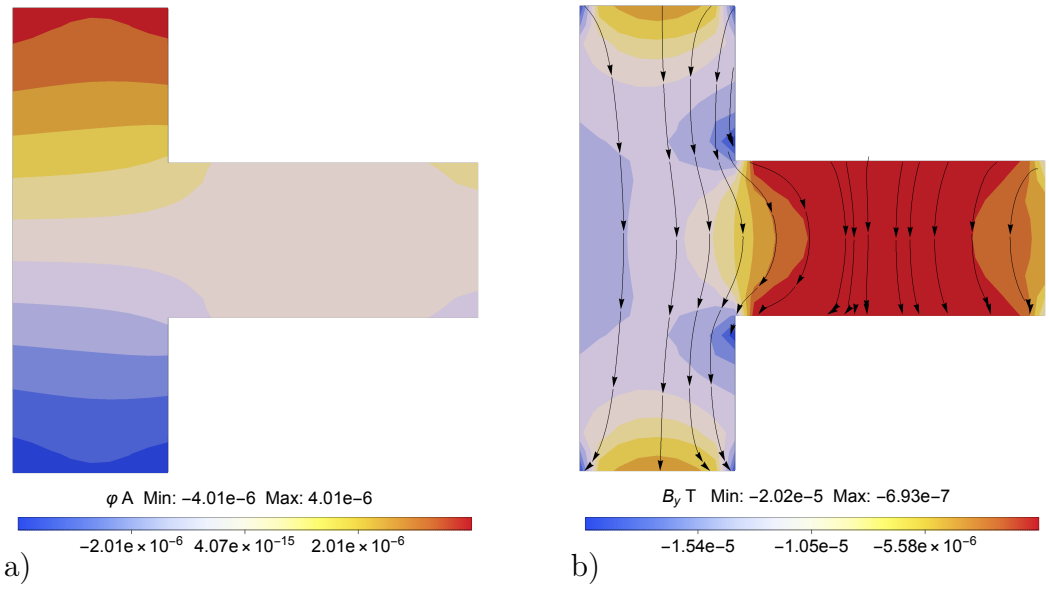

Figure 4.28: Contour plots of a) the magnetic potential φ and b) magnetic induction B_y. To highlight the orientation of the induction it is superimposed with the corresponding stream lines of $\boldsymbol{B}$. Taken from Birk et al. [2022].

4.5.3 Magnetic particles in free space

The considered domain is reduced onto the boundary of two magnetic particles $\mathcal{B}_1^{\text{sol}}$ and $\mathcal{B}_2^{\text{sol}}$ that are only separated by a gap consisting of vacuum $\mathcal{B}^{\text{vac}}$. The exact dimensions of the particles and the separating free space are shown in Fig. 4.29. In this example, the coordinate origin corresponds to the center of mass. The magnetic particles are characterized by different permeabilities. Namely the permeability of $\mathcal{B}_1^{\text{sol}}$ corresponds to $\mu_1 = 1.25{\cdot}10^{-1}$ H/m, while it is $\mu_2 = 1 \cdot 10^{-1}$ H/m for $\mathcal{B}_2^{\text{sol}}$. The vacuum permeability of $\mu_0 = 4\pi \cdot 10^{-7}$ H/m is assumed for the separating gap $\mathcal{B}^{\text{vac}}$.

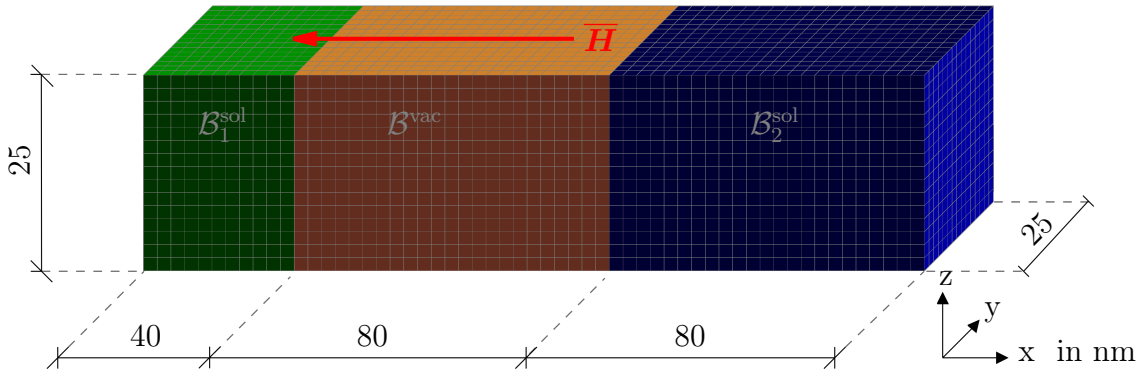

Figure 4.29: Two magnetic particles $\mathcal{B}_1^{\text{sol}}$ and $\mathcal{B}_2^{\text{sol}}$ of different size separated by an air gap $\mathcal{B}^{\text{vac}}$ and treated by an external magnetic field $\overline{\boldsymbol{H}} = \frac{1}{4\pi}\,[-1, 0, 0]^T$ A/nm. Taken from Birk et al. [2022].

In this case, the influence of the surrounding space, the far field, is approximated by the SBFEM. Its material behavior is the same as for the air gap $\mathcal{B}^{\text{vac}}$, thus also corresponding to vacuum. To generate a reaction of the system, an external magnetic field

$\overline{\boldsymbol{H}} = \frac{1}{4\pi}\,[-1,0,0]^T$ A/nm is applied. This example is intended to show that the coupling of the SBFEM and the FEM presented above can result in a strong reduction of the size of the overall system. For this purpose, the presented boundary value problem is reduced as far as possible, so that no surrounding free space is considered. However, this strong reduction also means that the results are calculated exclusively in the discretized region $\mathcal{B} = \mathcal{B}_1^{\text{sol}} \cup \mathcal{B}_2^{\text{sol}} \cup \mathcal{B}^{\text{vac}}$ and therefore, can only be displayed there.

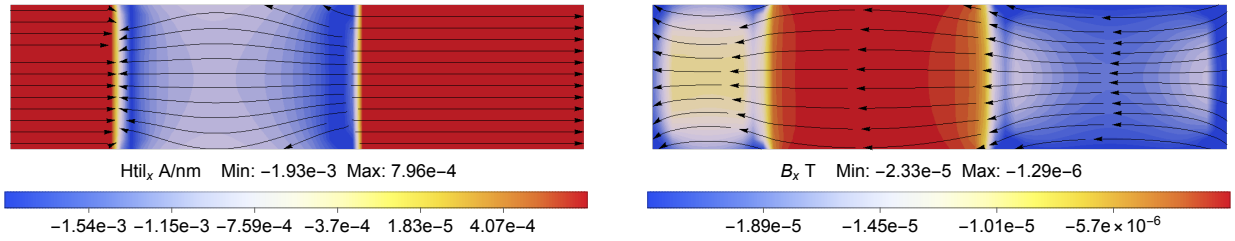

a) b)

Figure 4.30: The contour plots of a) the magnetic fluctuation field $\widetilde{\boldsymbol{H}}_{\text{x}}$ superimposed with the corresponding stream plot of the fluctuation field $\widetilde{\boldsymbol{H}}$ and b) the total magnetic induction B_{x} as well as the corresponding stream plot of $\boldsymbol{B}$. Taken from Birk et al. [2022].

To clarify the graphical representations, only two dimensional plots are presented showing values of the x–y plane at height z= 0 nm. The evolution of the magnetic fluctuation field $\widetilde{\boldsymbol{H}}$ is depicted in Fig. 4.30a). The contour plot shows the x-component of the fluctuations that are superimposed with the corresponding stream lines of $\widetilde{\boldsymbol{H}}$. Here, the typical contra orientation of the magnetic fluctuation field within the magnetic solids $\mathcal{B}_1^{\text{sol}}$ and $\mathcal{B}_2^{\text{sol}}$ can be observed, while the orientation within the free space $\mathcal{B}^{\text{vac}}$ follows the direction of the externally applied field $\overline{\boldsymbol{H}}$. The contour of the magnetic induction B_{x} is plotted in Fig. 4.30b). In this plot, the stream lines of the induction $\boldsymbol{B}$ highlight that an unhindered flow through the free space gap is possible and only the magnetic solids force a deviation from the applied field.

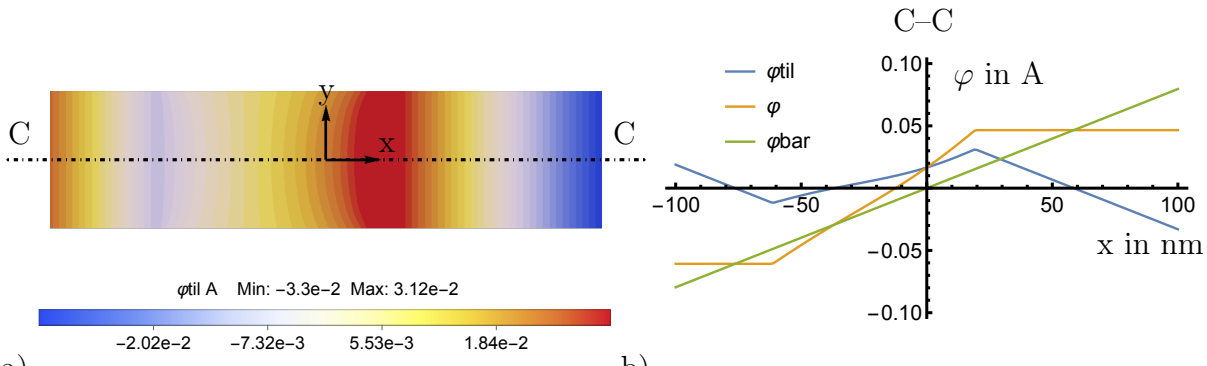

a) b)

Figure 4.31: a) the contour plot of the magnetic fluctuation potential $\widetilde{\varphi}$ with b) the corresponding evolution of all magnetic potentials φ, $\widetilde{\varphi}$, and $\overline{\varphi}$ along the intersection line C–C. Taken from Birk et al. [2022].

As already described in the previous example, $\widetilde{\varphi} = 0$ must hold for the fluctuation potential in a surrounding space Ω at infinity. However, in the vicinity of magnetic inclusions, it is not zero and certainly not within an inclusion. This also means that the potential on the boundary of $\mathcal{B}$ must be different to zero. This is confirmed in the contour plot of the potential $\widetilde{\varphi}$ presented in Fig. 4.31. Nevertheless, the plots of the discrete values of

all magnetic potentials φ, $\widetilde{\varphi}$, and $\overline{\varphi}$ taken along the intersection line C–C, in Fig. 4.31b) show their evolution and the difference to zero on $\partial\mathcal{B}$.

5 Micromagnetic theory

Magnetic materials can generally be divided into magnetically "hard" and "soft" materials, referring to the switching resistance of magnetic materials in the presence of externally applied magnetic fields. Magnetically hard materials posses wide hysteresis loops with larger energy products, while magnetically soft materials are typically featured by narrow hysteresis loops, cf. Inoue and Kong [2020]. These differently pronounced characteristics inherently lead to different fields of application of the materials. Both hard and soft magnetic materials make a significant contribution to further increase the efficiency of power generators (wind turbines), conversion equipment (transformers), sensors and means of transportation (electromobility) or data storage devices, as discussed in Gutfleisch et al. [2011], Gauss et al. [2021], and Khan et al. [2021]. Significantly enhanced properties of these magnetic materials are a key to improving energy efficiency, contributing substantially to flexible and intelligent designs of industrial applications as well as reducing their environmental impact. To obtain an in-depth understanding of the governing physical phenomena finite-element-based micromagnetic simulations are applied. Through the competition of different energy contributions magnetic domains are formed which are the origin for the hysteretic behavior, cf. Brown [1945]. These domains are variable in space and time and can be influenced by external stimuli like external magnetic fields or mechanical stresses, cf. Jiles [2015], Kittel [1949], and Hubert and Schäfer [1998]. Relying on the findings of Landau and Lifshitz [1935], Brown [1963] was eventually able to lay the foundations for micromagnetism. Later, Gilbert [2004] phenomenologically motivated the magnetic loss via a dissipation term. Today, Landau-Lifshitz-type equations are used within the most micromagnetic simulation tools. These can be applied to numerically investigate the impact of microstructure compositions onto magnetic properties, cf. Bolyachkin et al. [2022], DeSimone et al. [2006], Soderžnik et al. [2017], and Fischbacher et al. [2018] or the evolution of domain structures over time, cf. Alvandi-Tabrizi and Schwartz [2018] and Fidler et al. [2004].
For completeness it should be mentioned that micromagnetism is only one possibility to simulate magnetic materials. Out of a large number of available methods, a small selection is presented below. A very simple method for simulating the magnetic hysteresis loop is to apply a phenomenologically motivated model that uses a trigonometric function to fit the response to the physical behavior, as presented in Jiles and Atherton [1983; 1986] and Takács [2001]. Another very simple approach to simulate the behavior of magnetic single-domain particles minimizing the magnetic energy is known as the Stoner-Wohlfarth model, cf. Stoner and Wohlfarth [1948]. More complex in the numerical implementation, but still widely used, is the possibility to represent hysteresis of arbitrary shape by means of the so-called Preisach model, cf. Preisach [1935]. Thus, Adly et al. [1991] used a Preisach model to represent magnetostrictive hysteresis loops, Labusch et al. [2019] to simulate magneto-electro-mechanically coupled composites, and Sarker et al. [2020] to numerically analyze Fe-based alloys. In the context of numerical methods for magnetic simulations an overview is also provided by Bertotti and Mayergoyz [2005]. However, to take into account the microstructural influences in simulations of macroscopic components, homogenization methods such as the FE^2 method can provide a suitable numerical framework, cf. Schröder [2014]. Recently, Keip and Rambausek [2016] applied an FE^2-based homogenization proce-

dure to magnetorheological elastomers, while SCHRÖDER ET AL. [2016] took advantage of the FE^2 method during the simulation of magneto-electro-mechanically coupled composite materials. For a more comprehensive overview on the topic of homogenization of magneto-mechanical and magneto-electro-mechanical materials, the reader is referred to LABUSCH ET AL. [2018].

Parts of this chapter are published in:

M. Reichel, B.X. Xu and J. Schröder, A comparative study of finite element schemes for micromagnetic mechanically coupled simulations, *Journal of Applied Physics*, 132:183903, (2022), AIP Publishing.

M. Reichel, J. Schröder and B.X. Xu, Efficient micromagnetic finite element simulations using a perturbed Lagrange multiplier method, *Proceedings in Applied Mathematics and Mechanics*, 22:1 e202200016, (2022), Wiley.

M. Reichel, R. Niekamp and J. Schröder, Efficient micromagnetic-elastic simulations based on a perturbed Lagrangian function, *Journal of Applied Physics*, 134:103901, (2023), AIP Publishing.

In this chapter an overview of numerical methods in micromagnetic simulations is given, focusing on the conservation of the magnetization unit constraint. Subsequently, the magneto-elastic energy functional including all necessary energy contributions is introduced. Based on this energetic contribution, the main micromagnetic equations are derived. Afterwards, the micromagnetic-mechanical boundary value problem is transformed into its continuous and discrete weak forms. Thereby, the focus lies on different numerical schemes to preserve the magnetization amplitude. The general workability of these different schemes, as well as their individual advantages and disadvantages, are compared. Finally, the results, with respect to the benefits and drawbacks of the approaches, are summarized.

5.1 Overview on micromagnetic approaches

In 1935 Landau and Lifshitz published a work that is thematically focused on the description of magnetic moments, domains, and their boundaries, the so-called domain walls, cf. LANDAU AND LIFSHITZ [1935]. Later, this work is revisited by Gilbert and extended by a phenomenologically motivated damping approach of the magnetic moments, cf. GILBERT [1956]. A few years later, this is followed by Brown's work "Micromagnetics", which introduces the present name, cf. BROWN [1963]. This theory is quite early taken up by DÖRING [1968]. With increasing computer power, the field of numerical micromagnetism is emerging. The growth of this field increases rapidly, particularly since the late 1990s. A selection of early work includes FREDKIN AND KOEHLER [1987; 1988], KRONMÜLLER [1973], and CHEN ET AL. [1993]. Different numerical methods are used to discretize the governing equations. The most popular methods are probably the finite difference method (cf. DONAHUE AND MCMICHAEL [1997], MCMICHAEL ET AL. [2001], D'AQUINO ET AL. [2005], MILTAT AND DONAHUE [2007], and VANSTEENKISTE ET AL. [2014]), which proves to be very performant in terms of computational time, and the finite element method (cf. KRONMÜLLER ET AL. [1996], HERTEL AND KRONMULLER [1998],

Fidler and Schrefl [2000], Tsiantos et al. [2001], and Scholz et al. [2003]), which is particularly notable for its very flexible discretization of strongly heterogeneous structures. For micromagnetic simulations, the application temperature of magnetic materials is assumed to be far below the Curie temperature. This implies that the amplitude of a magnetization vector, denoted by $\boldsymbol{M} = M_s\,\boldsymbol{m}$, must satisfy the constraint that $\|\boldsymbol{M}\| = M_s$ and $\|\boldsymbol{m}\| = 1$, where M_s represents the saturation magnetization and $\boldsymbol{m}$ represents the unit magnetization director. This condition, which can be computationally difficult to handle, leads to various methods for approximating the unit director. The most straight forward approach to consider the unit constraint within the simulation is to apply a projection scheme to the magnetization vectors as done by, cf. Prohl [2001] and Kružík and Prohl [2006]. This procedure involves the solution of the system of equations without considering the unit constraint and the subsequent projection of the nodal magnetization vectors back onto the unit sphere after each converged time step. A slightly different projection scheme was more recently introduced by Sridhar et al. [2015], where the proposed method relies on a staggered solution procedure. Another very simple approach to fulfill the constraint is to incorporate a penalty term into the weak form, cf. Prohl [2001], Landis [2008], Wang and Zhang [2013], and Zhang et al. [2016]. This penalty term penalizes any deviation of the magnetization vectors from the Euclidean norm depending on the intensity of a penalty parameter. A slightly different way to enforce the constraint was applied by Szambolics et al. [2008], Ohmer et al. [2022], and Ohmer [2022]. They introduced (perturbed) Lagrange multipliers as additional degrees of freedom, to recalculate the required penalization intensity within each iteration step. Reichel et al. [2023c] and Reichel et al. [2023b] reduced the system of equations to the size of the penalty method by applying a static condensation on element level to the Lagrange multiplier. Each of the mentioned approaches adds something to the total energy, e.g. by adding a penalty term, or subtracts energy, e.g. by renormalizing the vectors. This can lead to energies of the considered magnetic systems that may deviate from the real magnetic energy. To circumvent this, a priori length conserving methods might be a choice. One possibility is to apply spherical coordinates as done by Fidler and Schrefl [2000], Süss et al. [2000], and Yi and Xu [2014] since they preserve Euclid's norm by construction. Furthermore, the local system of equations is reduced by one degree of freedom from three to two, since only the polar and azimuth angle need to be considered as primary variables. This reduced system of equations allows in principle for faster simulations compared to Cartesian coordinates, cf. Scholz et al. [2003]. The work of Yi and Xu [2014] was extended in Dornisch et al. [2018] by a restriction of the azimuth angle onto its defined domain $(-\pi, \pi]$ on the interpolation level. Miehe and Ethiraj [2012] proposed a rotational exact and length preserving scheme based on an exponential map combined with an incremental update formulation. Another finite-element-based approach was presented by Alouges [2008]. The author preserved the length of the magnetization vectors by restricting the interpolation functions onto the tangent space of the solution. A clever reformulation of the Landau-Lifshitz-Gilbert (LLG) equation utilizing the mid-point rule also enables to preserve the magnetization amplitude by construction, cf. d'Aquino et al. [2005].

5.2 Micromagnetic free energy

A competition of different energy contributions within a ferromagnetic free energy indicates the origin of magnetization patterns, better known as magnetic domains. Minimizing the free energy of the magnetic solid yields the most stable and favorable domain formation, cf. Landau and Lifshitz [1935]. In general, the individual parts of the energy are expressed in terms of the strains $\boldsymbol{\varepsilon}$, the magnetic field $\boldsymbol{H}$, the magnetization unit director $\boldsymbol{m}$ and its gradient $\nabla\boldsymbol{m}$. The considered total magnetic free energy $\mathcal{H}$ is an assemblage of

$$\mathcal{H}(\boldsymbol{\varepsilon},\boldsymbol{H},\boldsymbol{m},\nabla\boldsymbol{m}) = \mathcal{H}^{\mathrm{ela}}(\boldsymbol{\varepsilon},\boldsymbol{m}) + \mathcal{H}^{\mathrm{mag}}(\boldsymbol{H},\boldsymbol{m}) + \mathcal{H}^{\mathrm{exc}}(\nabla\boldsymbol{m}) + \mathcal{H}^{\mathrm{ani}}(\boldsymbol{m}), \tag{5.1}$$

where $\mathcal{H}^{\mathrm{ela}}$ is the magneto-elastic energy, $\mathcal{H}^{\mathrm{mag}}$ the magnetostatic energy, the exchange energy $\mathcal{H}^{\mathrm{exc}}$ and the anisotropic energy $\mathcal{H}^{\mathrm{ani}}$. All these energy terms contribute to the overall magnetization behavior and are eventually responsible for the macroscopic hysteresis loops, cf. Brown [1945]. In the following, the individual energy contributions are introduced as continuum mechanical expressions, i.e. their local energies h are integrated over the whole body $\mathcal{B}$. A general overview on possible energy contributions can also be found in standard literature as Bertotti [1998], Coey [2010], and Hubert and Schäfer [1998].

Magneto-elastic energy
The elastic energy includes the magnetostrictive and inverse magnetostrictive (Villari) effects, that relate mechanical and magnetic behaviors to each other. It is expressed in terms of the linear elastic strains $\boldsymbol{\varepsilon}^e$, a magnetization-induced initial strain tensor $\boldsymbol{\varepsilon}^0$, and the total strains $\boldsymbol{\varepsilon}$ as

$$\mathcal{H}^{\mathrm{ela}}(\boldsymbol{\varepsilon},\boldsymbol{m}) = \int_{\mathcal{B}} h^{\mathrm{ela}}(\boldsymbol{\varepsilon},\boldsymbol{m})\,\mathrm{dv} = \int_{\mathcal{B}} \frac{1}{2}\,\boldsymbol{\varepsilon}^e : \mathbb{C} : \boldsymbol{\varepsilon}^e\,\mathrm{dv}, \tag{5.2}$$

with $\boldsymbol{\varepsilon}^e = \hat{\boldsymbol{\varepsilon}}^e(\boldsymbol{\varepsilon},\boldsymbol{m}) = \boldsymbol{\varepsilon}(\boldsymbol{u}) - \boldsymbol{\varepsilon}^0(\boldsymbol{m})$, where $\mathbb{C}$ denotes the 4th-order elasticity tensor. The magnetization induced strains can be given for a cubic crystal lattice structure as

$$\boldsymbol{\varepsilon}^0(\boldsymbol{m}) = \frac{3}{2}\begin{bmatrix} \lambda_{100}\left(m_1m_1 - \frac{1}{3}\right) & \lambda_{111}m_1m_2 & \lambda_{111}m_1m_3 \\ \lambda_{111}m_2m_1 & \lambda_{100}\left(m_2m_2 - \frac{1}{3}\right) & \lambda_{111}m_2m_3 \\ \lambda_{111}m_3m_1 & \lambda_{111}m_3m_2 & \lambda_{100}\left(m_3m_3 - \frac{1}{3}\right) \end{bmatrix}, \tag{5.3}$$

with the magnetostrictive coefficients λ_{100} and λ_{111} as well as the individual magnetization components $\boldsymbol{m} = [m_1, m_2, m_3]^{\mathrm{T}}$. A fully isotropic modulation can be obtained by defining these constants to be equal $\lambda_{100} = \lambda_{111}$.

Magnetostatic energy
The magnetostatic energy $\mathcal{H}^{\mathrm{mag}}$ is composed of two different energetic contributions. These contributions are the so-called demagnetizing energy $\mathcal{H}^{\mathrm{Dem}}$ and the Zeeman energy $\mathcal{H}^{\mathrm{Zee}}$. The demagnetizing energy takes into account the influence of stray and demagnetizing fields $\widetilde{\boldsymbol{H}}$, which are formed according to the distribution of the magnetization within a magnetic body $\mathcal{B}_{\mathrm{sol}}$. Without the influence of an external magnetic field, this energy can be represented as

$$\begin{aligned} \mathcal{H}^{\mathrm{Dem}}(\widetilde{\boldsymbol{H}},\boldsymbol{m}) &= \int_{\mathcal{B}} h^{\mathrm{Dem}}(\widetilde{\boldsymbol{H}},\boldsymbol{m})\,\mathrm{dv} \\ &= -\frac{1}{2}\int_{\mathcal{B}} \mu_0\,\widetilde{\boldsymbol{H}}\cdot\widetilde{\boldsymbol{H}}\,\mathrm{dv} - \int_{\mathcal{B}_{\mathrm{sol}}} \mu_0 M_s\,\boldsymbol{m}\cdot\widetilde{\boldsymbol{H}}\,\mathrm{dv}. \end{aligned} \tag{5.4}$$

Self-contained magnetization patterns minimize this demagnetization energy. The Zeeman energy

$$\mathcal{H}^{\mathrm{Zee}}(\overline{\boldsymbol{H}}, \boldsymbol{m}) = \int_{\mathcal{B}_{\mathrm{sol}}} h^{\mathrm{Zee}}(\overline{\boldsymbol{H}}, \boldsymbol{m}) \,\mathrm{dv} = -\int_{\mathcal{B}_{\mathrm{sol}}} \mu_0 M_s \, \boldsymbol{m} \cdot \overline{\boldsymbol{H}} \,\mathrm{dv} \tag{5.5}$$

considers the interaction of an external magnetic field $\overline{\boldsymbol{H}}$ with the magnetization $\boldsymbol{M}$ inside a magnetic solid $\mathcal{B}_{\mathrm{sol}}$. Connecting Eq. 5.4 and Eq. 5.5, taking into account a constant external magnetic field $\overline{\boldsymbol{H}}$ distributed over the whole domain $\mathcal{B}$ (this includes the magnet as well as the surrounding free space), allows the representation of the magnetostatic energy[8.)] of the whole domain as

$$\mathcal{H}^{\mathrm{mag}}(\boldsymbol{H}, \boldsymbol{m}) = \int_{\mathcal{B}} h^{\mathrm{mag}}(\boldsymbol{H}, \boldsymbol{m}) \,\mathrm{dv} = -\int_{\mathcal{B}} \frac{1}{2} \mu_0 \, \boldsymbol{H} \cdot \boldsymbol{H} \,\mathrm{dv} - \int_{\mathcal{B}} \mu_0 M_s \, \boldsymbol{m} \cdot \boldsymbol{H} \,\mathrm{dv}, \tag{5.6}$$

where $\boldsymbol{H} = \overline{\boldsymbol{H}} + \widetilde{\boldsymbol{H}}$ represents the total magnetic field.

Magnetic exchange energy

A close examination of paramagnetic materials (compare to Sec. 2.4) reveals that the magnetic moments without the presence of an aligning magnetic field are disordered and do not posses any effectively measurable magnetization. However, in other magnetic materials, such as ferromagnets and antiferromagnets, these moments may be present in ordered structures of equally oriented magnetization. Thus, the difference between these materials must be an internal force that aligns the magnetic moments parallel to each other. This internal force, based on the Pauli principle and the Coulomb exchange, is also known as the exchange interaction. In consequence of the interaction of two spins (spin-spin coupling), the Heisenberg Hamiltonian operator can be constructed, which describes their interaction and ultimately the occurrence of the magnetic order. Mathematically this Hamiltonian can be expressed as

$$\mathbb{H}_{\mathrm{exc}} = -2 \sum_{i>j} J_{ij} \, \boldsymbol{s}_i \cdot \boldsymbol{s}_j = \sum_{i \neq j} J_{ij} \, \boldsymbol{s}_i \cdot \boldsymbol{s}_j, \tag{5.7}$$

where J_{ij} represents the exchange integral between the i-th and the j-th spin. In this context, the sign of the exchange integral indicates the orientation of the spins. Here $J > 0$ implies a parallel alignment of the spins, while $J < 0$ causes an antiparallel alignment of the spins, indicating ferromagnetic order and antiferromagnetic order. This exchange between spins can also be expressed on the continuum level. Inhomogeneous orientation patterns within the magnetization distribution, indicated by existing magnetization gradients $\nabla \boldsymbol{m}$, lead to an increased energy contribution. Hence, the exchange energy

$$\mathcal{H}^{\mathrm{exc}}(\nabla \boldsymbol{m}) = \int_{\mathcal{B}} h^{\mathrm{exc}}(\nabla \boldsymbol{m}) \,\mathrm{dv} = \int_{\mathcal{B}} A_{\mathrm{exc}} \nabla \boldsymbol{m} : \nabla \boldsymbol{m} \,\mathrm{dv}, \tag{5.8}$$

aims to minimize these inhomogeneous patterns by aligning the magnetic moments, depending on the influence of the exchange coefficient A_{exc}. Concluding this, the exchange energy prefers to minimize the amount of small individual domains and instead tries to facilitate the formation of very large domains.

[8.)] Since it is evident that magnetization can only be found in a magnetic body, the index $_{\mathrm{sol}}$ is omitted in the following.

5.3 Magnetocrystalline anisotropy

Many magnetic materials have preferred directions along that the magnetization is preferentially oriented. These directions are also referred to as easy-axes and originate from the crystallographic nature of the material under consideration. This behavior is commonly known as magnetocrystalline anisotropy. In 1929 the Russian physicist N.S. Akulov showed that the energy h^{ani} in the crystal lattice can be represented in the form of a series expansion of the direction cosines of the magnetization $\boldsymbol{M}$, which corresponds to the components of the magnetic unit directors $\boldsymbol{m} = [m_1, m_2, m_3]^{\text{T}}$, cf. Akulov [1929]. Within cubic crystal systems the anisotropy can be represented by the energetic expression

$$h^{\text{ani}}_{\text{cub}} = K_0^{\text{cub}} + K_1^{\text{cub}} \left(m_1^2 m_2^2 + m_2^2 m_3^2 + m_3^2 m_2^2\right) + K_2^{\text{cub}} \left(m_1^2 m_2^2 m_3^2\right) + \dots , \tag{5.9}$$

where K_0^{cub}, K_1^{cub}, and K_2^{cub} are the material specific anisotropy constants and m_1, m_2, and m_3 the direction cosines of the magnetization. Fig. 5.1b) shows the cubic unit cell of iron. Its corresponding energy surface is shown in Fig. 5.1c) for the parameters $K_0^{\text{cub}} = 0.1$, $K_1^{\text{cub}} = 1$, and $K_2^{\text{cub}} = 0$, taken from Bertotti [1998]. Starting from such an energy, the expected magnetization curves of a single crystal can be calculated for different directions.

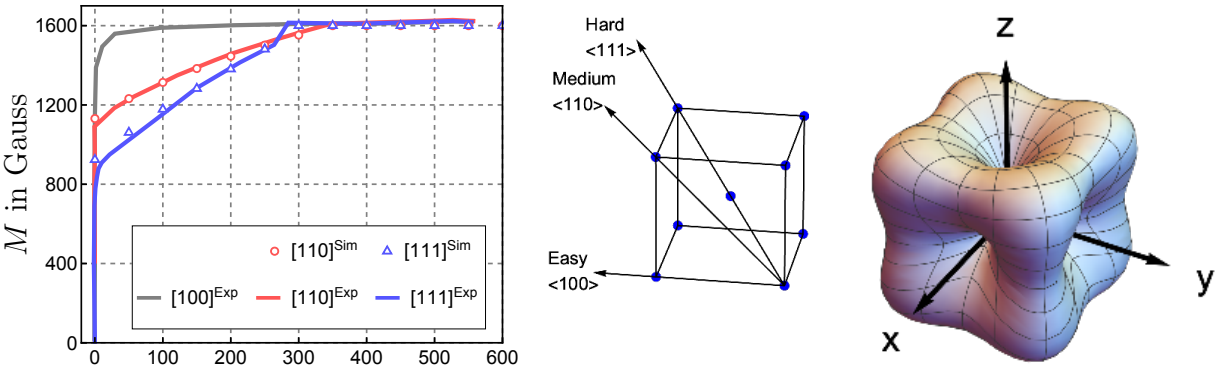

a) b) c)

Figure 5.1: a) comparison of the experimentally and theoretically obtained magnetization curves of an iron single crystal for the hard-, medium-, and easy-axis, adopted from Williams [1937] and Kneller et al. [1962]. Note that the results given in a) do not apply Si-units, to make a comparison with older literature more convenient. b) the cubic crystal cell of iron and c) the corresponding cubic anisotropy surface (for parameters K_0^{cub}=0.1, K_1^{cub}=1, and K_2^{cub}=0, cf. Bertotti [1998]).

The following considerations are based on the works Akulov [1929; 1931a;b] and Becker and Döring [1939] and serve as a starting point for the analysis of an iron single crystal subjected to an external magnetic field $\boldsymbol{H}^{\text{ext}}$ as outlined below. This field results from the energetic contribution

$$h^{\text{ext}} = M_{\text{s}}\, \boldsymbol{m} \cdot \boldsymbol{H}^{\text{ext}} \quad \text{with} \quad \boldsymbol{m} = [\sin\theta\cos\phi, \sin\theta\sin\phi, \cos\phi]^{\text{T}}, \tag{5.10}$$

with that the total energy can be formulated as

$$h^{\text{tot}}(\boldsymbol{m}) = h^{\text{ani}}(\boldsymbol{m}) - h^{\text{ext}}(\boldsymbol{m}). \tag{5.11}$$

Additionally, the iron single crystal is assumed to be fully saturated along its easy-axis closest to the external field, cf. Becker and Döring [1939]. As shown in Fig. 5.1b), the easy-axis of iron corresponds to the direction [100]. This implies no further increase in magnetization for the case of an externally applied magnetic field parallel to the [100] direction, presented in Fig. 5.2a), since it is already saturated along the [100] direction. If there are several energetically equivalent easy-axes, i.e. the magnetic field is applied exactly centered along the axes considered, the saturation is distributed evenly along these axes, see Figs. 5.2b) and c). To illustrate the magnetization distribution, the octant of the coordinate system between the positive x_1-, x_2-, and x_3-axis is shown here for an external magnetic field:

Case [100]: $\boldsymbol{H}^{\text{ext}}_{[100]}$ parallel to the [100] direction given in Fig. 5.2a),

Case [110]: $\boldsymbol{H}^{\text{ext}}_{[110]}$ parallel to the [110] direction given in Fig. 5.2b), and

Case [111]: $\boldsymbol{H}^{\text{ext}}_{[110]}$ parallel to the [111] direction given in Fig. 5.2c).

This means that for Case [100] the amount of magnetization $\|\boldsymbol{M}_{[100]}\| = M_s$ can be completely assigned to one orientation, see Fig. 5.2a). In Case [110] the part of the magnetization is distributed on two axes (x_1- and x_2-axis) such that $\|\boldsymbol{M}_{[100]}\| = \|\boldsymbol{M}_{[010]}\| = M_s/\sqrt{2}$ holds for the magnitude in each case. In Case [111] the result is a distribution of the magnetization onto the x_1-, x_2-, and x_3-axis with the corresponding magnetization magnitudes of $\|\boldsymbol{M}_{[100]}\| = \|\boldsymbol{M}_{[010]}\| = \|\boldsymbol{M}_{[001]}\| = M_s/\sqrt{3}$. Thus, the initial magnetizations along the corresponding field directions [100], [110], and [111] are $\|\boldsymbol{M}_{[100]}\| = M_s$, $\|\boldsymbol{M}_{[110]}\| = M_s/\sqrt{2}$, and $\|\boldsymbol{M}_{[111]}\| = M_s/\sqrt{3}$.

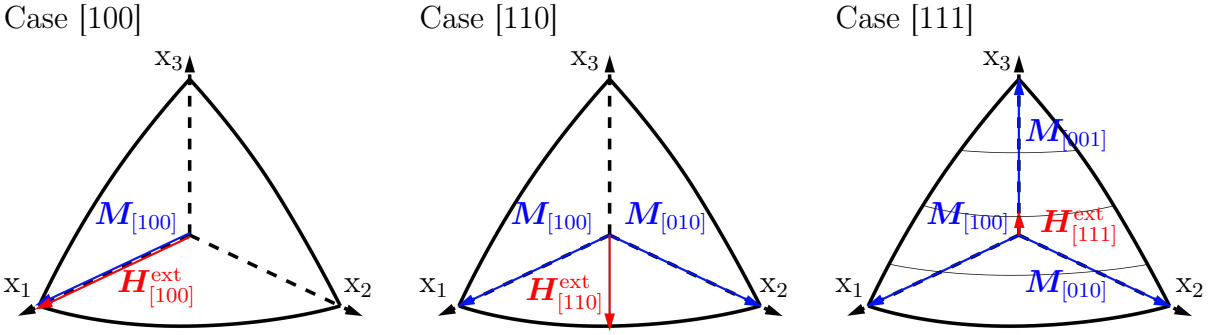

Figure 5.2: Octant between the x_1-, x_2-, and x_3-axis with the directions of the magnetization (blue) and the external magnetic field (red). a) the external magnetic field and magnetization align parallel to the [100] direction (x_1-axis), b) the external field points in [110] direction and the magnetization aligns to the x_1- and x_2-axis, and c) the external field points in [111] direction and the magnetization aligns to the x_1-, x_2-, and x_3-axis.

As the external field increases, the preferred position of the magentization shifts from the easy-axis towards the externally applied field. This can be calculated by minimizing the energy given in Eq. 5.11 as

$$\frac{d\,h^{\text{tot}}}{d\,\theta} = \frac{d}{d\,\theta}\left[h^{\text{ani}} - M_s\,\boldsymbol{m}\cdot\boldsymbol{H}\right] = 0. \tag{5.12}$$

Since only a constant magnetization results for Case [100], the interest in the following is on Case [110] and Case [111].
To simplify the calculation for Case [110] some assumptions follow. The process is considered only within the x_1-x_2 plane, which means that m_3=0, hence $m_1 = \cos\theta$, and $m_2 = \sin\theta$.

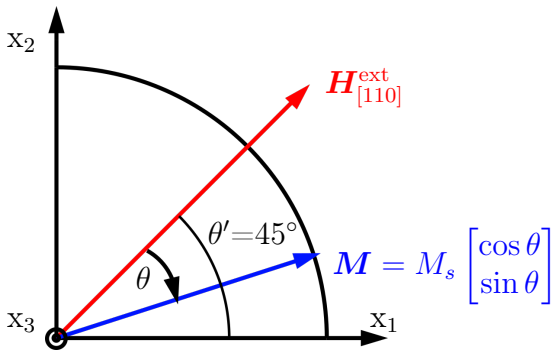

Figure 5.3: Representation of the magnetization process for a magnetization vector (blue), already rotated out of the easy-axis, within the x_1-x_2 plane and the external field (red).

For symmetry reasons, only the rotation from the positive x_1-axis in the direction of the field $\boldsymbol{H}^{\text{ext}}_{[110]}$ is considered for the derivation, as shown in Fig. 5.3. From Fig. 5.3 it can be seen that the magnetization projected in the direction of the magnetic field can be represented as a function of the angle θ formed between $\boldsymbol{H}^{\text{ext}}_{[110]}$ and the magnetization $\boldsymbol{M}$ as

$$M = M_s\,\eta, \quad \text{with} \quad \eta = \cos\theta. \tag{5.13}$$

Since the angle θ decreases from θ'=45° to 0° during the rotation of $\boldsymbol{M}$ towards the [110] position, an intermediate position can be defined by

$$m_1 = \cos(s-\theta) = \frac{1}{\sqrt{2}}(\cos\theta + \sin\theta) \quad \text{and} \quad m_2 = \cos(s+\theta) = \frac{1}{\sqrt{2}}(\cos\theta - \sin\theta). \tag{5.14}$$

By inserting Eq. 5.14 in Eq. 5.9, reformulating and neglecting K_0^{cub}, the anisotropic energy for the direction [110] is given by

$$h^{\text{ani}}_{\text{cub}} = K_1^{\text{cub}}(\frac{1}{2} - \cos^2\theta)^2 = K_1^{\text{cub}}(\frac{1}{2} - \eta^2)^2. \tag{5.15}$$

Since the position of the magnetization is directly related to the position of the external field, the external field can now be expressed as its scalar field strength $H = \|\boldsymbol{H}^{\text{ext}}_{[110]}\|$, see Fig. 5.3. Thus, Eq. 5.12 shown above, can be given as a function of η as

$$\frac{d\,h^{\text{tot}}}{d\,\eta} = \frac{d}{d\,\eta}\left[K_1^{\text{cub}}(\frac{1}{2} - \eta^2)^2 - M_s\,H\,\eta\right] = 4\,K_1^{\text{cub}}\,\eta\,(\eta^2 - \frac{1}{2}) - M_s\,H = 0. \tag{5.16}$$

Minimizing η in Eq. 5.16 (as well as in Eq. 5.20 later on) proceeds iteratively for each newly applied or increased external magnetic field $\boldsymbol{H}$, such that an optimal orientation of the magnetization $\boldsymbol{M}$, expressed in terms of η, results as a function of $\boldsymbol{H}$. The magnetization curve resulting from the minimization of h^{tot}, see Eq. 5.16, i.e. for a field

applied in the [110] direction, is presented in Fig. 5.1a). The used material parameters $K_1^{\text{cub}} = 2.8 \times 10^4$ J/m^3 and $M_\text{s} = 0.16$ T are taken from KNELLER ET AL. [1962].
For Case [111], the initial magnetization corresponds to the value $\|\boldsymbol{M}_{[111]}\| = M_s/\sqrt{3}$. Increasing the external magnetic field $\boldsymbol{H}^{\text{ext}}_{[111]}$ along the [111] direction causes the shift of the preferred position from the easy-axis towards the external field. Thus, the rotation of the magnetization in the direction of the magnetic field leads to an increase in saturation along this direction up to full saturation. In the following, for reasons of symmetry, only the rotation from the positive x_1-axis in the [111] direction is considered. Hence, the rotation takes place within the plane spanned by the positive x_1-axis and $\boldsymbol{H}^{\text{ext}}_{[111]}$, see Fig. 5.4. The angle between these two vectors (x_1-axis and $\boldsymbol{H}^{\text{ext}}_{[111]}$) is $\beta = 54.736°$, yielding $\cos\beta = 1/\sqrt{3}$ and $\sin\beta = \sqrt{2/3}$. Thus, analogous to the procedure of Case [110], an intermediate position can be defined as

$$m_1 = \cos(\beta - \theta) = \frac{1}{\sqrt{3}}\cos\theta + \sqrt{\frac{2}{3}}\sin\theta, \tag{5.17}$$

which can be reformulated to

$$m_1^2 = \frac{1}{3}(2 - \eta^2 + 2\sqrt{2}\,\eta\,\sqrt{1-\eta^2}) \quad \text{and} \quad m_2^2 = m_3^2 = \frac{1}{2}(1 - m_1^2) \tag{5.18}$$

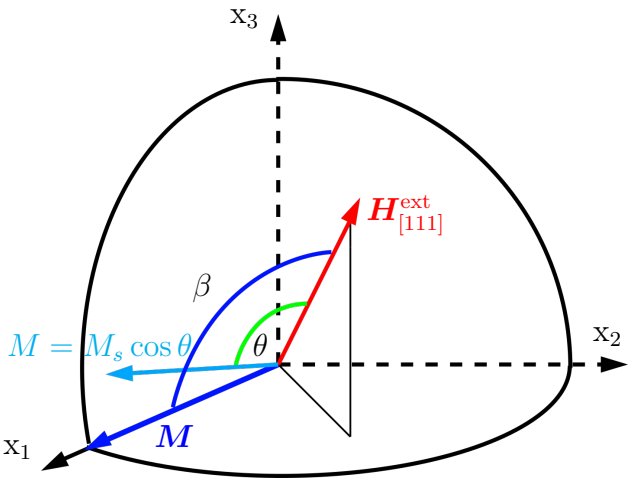

Figure 5.4: The magnetization process for a magnetization vector already rotated out of the easy-axis (light blue), within the x_1-$\boldsymbol{H}^{\text{ext}}_{[111]}$ plane, with the external field (red) and the initial magnetization (dark blue). The angle θ (green) spans between the external field and the rotated magnetization and the angle β (dark blue) spans between the external field and the initial magnetization.

using the abbreviation $\eta = \cos\theta$. For $K_0^{\text{cub}} = 0$, Eq. 5.9 can be represented as

$$h_{\text{cub}}^{\text{ani}} = \frac{K_1^{\text{cub}}}{4}(1 + 2\,m_1^2 - 3\,m_1^4)^2 \; + \; K_2^{\text{cub}} m_1^2 m_2^2 m_3^2 \tag{5.19}$$

for the case of an external magnetic field along the [111] direction. This results in

$$\frac{d\,h^{\mathrm{tot}}}{d\,\eta} = \frac{d}{d\,\eta}\left[\frac{K_1^{\mathrm{cub}}}{4}(1 + 2\,m_1^2 - 3\,m_1^4)^2 - M_s\,H\,\eta\right] = 0. \tag{5.20}$$

The magnetization curve resulting from the minimization of Eq. 5.20, i.e. for a field applied in [111] direction, can be taken from Fig. 5.1a). The used material parameters $K_1^{\mathrm{cub}} = 2.8 \times 10^4$ J/m^3, $K_2^{\mathrm{cub}} = 1.0 \times 10^4$ J/m^3, and $M_{\mathrm{s}} = 0.16$ T are taken from Kneller et al. [1962]. Indeed, there exist more magnetocrystalline energy contributions h^{ani} depending on the different crystal systems, cf. Hubert and Schäfer [1998]. However, the focus of this work remains on two variants of $\mathcal{H}^{\mathrm{ani}}$, namely the uniaxial anisotropy $\mathcal{H}_{\mathrm{uni}}^{\mathrm{ani}}$ that is introduced as

$$\mathcal{H}_{\mathrm{uni}}^{\mathrm{ani}}(\boldsymbol{m}) = \int_{\mathcal{B}} h_{\mathrm{uni}}^{\mathrm{ani}}(\boldsymbol{m})\ \mathrm{dv} = \int_{\mathcal{B}} K_1^{\mathrm{uni}}(1 - \boldsymbol{m}\cdot\boldsymbol{a})\ \mathrm{dv}, \tag{5.21}$$

with the anisotropy constant K_1^{uni} and the easy-axis vector $\boldsymbol{a} = [\sin\theta\cos\psi, \sin\theta\sin\psi, \cos\theta]^T$ as well as the cubic anisotropy $\mathcal{H}_{\mathrm{cub}}^{\mathrm{ani}}$ that yields the form

$$\begin{aligned}\mathcal{H}_{\mathrm{cub}}^{\mathrm{ani}}(\boldsymbol{m}) &= \int_{\mathcal{B}} h_{\mathrm{cub}}^{\mathrm{ani}}(\boldsymbol{m})\ \mathrm{dv} \\ &= \int_{\mathcal{B}} \left[K_1^{\mathrm{cub}}\left(m_1^2m_2^2 + m_2^2m_3^2 + m_1^2m_3^2\right) + K_2^{\mathrm{cub}}\left(m_1^2m_2^2m_3^2\right)\right]\ \mathrm{dv},\end{aligned} \tag{5.22}$$

with K_1^{cub} and K_2^{cub} as corresponding anisotropy constants for the cubic crystal system. Therefore, the preferred energetically minimum depends on the underlying crystal lattice.

5.4 Micromagnetic equations

Within this section, the most fundamental equations for the magnetization states and their corresponding evolution in the micromagnetic theory are derived. Starting with Brown's equations of equilibrium, stable magnetization states in an energetically preferred configuration can be described, cf. Brown [1963]. However, these equations cannot describe how a non-equilibrium system can reach this equilibrium state. Landau and Lifshitz [1935] have been the first to propose a model that is able to describe the way of such a non-equilibrium system towards a stable equilibrium state by incorporating precessional motion and dissipation of the magnetization vectors into a continuum framework. This approach has been adapted by Gilbert [2004], who has introduced a phenomenological damping term to incorporate the dissipation motion to describe the magnetization evolution. On the following pages Brown's equations of equilibrium and the magnetic equation of motion, which is a Landau-Lifshitz-type evolution equation, are derived. This is done by a minimization principle applied to the free energy, following the fundamental work of Gilbert [1956]. The derivations within this section are also strongly inspired by the works of Bertotti [1998] and d'Aquino et al. [2005]. Hence, for a more detailed derivation of these equations, the reader is referred to Gilbert [1956], Bertotti [1998], and d'Aquino et al. [2005].

5.4.1 Functional derivatives

In micromagnetism, the so-called effective field $\boldsymbol{H}^{\text{eff}}$ plays a crucial role. It differs from an external magnetic field, because it combines contributions of external magnetic fields, crystalline anisotropy, exchange interactions and other types of energetic contributions. Thus, it is not necessarily parallel to an external magnetic field. The calculation is obtained by a functional derivative of the micromagnetic free energy (Eq. 5.1) with respect to the magnetization degrees of freedom. The foundations of variational calculus dates back to the Swiss mathematician Leonhard Euler who published his findings in the fundamental works Euler [1744] and Euler [1766]. In addition to Euler, the Swiss mathematician Johann Bernoulli, the French mathematician Joseph-Louis Lagrange, the German mathematicians Karl Weierstraß and David Hilbert, and many others made important contributions to the calculus of variations. For a historical overview on the invention and the development of variational calculus over the centuries the work of Mariano [2021] is recommended. Therefore, the subject of functional derivatives is introduced by means of a generic example, based on the work of Bolza [1904], Szabó and Sauer [1967], and Fox [1987]. Starting with any functional of the form

$$\mathcal{H}(\boldsymbol{m}) = \int_{\mathcal{B}} h\left(\boldsymbol{x}, \boldsymbol{m}(\boldsymbol{x}), \nabla \boldsymbol{m}(\boldsymbol{x})\right) \mathrm{dv}, \tag{5.23}$$

the task is to find the extrema with respect to the unknown vector-valued function $\boldsymbol{m} \in \mathbb{R}^3$ and its derivatives $\nabla \boldsymbol{m}$. This may require prescribing boundary conditions of the form

$$\boldsymbol{m} = \overline{\boldsymbol{m}} \quad \text{on} \quad \partial\mathcal{B}, \tag{5.24}$$

with respect to the function $\boldsymbol{m}$ and the derivative $\nabla \boldsymbol{m}$. Thus, the main task is to find an unknown function $\boldsymbol{m}$ for which the functional $\mathcal{H}(\boldsymbol{m})$ becomes extremal. Assuming sufficient smoothness of all functions considered, the construction of a comparable function or test function is performed as

$$\widetilde{\boldsymbol{m}} = \boldsymbol{m} + \epsilon\, \boldsymbol{\eta}, \quad \text{with} \quad \widetilde{\boldsymbol{m}} \in \mathbb{R}^3, \tag{5.25}$$

where ϵ is an arbitrarily small number and $\boldsymbol{\eta} \in \mathbb{R}^3$ is a continuous function vanishing at the boundary ($\boldsymbol{\eta} = \boldsymbol{0}$ on $\partial\mathcal{B}$). As a variation of the extrema

$$\delta\boldsymbol{m} = \widetilde{\boldsymbol{m}} - \boldsymbol{m} = \epsilon\, \boldsymbol{\eta} \quad \text{with} \quad \delta\boldsymbol{m} = \boldsymbol{0} \text{ on } \partial\mathcal{B} \tag{5.26}$$

can be introduced. Substitution of $\boldsymbol{m}$ by the test function $\widetilde{\boldsymbol{m}}$ in Eq. 5.23 leads to an extremum at the position $\epsilon = 0$. Formally, this can be determined with the help of the so-called Gâteaux derivative or (first) variation

$$\begin{aligned} \delta\mathcal{H}(\boldsymbol{m}, \boldsymbol{\eta}) = \frac{\mathrm{d}}{\mathrm{d}\epsilon}\mathcal{H}(\boldsymbol{m} + \epsilon\, \boldsymbol{\eta})\bigg|_{\epsilon=0} \epsilon &= \int_{\mathcal{B}} \frac{\mathrm{d}}{\mathrm{d}\epsilon} h\left(\boldsymbol{x}, \widetilde{\boldsymbol{m}}, \nabla\widetilde{\boldsymbol{m}}\right)\bigg|_{\epsilon=0} \mathrm{dv}\, \epsilon \\ &= \int_{\mathcal{B}} \frac{\mathrm{d}}{\mathrm{d}\epsilon} h(\boldsymbol{x}, \boldsymbol{m} + \epsilon\, \boldsymbol{\eta}, \nabla\boldsymbol{m} + \epsilon\, \nabla\boldsymbol{\eta})\bigg|_{\epsilon=0} \mathrm{dv}\, \epsilon, \end{aligned} \tag{5.27}$$

for which the necessary criterion $\delta\mathcal{H}(\boldsymbol{m},\boldsymbol{\eta}) = 0$ holds. Further transforming the last part of Eq. 5.27 using the chain rule as

$$\begin{aligned}&\int_{\mathcal{B}} \left[\frac{\partial h}{\partial \widetilde{\boldsymbol{m}}} \cdot \frac{\partial \widetilde{\boldsymbol{m}}}{\partial \epsilon} + \frac{\partial h}{\partial \nabla\widetilde{\boldsymbol{m}}} : \frac{\partial \nabla\widetilde{\boldsymbol{m}}}{\partial \epsilon}\right]\Bigg|_{\epsilon=0} \mathrm{dv}\,\epsilon \\ &= \int_{\mathcal{B}} \left[\frac{\partial h}{\partial \widetilde{\boldsymbol{m}}} \cdot \boldsymbol{\eta} + \frac{\partial h}{\partial \nabla\widetilde{\boldsymbol{m}}} : \nabla\boldsymbol{\eta}\right]\Bigg|_{\epsilon=0} \mathrm{dv}\,\epsilon\end{aligned} \tag{5.28}$$

and taking advantage of the relations $\delta\boldsymbol{m} = \epsilon\,\boldsymbol{\eta}$ and $\nabla\delta\boldsymbol{m} = \epsilon\,\nabla\boldsymbol{\eta}$ allows the following expression:

$$\int_{\mathcal{B}} \left[\frac{\partial h}{\partial \boldsymbol{m}} \cdot \delta\boldsymbol{m} + \frac{\partial h}{\partial \nabla\boldsymbol{m}} : \nabla\delta\boldsymbol{m}\right]\Bigg|_{\epsilon=0} \mathrm{dv}. \tag{5.29}$$

In order to finally obtain the corresponding Euler-Lagrange differential equation $\bullet$ from the variational problem, first a few reformulations have to be made, so that, considering $\delta\mathcal{H}(\boldsymbol{m}) = 0$ the following is directly evident

$$\int_{\mathcal{B}} [\bullet] \cdot \delta\boldsymbol{m}\,\mathrm{dv} = 0 \quad \longrightarrow \quad [\bullet] = 0. \tag{5.30}$$

Accordingly, the last term inside the parentheses in Eq. 5.28 must be rewritten so that it becomes of the form $[\bullet] \cdot \delta\boldsymbol{m}$ as well. Applying partial integration

$$\frac{\partial h}{\partial \nabla\boldsymbol{m}} : \nabla\delta\boldsymbol{m} = \mathrm{div}\left(\frac{\partial h}{\partial \nabla\boldsymbol{m}}^{\mathrm{T}} \cdot \delta\boldsymbol{m}\right) - \mathrm{div}\,\frac{\partial h}{\partial \nabla\boldsymbol{m}} \cdot \delta\boldsymbol{m} \tag{5.31}$$

gets the expression closer to that required form. On that basis the Gauss integral theorem allows to express the volume integral in terms of a surface integral

$$\int_{\mathcal{B}} \mathrm{div}\left(\frac{\partial h}{\partial \nabla\boldsymbol{m}}^{\mathrm{T}} \cdot \delta\boldsymbol{m}\right) \mathrm{dv} = \int_{\partial\mathcal{B}} \left(\frac{\partial h}{\partial \nabla\boldsymbol{m}}^{\mathrm{T}} \cdot \boldsymbol{n}\right) \cdot \delta\boldsymbol{m}\,\mathrm{da}, \tag{5.32}$$

so that the latter yields with $\delta\boldsymbol{m} = 0$ on $\partial\mathcal{B}$ (Eq. 5.26)

$$\int_{\partial\mathcal{B}} \left(\frac{\partial h}{\partial \nabla\boldsymbol{m}}^{\mathrm{T}} \cdot \boldsymbol{n}\right) \cdot \delta\boldsymbol{m}\,\mathrm{da} = 0. \tag{5.33}$$

Thus, the resulting Euler-Lagrange equation becomes

$$\int_{\mathcal{B}} \left[\frac{\partial h}{\partial \boldsymbol{m}} - \mathrm{div}\,\frac{\partial h}{\partial \nabla\boldsymbol{m}}\right] \cdot \delta\boldsymbol{m}\,\mathrm{dv} = 0 \quad \longrightarrow \quad \left[\frac{\partial h}{\partial \boldsymbol{m}} - \mathrm{div}\,\frac{\partial h}{\partial \nabla\boldsymbol{m}}\right] = 0. \tag{5.34}$$

This section is intended to provide an understanding of the calculus of variations and to provide clarification for the derivation of Brown's equations of equilibrium, which is performed in the following but is significantly shorter.

5.4.2 Brown's equations of equilibrium

While in the previous section a generic functional is varied, this section refers to the functional of micromagnetism presented in Eq. 5.1 and following, which can be represented in its local form as follows

$$h(\boldsymbol{\varepsilon},\boldsymbol{H},\boldsymbol{m},\nabla\boldsymbol{m}) = h^{\mathrm{ela}}(\boldsymbol{\varepsilon},\boldsymbol{m}) + h^{\mathrm{mag}}(\boldsymbol{H},\boldsymbol{m}) + h^{\mathrm{exc}}(\nabla\boldsymbol{m}) + h^{\mathrm{ani}}(\boldsymbol{m}), \tag{5.35}$$

consisting of the mechanical, magnetostatic, exchange, and anisotropy contributions. Recalling Eq. 5.33 and Eq. 5.34 the variational reads as

$$\delta\mathcal{H} = \int_{\mathcal{B}} \underbrace{\left[\frac{\partial h}{\partial \boldsymbol{m}} - \operatorname{div}\frac{\partial h}{\partial \nabla \boldsymbol{m}}\right]}_{:=-\boldsymbol{H}^{\mathrm{eff}}} \cdot \delta\boldsymbol{m}\,\mathrm{dv} + \int_{\partial\mathcal{B}} \left(\frac{\partial h}{\partial \nabla \boldsymbol{m}}^{\mathrm{T}} \cdot \boldsymbol{n}\right) \cdot \delta\boldsymbol{m}\,\mathrm{da} = 0, \tag{5.36}$$

where $\boldsymbol{H}^{\mathrm{eff}}$ denotes the effective field. The sign of the effective field, which corresponds to the negative variational of the functional as $\boldsymbol{H}^{\mathrm{eff}} = -\frac{\delta\mathcal{H}}{\delta\boldsymbol{m}}$, has to be noted. Nevertheless, the norm constraint of the magnetization vector $||\boldsymbol{m}|| = 1$ must always be satisfied. A variational satisfying this constraint yields

$$\delta\boldsymbol{m} \;=\; \boldsymbol{m} \times \delta\boldsymbol{\theta}, \tag{5.37}$$

with $\delta\boldsymbol{\theta}$ defining a small and arbitrary vector that defines the direction of an arbitrary axis in space and the rotation of $\boldsymbol{m}$ around it. Applying Eq. 5.37, the triple product $\boldsymbol{a}\cdot(\boldsymbol{b}\times\boldsymbol{c}) = (\boldsymbol{a}\times\boldsymbol{b})\cdot\boldsymbol{c}$ and the rule $\boldsymbol{a}\times\boldsymbol{b} = -\boldsymbol{b}\times\boldsymbol{a}$ to Eq. 5.36 yields

$$\delta\mathcal{H} = \int_{\mathcal{B}} (\boldsymbol{m}\times\boldsymbol{H}^{\mathrm{eff}})\cdot\delta\boldsymbol{\theta}\,\mathrm{dv} - \int_{\partial\mathcal{B}} \boldsymbol{m}\times\left(\frac{\partial h}{\partial \nabla \boldsymbol{m}}^{\mathrm{T}}\cdot\boldsymbol{n}\right)\cdot\delta\boldsymbol{\theta}\,\mathrm{da} = 0 \tag{5.38}$$

resulting in Brown's equations

$$\boldsymbol{m}\times\boldsymbol{H}^{\mathrm{eff}} = \boldsymbol{0} \qquad \text{and} \qquad \boldsymbol{m}\times\underbrace{\left(\frac{\partial h}{\partial \nabla \boldsymbol{m}}^{\mathrm{T}}\cdot\boldsymbol{n}\right)}_{=\boldsymbol{0}} = \boldsymbol{0}, \tag{5.39}$$

if $\delta\mathcal{H} = 0$ holds true for any arbitrary variation of $\delta\boldsymbol{\theta}$, cf. Brown [1963]. Eventually, this indicates an extremum. Since any derivative of $\boldsymbol{m}$ must be perpendicular to $\boldsymbol{m}$ itself, the short expression of Eq. 5.39_2 can be given as $\left(\frac{\partial h}{\partial \nabla \boldsymbol{m}}^{\mathrm{T}}\cdot\boldsymbol{n}\right) = \boldsymbol{0}$. Whether the extremum is a minimum can only be determined by considering the second variation of $\mathcal{H}$. Eq. 5.39_1 holds for the whole body $\mathcal{B}$, while the Eq. 5.39_2 only accounts for the surface $\partial\mathcal{B}$ if no anisotropy is considered. In that case the second equation might differ to zero, cf. Bertotti [1998].

5.4.3 Magnetization dynamics

Brown's fundamental equations (Eq. 5.39) specify the conditions that must be fulfilled when the magnetic system remains in equilibrium, but they do not give any suggestions how a non-equilibrium system can approach this. In quantum mechanics, a single magnetic spin momentum $\boldsymbol{m}^{\mathrm{q}}$ can be directly related to its corresponding angular momentum $\boldsymbol{J}^{\mathrm{q}}$ via

$$\boldsymbol{m}^{\mathrm{q}} = \gamma_0 \boldsymbol{J}^{\mathrm{q}}, \tag{5.40}$$

where the gyromagnetic ratio γ_0 is the proportionality factor between both quantities. The change of an angular momentum over time $\dot{\boldsymbol{J}}^{\mathrm{q}}$[9.)] can be expressed by the torque/angular force $\boldsymbol{N}$ that is defined as a magnetic field $\boldsymbol{H}$ acting on a magnetic spin moment $\boldsymbol{m}^{\mathrm{q}}$ as

$$\dot{\boldsymbol{J}}^{\mathrm{q}} = \mu_0 \boldsymbol{m}^{\mathrm{q}} \times \boldsymbol{H} \quad \Leftrightarrow \quad \dot{\boldsymbol{m}}^{\mathrm{q}} = \mu_0\gamma_0 \boldsymbol{m}^{\mathrm{q}} \times \boldsymbol{H}. \tag{5.41}$$

[9.)] In this work, a point over a given quantity indicates the time derivative of that quantity as $\dot{\bullet} = \partial_{\mathrm{t}}\bullet$.

Precessional dynamics: This behavior can be transferred into a continuum mechanical context as

$$\dot{\boldsymbol{m}} = \mu_0 \gamma_0 \, \boldsymbol{m} \times \hat{\boldsymbol{H}}^{\mathrm{eff}}, \tag{5.42}$$

where the effective field $\hat{\boldsymbol{H}}^{\mathrm{eff}}$ is the driving force acting on the magnetization, incorporating influences as the lattice spacing (anisotropy) and magnetization distribution (magnetic exchange). For a zero magnetic rate $\dot{\boldsymbol{m}} = \boldsymbol{0}$, Eq. 5.42 exactly fulfills Brown's equilibrium equation Eq. 5.39_1. If the considered magnetic system is not initially in its equilibrium position (i.e. $\dot{\boldsymbol{m}} \neq \boldsymbol{0}$), Eq. 5.42 describes a pure precession of the magnetization vectors around the effective field. Since Eq. 5.42 does not involve any dissipation, the considered system will never approach an equilibrium state, cf. Bertotti [1998].

Damped dynamics: To avoid the system start to precess without ever approaching a stable equilibrium state, dissipation should be involved. This can be done by introducing a dissipation potential to Eq. 5.1 as

$$\mathcal{H}^{\mathrm{dis}}(\dot{\boldsymbol{m}}) = \int_{\mathcal{B}} h^{\mathrm{dis}}(\dot{\boldsymbol{m}}) \, \mathrm{dv} = \int_{\mathcal{B}} \frac{\eta}{2} \, \dot{\boldsymbol{m}} \cdot \dot{\boldsymbol{m}} \, \mathrm{dv} = \int_{\mathcal{B}} \frac{\alpha}{2 \, \gamma_0 \, M_{\mathrm{s}}} \, \dot{\boldsymbol{m}} \cdot \dot{\boldsymbol{m}} \, \mathrm{dv}, \tag{5.43}$$

where η denotes the so-called Gilbert damping parameter and $\dot{\boldsymbol{m}}$ the time rate of the magnetization unit director. The Gilbert parameter can be expressed in terms of the more common α damping parameter as $\eta = \alpha/(\gamma_0 \, M_{\mathrm{s}})$. Now the local form of the functional containing the dissipation potential can be stated as

$$h(\boldsymbol{\varepsilon}, \boldsymbol{H}, \boldsymbol{m}, \nabla \boldsymbol{m}) = h^{\mathrm{ela}}(\boldsymbol{\varepsilon}, \boldsymbol{m}) + h^{\mathrm{mag}}(\boldsymbol{H}, \boldsymbol{m}) + h^{\mathrm{exc}}(\nabla \boldsymbol{m}) + h^{\mathrm{ani}}(\boldsymbol{m}) + h^{\mathrm{dis}}(\dot{\boldsymbol{m}}). \tag{5.44}$$

Neglecting the surface term, which is zero as shown in Eq. 5.39_2, the functional can now be varied analogously to Eq. 5.36, yielding

$$\delta \mathcal{H} = \int_{\mathcal{B}} \left[\frac{\partial \, h^{\mathrm{dis}}}{\partial \, \dot{\boldsymbol{m}}} - \boldsymbol{H}^{\mathrm{eff}} \right] \cdot \, \delta \boldsymbol{m} \, \mathrm{dv} = 0 \quad \text{with} \quad \boldsymbol{H}^{\mathrm{eff}} = \frac{\partial \, h}{\partial \, \boldsymbol{m}} - \mathrm{div} \, \frac{\partial \, h}{\partial \, \nabla \boldsymbol{m}}. \tag{5.45}$$

Likewise, the partial derivative of the dissipation potential, using the chain rule, can be expressed as

$$\frac{\partial \, h^{\mathrm{dis}}}{\partial \, \dot{\boldsymbol{m}}} \frac{\partial \, \dot{\boldsymbol{m}}}{\partial \, \boldsymbol{m}} = \dot{\boldsymbol{m}}. \tag{5.46}$$

Considering the norm constraint in the variational (Eq. 5.37) leads to the representation

$$\delta \mathcal{H} = \int_{\mathcal{B}} \boldsymbol{m} \times (\boldsymbol{H}^{\mathrm{eff}} - \frac{\alpha}{\gamma_0 \, M_{\mathrm{s}}} \dot{\boldsymbol{m}}) \cdot \delta \boldsymbol{\theta} \, \mathrm{dv} = 0 \tag{5.47}$$

that can be expressed in its local form as

$$\boldsymbol{m} \times (\boldsymbol{H}^{\mathrm{eff}} - \frac{\alpha}{\gamma_0 \, M_{\mathrm{s}}} \dot{\boldsymbol{m}}) = \boldsymbol{0} \quad \text{with} \quad \hat{\boldsymbol{H}}^{\mathrm{eff}} = \boldsymbol{H}^{\mathrm{eff}} - \frac{\alpha}{\gamma_0 \, M_{\mathrm{s}}} \dot{\boldsymbol{m}}. \tag{5.48}$$

The newly defined effective field $\hat{\boldsymbol{H}}^{\mathrm{eff}}$ can already be found in Eq. 5.42 and is identical to the effective field $\boldsymbol{H}^{\mathrm{eff}}$ for a system at rest and $\alpha = 0$.

Damped precessional dynamics: Inserting Eq. 5.48 into Eq. 5.42 leads to the so-called Gilbert equation

$$\dot{\boldsymbol{m}} = \underbrace{\mu_0 \gamma_0 \boldsymbol{m} \times \boldsymbol{H}^{\mathrm{eff}}}_{\text{precession}} - \underbrace{\alpha \, \boldsymbol{m} \times \dot{\boldsymbol{m}}}_{\text{damping}}, \tag{5.49}$$

with the clearly indicated precessional and damping parts. A graphical interpretation of those is presented in Fig. 5.5.

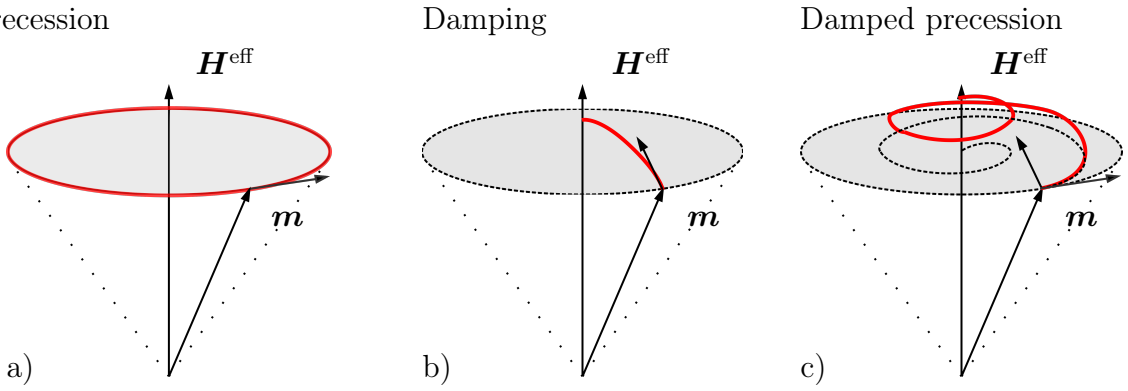

Figure 5.5: The effective field $\boldsymbol{H}^{\text{eff}}$ makes the magnetization vector a) precess if no damping is considered or b) align parallel if no precession is considered. If both modes are considered, the switching yields a damped precession, as sketched in c).

5.5 Summary of the coupled problem: Field equations and boundary conditions

The properties of ferromagnetic materials can be stimulated by external influences. In addition to the external magnetic field, mechanical strains and stresses can also have a great influence on the magnetic response. Accordingly, it is reasonable to couple the magnetic field equations (magnetic Gauss law and LLG equation) with the mechanical field equation (balance of linear momentum). Therefore, the complete micromagnetic-mechanically coupled boundary value problem is presented below. The governing field equation, that reproduces a mechanical quasi-static state, is the balance of linear momentum (Eq. 3.14) which yields

$$\operatorname{div}\boldsymbol{\sigma} = \mathbf{0} \quad \text{in} \quad \mathcal{B}, \quad \text{with} \quad \boldsymbol{\sigma} = \mathbb{C} : \boldsymbol{\varepsilon} \quad \text{and} \quad \boldsymbol{\varepsilon} = \frac{1}{2}\left[\nabla\boldsymbol{u} + (\nabla\boldsymbol{u})^{\mathrm{T}}\right], \tag{5.50}$$

where $\boldsymbol{\sigma}$ is the symmetric Cauchy stress tensor, $\mathbb{C}$ the material tensor, $\boldsymbol{\varepsilon}$ the linear strain tensor and $\boldsymbol{u}$ denotes the displacement vector. The solution of Eq. 5.50 requires boundary conditions on $\partial\mathcal{B} = \partial\mathcal{B}_u \cup \partial\mathcal{B}_\sigma$, with $\partial\mathcal{B}_u \cap \partial\mathcal{B}_\sigma = \emptyset$ prescribed in terms of Dirichlet- and Neumann-type as

$$\boldsymbol{u} = \boldsymbol{u}_0 \quad \text{on } \partial\mathcal{B}_u \qquad \text{and} \qquad \boldsymbol{\sigma}\cdot\boldsymbol{n} = \boldsymbol{t}_0 \quad \text{on } \partial\mathcal{B}_\sigma, \tag{5.51}$$

where $\boldsymbol{u}_0$ denotes a prescribed displacement and $\boldsymbol{t}_0$ an acting traction force vector. The evolving magnetic fields are governed by the magnetic Gauss law

$$\operatorname{div}\,\boldsymbol{B} = 0 \quad \text{in } \mathcal{B}, \tag{5.52}$$

with

$$\boldsymbol{B} = \mu_0\left(\boldsymbol{H} + \boldsymbol{M}\right), \quad \boldsymbol{H}\left(\boldsymbol{x}\right) := -\nabla\varphi, \quad \text{and} \quad \boldsymbol{M} := M_s\boldsymbol{m}, \tag{5.53}$$

where the magnetic induction $\boldsymbol{B}$ consists of the magnetic field $\boldsymbol{H}$, the magnetization $\boldsymbol{M}$, and the magnetic permeability of vacuum μ_0, see Eq. 2.18. The saturation magnetization M_s is material specific and $\boldsymbol{m}$ the magnetic unit director. The boundary conditions for the scalar potential on $\partial\mathcal{B} = \partial\mathcal{B}_\varphi \cup \partial\mathcal{B}_B$ with $\partial\mathcal{B}_\varphi \cap \partial\mathcal{B}_B = \emptyset$ can be specified as

$$\varphi = \varphi_0 \quad \text{on } \partial\mathcal{B}_\varphi \qquad \text{and} \qquad \boldsymbol{B}\cdot\boldsymbol{n} = \zeta_0 \quad \text{on } \partial\mathcal{B}_B. \tag{5.54}$$

The time and space evolution of the magnetization vectors requires the consideration of a Landau-Lifshitz-type equation, in this case the so-called Gilbert equation

$$\dot{\boldsymbol{m}} = -\gamma_0 \mu_0 \, \boldsymbol{m} \times \boldsymbol{H}^{\text{eff}} + \alpha \, \boldsymbol{m} \times \dot{\boldsymbol{m}}. \tag{5.55}$$

For its derivation compare to Sec. 5.4.

5.6 Finite-element-based micromagnetism

The magnetic Gauss Law (Eq. 2.18), the balance of linear momentum (Eq. 3.14) as well as the Gilbert equation (Eq. 5.49) are later approximated using finite elements. Hence, the weak forms and their corresponding linear increments needs to be derived, following the procedure presented extensively in Sec. 4.1. Within this chapter, five different ways to enforce the magnetization constraint are compared against each other. This implies, that the corresponding parts in the coupled system of equations differ for the compared approaches. Since the weak forms of the balance of momentum and the Gaussian law remain the same for all five considered systems, they are introduced firstly, followed by the weak form of the Gilbert equation corresponding to the projection method, the penalty method, Lagrange as well as perturbed Lagrange approaches, and the spherical coordinates.

Weak forms of the magnetic and mechanical balance laws

The derivation of the weak forms of the balance of momentum (Eq. 3.14) and the magnetic Gauss law (Eq. 4.1) follow Galerkin's method presented in Sec. 4.1. Multiplication with the test functions, i.e. the virtual displacements $\delta\boldsymbol{u}$ and the virtual scalar potential $\delta\varphi$, the subsequent application of the divergence and Cauchy's theorem yield the weak forms as

$$\begin{aligned} G_u &= -\int_{\mathcal{B}} \delta\boldsymbol{\varepsilon} : \boldsymbol{\sigma} \, \mathrm{dv} + \int_{\partial\mathcal{B}} \delta\boldsymbol{u} \cdot \boldsymbol{t}_0 \, \mathrm{da} \\ \text{and} \quad G_\varphi &= -\int_{\mathcal{B}} \delta\boldsymbol{H} \cdot \boldsymbol{B} \, \mathrm{dv} + \int_{\partial\mathcal{B}} \delta\varphi \, \zeta_0 \, \mathrm{da}. \end{aligned} \tag{5.56}$$

The virtual magnetic strains are denoted as $\delta\boldsymbol{\varepsilon} = \frac{1}{2}\left(\nabla\delta\boldsymbol{u} + (\nabla\delta\boldsymbol{u})^{\mathrm{T}}\right)$ and the virtual magnetic field is denoted as $\delta\boldsymbol{H} = -\nabla\delta\varphi$, while the mechanical traction vector and the magnetic flux are introduced as $\boldsymbol{t}_0$ and ζ_0. The approximation of the independent variables $\underline{\boldsymbol{u}}$ and φ, their virtual counterparts $\delta\underline{\boldsymbol{u}}$ and $\delta\varphi$ as well as their increments $\Delta\underline{\boldsymbol{u}}$ and $\Delta\varphi$ is realized in terms of a finite element implementation

$$\begin{aligned} \underline{\boldsymbol{u}} &\approx \sum_{\mathrm{I}=1}^{\mathrm{n_{node}}} \mathbb{N}^{\mathrm{I}} \underline{\boldsymbol{d}}_u^{\mathrm{I}}, \quad \delta\underline{\boldsymbol{u}} \approx \sum_{\mathrm{I}=1}^{\mathrm{n_{node}}} \mathbb{N}^{\mathrm{I}} \delta\underline{\boldsymbol{d}}_u^{\mathrm{I}}, \quad \Delta\underline{\boldsymbol{u}} \approx \sum_{\mathrm{I}=1}^{\mathrm{n_{node}}} \mathbb{N}^{\mathrm{I}} \Delta\underline{\boldsymbol{d}}_u^{\mathrm{I}}, \\ \text{and} \quad \varphi &\approx \sum_{\mathrm{I}=1}^{\mathrm{n_{node}}} \mathbb{N}^{\mathrm{I}} d_\varphi^{\mathrm{I}}, \quad \delta\varphi \approx \sum_{\mathrm{I}=1}^{\mathrm{n_{node}}} \mathbb{N}^{\mathrm{I}} \delta d_\varphi^{\mathrm{I}}, \quad \Delta\varphi \approx \sum_{\mathrm{I}=1}^{\mathrm{n_{node}}} \mathbb{N}^{\mathrm{I}} \Delta d_\varphi^{\mathrm{I}}, \end{aligned} \tag{5.57}$$

with $\mathbb{N}^{\mathrm{I}}$ denoting standard Lagrangian interpolation functions and the index I indicates the current node number. The nodal degrees of freedom are represent by $\underline{\boldsymbol{d}}_u^{\mathrm{I}}$ and d_φ^{I}, while their variational counterparts yield $\delta\underline{\boldsymbol{d}}_u^{\mathrm{I}}$ and $\delta d_\varphi^{\mathrm{I}}$, and their incremental counterparts $\Delta\underline{\boldsymbol{d}}_u^{\mathrm{I}}$

and $\Delta d_\varphi^{\mathrm{I}}$. As introduced in Sec. 4.1.2, $\underline{\bullet}$ indicates matrix notation of the corresponding quantity. This notation is not applied to scalars. While the structure of the discretized magnetic induction $\underline{\boldsymbol{B}}$ as well as the discretized magnetic field $\underline{\boldsymbol{H}}$ keep their dimensions, the discrete mechanical strains $\underline{\boldsymbol{\varepsilon}}$ and stresses $\underline{\boldsymbol{\sigma}}$ adopt the matrix notations

$$\underline{\boldsymbol{\varepsilon}} = [\varepsilon_{11}, \varepsilon_{22}, \varepsilon_{33}, 2\varepsilon_{12}, 2\varepsilon_{23}, 2\varepsilon_{12}]^{\mathrm{T}} \quad \text{and} \quad \underline{\boldsymbol{\sigma}} = [\sigma_{11}, \sigma_{22}, \sigma_{33}, \sigma_{12}, \sigma_{23}, \sigma_{13}]^{\mathrm{T}}. \tag{5.58}$$

Analogously to Eq. 5.57, the discrete strains $\underline{\boldsymbol{\varepsilon}}$ as well as the magnetic field $\underline{\boldsymbol{H}}$, their variations and increments are approximated as

$$\begin{aligned} \underline{\boldsymbol{\varepsilon}} &\approx \sum_{\mathrm{I}=1}^{\mathrm{n_{node}}} \underline{\mathbb{B}}_u^{\mathrm{I}} \underline{\boldsymbol{d}}_u^{\mathrm{I}}, \quad \delta\underline{\boldsymbol{\varepsilon}}, \approx \sum_{\mathrm{I}=1}^{\mathrm{n_{node}}} \underline{\mathbb{B}}_u^{\mathrm{I}} \delta\underline{\boldsymbol{d}}_u^{\mathrm{I}}, \quad \Delta\underline{\boldsymbol{\varepsilon}} \approx \sum_{\mathrm{I}=1}^{\mathrm{n_{node}}} \underline{\mathbb{B}}_u^{\mathrm{I}} \Delta\underline{\boldsymbol{d}}_u^{\mathrm{I}} \\ \text{and} \quad -\underline{\boldsymbol{H}} &\approx \sum_{\mathrm{I}=1}^{\mathrm{n_{node}}} \underline{\mathbb{B}}_\varphi^{\mathrm{I}} d_\varphi^{\mathrm{I}}, \quad -\delta\underline{\boldsymbol{H}} \approx \sum_{\mathrm{I}=1}^{\mathrm{n_{node}}} \underline{\mathbb{B}}_\varphi^{\mathrm{I}} \delta d_\varphi^{\mathrm{I}}, \quad -\Delta\underline{\boldsymbol{H}} \approx \sum_{\mathrm{I}=1}^{\mathrm{n_{node}}} \underline{\mathbb{B}}_\varphi^{\mathrm{I}} \Delta d_\varphi^{\mathrm{I}}. \end{aligned} \tag{5.59}$$

Thereby, the cartesian derivatives of the interpolation function $\mathbb{N}^{\mathrm{I}}$ are sorted into the so-called $\underline{\mathbb{B}}$–matrices as

$$\underline{\mathbb{B}}_u^{\mathrm{I}} = \begin{bmatrix} \mathbb{N}_{,1}^{\mathrm{I}} & 0 & 0 \\ 0 & \mathbb{N}_{,2}^{\mathrm{I}} & 0 \\ 0 & 0 & \mathbb{N}_{,3}^{\mathrm{I}} \\ \mathbb{N}_{,2}^{\mathrm{I}} & \mathbb{N}_{,1}^{\mathrm{I}} & 0 \\ 0 & \mathbb{N}_{,3}^{\mathrm{I}} & \mathbb{N}_{,2}^{\mathrm{I}} \\ \mathbb{N}_{,3}^{\mathrm{I}} & 0 & \mathbb{N}_{,1}^{\mathrm{I}} \end{bmatrix} \quad \text{and} \quad \underline{\mathbb{B}}_\varphi^{\mathrm{I}} = \begin{bmatrix} \mathbb{N}_{,1}^{\mathrm{I}} \\ \mathbb{N}_{,2}^{\mathrm{I}} \\ \mathbb{N}_{,3}^{\mathrm{I}} \end{bmatrix} \tag{5.60}$$

for the displacements and the scalar potential respectively. Inserting Eq. 5.57 and Eq. 5.59 into Eq. 5.56 yields the residual vectors and the corresponding stiffness matrices

$$\begin{aligned} \underline{\mathbb{R}}_u^{\mathrm{I}} &= -\int_{\mathcal{B}^e} (\underline{\mathbb{B}}_u^{\mathrm{I}})^{\mathrm{T}}\, \underline{\boldsymbol{\sigma}}\, \mathrm{dv} + \int_{\partial\mathcal{B}_\sigma^e} \mathbb{N}^{\mathrm{I}}\, \underline{\boldsymbol{t}}\, \mathrm{da}, \quad \underline{\mathbb{K}}_{uu}^{\mathrm{IJ}} = -\frac{\partial \underline{\mathbb{R}}_u^{\mathrm{I}}}{\partial \underline{\boldsymbol{d}}_u^{\mathrm{J}}} = \int_{\mathcal{B}^e} (\underline{\mathbb{B}}_u^{\mathrm{I}})^{\mathrm{T}}\, \underline{\mathbb{C}}\, \underline{\mathbb{B}}_u^{\mathrm{J}}\, \mathrm{dv} \quad \text{and} \\ \mathbb{R}_\varphi^{\mathrm{I}} &= -\int_{\mathcal{B}^e} (\underline{\mathbb{B}}_\varphi^{\mathrm{I}})^{\mathrm{T}}\, \underline{\boldsymbol{B}}\, \mathrm{dv} + \int_{\partial\mathcal{B}_B^e} \mathbb{N}^{\mathrm{I}}\, \zeta_0\, \mathrm{da}, \quad \mathbb{K}_{\varphi\varphi}^{\mathrm{IJ}} = -\frac{\partial \mathbb{R}_\varphi^{\mathrm{I}}}{\partial d_\varphi^{\mathrm{J}}} = -\int_{\mathcal{B}^e} (\underline{\mathbb{B}}_\varphi^{\mathrm{I}})^{\mathrm{T}}\, \underline{\boldsymbol{\mu}}\, \underline{\mathbb{B}}_\varphi^{\mathrm{J}}\, \mathrm{dv}. \end{aligned} \tag{5.61}$$

5.7 Enforcement of the unity constraint

In this section, the constraint of the magnetization vectors onto a unit length is addressed. Therefore, different approaches are introduced and compared. These approaches involve different ways of constraining the length of the vectors based on renormalizations, penalty expressions, variational methods, and rotational exact methods. After detailed analyses, these different methods are evaluated and their advantages and disadvantages are discussed.

5.7.1 Projection method

The probably most easiest way to consider the unit length constraint $\|\boldsymbol{m}\| = 1$ of the magnetization vectors is to apply a renormalization or projection scheme. Such schemes

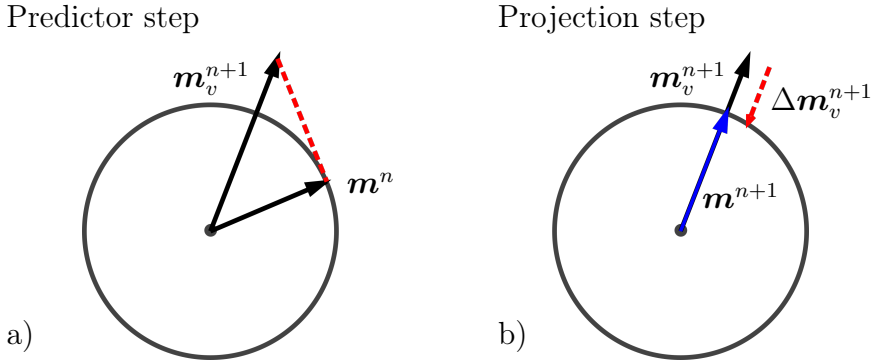

Figure 5.6: a) a unit magnetization vector $\boldsymbol{m}^n$ from the latest time step n evolving in time and space to $\boldsymbol{m}_v^{n+1}$ at time n+1. This configuration violates the unit constraint. The violation $\Delta\boldsymbol{m}_v^{n+1}$ is corrected via a projection step, depicted in b) back onto the unit sphere as $\boldsymbol{m}^{n+1}$, cf. Cimrák [2007]. Taken from Reichel et al. [2022].

in general apply two steps, which are sketched in Fig. 5.6. Within a first step, the so-called predictor step, the LLG equation is solved without fulfilling the unit constraint (Fig. 5.6a) for simplicity utilizing a 2D circle). Thus, the length of the magnetization vectors can deviate from Euclid's norm. Subsequently, after the considered time step has converged, the nodal magnetization degrees of freedom are renormalized and projected back onto the unit sphere. This projection is depicted in Fig. 5.6b). The procedure is applied at each node I as $\underline{\boldsymbol{d}}_m^{\mathrm{I}} = \underline{\boldsymbol{d}}_m^{\mathrm{I}}/\|\underline{\boldsymbol{d}}_m^{\mathrm{I}}\|$. The algorithmic projection procedure is highlighted in Table 5.1. Such a pure projection method was applied among others by Kružík and Prohl [2006]. However, it has been critically evaluated by Cimrák [2007] and Lewis and Nigam [2003], among others. The projection of the magnetization back onto the unit sphere indicates a non-linear modification of the solution, what can lead to seriously erroneous results. To obtain better results within this scheme small time increments should be applied for the costs of a massive increase in computational time. Hence, the weak form yields

$$G_m = -\int_{\mathcal{B}} \left\{ \left[\frac{M_s}{\gamma_0}(\alpha\,\dot{\boldsymbol{m}} + \boldsymbol{m}\times\dot{\boldsymbol{m}}) + (\boldsymbol{I} - \boldsymbol{m}\otimes\boldsymbol{m})\cdot\partial_{\boldsymbol{m}}\mathcal{H} \right] \cdot \delta\boldsymbol{m} + \boldsymbol{\Pi} : \nabla\delta\boldsymbol{m} \right\} \mathrm{dv} = 0, \tag{5.62}$$

with the virtual magnetization $\delta\boldsymbol{m}$ and its virtual gradient $\nabla\delta\boldsymbol{m}$. The discrete magnetization $\underline{\boldsymbol{m}}$ as well as the corresponding variation and increment are interpolated node-wise using the interpolation functions $\mathbb{N}^{\mathrm{I}}$, and the nodal degrees of freedom $\underline{\boldsymbol{d}}_m^{\mathrm{I}}$ as

$$\underline{\boldsymbol{m}} \approx \sum_{\mathrm{I}=1}^{\mathrm{n_{node}}} \mathbb{N}^{\mathrm{I}}\underline{\boldsymbol{d}}_m^{\mathrm{I}}, \quad \delta\underline{\boldsymbol{m}} \approx \sum_{\mathrm{I}=1}^{\mathrm{n_{node}}} \mathbb{N}^{\mathrm{I}}\delta\underline{\boldsymbol{d}}_m^{\mathrm{I}}, \quad \text{and} \quad \Delta\underline{\boldsymbol{m}} \approx \sum_{\mathrm{I}=1}^{\mathrm{n_{node}}} \mathbb{N}^{\mathrm{I}}\Delta\underline{\boldsymbol{d}}_m^{\mathrm{I}}. \tag{5.63}$$

The gradient related quantities of the magnetization are analogously to Eq. 5.59 approximated as

$$\nabla\underline{\boldsymbol{m}} \approx \sum_{\mathrm{I}=1}^{\mathrm{n_{node}}} \mathbb{B}_m^{\mathrm{I}}\underline{\boldsymbol{d}}_m^{\mathrm{I}}, \quad \delta\nabla\underline{\boldsymbol{m}} \approx \sum_{\mathrm{I}=1}^{\mathrm{n_{node}}} \mathbb{B}_m^{\mathrm{I}}\delta\underline{\boldsymbol{d}}_m^{\mathrm{I}}, \quad \text{and} \quad \Delta\nabla\underline{\boldsymbol{m}} \approx \sum_{\mathrm{I}=1}^{\mathrm{n_{node}}} \mathbb{B}_m^{\mathrm{I}}\Delta\underline{\boldsymbol{d}}_m^{\mathrm{I}}, \tag{5.64}$$

utilizing the structured matrix $\underline{\mathbb{B}}^{\mathrm{I}}_m$ containing the derivatives of the interpolation functions

$$\left(\underline{\mathbb{B}}^{\mathrm{I}}_m\right)^{\mathrm{T}} = \begin{bmatrix} \mathbb{N}^{\mathrm{I}}_{,1} & \mathbb{N}^{\mathrm{I}}_{,2} & \mathbb{N}^{\mathrm{I}}_{,3} & 0 & 0 & 0 & 0 & 0 & 0 \\ 0 & 0 & 0 & \mathbb{N}^{\mathrm{I}}_{,1} & \mathbb{N}^{\mathrm{I}}_{,2} & \mathbb{N}^{\mathrm{I}}_{,3} & 0 & 0 & 0 \\ 0 & 0 & 0 & 0 & 0 & 0 & \mathbb{N}^{\mathrm{I}}_{,1} & \mathbb{N}^{\mathrm{I}}_{,2} & \mathbb{N}^{\mathrm{I}}_{,3} \end{bmatrix}. \tag{5.65}$$

Thus, the gradient of the magnetization in matrix notation results in

$$\underline{\boldsymbol{\Pi}} = 2A_{\mathrm{exc}} \left[m_{1,1}, m_{1,2}, m_{1,3}, m_{2,1}, m_{2,2}, m_{2,3}, m_{3,1}, m_{3,2}, m_{3,3}\right]^T. \tag{5.66}$$

The residuals $\mathbb{R}^{\mathrm{I}}_{\varphi}$ and $\underline{\mathbb{R}}^{\mathrm{I}}_u$ of the displacements and the scalar potential as well as their corresponding system matrices $\mathbb{K}^{\mathrm{IJ}}_{\varphi\varphi}$ and $\underline{\mathbb{K}}^{\mathrm{IJ}}_{uu}$ can be taken from Eq. 5.56. The discrete residual corresponding to Eq. 5.62 appears as

$$\underline{\mathbb{R}}^{\mathrm{I}}_m = -\int_{\mathcal{B}^{\mathrm{e}}} \left\{ \mathbb{N}^{\mathrm{I}} \left[\frac{M_s}{\gamma_0} (\alpha\, \underline{\dot{\boldsymbol{m}}} + \underline{\boldsymbol{m}} \times \underline{\dot{\boldsymbol{m}}}) + \underline{\mathbb{P}} \cdot \partial_{\underline{\boldsymbol{m}}} \mathcal{H} \right] + (\underline{\mathbb{B}}^{\mathrm{I}}_m)^{\mathrm{T}}\, \underline{\boldsymbol{\Pi}} \right\} \mathrm{dv} = 0, \tag{5.67}$$

with $\underline{\mathbb{P}} = (\underline{\boldsymbol{I}} - \underline{\boldsymbol{m}} \otimes \underline{\boldsymbol{m}})$. The approximation of the rate of the magnetization vectors $\underline{\dot{\boldsymbol{m}}}$ is realized by applying a backward Euler time integration scheme as $\underline{\dot{\boldsymbol{m}}} = (\underline{\boldsymbol{m}} - \underline{\boldsymbol{m}}_n)/\Delta t$, where $\underline{\boldsymbol{m}}$ denotes the actual magnetization configuration at time $n+1$, $\underline{\boldsymbol{m}}_n$ the former configuration at time n, and Δt the time step between both configurations. The iteration matrix $\underline{\mathbb{K}}^{\mathrm{IJ}}_{\mathrm{eff}}$ resulting of the residuals given in Eq. 5.61 and Eq. 5.67 consists of the system matrices and a damping matrix $\underline{\mathbb{D}}^{\mathrm{IJ}}$ as

$$\underline{\mathbb{K}}^{\mathrm{IJ}}_{\mathrm{eff}} = \underline{\mathbb{K}}^{\mathrm{IJ}} + \frac{1}{\Delta t}\, \underline{\mathbb{D}}^{\mathrm{IJ}}, \tag{5.68}$$

with the individual parts

$$\begin{aligned}
\underline{\mathbb{K}}^{\mathrm{IJ}}_{mm} &= -\frac{\partial \underline{\mathbb{R}}^{\mathrm{I}}_m}{\partial \underline{\boldsymbol{d}}^{\mathrm{J}}_m} = \int_{\mathcal{B}^{\mathrm{e}}} \left\{ \mathbb{N}^{\mathrm{I}} \left[\frac{M_s}{\gamma_0}\, \underline{\boldsymbol{\Omega}}_{[\underline{\dot{\boldsymbol{m}}}]} + \right. \right. \\
&\qquad \left. \left. \partial_{\underline{\boldsymbol{m}}} \underline{\mathbb{P}}\, \partial_{\underline{\boldsymbol{m}}} \mathcal{H} + \underline{\mathbb{P}}\, \partial_{\underline{\boldsymbol{m}}\underline{\boldsymbol{m}}} \mathcal{H} \right] \mathbb{N}^{\mathrm{J}} + (\underline{\mathbb{B}}^{\mathrm{I}}_m)^T\, \frac{\partial \underline{\boldsymbol{\Pi}}}{\partial \nabla \underline{\boldsymbol{m}}}\, \underline{\mathbb{B}}^{\mathrm{J}}_m \right\} \mathrm{dv}, \\
\underline{\mathbb{K}}^{\mathrm{IJ}}_{m\varphi} &= -\frac{\partial \underline{\mathbb{R}}^{\mathrm{I}}_m}{\partial d^{\mathrm{J}}_{\varphi}} = \int_{\mathcal{B}^{\mathrm{e}}} \mathbb{N}^{\mathrm{I}} (\mu_0\, M_s \underline{\boldsymbol{I}}\, \underline{\mathbb{P}})\, \underline{\mathbb{B}}^{\mathrm{J}}_{\varphi}\, \mathrm{dv}, \\
\underline{\mathbb{K}}^{\mathrm{IJ}}_{mu} &= -\frac{\partial \underline{\mathbb{R}}^{\mathrm{I}}_m}{\partial \underline{\boldsymbol{d}}^{\mathrm{J}}_u} = -\int_{\mathcal{B}^{\mathrm{e}}} \mathbb{N}^{\mathrm{I}} \underline{\mathbb{P}}\, \frac{\partial\, \underline{\boldsymbol{\varepsilon}}^0}{\partial \underline{\boldsymbol{m}}}\, \underline{\mathbb{C}}\, \underline{\mathbb{B}}^{\mathrm{J}}_u\, \mathrm{dv}, \\
\underline{\mathbb{K}}^{\mathrm{IJ}}_{\varphi m} &= -\frac{\partial \mathbb{R}^{\mathrm{I}}_{\varphi}}{\partial \underline{\boldsymbol{d}}^{\mathrm{J}}_m} = \int_{\mathcal{B}^{\mathrm{e}}} (\underline{\mathbb{B}}^{\mathrm{I}}_{\varphi})^T\, (\mu_0 M_s \underline{\boldsymbol{I}})\, \underline{\mathbb{N}}^{\mathrm{J}}\, \mathrm{dv}, \\
\underline{\mathbb{K}}^{\mathrm{IJ}}_{um} &= -\frac{\partial \underline{\mathbb{R}}^{\mathrm{I}}_u}{\partial \underline{\boldsymbol{d}}^{\mathrm{J}}_m} = -\int_{\mathcal{B}^{\mathrm{e}}} (\underline{\mathbb{B}}^{\mathrm{I}}_u)^T\, \underline{\mathbb{C}}\, \frac{\partial\, \underline{\boldsymbol{\varepsilon}}^0}{\partial \underline{\boldsymbol{m}}}\, \underline{\mathbb{N}}^{\mathrm{J}}_m,\, \mathrm{dv},
\end{aligned} \tag{5.69}$$

and the damping part

$$\underline{\mathbb{D}}^{\mathrm{IJ}}_{mm} = -\frac{\partial \underline{\mathbb{R}}^{\mathrm{I}}_{m}}{\partial \underline{\dot{\boldsymbol{d}}}^{\mathrm{J}}_{m}} = \int_{\mathcal{B}^e} \mathbb{N}^{\mathrm{I}} \left(\alpha \, \boldsymbol{I} + \underline{\boldsymbol{\Omega}}_{[\underline{\boldsymbol{m}}]} \right) \mathbb{N}^{\mathrm{J}} \, \mathrm{dv}. \tag{5.70}$$

The definition of the skew-symmetric matrix $\boldsymbol{\Omega}$, for an exemplarily chosen magnetization vector $\underline{\boldsymbol{m}}$, yields the form

$$\underline{\boldsymbol{\Omega}}_{[\underline{\boldsymbol{m}}]} = -\underline{\boldsymbol{\Omega}}^{\mathrm{T}}_{[\underline{\boldsymbol{m}}]} = \begin{bmatrix} 0 & -m_3 & m_2 \\ m_3 & 0 & -m_1 \\ -m_2 & m_1 & 0 \end{bmatrix} \tag{5.71}$$

and allows the substitution of the cross product as

$$\underline{\boldsymbol{m}} \times \underline{\boldsymbol{m}} = \underline{\boldsymbol{\Omega}}_{[\underline{\boldsymbol{m}}]} \, \underline{\boldsymbol{m}}. \tag{5.72}$$

The nodal residuals, the system matrices, and the damping matrices can be sorted into the system of equations as

$$\begin{bmatrix} \mathbb{R}^{\mathrm{I}}_{\varphi} \\ \underline{\mathbb{R}}^{\mathrm{I}}_{m} \\ \underline{\mathbb{R}}^{\mathrm{I}}_{u} \end{bmatrix} = \begin{bmatrix} \mathbb{K}^{\mathrm{IJ}}_{\varphi\varphi} & \underline{\mathbb{K}}^{\mathrm{IJ}}_{\varphi m} & \underline{\mathbf{0}} \\ \underline{\mathbb{K}}^{\mathrm{IJ}}_{m\varphi} & \underline{\mathbb{K}}^{\mathrm{IJ}}_{mm} + \frac{1}{\Delta t}\underline{\mathbb{D}}^{\mathrm{IJ}}_{mm} & \underline{\mathbb{K}}^{\mathrm{IJ}}_{mu} \\ \underline{\mathbf{0}} & \underline{\mathbb{K}}^{\mathrm{IJ}}_{um} & \underline{\mathbb{K}}^{\mathrm{IJ}}_{uu} \end{bmatrix} \begin{bmatrix} \Delta d^{\mathrm{I}}_{\varphi} \\ \Delta \underline{\boldsymbol{d}}^{\mathrm{I}}_{m} \\ \Delta \underline{\boldsymbol{d}}^{\mathrm{I}}_{u} \end{bmatrix}. \tag{5.73}$$

To obtain the element residual $\underline{\mathbb{R}}^{\mathrm{e}}$ and system matrix $\underline{\mathbb{K}}^{\mathrm{e}}_{\mathrm{eff}}$ the procedure introduced in Sec. 4.1.2 can be applied to Eq. 5.73. With this the element vector and the system matrix can be assembled into a global residual $\underline{\mathbb{R}}$ and system matrix $\underline{\mathbb{K}}_{\mathrm{eff}}$, using Sec. 4.1.2.

Table 5.1: Projection of magnetization degrees of freedom after each time step.

1) Given $\underline{\boldsymbol{D}} = \left[\, \underline{\boldsymbol{D}}^{\mathrm{T}}_{\varphi}, \underline{\boldsymbol{D}}^{\mathrm{T}}_{m}, \underline{\boldsymbol{D}}^{\mathrm{T}}_{u} \, \right]^{\mathrm{T}}$ the global DOFs at time t_n

2) Compute global residuum $\underline{\mathbb{R}}$ and tangent $\underline{\mathbb{K}}_{\mathrm{eff}}$

$$\underline{\mathbb{R}} = \mathop{\mathsf{A}}_{\mathrm{e}=1}^{num_{ele}} \underline{\mathbb{R}}^{\mathrm{e}} \quad \text{and} \quad \underline{\mathbb{K}}_{\mathrm{eff}} = \mathop{\mathsf{A}}_{\mathrm{e}=1}^{num_{ele}} \underline{\mathbb{K}}^{\mathrm{e}}_{\mathrm{eff}}$$

3) Solve $\underline{\mathbb{K}}_{\mathrm{eff}} \, \Delta \underline{\boldsymbol{D}} = \underline{\mathbb{R}}$ and Update $\underline{\boldsymbol{D}} \Leftarrow \underline{\boldsymbol{D}} + \Delta \underline{\boldsymbol{D}}$

4) If $\|\underline{\mathbb{R}}\| \leq 10^{-10}$ Go To 5 Else Go To 2

5) Project DOFs nodewise onto unit sphere $\underline{\boldsymbol{d}}^{\mathrm{I}}_{m} \Leftarrow \underline{\boldsymbol{d}}^{\mathrm{I}}_{m} / \|\underline{\boldsymbol{d}}^{\mathrm{I}}_{m}\|$ and Go To 1

5.7.2 Penalty approach

Besides the projection method introduced in Sec. 5.7.1, the penalty method is a very straight forward way to limit the length of the magnetization vectors to the unit length

$\|\boldsymbol{m}\| = 1$. Penalization strategies have been analyzed within the framework of the micromagnetic theory, e.g. by Landis [2008], Prohl [2001], Wang and Zhang [2013], and Zhang et al. [2016]. To satisfy the unit constraint, the weak form given in Eq. 5.62 is extended by a penalization term that penalizes any deviation from the prescribed length as

$$G_m^{\text{pen}} = G_m + G^{\text{pen}} = G_m - 2\kappa \left(\|\boldsymbol{m}\| - 1\right) \frac{\boldsymbol{m}}{\|\boldsymbol{m}\|} \cdot \delta\boldsymbol{m} = 0, \tag{5.74}$$

where the intensity of the penalty can be controlled by the penalty parameter κ. The residual and the system matrix change by adding the penalty as

$$\underline{\mathbb{R}}_m^{\text{I pen}} = \underline{\mathbb{R}}_m^{\text{I}} - \int_{\mathcal{B}^e} \mathbb{N}^{\text{I}}\, 2\kappa \left(\|\underline{\boldsymbol{m}}\| - 1\right) \frac{\underline{\boldsymbol{m}}}{\|\underline{\boldsymbol{m}}\|} \,\mathrm{dv} = 0 \tag{5.75}$$

and

$$\underline{\mathbb{K}}_{mm}^{\text{IJ pen}} = -\frac{\partial \underline{\mathbb{R}}_m^{\text{I pen}}}{\partial \underline{\boldsymbol{d}}_m^{\text{J}}} = \underline{\mathbb{K}}_{mm}^{\text{IJ}} + \int_{\mathcal{B}^e} \mathbb{N}^{\text{I}}\, 2\kappa \left(\frac{\underline{\boldsymbol{\Omega}}_{[\underline{\boldsymbol{m}}]}\, \underline{\boldsymbol{\Omega}}_{[\underline{\boldsymbol{m}}]}}{(\underline{\boldsymbol{m}}\, \underline{\boldsymbol{m}})^{3/2}} + \underline{\boldsymbol{I}} \right) \mathbb{N}^{\text{J}} \,\mathrm{dv}. \tag{5.76}$$

The resulting system of equations does not differ in terms of dimensions from the system of equations of the projection method shown in Eq. 5.73. Its structure remains similar as well.

5.7.3 Lagrange and perturbed Lagrange approach

Another method to enforce the unit constraint of the magnetization vectors as $\|\boldsymbol{m}\| = 1$ uses a Lagrange multiplier λ, that adds a new degree of freedom to the system of equations. In contrast to the penalty method, the Lagrange multiplier fulfills the unit constraint exact in a variational sense. Nevertheless, the additional degree of freedom in the system of equations leads to additional computational costs. A Lagrange multiplier is introduced in terms of an additional energy contribution as

$$\Pi^{\text{L}} = \int_{\mathcal{B}} \lambda \left[\|\boldsymbol{m}\|^2 - 1\right] \,\mathrm{dv}, \tag{5.77}$$

which is a classical Lagrange multiplier approach, such as used in Szambolics et al. [2008]. However, this formulation leads to singular system matrices, since it contains zero entries on their main diagonal. Hence, this often requires special and challenging treatments. In order to counteract this problem, a so-called perturbed Lagrange multiplier can be used instead, cf. Simo et al. [1985] and Carey and Oden [1982]. This method adds a quadratic part in λ to Eq. 5.77, so that differentiating twice leads to non-zero entries on the main diagonal in the system matrix. In the context of micromagnetism, such a perturbed Lagrange multiplier is applied by Ohmer [2022] and by Ohmer et al. [2022] in the form of

$$\Pi^{\text{p}} = \int_{\mathcal{B}} \left(\lambda \left[\|\boldsymbol{m}\|^2 - 1\right] - \frac{\lambda^2}{2k_L} \right) \,\mathrm{dv}, \tag{5.78}$$

where k_L is a dimensionless scaling parameter, that is assumed to be in the range of $\sim 10^5$. In the following, only the perturbed Lagrange multiplier method (Eq. 5.78) is considered for derivation, since it contains the derivations of the classical Lagrange multiplier

(Eq. 5.77). To obtain an expression that can be solved by finite elements, Eq. 5.78 must be varied according to the primary variables λ and $\boldsymbol{m}$ as

$$\delta\Pi^{\mathrm{p}} = \underbrace{\frac{\partial\,\Pi^{\mathrm{p}}}{\partial\,\lambda}\,\delta\lambda}_{\delta\Pi^{\mathrm{p}}_{\lambda}} + \underbrace{\frac{\partial\,\Pi^{\mathrm{p}}}{\partial\,\boldsymbol{m}}\cdot\delta\boldsymbol{m}}_{\delta\Pi^{\mathrm{p}}_{m}}, \tag{5.79}$$

with

$$\delta\Pi^{\mathrm{p}}_{\lambda} = \int_{\mathcal{B}} \left[(\|\boldsymbol{m}\|^2 - 1) - \frac{\lambda}{k_L}\right]\delta\lambda\,\mathrm{dv} \quad \text{and} \quad \delta\Pi^{\mathrm{p}}_{m} = \int_{\mathcal{B}} 2\,\lambda\boldsymbol{m}\cdot\delta\boldsymbol{m}\,\mathrm{dv}. \tag{5.80}$$

The discrete Lagrange multiplier is obtained by multiplying the corresponding interpolation functions $\mathbb{N}^{\mathrm{I}}$ and the nodal degrees of freedom d^{I}_{λ} as

$$\lambda \approx \sum_{\mathrm{I}=1}^{\mathrm{n_{node}}} \mathbb{N}^{\mathrm{I}} d^{\mathrm{I}}_{\lambda}, \quad \delta\lambda \approx \sum_{\mathrm{I}=1}^{\mathrm{n_{node}}} \mathbb{N}^{\mathrm{I}} \delta d^{\mathrm{I}}_{\lambda}, \quad \text{and} \quad \Delta\lambda \approx \sum_{\mathrm{I}=1}^{\mathrm{n_{node}}} \mathbb{N}^{\mathrm{I}} \Delta d^{\mathrm{I}}_{\lambda}. \tag{5.81}$$

The residuals $\mathbb{R}^{\mathrm{I}}_{\varphi}$, $\underline{\mathbb{R}}^{\mathrm{I}}_{u}$, and $\underline{\mathbb{R}}^{\mathrm{I}}_{m}$ as well as their corresponding system matrices can be taken from Eq. 5.56 and Eq. 5.69. Of course, the here considered weak form does not include the penalty contribution as used within section 5.7.2. The residuals $\mathbb{R}^{\mathrm{I\,p}}_{\lambda}$ and $\underline{\mathbb{R}}^{\mathrm{I\,p}}_{m}$ are obtained from Eq. 5.80, where the superscript p indicates that these terms can be traced back to the perturbed Lagrange multiplier. Hence, the $\mathbb{R}$- and $\mathbb{K}$- matrices yield

$$\begin{aligned}
&\mathbb{R}^{\mathrm{I\,p}}_{\lambda} = \int_{\mathcal{B}^{\mathrm{e}}} \mathbb{N}^{\mathrm{I}} \left[(\|\underline{\boldsymbol{m}}\|^2 - 1) - \frac{\lambda}{k_L}\right]\mathrm{dv}, \quad \underline{\mathbb{R}}^{\mathrm{I\,p}}_{m} = \int_{\mathcal{B}^{\mathrm{e}}} \mathbb{N}^{\mathrm{I}}\, 2\underline{\boldsymbol{m}}\,\lambda\,\mathrm{dv},\\
&\underline{\mathbb{K}}^{\mathrm{IJ\,p}}_{mm} = -\frac{\partial\,\underline{\mathbb{R}}^{\mathrm{I\,p}}_{m}}{\partial\,\underline{\boldsymbol{d}}^{\mathrm{J}}_{m}} = -\int_{\mathcal{B}^{e}} \mathbb{N}^{I}\,2\lambda\,\underline{\mathbb{N}}^{J}\mathrm{dv}, \quad \underline{\mathbb{K}}^{\mathrm{IJ\,p}}_{m\lambda} = -\frac{\partial\,\underline{\mathbb{R}}^{\mathrm{I\,p}}_{m}}{\partial\,d^{\mathrm{J}}_{\lambda}} = -\int_{\mathcal{B}^{\mathrm{e}}} \mathbb{N}^{\mathrm{I}}\,2\,\underline{\boldsymbol{m}}\,\underline{\mathbb{N}}^{\mathrm{J}}\mathrm{dv},\\
&\underline{\mathbb{K}}^{\mathrm{IJ\,p}}_{\lambda m} = -\frac{\partial\,\mathbb{R}^{\mathrm{I\,p}}_{\lambda}}{\partial\,\underline{\boldsymbol{d}}^{\mathrm{J}}_{m}} = -\int_{\mathcal{B}^{\mathrm{e}}} \mathbb{N}^{\mathrm{I}}\,2\underline{\boldsymbol{m}}\,\underline{\mathbb{N}}^{\mathrm{J}}\mathrm{dv}, \quad \mathbb{K}^{\mathrm{IJ\,p}}_{\lambda\lambda} = -\frac{\partial\,\mathbb{R}^{\mathrm{I\,p}}_{\lambda}}{\partial\,d^{\mathrm{J}}_{\lambda}} = -\int_{\mathcal{B}^{\mathrm{e}}} \mathbb{N}^{\mathrm{I}}\,k_L^{-1}\,\underline{\mathbb{N}}^{\mathrm{J}}\mathrm{dv}.
\end{aligned} \tag{5.82}$$

The resulting system of equations appears as

$$\begin{bmatrix} \mathbb{R}^{\mathrm{I}}_{\varphi} \\ \underline{\mathbb{R}}^{\mathrm{I}}_{m} + \underline{\mathbb{R}}^{\mathrm{I\,p}}_{m} \\ \mathbb{R}^{\mathrm{I\,p}}_{\lambda} \\ \underline{\mathbb{R}}^{\mathrm{I}}_{u} \end{bmatrix} = \begin{bmatrix} \mathbb{K}^{\mathrm{IJ}}_{\varphi\varphi} & \underline{\mathbb{K}}^{\mathrm{IJ}}_{\varphi m} & 0 & \underline{\mathbf{0}} \\ \underline{\mathbb{K}}^{\mathrm{IJ}}_{m\varphi} & \underline{\mathbb{K}}^{\mathrm{IJ}}_{mm} + \underline{\mathbb{K}}^{\mathrm{IJ\,p}}_{mm} + \frac{1}{\Delta t}\underline{\mathbb{D}}^{\mathrm{IJ}}_{mm} & \underline{\mathbb{K}}^{\mathrm{IJ\,p}}_{m\lambda} & \underline{\mathbb{K}}^{\mathrm{IJ}}_{mu} \\ 0 & \underline{\mathbb{K}}^{\mathrm{IJ\,p}}_{\lambda m} & \mathbb{K}^{\mathrm{IJ\,p}}_{\lambda\lambda} & \underline{\mathbf{0}} \\ \underline{\mathbf{0}} & \underline{\mathbb{K}}^{\mathrm{IJ}}_{um} & \underline{\mathbf{0}} & \underline{\mathbb{K}}^{\mathrm{IJ}}_{uu} \end{bmatrix} \begin{bmatrix} \Delta d^{\mathrm{J}}_{\varphi} \\ \Delta\underline{\boldsymbol{d}}^{\mathrm{J}}_{m} \\ \Delta d^{\mathrm{J}}_{\lambda} \\ \Delta\underline{\boldsymbol{d}}^{\mathrm{J}}_{u} \end{bmatrix}. \tag{5.83}$$

To adapt Eq. 5.82 to a classical Lagrange multiplier, $-\frac{\lambda}{k_L} = 0$ needs to be defined. As a consequence a zero on the main diagonal results at position $\mathbb{K}^{\mathrm{IJ\,p}}_{\lambda\lambda} = 0$, see Eq. 5.83. This may lead to instabilities during numerical solution procedures. By following the same procedure as already described in Sec. 4.1.2, the element residual $\underline{\mathbb{R}}^{\mathrm{e}}$ and the corresponding element system matrix $\underline{\mathbb{K}}^{\mathrm{e}}$ can be formulated.

5.7.4 Condensed perturbed Lagrange approach

The system matrices derived above use the so-called perturbed Lagrange approach. This method restricts the length of the magnetization vectors in a variational sense to the unit length, to the drawback of additional degrees of freedom in the system of equations. Compared to the penalty method, better results are obtained at longer calculation time. This problem can be reduced by a static condensation of the Lagrange multiplier on element level. Compared to the non-condensed Lagrange multiplier, this leads to shorter computation times with equivalent results. Using the definitions and requirements of function spaces introduced in Sec. 4.1.1, statements on the function spaces of the primary variables are made in order to analyze and discuss the boundary value problem introduced in Sec. 5.5. To keep the notation short, the abbreviation $\Xi := \{\varphi, \underline{\boldsymbol{m}}, \underline{\boldsymbol{u}}\}$ is considered within the context of the following section. The approximation of the displacements, the scalar potential, the magnetization vector, and the Lagrange multiplier in the function spaces

$$\begin{aligned}
\left(\boldsymbol{v}^h, \boldsymbol{\mu}^h\right)_i &= \left\{ \{\boldsymbol{u}, \boldsymbol{m}\} \in H^1\left(\mathcal{B}\right)^3 : \{\boldsymbol{u}, \boldsymbol{m}\}|_{\mathcal{B}_e} \in P_i\left(\mathcal{B}_e\right)^3 \ \forall\, \mathcal{B}_e \right\}, \\
\Phi_i^h &= \left\{ \varphi \in H^1\left(\mathcal{B}\right) : \varphi|_{\mathcal{B}_e} \in P_i\left(\mathcal{B}_e\right) \ \forall\, \mathcal{B}_e \right\}, \\
\Lambda_j^h &= \left\{ \lambda \in L^2\left(\mathcal{B}\right) : \lambda|_{\mathcal{B}_e} \in P_j^d\left(\mathcal{B}_e\right) \ \forall\, \mathcal{B}_e \right\},
\end{aligned} \tag{5.84}$$

utilizes continuous and discontinuous Lagrangian type finite element interpolation functions $P_i(\mathcal{B}_e)^3$ and $P_j^d(\mathcal{B}_e)^3$, where i and j denote the considered interpolation orders. The following considerations are based on the element system of equations that can be formulated from Eq. 5.83 as

$$\underbrace{\begin{bmatrix}
\underline{\mathbb{K}}_{\varphi\varphi}^{\mathrm{e,it}} & \underline{\mathbb{K}}_{\varphi m}^{\mathrm{e,it}} & \underline{\mathbf{0}} & \underline{\mathbf{0}} \\
\underline{\mathbb{K}}_{m\varphi}^{\mathrm{e,it}} & \underline{\mathbb{K}}_{mm}^{\mathrm{e,it}} & \underline{\mathbb{K}}_{m\lambda}^{\mathrm{e,it}} & \underline{\mathbb{K}}_{mu}^{\mathrm{it}} \\
\underline{\mathbf{0}} & \underline{\mathbb{K}}_{\lambda m}^{\mathrm{e,it}} & \underline{\mathbb{K}}_{\lambda\lambda}^{\mathrm{e,it}} & \underline{\mathbf{0}} \\
\underline{\mathbf{0}} & \underline{\mathbb{K}}_{um}^{\mathrm{e,it}} & \underline{\mathbf{0}} & \underline{\mathbb{K}}_{uu}^{\mathrm{e,it}}
\end{bmatrix}}_{\underline{\mathbb{K}}^{\mathrm{e,it}}}
\underbrace{\begin{bmatrix}
\Delta\underline{\boldsymbol{d}}_{\varphi}^{\mathrm{e,it}} \\
\Delta\underline{\boldsymbol{d}}_{m}^{\mathrm{e,it}} \\
\Delta\underline{\boldsymbol{d}}_{\lambda}^{\mathrm{e,it}} \\
\Delta\underline{\boldsymbol{d}}_{u}^{\mathrm{e,it}}
\end{bmatrix}}_{\underline{\boldsymbol{d}}^{\mathrm{e,it}}}
=
\underbrace{\begin{bmatrix}
\underline{\mathbb{R}}_{\varphi}^{\mathrm{e,it}} \\
\underline{\mathbb{R}}_{m}^{\mathrm{e,it}} \\
\underline{\mathbb{R}}_{\lambda}^{\mathrm{e,it}} \\
\underline{\mathbb{R}}_{u}^{\mathrm{e,it}}
\end{bmatrix}}_{\underline{\mathbb{R}}^{\mathrm{e,it}}}, \tag{5.85}$$

where the index "it" indicates the current iteration. To reduce the size of the system of equations and thus the computational effort, it is convenient to form the Schur complement and to perform further finite element simulations in the reduced form. In solid mechanics it is a convenient and well known procedure, that has been utilized several times, cf. Korelc and Wriggers [2016] and Wriggers [2008]. The local elimination of the Lagrange multiplier is possible because $\lambda \in L^2\left(\mathcal{B}\right)^3$ holds and a discontinuous approximation of it is feasible. Applying the Schur complement to Eq. 5.85 yields the reduced system of equations

$$\underbrace{\begin{bmatrix}
\underline{\mathbb{K}}_{\varphi\varphi}^{\mathrm{e,it}} & \underline{\mathbb{K}}_{\varphi m}^{\mathrm{e,it}} & \underline{\mathbf{0}} \\
\underline{\mathbb{K}}_{m\varphi}^{\mathrm{e,it}} & \underline{\mathbb{K}}_{\mathrm{cond}}^{\mathrm{e,it}} & \underline{\mathbb{K}}_{mu}^{\mathrm{e,it}} \\
\underline{\mathbf{0}} & \underline{\mathbb{K}}_{um}^{\mathrm{e,it}} & \underline{\mathbb{K}}_{uu}^{\mathrm{e,it}}
\end{bmatrix}}_{\underline{\mathbb{K}}_{\mathrm{red}}^{\mathrm{e,it}}}
\underbrace{\begin{bmatrix}
\Delta\underline{\boldsymbol{d}}_{\varphi}^{\mathrm{e,it}} \\
\Delta\underline{\boldsymbol{d}}_{m}^{\mathrm{e,it}} \\
\Delta\underline{\boldsymbol{d}}_{u}^{\mathrm{e,it}}
\end{bmatrix}}_{\underline{\boldsymbol{d}}_{\mathrm{red}}^{\mathrm{e,it}}}
=
\underbrace{\begin{bmatrix}
\underline{\mathbb{R}}_{\varphi}^{\mathrm{e,it}} \\
\underline{\mathbb{R}}_{\mathrm{cond}}^{\mathrm{e,it}} \\
\underline{\mathbb{R}}_{u}^{\mathrm{e,it}}
\end{bmatrix}}_{\underline{\mathbb{R}}_{\mathrm{red}}^{\mathrm{e,it}}}, \tag{5.86}$$

with

$$\underline{\mathbb{R}}^{\mathrm{e,it}}_{\mathrm{cond}} = \underline{\mathbb{R}}^{\mathrm{e,it}}_{m} - \underline{\mathbb{K}}^{\mathrm{e,it}}_{m\lambda} \underbrace{\underline{\mathbb{K}}^{\mathrm{e,it}\,-1}_{\lambda\lambda} \underline{\mathbb{R}}^{\mathrm{e,it}}_{\lambda}}_{\underline{\mathrm{L}}^{\mathrm{e,it}}_{\lambda}} \quad \text{and} \quad \underline{\mathbb{K}}^{\mathrm{e,it}}_{\mathrm{cond}} = \underline{\mathbb{K}}^{\mathrm{e,it}}_{mm} - \underline{\mathbb{K}}^{\mathrm{e,it}}_{m\lambda} \underbrace{\underline{\mathbb{K}}^{\mathrm{e,it}\,-1}_{\lambda\lambda} \underline{\mathbb{K}}^{\mathrm{e,it}}_{\lambda m}}_{\underline{\mathrm{L}}^{\mathrm{e,it}}_{\lambda m}}. \tag{5.87}$$

An update of the condensed degrees of freedom for each iteration "it" can be achieved via the relation

$$\underline{\boldsymbol{d}}^{\mathrm{e,it+1}}_{\lambda} = \underline{\boldsymbol{d}}^{\mathrm{e,it}}_{\lambda} + \underline{\mathbb{L}}^{\mathrm{e,it}}_{\lambda} - \underline{\mathbb{L}}^{\mathrm{e,it}}_{\lambda m} \Delta \underline{\boldsymbol{d}}^{\mathrm{e,it}}_{m}. \tag{5.88}$$

Finally, the element matrices are available and the reduced global system of equations yields

$$\underline{\mathbb{K}}_{\mathrm{red}}\, \Delta \underline{\boldsymbol{D}}_{\mathrm{red}} \;=\; \underline{\mathbb{R}}_{\mathrm{red}}, \quad \text{with} \quad \underline{\mathbb{K}}_{\mathrm{red}} = \mathop{\mathbf{A}}_{\mathrm{e}=1}^{num_{ele}} \underline{\mathbb{K}}^{\mathrm{e,it}}_{\mathrm{red}} \quad \text{and} \quad \underline{\mathbb{R}}_{\mathrm{red}} = - \mathop{\mathbf{A}}_{\mathrm{e}=1}^{num_{ele}} \underline{\mathbb{R}}^{\mathrm{e,it}}_{\mathrm{red}} \tag{5.89}$$

as the assembled system matrix and vector. The algorithmic steps are summarized in Table 5.2.

Table 5.2: Static condensation of Lagrangian multipliers on element level.

1) $\underline{\boldsymbol{d}}^{\mathrm{e,it}} = \left[\underline{\boldsymbol{d}}^{\mathrm{e,it,T}}_{\varphi}, \underline{\boldsymbol{d}}^{\mathrm{e,it,T}}_{u}, \underline{\boldsymbol{d}}^{\mathrm{e,it,T}}_{m}, \underline{\boldsymbol{d}}^{\mathrm{e,it,T}}_{\lambda}\right]^{\mathrm{T}}$ the element unknown vector at iteration "it"
   And $\underline{\mathbb{R}}^{\mathrm{e,it}}_{m}$, $\underline{\mathbb{R}}^{\mathrm{e,it}}_{\lambda}$, $\underline{\mathbb{K}}^{\mathrm{e,it}}_{mm}$, $\underline{\mathbb{K}}^{\mathrm{e,it}}_{m\lambda}$, $\underline{\mathbb{K}}^{\mathrm{e,it}}_{\lambda m}$, $\underline{\mathbb{K}}^{\mathrm{e,it}}_{\lambda\lambda}$ the decomposed system matrices
2) Computation of Matrices
   $\underline{\mathbb{L}}^{\mathrm{e,it}}_{\lambda} := \underline{\mathbb{K}}^{\mathrm{e,it}\,-1}_{\lambda\lambda} \underline{\mathbb{R}}^{\mathrm{e,it}}_{\lambda}$, $\underline{\mathbb{L}}^{\mathrm{e,it}}_{\lambda m} := \underline{\mathbb{K}}^{\mathrm{e,it}\,-1}_{\lambda\lambda} \underline{\mathbb{K}}^{\mathrm{e,it}}_{\lambda m}$
3) Compute Condensed Right-Hand and Left-Hand Side
   $\underline{\mathbb{R}}^{\mathrm{e,it}}_{\mathrm{cond}} = \underline{\mathbb{R}}^{\mathrm{e,it}}_{m} - \underline{\mathbb{K}}^{\mathrm{e,it}}_{m\lambda}\, \underline{\mathbb{L}}^{\mathrm{e,it}}_{\lambda}$ and $\underline{\mathbb{K}}^{\mathrm{e,it}}_{\mathrm{cond}} = \underline{\mathbb{K}}^{\mathrm{e,it}}_{mm} - \underline{\mathbb{K}}^{\mathrm{e,it}}_{m\lambda}\, \underline{\mathbb{L}}^{\mathrm{e,it}}_{\lambda m}$
4) Solve $\underline{\mathbb{K}}^{\mathrm{e,it}}_{\mathrm{red}}\, \Delta \underline{\boldsymbol{d}}^{\mathrm{e,it}}_{\mathrm{red}} = \underline{\mathbb{R}}^{\mathrm{e,it}}_{\mathrm{red}}$
5) Update $\underline{\boldsymbol{d}}^{\mathrm{e,it+1}}_{\lambda} \Leftarrow \underline{\boldsymbol{d}}^{\mathrm{e,it}}_{\lambda} + \underline{\mathbb{L}}^{\mathrm{e,it}}_{\lambda} - \underline{\mathbb{L}}^{\mathrm{e,it}}_{\lambda m} \Delta \underline{\boldsymbol{d}}^{\mathrm{e,it}}_{m}$

5.7.5 Spherical coordinates

A method that restricts the magnetization vectors a priori on unit length, is provided by spherical coordinates, which have been widely used by e.g. Süss et al. [2000], Fidler and Schrefl [2000], Yi and Xu [2014], and Dornisch et al. [2018]. Not the magnetization vectors, but the polar and azimuth angles, exemplarily depicted in Fig. 5.7, are considered as primary variables, which can be collected within the array $\boldsymbol{\theta} = [\theta_1, \theta_2]^{\mathrm{T}}$. These can be used to describe the magnetization vector as $\boldsymbol{m} = [\sin\theta_1 \cos\theta_2, \sin\theta_1 \sin\theta_2, \cos\theta_1]^{\mathrm{T}}$. Following the works of Yi and Xu [2014] and Dornisch et al. [2018], the LLG equation can be expressed directly in terms of the two angles

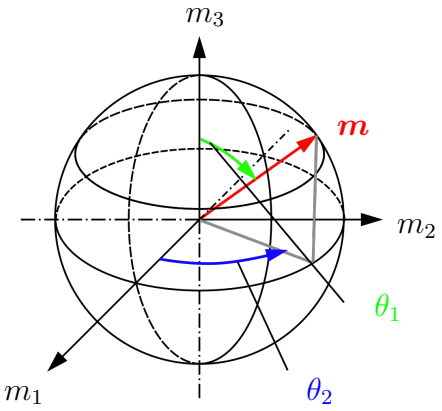

Figure 5.7: Representation of spherical coordinates defined by the polar angle $\theta_1 \in [0, \pi]$ (green) and the azimuth angle $\theta_2 \in (-\pi, \pi]$ (blue).

$$\operatorname{div} \overline{\boldsymbol{\Pi}} - \partial_{\boldsymbol{\theta}} \mathcal{H} + M_s \boldsymbol{\zeta}^{\text{ext}} - \frac{M_s}{\gamma_0} \boldsymbol{L} \cdot \dot{\boldsymbol{\theta}} = 0, \quad \text{with} \quad \boldsymbol{L} = \begin{bmatrix} \alpha & -\sin\theta_1 \\ \sin\theta_1 & \alpha \sin^2\theta_1 \end{bmatrix}, \tag{5.90}$$

where $\overline{\boldsymbol{\Pi}} = \dfrac{\partial\, \mathcal{H}}{\partial \nabla \boldsymbol{\theta}}$ is the derivative of the energy functional, the external forces $\boldsymbol{\zeta}^{\text{ext}}$, and the time derivative of the angles $\dot{\boldsymbol{\theta}}$. For a detailed derivation of Eq. 5.90 the readers are referred to Yi and Xu [2014]. The corresponding weak form can be gained by multiplication of Eq. 5.90 with the virtual angles $\delta\boldsymbol{\theta} = [\delta\theta_1, \delta\theta_2]^{\mathrm{T}}$. Further reformulation delivers the final weak form of the LLG equation in spherical coordinates as

$$G_\theta = -\int_{\mathcal{B}} \left\{ \left(\frac{M_s}{\gamma_0} \boldsymbol{L} \cdot \dot{\boldsymbol{\theta}} + \frac{\partial \mathcal{H}}{\partial \boldsymbol{\theta}} \right) \cdot \delta\boldsymbol{\theta} + \overline{\boldsymbol{\Pi}} : \nabla \delta\boldsymbol{\theta} \right\} \mathrm{dv} + \int_{\partial\mathcal{B}} \left(\overline{\boldsymbol{\Pi}} \cdot \boldsymbol{n} \right) \cdot \delta\boldsymbol{\theta}\, \mathrm{da} = 0. \tag{5.91}$$

Since external magnetic loads can be considered by applying appropriate boundary conditions of φ, $\boldsymbol{\zeta}^{\text{ext}}$ is neglected in Eq. 5.91. In contrast to the previous three sections, not the magnetization vectors are discretized, but their angles and their virtual and incremental counterparts of the spherical coordinates. However, when approximating the angles with finite elements, it is important to ensure that the definition ranges of the angles $\theta_1 \in [0, \pi]$ and $\theta_2 \in (-\pi, \pi]$ are preserved. Yi and Xu [2014] applied a standard arithmetic interpolation of the angles, what may lead to non-physical switching behavior when exceeding the limit of the definition domain, compare Fig. 5.8b)–e) for a 1D interpolation of this behavior denoted as "curly" switching. To prevent this, Dornisch et al. [2018] used a so-called circular interpolation including an arctan2[10.)] function. The corresponding, physically sound switching of a 1D element is given in Fig. 5.8f)–i). The difference within the switching behavior is clearly visible. Responsible for the curly behavior are element interpolations between values of different definition domains. This point is shown graphically in Fig. 5.9. There, the evolution of the azimuth angle at node 1 is shown. It can be seen that the arithmetic interpolation (red dots) can take unlimited values, while the circular interpolation (blue dots) alternates between $(-\pi, \pi]$. The virtual angles

[10.)] The arctan2 function is an extension of the arctan function, that appears the first time in the programming language Fortran. The function is intended to provide unambiguous values for the angle θ=arctan2(y,x), defined between the positive x-axis and the vector that is defined between the coordinate origin and a point p(x,y). It is defined on $-\pi < \theta \leq \pi$.

and their gradients are interpolated in the same way for both (arithmetic and circular) interpolations, using the virtual discrete degrees of freedom $\delta\underline{\boldsymbol{d}}^{\mathrm{I}}_{\theta}$ as

$$\delta\underline{\boldsymbol{\theta}} \approx \sum_{\mathrm{I}=1}^{\mathrm{n_{node}}} \mathbb{N}^{\mathrm{I}}\delta\underline{\boldsymbol{d}}^{\mathrm{I}}_{\theta}, \quad \nabla\delta\underline{\boldsymbol{\theta}} \approx \sum_{\mathrm{I}=1}^{\mathrm{n_{node}}} \underline{\mathbb{B}}^{\mathrm{I}}_{\theta}\delta\underline{\boldsymbol{d}}^{\mathrm{I}}_{\theta}, \quad \text{and} \quad \underline{\mathbb{B}}^{I}_{\delta\theta} = \left[\mathbb{N}^{\mathrm{I}}_{,1}\,\mathbf{1}_{\theta}, \mathbb{N}^{\mathrm{I}}_{,2}\,\mathbf{1}_{\theta}, \mathbb{N}^{\mathrm{I}}_{,3}\,\mathbf{1}_{\theta}\right]^{\mathrm{T}}, \tag{5.92}$$

with $\mathbf{1}_{\theta}$ denoting a 2×2 unit matrix. The virtual gradient yields in matrix representation $\nabla\delta\underline{\boldsymbol{\theta}} = [\theta_{1,1}, \theta_{2,1}, \theta_{1,2}, \theta_{2,2}, \theta_{1,3}, \theta_{2,3}]^{\mathrm{T}}$. The surface term is taken into account with homogeneous Neumann boundary conditions $\overline{\boldsymbol{\Pi}} \cdot \boldsymbol{n} = \mathbf{0}$ so that the residual form yields

$$\underline{\mathbb{R}}^{\mathrm{I}}_{\theta} = -\int_{\mathcal{B}^{\mathrm{e}}} \left\{ \mathbb{N}^{\mathrm{I}} \left(\frac{M_{\mathrm{s}}}{\gamma_0} \underline{\boldsymbol{L}} \cdot \underline{\dot{\boldsymbol{\theta}}} + \frac{\partial \mathcal{H}}{\partial \underline{\boldsymbol{\theta}}} \right) + (\underline{\mathbb{B}}^{\mathrm{I}}_{\delta\theta})^{\mathrm{T}}\, \overline{\boldsymbol{\Pi}} \right\} \mathrm{dv}. \tag{5.93}$$

The rates of the angles are approximated by an implicit backward Euler

$$\underline{\dot{\boldsymbol{\theta}}} \;\approx\; \sum_{\mathrm{I}=1}^{\mathrm{n_{node}}} \mathbb{N}^{\mathrm{I}}(\underline{\boldsymbol{d}}^{\mathrm{I}}_{\theta} - \underline{\boldsymbol{d}}^{\mathrm{I}}_{\theta_n})/\Delta t, \tag{5.94}$$

where $\underline{\boldsymbol{d}}^{\mathrm{I}}_{\theta}$ denotes the angle degrees of freedom at the current time step n+1 and $\underline{\boldsymbol{d}}^{\mathrm{I}}_{\theta_n}$ represents the angle degrees of freedom of the previous time step n. The time increment is represented by Δt. The difference between the arithmetic and the circular interpolation is highlighted in the following two subsections, where both methods are shortly derived and their advantages and disadvantages are discussed.

5.7.6 Arithmetic interpolation

The great benefit of the arithmetic interpolation presented by Yi and Xu [2014], is the straight forward implementation into finite element environments. Since the virtual quantities are already introduced within the section above, the remaining angles can be interpolated using the nodal degrees of freedom $\underline{\boldsymbol{d}}^{\mathrm{I}}_{\theta}$ as

$$\underline{\boldsymbol{\theta}} \approx \sum_{\mathrm{I}=1}^{\mathrm{n_{node}}} \mathbb{N}^{\mathrm{I}}\underline{\boldsymbol{d}}^{\mathrm{I}}_{\theta}, \quad \text{and} \quad \nabla\underline{\boldsymbol{\theta}} \approx \sum_{\mathrm{I}=1}^{\mathrm{n_{node}}} \underline{\mathbb{B}}^{\mathrm{I}}_{\theta}\underline{\boldsymbol{d}}^{\mathrm{I}}_{\theta}, \quad \text{with} \quad \underline{\mathbb{B}}^{\mathrm{I}}_{\theta} = \underline{\mathbb{B}}^{\mathrm{I}}_{\delta\theta}. \tag{5.95}$$

To gain a closed form system of equations, the residuals in Eq. 5.61 and Eq. 5.93 needs to be linearized. Together with the system matrices in Eq. 5.61, that have already been derived, the entire system results in

$$\underline{\mathbb{K}}^{\mathrm{IJ}}_{\theta\theta} = -\frac{\partial\, \underline{\mathbb{R}}^{\mathrm{I}}_{\theta}}{\partial\, \underline{\boldsymbol{d}}^{\mathrm{J}}_{\theta}} = \int_{\mathcal{B}^{\mathrm{e}}} \left\{ \mathbb{N}^{\mathrm{I}} \left[\frac{M_s}{\gamma_0} \frac{\partial(\underline{\boldsymbol{L}}\,\underline{\dot{\boldsymbol{\theta}}})}{\partial \underline{\boldsymbol{d}}^{\mathrm{J}}_{\theta}} + \frac{\partial \mathcal{H}}{\partial \underline{\boldsymbol{\theta}} \partial \underline{\boldsymbol{d}}^{\mathrm{J}}_{\theta}} \right] + (\underline{\mathbb{B}}^{\mathrm{I}}_{\delta\theta})^{\mathrm{T}}\, \frac{\partial \overline{\boldsymbol{\Pi}}}{\partial \underline{\boldsymbol{\theta}} \partial \underline{\boldsymbol{d}}^{\mathrm{J}}_{\theta}} \right\} \mathrm{dv},$$

$$\underline{\mathbb{K}}^{\mathrm{IJ}}_{\theta\varphi} = -\frac{\partial\, \underline{\mathbb{R}}^{\mathrm{I}}_{\theta}}{\partial\, d^{\mathrm{J}}_{\varphi}} = \int_{\mathcal{B}^{\mathrm{e}}} \mathbb{N}^{\mathrm{I}}\, (\mu_0 M_s \underline{\boldsymbol{A}})\, \underline{\mathbb{B}}^{\mathrm{J}}_{\varphi}\, \mathrm{dv},$$

$$\underline{\mathbb{K}}^{\mathrm{IJ}}_{\theta u} = -\frac{\partial\, \underline{\mathbb{R}}^{I}_{\theta}}{\partial\, \underline{\boldsymbol{d}}^{\mathrm{J}}_{u}} = -\int_{\mathcal{B}^{\mathrm{e}}} \mathbb{N}^{\mathrm{I}} \left(\frac{\partial \underline{\boldsymbol{\varepsilon}}^{0}}{\partial \underline{\boldsymbol{\theta}}} \right)^{\mathrm{T}} \underline{\mathbb{C}}\, \underline{\mathbb{B}}^{\mathrm{J}}_{u}\, \mathrm{dv}, \tag{5.96}$$

$$\underline{\mathbb{K}}^{\mathrm{IJ}}_{\varphi\theta} = -\frac{\partial\, \mathbb{R}^{\mathrm{I}}_{\varphi}}{\partial\, \underline{\boldsymbol{d}}^{\mathrm{J}}_{\theta}} = \int_{\mathcal{B}^{\mathrm{e}}} (\underline{\mathbb{B}}^{\mathrm{I}}_{\varphi})^{\mathrm{T}} \left(\mu_0 M_s \underline{\boldsymbol{A}}^{\mathrm{T}} \right) \mathbb{N}^{\mathrm{J}}\, \mathrm{dv},$$

$$\underline{\mathbb{K}}^{\mathrm{IJ}}_{u\theta} = -\frac{\partial\, \underline{\mathbb{R}}^{\mathrm{I}}_{u}}{\partial\, \underline{\boldsymbol{d}}^{\mathrm{J}}_{\theta}} = -\int_{\mathcal{B}^{\mathrm{e}}} (\underline{\mathbb{B}}^{\mathrm{I}}_{u})^{\mathrm{T}} \underline{\mathbb{C}} \left(\frac{\partial \underline{\boldsymbol{\varepsilon}}^{0}}{\partial \underline{\boldsymbol{\theta}}} \right)\, \mathbb{N}^{\mathrm{J}}\, \mathrm{dv},$$

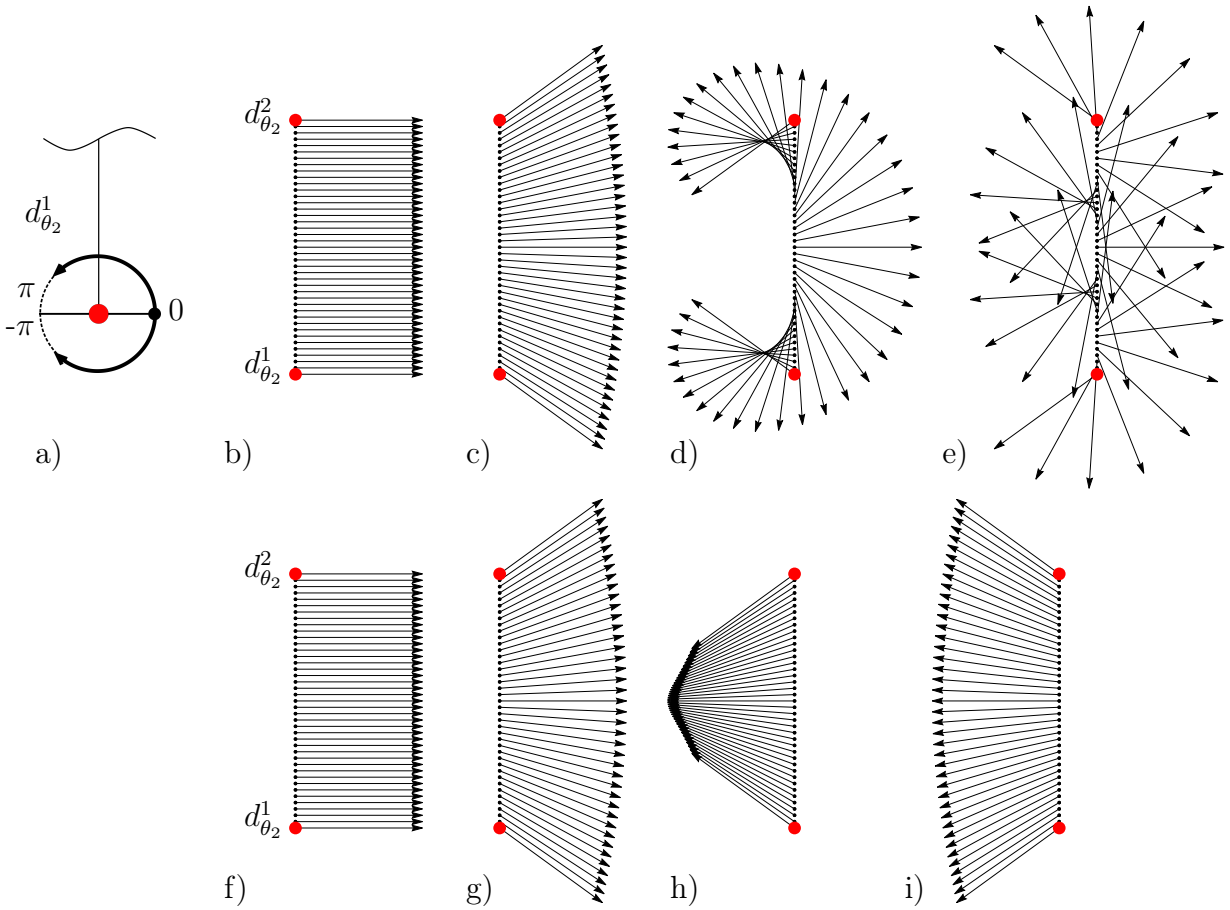

Nodal values:

$d^1_{\theta_2} = 0\pi$	$d^1_{\theta_2} = 0.2\pi$	$d^1_{\theta_2} = 1.2\pi$	$d^1_{\theta_2} = 2.8\pi$
$d^2_{\theta_2} = 0\pi$	$d^2_{\theta_2} = -0.2\pi$	$d^2_{\theta_2} = -1.2\pi$	$d^2_{\theta_2} = -2.8\pi$

Figure 5.8: The non-physical evolution of the magnetization vector using the arithmetic interpolation within the azimuthal plane as well as the physically correct interpolation using the arctan2 for the case of a one dimensional line element. a) the sign rotation convention of the nodal values exemplarily for the nodal DOF $d^1_{\theta_2}$, b)–d) the interpolation between the below given nodal values, that lead to the presented unphysical movements without further restrictions as proposed by Yi and Xu [2014], while f)–i) presents the physically correct switching behavior utilizing the arctan2 function proposed by Dornisch et al. [2018]. Taken from Reichel et al. [2022].

with $\underline{\boldsymbol{A}} = \partial_{\underline{\boldsymbol{\theta}}} \underline{\boldsymbol{m}}$ and the damping matrix

$$\underline{\mathbb{D}}^{\mathrm{IJ}}_{\theta\theta} = -\frac{\partial \underline{\mathbb{R}}^{\mathrm{I}}_{m}}{\partial \dot{\underline{\boldsymbol{d}}}^{\mathrm{J}}_{m}} = \int_{\mathcal{B}^{\mathrm{e}}} \mathbb{N}^{\mathrm{I}} \underline{\boldsymbol{L}}\, \mathbb{N}^{\mathrm{J}} \,\mathrm{dv}. \tag{5.97}$$

The structure of the system of equations can be given as

$$\begin{bmatrix} \mathbb{R}^{\mathrm{I}}_{\varphi} \\ \underline{\mathbb{R}}^{\mathrm{I}}_{\theta} \\ \underline{\mathbb{R}}^{\mathrm{I}}_{u} \end{bmatrix} = \begin{bmatrix} \mathbb{K}^{\mathrm{IJ}}_{\varphi\varphi} & \underline{\mathbb{K}}^{\mathrm{IJ}}_{\varphi\theta} & \underline{\mathbf{0}} \\ \underline{\mathbb{K}}^{\mathrm{IJ}}_{\theta\varphi} & \underline{\mathbb{K}}^{\mathrm{IJ}}_{\theta\theta} + \frac{1}{\Delta t}\underline{\mathbb{D}}^{\mathrm{IJ}}_{\theta\theta} & \underline{\mathbb{K}}^{\mathrm{IJ}}_{\theta u} \\ \underline{\mathbf{0}} & \underline{\mathbb{K}}^{\mathrm{IJ}}_{u\theta} & \underline{\mathbb{K}}^{\mathrm{IJ}}_{uu} \end{bmatrix} \begin{bmatrix} \Delta d^{\mathrm{I}}_{\varphi} \\ \Delta \underline{\boldsymbol{d}}^{\mathrm{I}}_{\theta} \\ \Delta \underline{\boldsymbol{d}}^{\mathrm{I}}_{u} \end{bmatrix}. \tag{5.98}$$

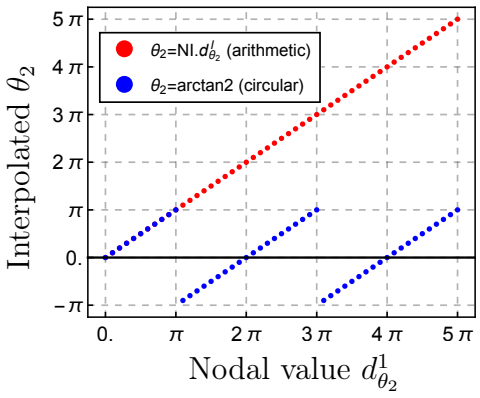

Figure 5.9: Evolution of the polar angle θ_2 arithmetically interpolated and with restrictions using the arctan2 function.

5.7.7 Circular interpolation

Compared to the arithmetic interpolation, the circular interpolation presented by Dornisch et al. [2018], is not that trivial to incorporate into a finite element environment, but guarantees for the azimuthal angle the restriction onto its definition domain. The interpolation of the angles follows the scheme

$$\theta_1 \approx \sum_{\mathrm{I}=1}^{\mathrm{n_{node}}} \mathbb{N}^{\mathrm{I}} d^{\mathrm{I}}_{\theta_1} \quad \text{and} \quad \theta_2 \approx \arctan2(c_{\theta_2}, s_{\theta_2}), \quad \text{with} \quad \underline{\boldsymbol{\theta}} = [\theta_1, \theta_2]^{\mathrm{T}}, \tag{5.99}$$

where the arguments of θ_2 are the nodal degrees of freedom $d^{\mathrm{I}}_{\theta_2}$ interpolated as

$$s_{\theta_2} \approx \sum_{\mathrm{I}=1}^{\mathrm{n_{node}}} \mathbb{N}^{\mathrm{I}} \sin(d^{\mathrm{I}}_{\theta_2}) \quad \text{and} \quad c_{\theta_2} \approx \sum_{\mathrm{I}=1}^{\mathrm{n_{node}}} \mathbb{N}^{\mathrm{I}} \cos(d^{\mathrm{I}}_{\theta_2}). \tag{5.100}$$

This leads to different representations of the gradients and time derivatives of the azimuthal angle θ_2, while the corresponding quantities of the polar angle θ_1 are unaltered compared to the arithmetic interpolation of Sec. 5.7.6. In the following the whole set of discrete values, including the polar and azimuth angels, is given for completeness. The gradients of the angles yield

$$\nabla \underline{\theta}_1 \approx \sum_{\mathrm{I}=1}^{\mathrm{n_{node}}} \underline{\mathbb{B}}^{\mathrm{I}}_{\theta_1} d^{\mathrm{I}}_{\theta_1} \quad \text{and} \quad \nabla \underline{\theta}_2 \approx \frac{1}{c^2_{\theta_2} + s^2_{\theta_2}} \left(c_{\theta_2} \, \nabla \underline{s}_{\theta_2} - s_{\theta_2} \, \nabla \underline{c}_{\theta_2} \right), \tag{5.101}$$

where the gradients of the sine and cosine are interpolated as

$$\nabla \underline{s}_{\theta_2} \approx \sum_{\mathrm{I}=1}^{\mathrm{n_{node}}} \underline{\mathbb{B}}^{\mathrm{I}}_{\theta_2} \sin(d^{\mathrm{I}}_{\theta_2}) \quad \text{and} \quad \nabla \underline{c}_{\theta_2} \approx \sum_{\mathrm{I}=1}^{\mathrm{n_{node}}} \underline{\mathbb{B}}^{\mathrm{I}}_{\theta_2} \cos(d^{\mathrm{I}}_{\theta_2}), \tag{5.102}$$

with the derivative matrices $\underline{\mathbb{B}}^{\mathrm{I}}_{\theta_1} = \underline{\mathbb{B}}^{\mathrm{I}}_{\theta_2} = [\mathbb{N}^{\mathrm{I}}_{,1}, \mathbb{N}^{\mathrm{I}}_{,2}, \mathbb{N}^{\mathrm{I}}_{,3}]^{\mathrm{T}}$. The time discrete values of the circular interpolation also increase the complexity of the whole formulation as

$$\dot{\theta}_1 \approx \sum_{\mathrm{I}=1}^{\mathrm{n_{node}}} \mathbb{N}^{\mathrm{I}} \dot{d}^{\mathrm{I}}_{\theta_1} \quad \text{and} \quad \dot{\theta}_2 \approx \frac{c_{\theta_2} \dot{c}_{\theta_2} - s_{\theta_2} \dot{s}_{\theta_2}}{c^2_{\theta_2} + s^2_{\theta_2}}, \tag{5.103}$$

with the time discrete approximations of the sine and cosine as

$$\dot{s}_{\theta_2} \approx -\sum_{\mathrm{I}=1}^{\mathrm{n_{node}}} \mathbb{N}^{\mathrm{I}} \sin(d^{\mathrm{I}}_{\theta_2}) \dot{d}^{\mathrm{I}}_{\theta_2} \quad \text{and} \quad \dot{c}_{\theta_2} \approx \sum_{\mathrm{I}=1}^{\mathrm{n_{node}}} \mathbb{N}^{\mathrm{I}} \cos(d^{\mathrm{I}}_{\theta_2}) \dot{d}^{\mathrm{I}}_{\theta_2}. \tag{5.104}$$

The structure of the coupled system is similar to the system of equations presented in Eq. 5.98.

5.8 Numerical examples

To demonstrate the advantages and disadvantages of the methods presented above, different numerical examples are carried out within this section. All discretization methods should give exactly the same results for each boundary value problem with the particular set of material parameters. For the first examples the magnetostrictive material Galfenol $Fe_{81.3}Ga_{18.7}$ is used. The material properties have been taken from Yi and Xu [2014] and are listed in Table 5.3. A damping coefficient $\alpha = 1$ is assumed if not mentioned differently. In all simulations presented below, the build-in automatic time stepping procedure of AceFEM was applied. For physically correct results the employed mesh density is of crucial importance. To guarantee a sufficiently good resolution, the size of each finite element should not fall below the characteristic length $l_c = \min(l_{\mathrm{exc}}, \delta_0) = \min\left(\sqrt{\frac{2A_{\mathrm{exc}}}{\mu_0 M_s^2}}, \sqrt{\frac{A_{\mathrm{exc}}}{K_1}}\right)$, where l_{exc} is the exchange length and δ_0 the Bloch parameter, cf. Forster et al. [2002].

Table 5.3: Material parameters of $Fe_{81.3}Ga_{18.7}$. Taken from Yi and Xu [2014] and Reichel et al. [2022].

Parameter		Value	Parameter		Value
anisotropy const.	K_1 $\frac{\mathrm{J}}{\mathrm{m}^3}$	2×10^4	anisotropy const.	K_2 $\frac{\mathrm{J}}{\mathrm{m}^3}$	-4.5×10^4
exchange const.	A_{exc} $\frac{\mathrm{J}}{\mathrm{m}}$	$\approx 10^{-11}$	sat. magnetization	M_{s} $\frac{\mathrm{A}}{\mathrm{m}}$	1.432×10^6
vac. permeability	μ_0 $\frac{\mathrm{H}}{\mathrm{m}}$	$4\pi \times 10^{-7}$	gyromagnetic ratio	γ_0 $\frac{1}{\mathrm{Ts}}$	1.76×10^{11}
elastic const.	$\mathbb{C}_{11}$ $\frac{\mathrm{N}}{\mathrm{m}^2}$	1.96×10^{11}	elastic const.	$\mathbb{C}_{12}$ $\frac{\mathrm{N}}{\mathrm{m}^2}$	1.56×10^{11}
elastic const.	$\mathbb{C}_{44}$ $\frac{\mathrm{N}}{\mathrm{m}^2}$	1.23×10^{11}	mag. strictive const.	λ_{100}	2.64×10^{-4}

5.8.1 Rotation across the poles

In this first example, the critical points, also called singularities, within the above introduced formulations are examined. For this purpose a single finite element cell with initial magnetization $\boldsymbol{m} = [1, 0, 0]^{\mathrm{T}}$ is considered (Fig. 5.10b)). The damping coefficient is set to be $\alpha = 0$ and an external magnetic field of $H_2 = 126157$ A/m is applied. Since there is no damping, the magnetization vectors will precess around the x_2-axis without ever moving in the direction of the effective field $\boldsymbol{H}^{\mathrm{eff}}$. The spherical coordinates possess singularities in the poles, i.e. at $\theta_1 = 0$ and $\theta_1 = \pi$, what corresponds to a position of the magnetization vectors of $\boldsymbol{m} = [0, 0, 1]^{\mathrm{T}}$ and $\boldsymbol{m} = [0, 0, -1]^{\mathrm{T}}$.

As soon as the magnetization vectors approach one of these poles, the simulation no longer delivers correct results (Fig.5.10a)) or it leads to direct divergence of the entire

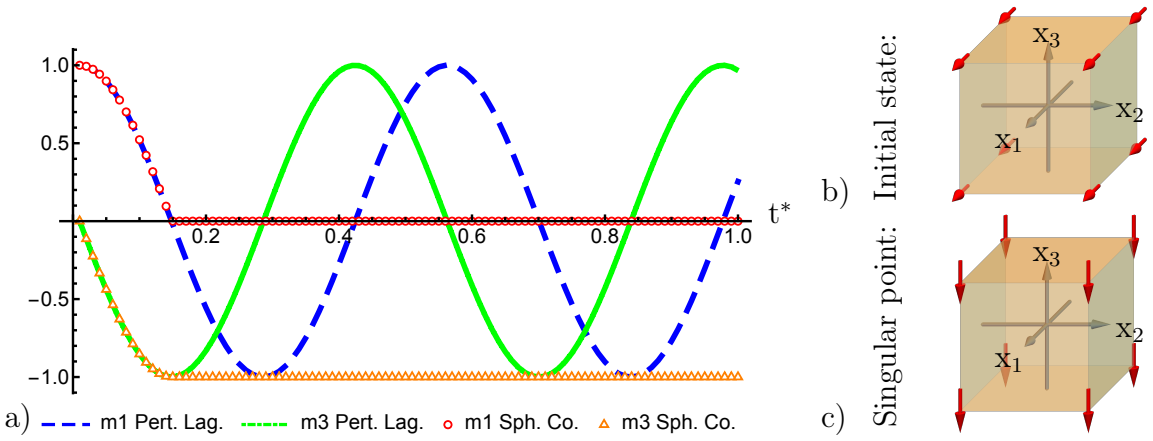

Figure 5.10: a) the evolution of the magnetization vectors for the perturbed Lagrange multiplier and the spherical coordinates. Starting from the initial configuration in b) the spherical-coordinate-based simulation fails when approaching the singularity in the south pol in c). Taken from Reichel et al. [2022].

simulation. Both, the penalty method and the Lagrange multipliers, do not suffer from any of such singularities. The evolution of their magnetization vectors match perfectly. For presentation purpose, only the evolution of the m_1 and m_3 components of the magnetization vectors, described by the perturbed Lagrange method (green and blue line) and the spherical coordinates (red circles and orange triangles), are plotted in Fig. 5.10. The component $m_2 = 0$ is neglected within this plot. The externally applied magnetic field drives the magnetization vectors, starting from the initial configuration $m_1 = 1$, first into the direction of the south pole. That corresponds to the state $m_3 = -1$ depicted in Fig. 5.10c). While the perturbed Lagrange-based simulation delivers correct results, the results based on the spherical coordinates are wrong when the singularity is reached. From this point in time, the data of the simulation no longer correspond to a result that can be physically interpreted. The results shown in Fig. 5.10 highlight that the use of spherical-coordinate-based micromagnetic simulations has to be considered at least critically.

5.8.2 Domain formation in a thin film structure

Within this example, a magnetic nanostructure of dimensions $30\times60\times3$ nm^3 is discretized with $10\times20\times1$ hexahedron elements. This results in 2772, 3234, and 3896 degrees of freedom for the spherical coordinates, the penalty method as well as the perturbed Lagrange method. The system is initialized with an energetically high, random distribution of the magnetization vectors, as shown in Fig. 5.11a) and c). Without the influence of any external source, the system is supposed to find its minimal and therefore energetically stable configuration.

This means that the considered boundary value problem is free of any external magnetic fields and mechanical loads, which corresponds to Neumann boundary conditions of $\zeta_0 = \boldsymbol{B} \cdot \boldsymbol{n} = 0$ and $\boldsymbol{t}_0 = \boldsymbol{\sigma} \cdot \boldsymbol{n} = \boldsymbol{0}$. The scalar magnetic potential is prescribed as $\varphi(\boldsymbol{x}) = 0$ at $\boldsymbol{x} = (0,0,0)^{\mathrm{T}}$. No stray field influences are considered. Starting from the random distribution, small domains begin to form. With proceeding time these areas begin to merge and eventually form the vortex structures, shown in Fig. 5.11b) and d).

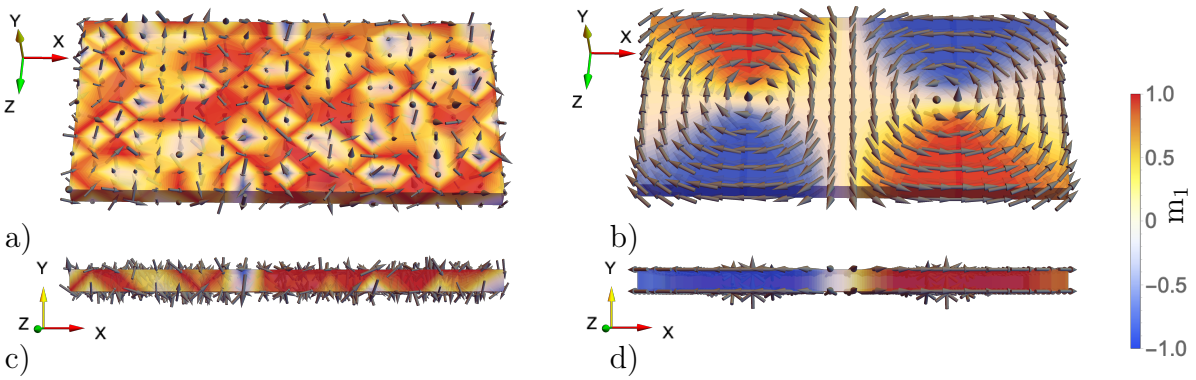

Figure 5.11: Initial random magnetization distribution in a thin film of Galfenol in a) and c) and the simulated self-equilibrium configuration in b) and d) known as diamond state. The simulations have been done using circularly interpolated angles in the spherical coordinate approach. Taken from Reichel et al. [2022].

As soon as the equilibrium is reached the simulation is terminated. After the nanostructure has reached the energetically most reasonable state, all magnetization vectors are aligned within the $x - z$ plane, except in the center of the vortex cores. The magnetization vectors point orthogonal out of the $x - z$ plane. The results of the simulations are not merely in very good agreement with each other, but match the simulated results of Yi and Xu [2014], Dornisch et al. [2018], and the experimental observations of Wachowiak et al. [2002]. To verify the agreement of the results of the outlined methods, intersection lines through the vortex cores are shown in Fig. 5.12a). The respective evolution of the considered components m_1 and m_2 is compared in Fig. 5.12b) and c), for all methods and experimental results, over the length of the drawn intersection lines with each other. The results are in very good agreement with each other as well as with the experimental results.

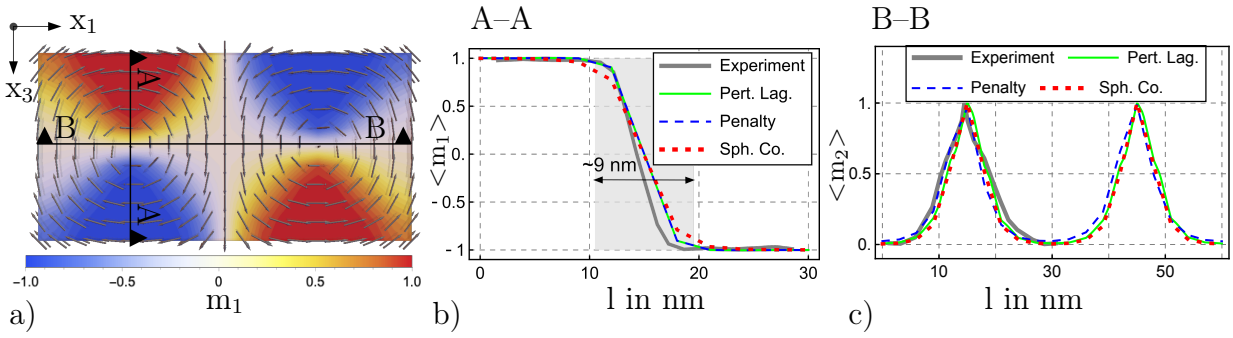

Figure 5.12: a) an energetically stable state of the Galfenol nano structure including intersection lines across the vortex cores. b) and c) the evolution of the m_1 and the m_2 component along the intersection lines. The abbreviation "Sph. Co." indicate both, arithmetical and circular interpolations. The simulated results are in good agreement with the experimental results taken from Wachowiak et al. [2002]. Taken from Reichel et al. [2022].

5.8.3 Fitting of penalty parameters

While no preparations have to be made for the simulations with the spherical coordinates and the Lagrangian methods, the penalty method requires a new fitting of the penalty parameter within each new boundary value problem. Penalties that are set too weak usually lead to a poorly fulfilled length condition, while a parameter that is defined too

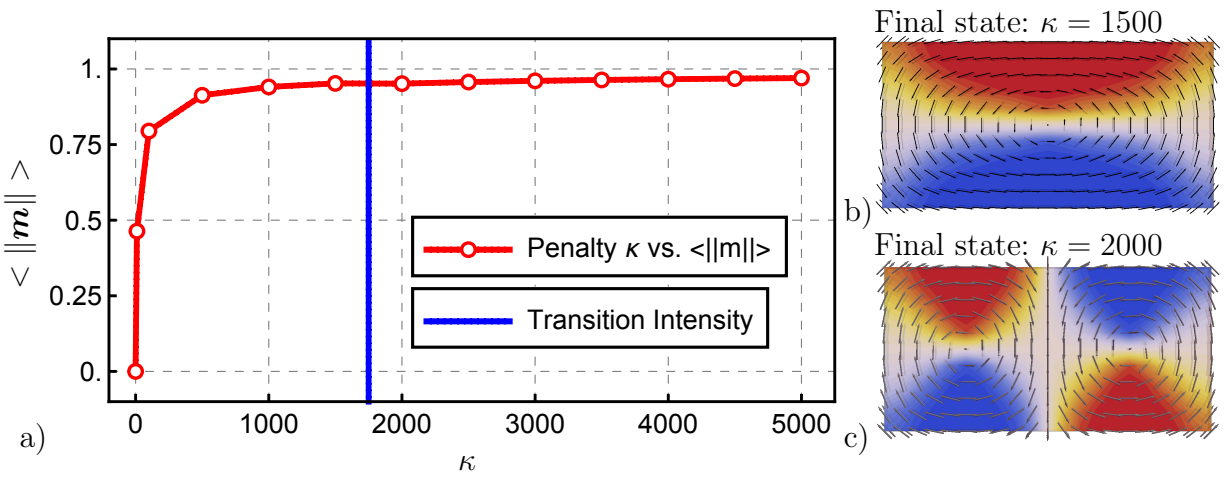

Figure 5.13: The normalized mean magnetization $< \|\boldsymbol{m}\| >$ a) in dependency of the intensity of the penalty parameter κ. The blue line indicates a change in the resulting domain patterns for weak and strong penalty parameters, denoted as transition intensity. b) the final state of a simulation with $\kappa = 1500$ is and c) a stricter penalization with $\kappa = 2000$. Taken from Reichel et al. [2022].

large can drive up the condition of the equation system. The consequences are either wrong results or unsolvable systems of equations. To highlight the influence of the penalty parameter on the results, the boundary value problem presented above is calculated for different penalty values κ. The dependency of the results is displayed in Fig. 5.13 by the penalty intensity versus the normalized mean magnetization $< \|\boldsymbol{m}\| >$. The convergence study also shows clearly that the final state splits from one vortex into two vortices for penalty parameters $\kappa > 1750$, in the context of this work denoted as transition intensity. Hence, the results presented in Fig. 5.13 stress the requirement of additional effort in advance of the simulations, to deliver correct results.

5.8.4 Different stable states

In this example, the boundary value problem from section 5.8.2 was initiated for the penalty method, the perturbed Lagrange multiplier, and the circular interpolated spherical coordinates with different uniformly distributed random initial magnetization states. From the different distribution states, the nanostructure is relaxed to its energetically stable equilibrium state. Thus, a total of three different equilibrium states can be found, each with a different number of domain formations. The possible domain formations have either one, two or three vortices, whose direction of orientation can also vary. The three states are shown in Fig. 5.14.

Each of the above discretization variants are initialized with a total of 100 different uniformly distributed initial states, subsequently then relaxed, and examined for the resulting occurrence of the domain formations shown in Fig. 5.14. The results are summarized in Table 5.4 below. As the evolution of the magnetic energy in Fig. 5.14d) shows, the single vortex state possesses the lowest energy level and is thus the most stable configuration. Both, the double and triple vortex states, are higher in terms of their energy contribution within the system. However, while the single and double vortex states are energetically very close to each other, the energy level for the triple vortex state is significantly higher. For this reason, it can be assumed that the last pattern may be a local energy minimum, that would rarely be obtained in nature. This can also be supported by the frequency of

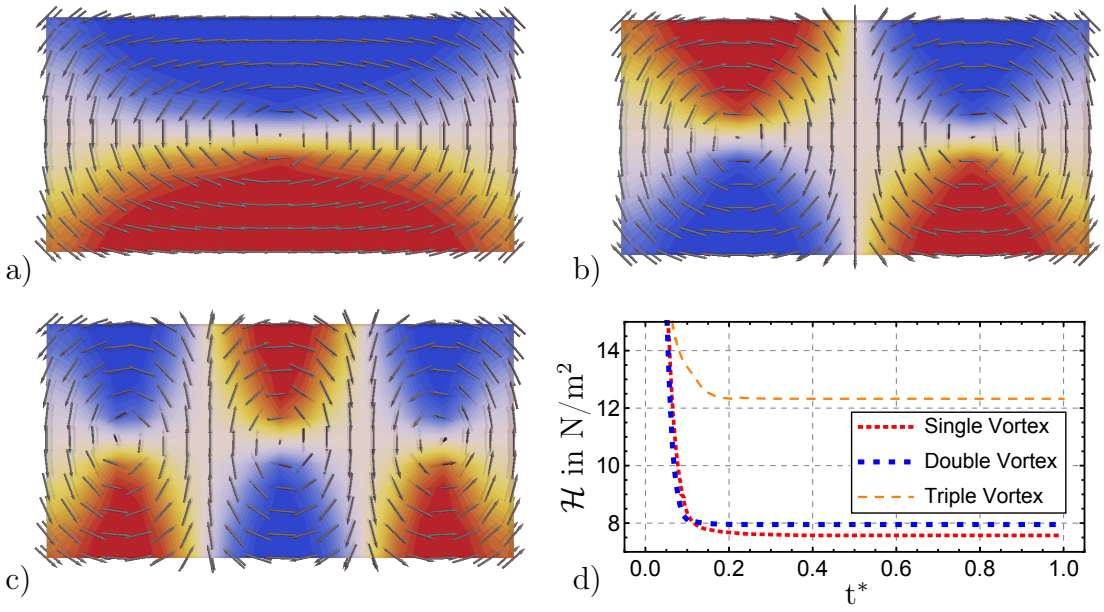

Figure 5.14: Three different self equilibrium states with a) one vortex core, b) two vortex cores, and c) three vortex cores, obtained by the circular interpolated spherical coordinates. d) the evolution of the magnetic energy of the systems over the normalized time. Taken from Reichel et al. [2022].

occurrence of the triple vortex configuration, see Table 5.4. The appearance of the triple vortex state is the least likely of all three states.

Table 5.4: Comparison of the absolute occurrence of the three different domain formations in a sample of 100 simulations per material model. Taken from Reichel et al. [2022].

Number of Vortices	Penalty	Pert. Lag.	Circ. Sph.Co.
1	28	37	44
2	64	54	48
3	8	9	8

5.8.5 Simulation of Permalloy nanodots

Magnetic nanoparticles have been a wide field of research within the last decades and offer many opportunities to study their phenomena with magnetostatic and micromagnetic simulations, cf. Cowburn et al. [1999]. The effects resulting from the shape anisortopy should be placed in the same order of magnitude as the magnetocrystalline and the magneto-elastic anisotropy, cf. Mahato et al. [2015]. In the present work, round nanoparticles are considered, as they have already been studied in other works, cf. Kuchibhotla et al. [2021], Scholz et al. [2003], and Sudsom et al. [2020]. The goal of this example is less the generation of new physical knowledge, but the comparison of the simulation results of the different methods and the elaboration of their corresponding advantages and disadvantages. For this purpose, a disk made of Permalloy with a radius of r = 120 nm and a height of h = 20 nm is considered (Fig. 5.15). To

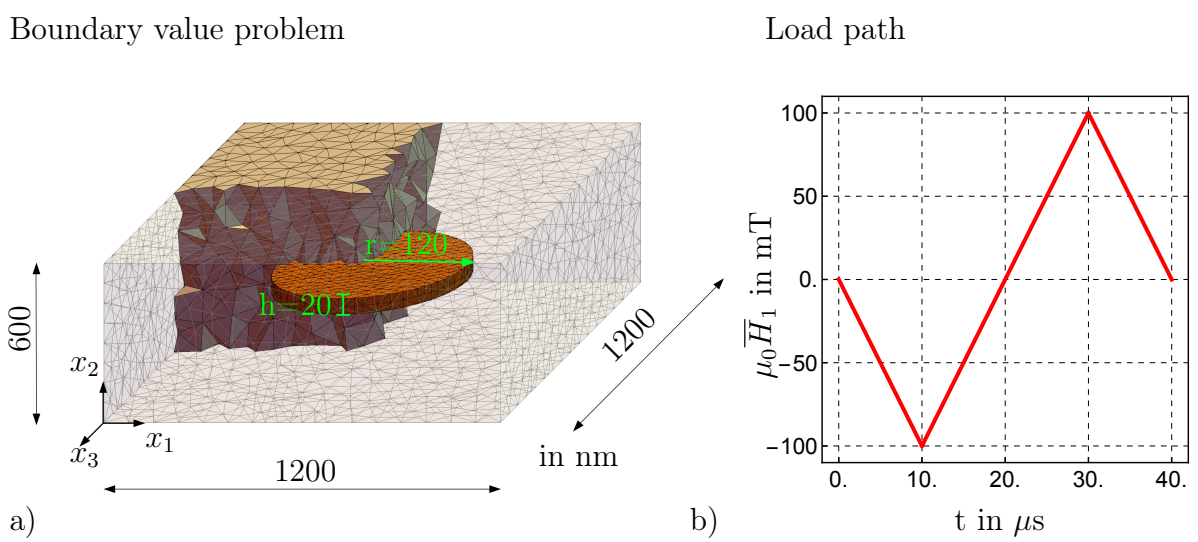

Figure 5.15: The nano disk in a) is placed within a free space matrix, to capture external influences like stray fields. The sketched free space is shrunk only for presentation purpose, but the dimensions used within the simulation correspond to the stated values. The hysteresis loops in b) are gained by treating the disk with a magnetic field $\mu_0\overline{H}_1$ following the load path. Taken from Reichel et al. [2022].

simulate the magnetostatic fields evolving around the magnetic solid, some surrounding free space has to be included into the boundary value problem and hence needs to be discretized with finite elements (Fig. 5.15). The considered free space must not be to small, since errors may occur due to the truncated boundaries. This results in wrong intensities of the magnetic fields and therefore in incorrect magnetization behavior. An estimate for the dimensions of the surrounding free space box is given in Chen and Konrad [1997]. These dimensions of the free space correspond to be at least five times larger than the magnetic solid to minimize the truncation error of the magnetic fields. For this reason, the nano disk is positioned in a free space with dimensions of 1200 nm ×600 nm ×1200 nm. All subsequent simulations consider a homogeneous support of the mechanical properties on the boundary of the magnetic solid $\partial\mathcal{B}_u$. The discretization of the boundary value problem considers $\sim 80,000$ linear tetrahedron elements, that result in $\sim 50,000$, $\sim 57,000$, and $\sim 65,000$ degrees of freedom for the simulations based on the spherical coordinates, the penalty method, and the perturbed Lagrange multiplier. The number of degrees of freedom in the projection method is similar to the penalty method. The material parameters can be taken from Table 5.5.

Table 5.5: Material parameters of Permalloy ($Ni_{80}Fe_{20}$). Taken from Kuchibhotla et al. [2021], Miehe and Ethiraj [2012], and Reichel et al. [2022].

Parameter		Value	Parameter		Value
exchange const.	A_e $\frac{J}{m}$	1.3×10^{-11}	sat. magnetization	M_s $\frac{A}{m}$	8×10^5
vac. permeability	μ_0 $\frac{H}{m}$	$4\pi \times 10^{-7}$	anisotropy const.	K_1 $\frac{J}{m^3}$	0
elastic const.	$\mathbb{C}_{11}$ $\frac{N}{m^2}$	1.27×10^{11}	elastic const.	$\mathbb{C}_{12}$ $\frac{N}{m^2}$	0.75×10^{11}
elastic const.	$\mathbb{C}_{44}$ $\frac{N}{m^2}$	0.52×10^{11}	mag. strictive const.	λ_{100}	7.0×10^{-6}

The damping parameter of Permalloy is usually around $\alpha = 0.008$. In order to reproduce the quasi-static states and replicate the switching of the magnetization vectors, a slightly higher damping parameter of $\alpha = 0.5$ is chosen. This practice, which is quite common in micromagnetic simulations, does not lead to large deviations in the results, cf. Sudsom et al. [2020] and Kuchibhotla et al. [2021].

5.8.6 Vortex state

In analogy to Section 5.8.2, the nanostructure is initialized with a randomized magnetization distribution, as shown in Fig. 5.16a). The distinct and competing energy contributions eventually lead, without externally applied magnetic fields or mechanical loads, to a vortex whose core is located in the center of the disk. The relaxed nanodot, generated with the penalty method, is shown in Fig. 5.16b). The magnetization in the vortex core points out of plane orthogonal to the disk. The stable states of the other methods barely differ from the one shown in Fig. 5.16b). This vortex state marks the ground state for the subsequent simulations.

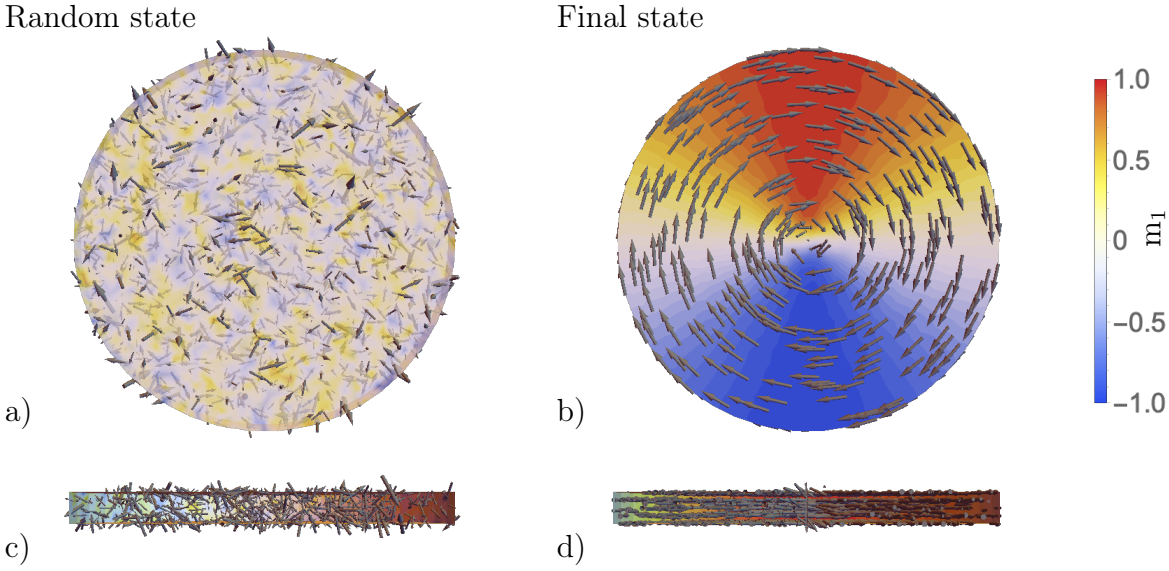

Figure 5.16: a) and c) the initial random magnetization distribution as well as b) and d) the corresponding simulated self-equilibrium configuration in a nano disk of Permalloy obtained by utilizing the penalty method. Taken from Reichel et al. [2022].

5.8.7 Comments on the projection method

The projection method is the simplest way to restrict the magnetization vectors onto the unit length. However, it has several drawbacks regarding accuracy of the simulation results especially when simulations in the dynamic regime, e.g. analysis of hysteresis, are considered. Within this section, these drawbacks are highlighted utilizing the boundary value problem outlined in Fig. 5.15. A source of error results from non-matching residuals. The meaning of and the reason for this is explained in the following. Since Newton-like methods are applied to solve the system of equations, the residual norm decreases within each iteration step, as depicted in Tab. 5.6 (iteration table). A time step is considered to be converged if the norm of the residual equals 10^{-10}. Each nodal degree of freedom $\boldsymbol{d}_m^{\mathrm{I}}$

resulting from such a time step is projected back onto the unit sphere as $\boldsymbol{d}_m^{\mathrm{I}} \leftarrow \boldsymbol{d}_m^{\mathrm{I}}/\|\boldsymbol{d}_m^{\mathrm{I}}\|$ within the next algorithmic step, presented in Tab. 5.6 (projection table). If these projected degrees of freedom are inserted into the previously calculated residual (Tab. 5.6 (iteration table)), the norm is significantly different to zero (Tab. 5.6 (projection table)). This means that the projected degrees of freedom do not correspond to the actual solution and, from a numerical point of view, the simulation results must be critically questioned.

Table 5.6: The cause of miss-match of the residuals for one time increment. The residual norm within the iterative procedure decreases until 10^{-10} is reached. Subsequently, the DOFs are projected onto the unit sphere. Re-inserting the projected DOFs into the residual shows that they do not match the real solution and the residual is non-zero. Taken from Reichel et al. [2022].

Iteration table $\Longrightarrow$ Projection table

Iteration	Residual norm
1	1.085
2	0.705×10^{-3}
3	2.249×10^{-7}
4	1.713×10^{-14}

Project DOF onto unit sphere:
$\boldsymbol{d}_m^{\mathrm{I}} \leftarrow \boldsymbol{d}_m^{\mathrm{I}}/\|\boldsymbol{d}_m^{\mathrm{I}}\|$

Insert projected DOF in residuum:
Residual norm: $0.890 \neq 0$

Furthermore, Lewis and Nigam [2003] show that a required divergence-free magnetic induction cannot be divergence-free after a projection step. This means that the simulated magnetic induction may have sources and sinks, which do not exist. Hence, a general problem of this method is the reliability of the results. The projection method strongly depends on the chosen time step size. Too large time steps end in wrong results, while very small time steps give better results, but lead to a drastic increase of the computational time. This is also the reason why no adaptive time stepping procedure is used for this method, as it could lead to poorly chosen time steps. The nano disk is again initiated with an energetically high random distribution of the magnetization vectors and subsequently relaxes to its energetically more favorable self-equilibrium state. This relaxation procedure is simulated using different time increments of 10^{-3} ns and 10^{-4} ns. Both vortices presented in Fig. 5.17 should correspond to an in-plane vortex configuration with an out-of-plane component in the center of the vortex core, as already shown in Fig. 5.12.

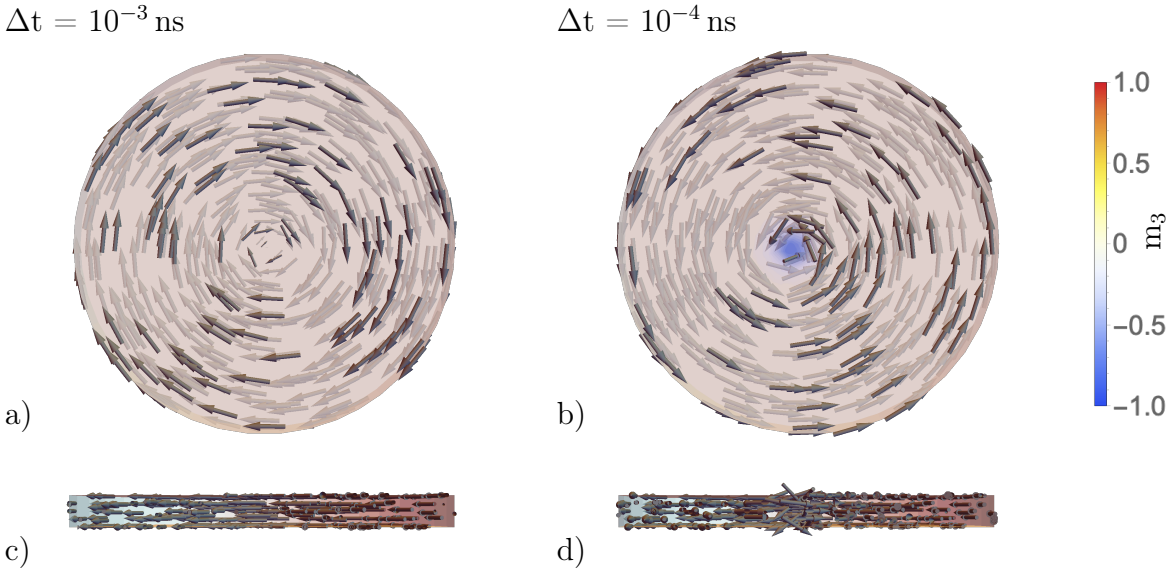

Figure 5.17: Top view and cut through the vortex configuration for the time increment $\Delta t = 10^{-3}$ ns in a) and c) as well as for the time increment $\Delta t = 10^{-4}$ ns in b) and d). Taken from Reichel et al. [2022].

Such an out-of-plane component within the vortex core is a consequence of the constantly enforced magnitude of the magnetization vectors, cf. Yi and Xu [2014]. If this constraint is not constantly observed, as is the case with the projection method, the vortex core can easily lead to points of near-zero out of plane magnetization (Fig. 5.17a)), which is physically incorrect for magnetic materials. To obtain better simulation results this problem can be treated with smaller time increments, leading to a more pronounced out-of-plane magnetization within the vortex core (Fig. 5.17b)). In this work the hysteresis properties of the nano disk using the projection method are not analyzed.

5.8.8 Hysteresis properties

Starting from the ground state shown in Fig. 5.16b), a magnetic field $\mu_0 \overline{H}_1 = 0.1\,\mathrm{T}$ is applied via a magnetic scalar potential, that is prescribed on the boundary of the free space domain. The field intensity follows the load path given in Fig. 5.15b). The hystereses are generated by a dynamic analysis of the magnetic material. This implies that the variation of the magnetic field strength and the convergence of the simulation take place

simultaneously, cf. Insinga et al. [2020]. Each time step is assumed to be converged when the residual approaches zero, in this case 10^{-10}. For circular nanoparticles, the switching process usually involves the formation, motion, and decay of vortex structures. They are formed as soon as the field strength of the external field falls below the so-called nucleation field (H_n). If the vortex has already been formed and the external magnetic field increases again, the vortex core moves from its (without external fields mostly central) position to the edge of the nanodot. When the external field has exceeded a critical field strength (H_a), the vortex annihilates and the nanodot is almost completely aligned parallel to the external field. Further explanations of the magnetization reversal mechanism are given in Cowburn et al. [1999] and Kuchibhotla et al. [2021]. Hence, the behavior of the nanoparticle considered here is already well known and can therefore be used as a comparative object for the different methods.

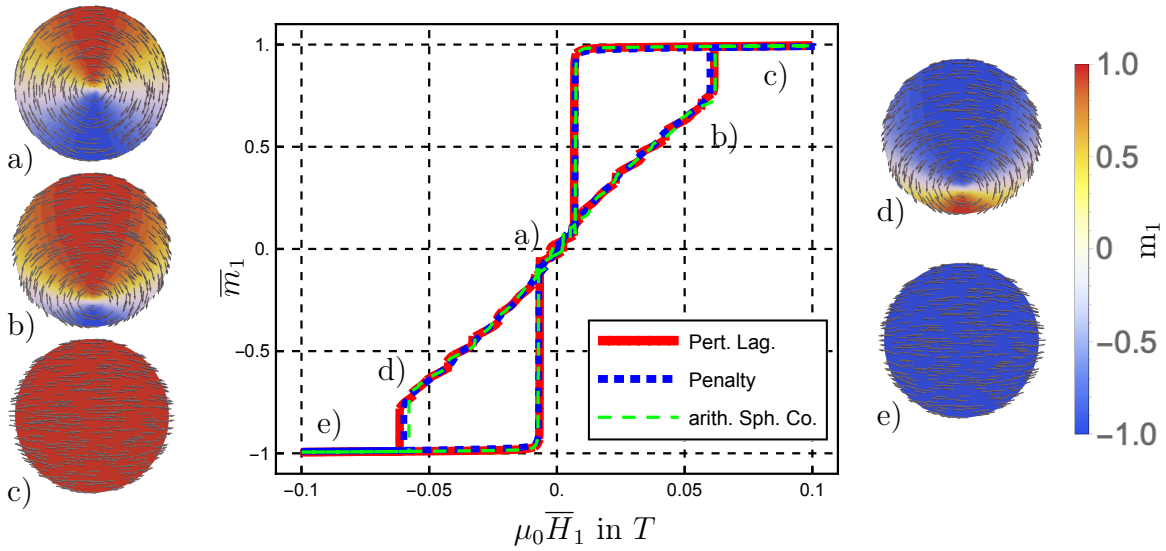

Figure 5.18: The hysteresis loops of the nano disk, obtained from different discretization methods framed by their most characteristic magnetization states a)–e). These magnetization states correspond to the points indicated within the loops. Taken from Reichel et al. [2022].

The hystereses of the different methods are depicted in Fig. 5.18 and are in very good agreement with each other as well as with the results stated in Kuchibhotla et al. [2021]. The corresponding distributions of the magnetization vectors are assigned to the states a)-e) along the hystereses in Fig. 5.18. They are calculated using the perturbed Lagrangian method. Starting from the initial vortex state (Fig. 5.18a)) with an increasing external magnetic field, the vortex core is displaced from the center (Fig. 5.18b)) until the critical field strength H_a is reached. Subsequently the vortex decays abruptly and the magnetization vectors align parallel to the external field (Fig. 5.18c)). The magnetization remains aligned parallel to the external magnetic field until the nucleation field strength H_n is reached. By falling below H_n the nano disk returns to the vortex state. Decreasing the external magnetic field further leads to the renewed decay of the vortex (Fig. 5.18d)), analogous to the steps just described. As a result, the magnetization vectors align parallel to the external magnetic field (Fig. 5.18e)). The final state of the magnetization distribution corresponds to the initial state (Fig. 5.18a)).

5.8.9 Coordinate invariant issue in the arithmetic spherical coordinate approach

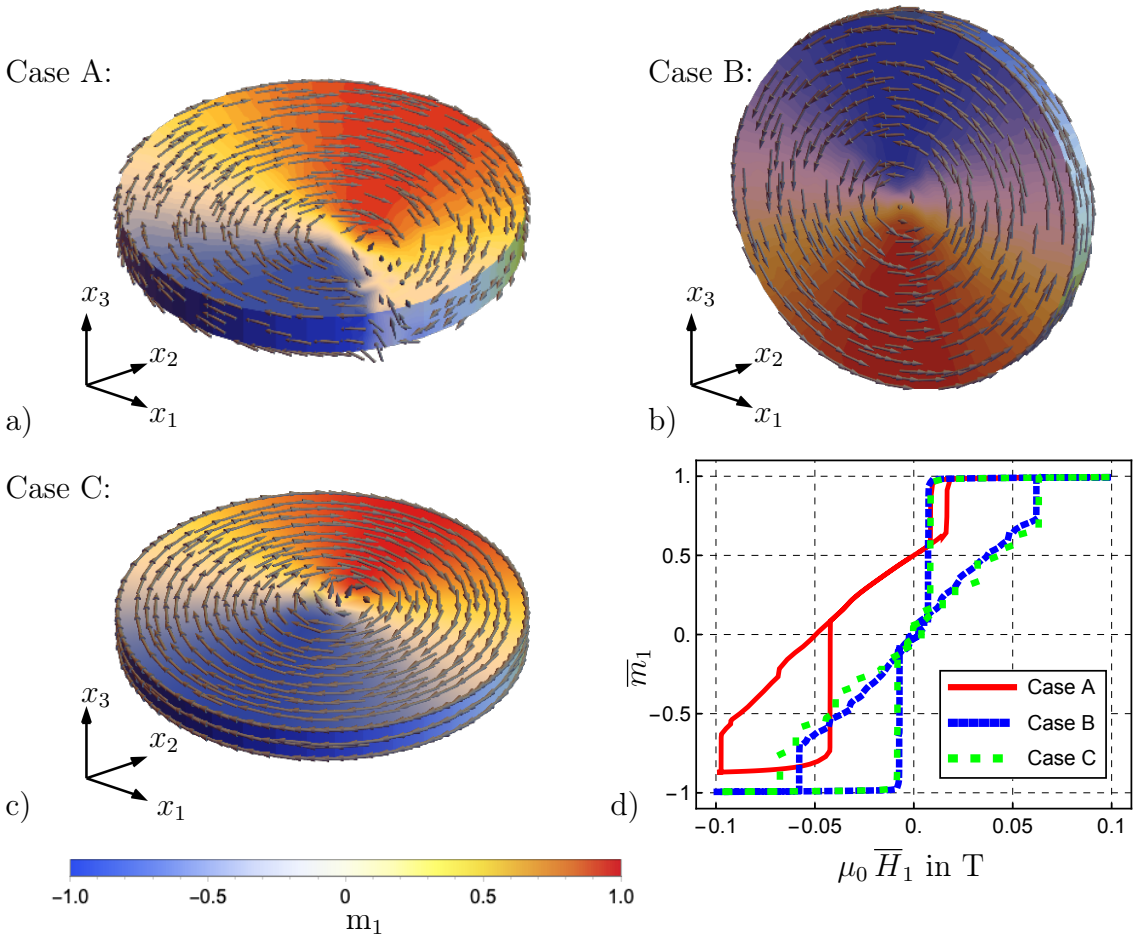

Figure 5.19: A nano disk with a) non-physical vortex configuration within the x_1-x_2 plane, b) physical vortex configuration within the x_1-x_3 plane, c) physical vortex configuration within the x_1-x_2 plane, and d) the corresponding hysteresis loops. Taken from Reichel et al. [2022].

Coordinate invariant material models are important, since they deliver always the same simulation results regardless of spatial orientations of the considered boundary value problem. Depending on the chosen orientation of the coordinate system, arithmetically interpolated spherical coordinates can lead to physically incorrect representations of the magnetization vectors and their reversal, cf. Dornisch et al. [2018]. To highlight this difficulty in more detail, the boundary value problem from Fig. 5.15 is simulated again using its original orientation as well as an orientation rotated by 90° around the x_1-axis. Both, the arithmetic and circular interpolated spherical coordinates, are applied. In total, the following four cases are considered:

Case A: Arithmetic interpolation of disk within x_1-x_2 plane,

Case B: Arithmetic interpolation of disk within x_1-x_3 plane,

Case C: Circular interpolation of disk within x_1-x_2 plane, and

Case D: Circular interpolation of disk within x_1-x_3 plane.

All four cases are initialized with an energetically high random magnetization distribution and subsequently relaxed into their respective energetically most stable states. This already reveals fundamental differences between both discretizations. All vortex configurations should correspond to the pattern in Fig. 5.16b). However, the pattern resulting from Case A does not match Fig. 5.16b). The vortex resulting from Case A (Fig. 5.19a)) shows a clear deviation due to a non-closed vortex, which corresponds to a non-physical behavior. This non-physical behavior can be explained by the fact that the azimuth angle is not limited to its definition range $\theta_2 \in (-\pi, \pi]$ and exceeds this at the non-closed part of the vortex. The interpolation of the values on the definition range with those outside the definition range ultimately creates this physical anomaly. However, if the nano disk is rotated by 90°, as shown in Case B (Fig. 5.19b)), a closed vortex can form. This behavior can be explained by the circumstance that the distribution of the magnetization vectors arising from this orientation is mainly expressed by the change of the polar angle and the azimuthal angle is of secondary importance. To generate a closed and physically correct vortex within the x_1-x_2 plane using spherical coordinates, the circular interpolated spherical coordinates are applied in Case C. The vortex of Case C is shown in Fig. 5.19c). Here the function values of the azimuth angle are always restricted by means of the arctan2 function to the corresponding definition range, so that an unambiguous assignment of the angle to the position of the vector within the Cartesian coordinates can take place. The distribution of the magnetization vectors from Case D corresponds to that from Case B. Starting from these self-equilibrium states, Cases A-C are subjected to an external magnetic field $\mu_0 \overline{H}_1$ that follows in intensity the loadpath given in Fig. 5.15b). This is used to calculate the corresponding hysteresis loops, which are superimposed in Fig. 5.19d). Between the evaluated hysteresis loops, the hysteresis that primarily attracts attention is the one that can be assigned to Case A. While the different orientations of the magnetization within the vortex equilibrium state typically cancel each other out, as it is present in equal proportions in opposite directions, e.g. in Case A there is a significantly larger amount of positive m_1 oriented magnetization compared to negative m_1 oriented magnetization (Fig. 5.19a)). Thus, the computation of the volume average shows a non-zero remanent behavior of the disk as shown in Fig. 5.19d) by means of the red hysteresis that exhibits an incorrect prediction of the magnetization behavior. This problem can be solved by the rotation of the nano disk considered in Case B, resulting in the blue dashed hysteresis presented in Fig. 5.19d). The hysteresis agrees very well with the hysteresis resulting from Case C depicted as green dots in Fig. 5.19d). However, it should be mentioned that restricting the azimuth angle to the definition range for magnetization motions near the poles, due to steeper tangents, has an overall negative effect on the convergence behavior of the simulation. Significantly smaller time increments are required so that adaptive time-stepping controls frequently need to be refined. For this reason, the calculation of the hysteresis loop for Case D has been omitted. Based on these observations, the use of spherical coordinates is not recommended for the investigation of complex magnetization processes, where a rotation of the magnetization vectors into the poles cannot be excluded.

5.8.10 Mechanical influences on hysteretic properties

Besides the ferromagnetic switching discussed above, ferroelastic switching is investigated. External mechanical influences can have a huge effect on the magnetic properties of materials and the numerical models presented above must be able to provide the same results

with this additional influence. This ability to analyze other properties of magnetic solids distinguishes the phase-field models presented here from classical micromagnetic models, which are usually limited to magnetic effects. The boundary value problem shown in Fig. 5.15 remains unchanged in terms of dimensions and applied external magnetic fields. However, the shell surface of the disk is uniformly stretched by a displacement of 1 nm acting normal on the surface, as presented in Fig. 5.20a). Mechanical coupling can influence the magnetization vectors such that the switching behavior changes. Due to the tension of the nano disk, differences in the hysteresis property compared to the mechanically unstressed nano disk can be observed. The mechanically unstressed nano disk has no remanent behavior, while the mechanically stressed nano disk shows remanence (Fig. 5.20b)). The hysteresis of the mechanically unstressed nano disk is taken from Fig. 5.18 and is simulated using the penalty method. However, it is used here only for a direct comparison of the different effects of the boundary conditions on the hysteresis behavior. The hysteresis behavior of the mechanically stressed nano disk is simulated using the perturbed Lagrange method, the penalty method as well as the circularly interpolated spherical coordinates. The corresponding simulation results are presented in terms of hysteresis loops in Fig. 5.20b) being in very good agreement with each other.

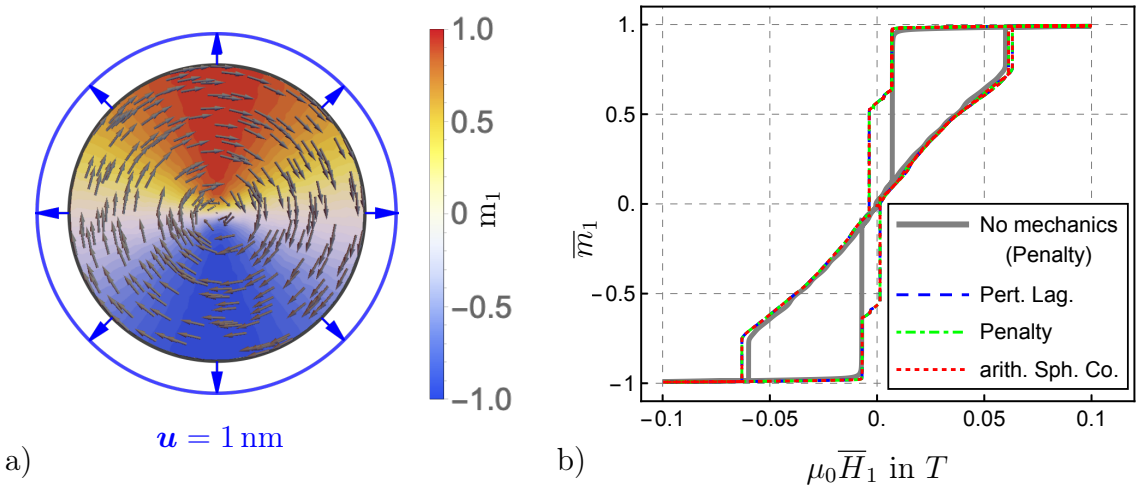

Figure 5.20: a) the disk in its vortex configuration is subject to displacements applied on the shell surface. b) the hysteresis loops of the mechanically stressed nano disk are compared against each other and the loop obtained from the unstressed nano disk. Taken from Reichel et al. [2022].

5.8.11 Ni-thin film under magnetic and mechanical loads

In the following two sections, the functionality of the condensed Lagrange multiplier method is demonstrated. This includes the preservation of the unit length during the simulation, the physically correct representation of micromagnetic-mechanically coupled effects, and the computational performance compared to the non-condensed Lagrange method. Hence, a magnetostrictive material such as Nickel (Ni) is investigated at this point. The focus lies on the Villari or also called inverse magnetostrictive effect, cf. Coey [2010]. While magnetostriction describes the change of the shape of the magnet under varying magnetization, inverse magnetostriction describes the change of the magnetic properties under the influence of shape-changing effects, such as external stresses or strains acting on the magnetic solid.

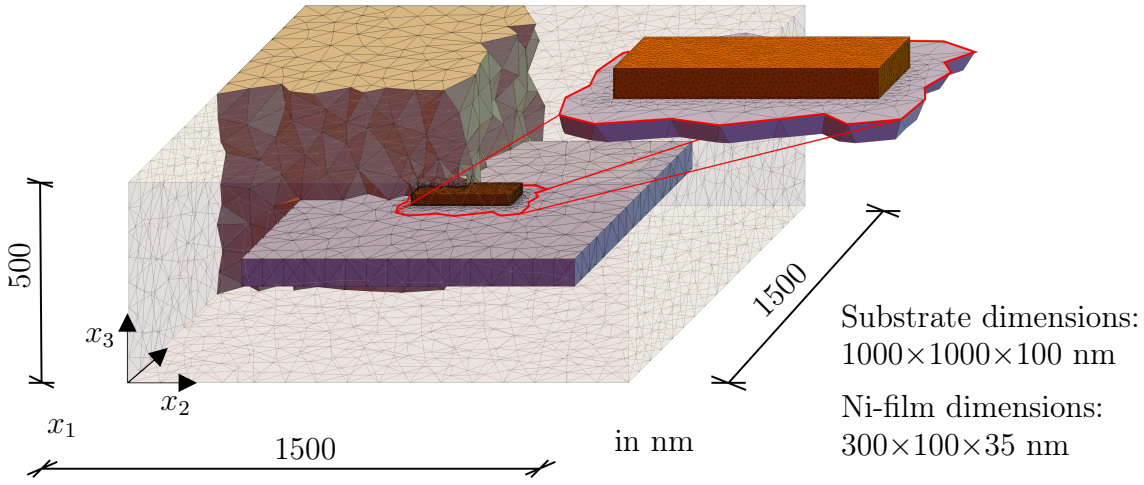

Figure 5.21: The Ni nano structure and the carrier substrate surrounded by a free space matrix to capture evolving external influences like stray fields. Taken from Reichel et al. [2023b].

This phenomenon has been observed in nanowires by Muscas et al. [2021], among others, who compared both experimental and numerical results. However, the numerical simulations performed are purely micromagnetic in nature. In contrast, a fully micromagnetic-mechanically coupled material model is used by Liang et al. [2014] to correctly incorporate the influence of the Villari effect. In a comparison Liang et al. [2014] show that their numerical results agree well with the experimental results of Bur et al. [2011]. Hence, the boundary value problem described in Liang et al. [2014] is adopted within this work to verify the method presented above, i.e. the magnetic Ni nano structure with the dimensions 300×100×35 nm is fixed on top of a pure mechanical carrier substrate with dimensions 1000×1000×100 nm. To consider the evolving stray fields surrounding the magnetic mater, some of the surrounding space is discretized with finite elements. A rule of thumb is that the outer space area to be discretized should be at least five times larger than the actual inclusion, cf. Chen and Konrad [1997]. The Lagrange multiplier is approximated using constant interpolation functions, while the other degrees of freedom are linearly interpolated. That corresponds to 61,099 finite elements and 49,099 degrees of freedom. A sketch of the boundary value problem is given in Fig. 5.21, while the corresponding material parameters can be taken from Tab. 5.7. The Gilbert damping parameter is set to be $\alpha = 0.5$, cf. Liang et al. [2014].

Table 5.7: Material parameters of Nickel. Taken from LIANG ET AL. [2014] and REICHEL ET AL. [2023b].

Parameter		Value	Parameter		Value
exchange const.	$A_e \ \frac{\mathrm{J}}{\mathrm{m}}$	$1.05 \cdot 10^{-11}$	sat. magnetization	$M_s \ \frac{\mathrm{A}}{\mathrm{m}}$	$4.8 \cdot 10^{5}$
elastic const.	$\mathbb{C}_{11} \ \frac{\mathrm{N}}{\mathrm{m}^2}$	$2.5 \cdot 10^{11}$	anisotropy const.	$K_1 \ \frac{\mathrm{J}}{\mathrm{m}^3}$	0
elastic const.	$\mathbb{C}_{12} \ \frac{\mathrm{N}}{\mathrm{m}^2}$	$1.6 \cdot 10^{11}$	mag. strictive const.	λ_{100}	$-46 \cdot 10^{-6}$
elastic const.	$\mathbb{C}_{44} \ \frac{\mathrm{N}}{\mathrm{m}^2}$	$1.18 \cdot 10^{11}$	mag. strictive const.	λ_{111}	$-24 \cdot 10^{-6}$

To analyze the influence of mechanical strains on the Ni structure mechanical boundary conditions are applied on the surface of the substrate such that the relative strain $\mu\varepsilon = \varepsilon \times 10^{-6} = (\varepsilon_{22} - \varepsilon_{11})$ within the substrate yields -1210$\mu\varepsilon$, 0$\mu\varepsilon$, and 1060$\mu\varepsilon$, where $\varepsilon_{11} = -\nu\varepsilon_{22}$ and $\nu = 0.2$. This implies the homogeneous support of the substrate is prescribed as $\mathrm{u_x}(\mathrm{x} = -500\mathrm{nm}) = \mathrm{u_y}(\mathrm{y} = -500\mathrm{nm}) = \mathrm{u_z}(\mathrm{z} = -100\mathrm{nm}) = 0\mathrm{nm}$ and the mechanical loads correspond to the values given in Tab. 5.8, cf. LIANG ET AL. [2014].

Table 5.8: Mechanical boundary conditions applied on the substrate. Taken from REICHEL ET AL. [2023b].

	-1210$\mu\varepsilon$	0$\mu\varepsilon$	1060$\mu\varepsilon$
$\mathrm{u_x}(\mathrm{x} = 500\mathrm{nm})$ in nm	0.21	-	0.06
$\mathrm{u_y}(\mathrm{y} = 500\mathrm{nm})$ in nm	-1.00	-	1.00

To obtain hysteresis loops the Ni film is subjected to an alternating external magnetic field following the load path shown in Fig. 5.22a) with a maximal field intensity of $\mu_0\overline{\boldsymbol{H}} = [0.1, 0, 0]^{\mathrm{T}}\mathrm{T}$. Initially, the mechanically unstressed nano structure is subjected to the alternating field which generates a hysteresis, see Fig. 5.22b). Subsequently, the carrier substrate is exposed to the mechanical displacements so that the Ni nanostructure also deforms. These deformed states are treated with the alternating magnetic field. The corresponding hystereses are shown along with the hysteresis of the undeformed structure in Fig. 5.22b) and indicate good agreement with the results from literature, cf. LIANG ET AL. [2014]. The influence of the mechanical loads on the hysteresis behavior of the material can be clearly seen in the hystereses shown in Fig. 5.22b). Negative relative strains produce a much more pronounced coercivity compared to an undistorted structure, while positive strains have the opposite effect. The origin of this behavior lies in the so-called Villari effect also known as inverse magnetostriction, cf. COEY [2010].

5.8.12 Computational time saving by condensation

The Lagrange multipliers considered here do not necessarily require continuity across element boundaries, thus these degrees of freedom can be approximated both continuously or discontinuously. The discontinuity of the degrees of freedom ultimately allows their condensation. Classical Lagrange multipliers can lead to numerical difficulties due to zero entries on the main diagonal of the system matrix. In this work, the Lagrange multiplier is extended by a quadratic perturbation term $-\frac{\lambda^2}{2\kappa}$, so that the main diagonal of the system

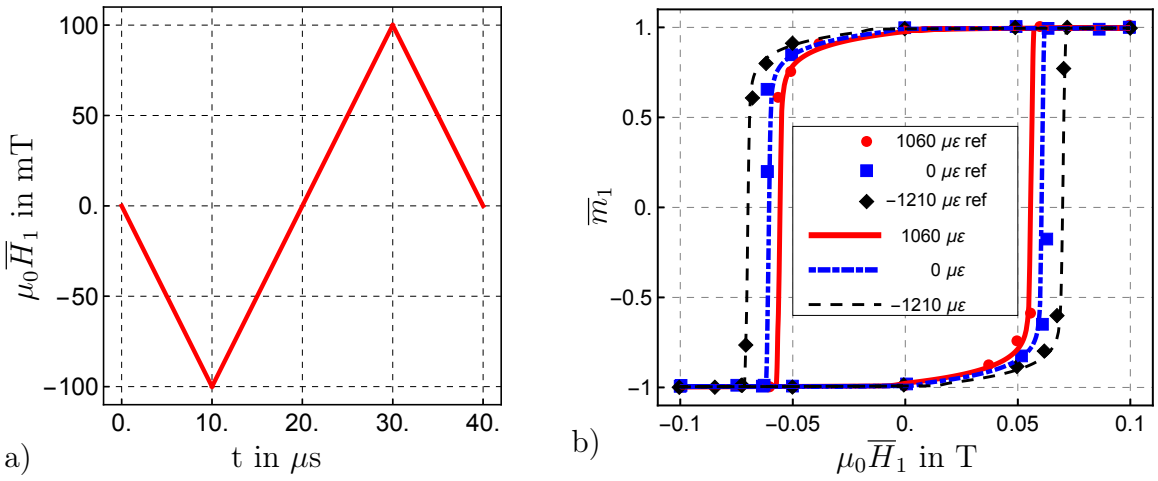

Figure 5.22: The load path shown in a) defines the intensity of the externally applied magnetic field governing the hystereses loops presented in b). The different characteristics of the hystereses arise from varying induced strain states within the nanostructure. Reference solution, see Liang et al. [2014]. Taken from Reichel et al. [2023b].

matrix contains non-zero entries. Thus, numerical difficulties in the solution process can be circumvented, cf. Wriggers [2008] and Carey and Oden [1982]. In addition, the number of constraints must be at least less than or equal to the number of quantities to be constrained, i.e. number of $\boldsymbol{d}_\lambda \leq \boldsymbol{d}_\mathrm{m}$. Hence, different interpolation orders for the Lagrange multiplier are examined in the following for their performance. The considered discretization of the individual degrees of freedom $\boldsymbol{\Xi} := \{\varphi, \underline{\boldsymbol{m}}, \underline{\boldsymbol{u}}\}$ and λ are restricted in this work to tetrahedral elements, denoted as T. The interpolation order of the tetrahedral elements is indicated as a subscript index as T_i with i=0,1,2 for constant, linear, and quadratic polynomials. The degrees of freedom $\boldsymbol{\Xi}$ are be interpolated using linear and quadratic interpolation functions and therefore denoted as T_1^{Ξ} or T_2^{Ξ}. Since the here considered Lagrange multiplier can be interpolated continuously, discontinuously or discontinuously with condensation, additional subscript indices indicate their continuity as $T^{\lambda}_{\mathrm{i,c}}$, $T^{\lambda}_{\mathrm{i,d}}$ or $T^{\lambda}_{\mathrm{i,d,cond}}$.

Table 5.9: Relative simulation times of all schemes w.r.t the required time of the condensed schemes, i.e. simulation time/simulation time of $T_i^{\Xi}T^{\lambda}_{i,\mathrm{c}}$. Taken from Reichel et al. [2023b].

	Discontinuous condensed	Discontinuous	Continuous
linear T^{Ξ}	$T_1^{\Xi}T^{\lambda}_{0,\mathrm{d,cond}}$	$T_1^{\Xi}T^{\lambda}_{0,\mathrm{d}}$	$T_1^{\Xi}T^{\lambda}_{1,\mathrm{c}}$
ratio: $T_1^{\Xi}T^{\lambda}_{\bullet}/T_1^{\Xi}T^{\lambda}_{1,\mathrm{c}}$	0.783	0.917	1.00
num. elem./ DOF	61,099/49,099	61,099/77,235	61,099/55,068
quadratic T^{Ξ}	$T_2^{\Xi}T^{\lambda}_{1,\mathrm{d,cond}}$	$T_2^{\Xi}T^{\lambda}_{1,\mathrm{d}}$	$T_2^{\Xi}T^{\lambda}_{2,\mathrm{c}}$
ratio: $T_2^{\Xi}T^{\lambda}_{\bullet}/T_2^{\Xi}T^{\lambda}_{2,\mathrm{c}}$	0.708	0.828	1.00
num. elem./ DOF	30,269/86,285	30,269/162,316	30,269/116,697

This allows for some combinations of interpolations of the considered micromagnetic formulation, if the interpolation order of the Lagrange multiplier is equal or an order below

the other degrees of freedom. However, this contribution addresses only six different interpolation combinations as shown in Tab. 5.9, to point out the workability of the proposed method. The time comparison is performed using the undeformed Ni structure from Sec. 5.8.11. All six variants of interpolation are used to calculate the demagnetization branch of the hysteresis loop of the Ni stripe. The number of finite elements and resulting degrees of freedom within each simulation is given in Tab. 5.9. The comparison between the condensed and non-condensed Lagrange multipliers shows a significant speedup in the simulations of the condensed Lagrange multipliers in Tab. 5.9 while the quality of the results remains the same.

5.9 Standard problem #4 – proof of dynamic capabilities of the model

A well known example to validate dynamic micromagnetism is the μMag standard problem #4, cf. μMAG [1995]. The considered boundary value problem corresponds to a cuboid shaped thin film of dimensions 500 nm×125 nm×3 nm discretized with 100×30×3 quadratic tetrahedron elements resulting in 268,905 degrees of freedom. This thin film is considered to mimic the material behavior of Permalloy with the following material parameters assigned to the simulation: $A_{exc} = 1.3 \times 10^{-11}$ J/m, $M_s = 8.0 \times 10^5$ A/m, and $K_{ani} = 0$ as well as $\alpha = 0.02$.

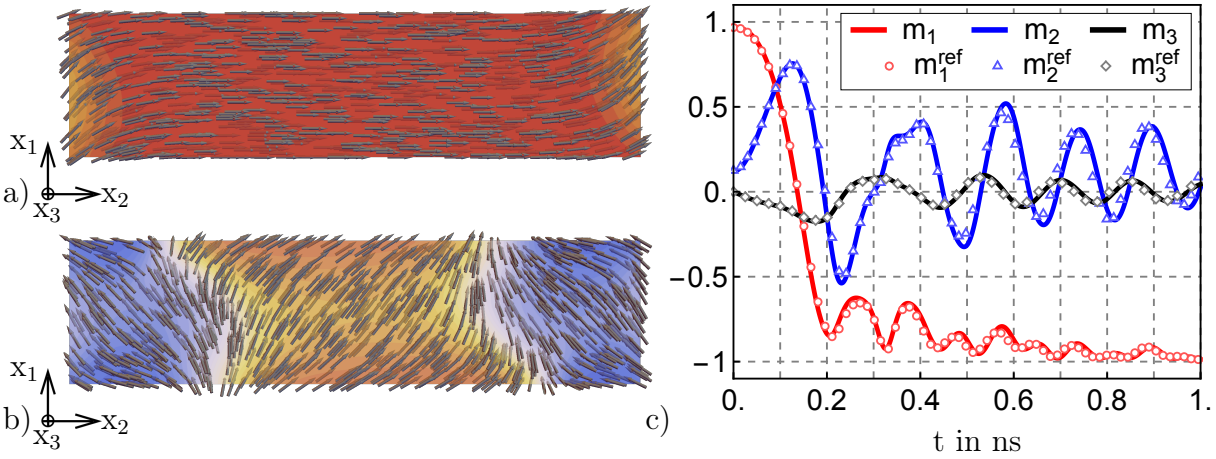

Figure 5.23: a) the initial magnetization pattern, the so-called S-state and b) the magnetization distribution when the volume average of the m_1 component exceeds zero for the first time. c) the time evolution of the magnetization components. Reference values are provided by MagTense (BJØRK ET AL. [2021]) taken from the μMag homepage, cf. μMAG [1995]. Taken from REICHEL ET AL. [2023b].

The initial magnetization configuration corresponds to the so-called S-state, compare Fig. 5.23a). This S-state can be obtained by a full saturation along the [1,1,1] axis caused by a magnetic field and a subsequent relaxation by slowly removing this field. After the relaxation a constant magnetic field $\mu_0 \overline{\boldsymbol{H}} = [-24.6, 4.3, 0.0]^{\mathrm{T}}$ mT is applied to the thin film causing an instantaneous reversal. The thin film is discretized with 100×30×3 quadratic tetrahedron elements along the corresponding axis. The time integration is accomplished by applying time increments $\Delta t = 10^{-4}$ ns. For the comparison of the time evolution of the averaged magnetization components the results generated by the software MagTens (BJØRK ET AL. [2021]) provided on the μMag homepage are used. Both results, the reference as well as the generated solution presented in Fig. 5.23c), show good agreement with each other. Also the magnetization distribution in Fig. 5.23,

when m_1 equals zero for the first time, indicates very good agreement with the patterns provided on the μMag homepage, cf. μMag [1995]. Besides the validation of the dynamical properties of the proposed model, a comparison with the implicit Midpoint rule (Bartels and Prohl [2006], d'Aquino et al. [2005], and Shepherd et al. [2019]) proves the proposed method to be equal for the convergence behavior and the required simulation time. A direct comparison of the relative residual norms of the condensed perturbed Lagrange method and the Midpoint rule is shown in Tab. 5.10 for the time step no. 100 of 101 at time 0.1485 ns. The applied increment corresponds to $\Delta t = 0.15 \times 10^{-2}$ ns. After the respective iterations in the corresponding time step, the direct comparison of these residual norms shows an equally good convergence behavior of both methods.

Table 5.10: Comparison of relative residual norms during iterations of the proposed method and the implicit Midpoint rule evaluated at time step no. 100 after 0.1485 ns for the standard problem #4. Taken from Reichel et al. [2023b].

Iteration	cond. pert. Lagrange	Midpoint
1.	1.00×10^{0}	1.00×10^{0}
2.	5.56×10^{-4}	7.63×10^{-5}
3.	8.99×10^{-7}	5.65×10^{-8}
4.	9.47×10^{-12}	3.14×10^{-12}

5.10 Conclusion

In the present work, different micromagnetic models are compared with each other. The characteristic of micromagnetic simulations is the conservation of the unit length of the magnetization vectors during the simulations. This constraint is fulfilled in different ways in the demonstrated models. The projection method is the simplest way to limit the length of the magnetization vectors. During the Newton iteration of a time step the vectors are not constrained in their length, but can evolve freely. After the iteration has converged, the projection onto the unit sphere is done by renormalizing the vectors. Thus, at the beginning of each time step all vectors correspond to the unit length. However, the disadvantages of this method compared to its simple implementation predominate. The iterated residual does not match the projected magnetization vectors. Due to the projection of the vectors, the induction may not be divergence-free and physically correct results can only be achieved by very fine time stepping, which leads to a massive increase in computation time. In general, but especially for longer simulations the use of a projection method is not recommended due to the above mentioned uncertainties.

In the penalty method, a penalty term is added to the enthalpy functional, which penalizes the deviations of the magnetization vectors from the Euclidean norm depending on a penalty parameter. This method is simple to implement, but the parameter must be adjusted for each new boundary value problem considered. The more accurate the constraint is to be satisfied, the larger penalty parameters are required. This can lead to very stiff systems of equations and poor convergence.

A Lagrange multiplier is somehow similar to the penalty method in the sense that the

deviation from the Euclidean norm is also penalized. The difference lies in the Lagrange multiplier itself, which replaces the penalty parameter. The Lagrange multiplier is an additional degree of freedom that recalculates the required penalization intensity in each iteration depending on the actual deviation and distribution of the magnetization vectors. This can be an advantage regarding the length conservation of the magnetization vectors, but also implies longer computational times since another degree of freedom has to be considered. Because a classical Lagrange multiplier leads to zero entries on the main diagonal of the system matrix, additional measures have to be considered to solve the system of equations. For this reason, a perturbed Lagrange multiplier can be applied, which contains an additional quadratic term that generates non-zero entries within the system matrix. To reduce the increased computational times, but still benefit from the advantages of the Lagrange multiplier, a static condensation of the Lagrange parameter is recommended. This can be done by means of the Schur complement at element level. The condensation of the Lagrange parameter has shown a reduction of computational costs of up to 29.8% for a comparison with the continuously discretized parameter.
The spherical coordinates fulfill the unit constraint a priori and do not require any additional restrictions in that sense. Additionally, the degrees of freedom associated with the magnetization are reduced by one, since not the components of the vectors are interpolated, but their corresponding angles. Correct switching behavior may be obtained by restricting the angles onto their defined definition domain considering the circular interpolation proposed by Dornisch et al. [2018]. In general, the use of micromagnetic formulations based on spherical coordinates requires caution as they have singular points at the poles. A rotation of magnetization vectors through these points leads with very high probability to an abortion of the simulation. Since for complex and very inhomogeneous microstructures the penalty parameters are often very difficult to adjust, it is also hardly possible to exclude the possibility that magnetization vectors rotate through one of the poles. The Lagrange multiplier has proven to be a particularly suitable method, since it restricts the length of the magnetization vectors in a variational sense directly to the unit length, to the disadvantage of additional degrees of freedom in the system of equations resulting in a longer computational time. This additional computational effort can be drastically reduced by their static condensation.

6 Microstructure characterization

Magnetic materials contribute to the efficiency improvements of energy conversion equipment (transformers), power generators (wind turbines), sensors and, electric motors for E-mobility (electromobility) as outlined in Gutfleisch et al. [2011]. In order to meet the resulting increasing demand, the performance of the magnetic materials themselves must be significantly improved. The addition of heavy rare earths such as dysprosium (Dy) or terbium (Ty) can contribute to this desired increase in performance, cf. Soderžnik et al. [2016] and Herbst and Croat [1991]. However, this performance gain, i.e. the increase in coercivity in this particular case, implies a dependence on materials that are mined under severe environmental as well as social impact and originate from countries with markets that are not continuously accessible, cf. Rostek-Buetti [2019]. In addition to the above-mentioned modification of chemical compositions, microstructure engineering plays a very prominent and important role as well. Particularly high-performance permanent magnets are characterized by a fine grain structure with strongly pronounced uni-axial magneto-crystalline anisotropy, cf. Kronmüller [1987]. Ideally, the ferromagnetic grains are magnetically separated from each other by a paramagnetic grain boundary phase. This grain boundary phase hinders the magnetic exchange interaction and can thus prevent a cascade-like reversal. The diameter of such magnetic grains can often reach several μm, while the grain boundary phase is usually a few nm thick. Since the exchange length of $Nd_2Fe_{14}B$ magnets is small $\sim$1.9 nm (cf. Coey [2010]), grain boundaries wider than this length can already lead to an improvement of magnetic properties, cf. Soderžnik et al. [2017]. Consequently, a considerable research interest is to apply new techniques in the fabrication process that allow a more flexible manipulation of local microstructural properties, as e.g. techniques based on additive manufacturing (AM), cf. Yang et al. [2023] and Schäfer et al. [2021]. Besides the local tailoring of microstructures, energy consumption during the manufacturing process is of course also a crucial factor. In addition to the already mentioned AM, which is rather energy intensive, this brings up techniques based on severe plastic deformation (SPD), as e.g. the continuous rotary swaging (CRS) or the high pressure torsion (HPT), cf. Chi et al. [2019], Staab et al. [2023] and Weissitsch et al. [2023]. The goal of this section is the numerical characterization of permanent magnetic materials with polycrystalline microstructures resulting of different underlying process routes.

In Sec. 6.1 the influence of different imperfections on the effective magnetization behavior is investigated. The simulations are based on idealized microstructures that are expected as a result of the CRS process, cf. Marr et al. [2011]. In addition to the analysis of the influence of the grain size on the magnetic hysteresis, the influence of local inhomogeneities, misorientations, and process-related defects is analyzed. In Sec. 6.2 the influence of different grain boundary phases on the effective behavior of a real microstructure produced by the current industry standard - sintering - is investigated. Sec. 6.3 is dedicated to the exact description of the demagnetization process in a 3D polycrystalline microstructure.

Parts of this chapter are published in:
M. Reichel, P. Groche, O. Gutfleisch and J. Schröder, Impact of soft magnetic α-Fe in hard $Nd_2Fe_{14}B$ magnetic materials: A micromagnetic study, *Proceedings in Applied Mathematics and Mechanics*, e202300104, (2023).

Since all subsequent sections deal with the simulation of $Nd_2Fe_{14}B$, the material parameters are defined below in Tab. 6.1. To capture the magnetic quasi static states, a damping parameter of $\alpha = 1$ is applied. This reduces the impact of the precession term within the magnetic evolution equation.

Table 6.1: Material parameters of $Nd_2Fe_{14}B$, taken from Coey [2010].

Parameter	$A_{\text{exc}}\ \frac{J}{m}$	$M_{\text{s}}\ \frac{A}{m}$	$K\ \frac{J}{m^3}$
$Nd_2Fe_{14}B$	$8 \cdot 10^{-12}$	$1.28 \cdot 10^6$	$4.9 \cdot 10^6$

6.1 Study of influencing parameters on effective coercivity

In this section the focus remains on the analysis of factors impacting the effective properties (here coercivity and remanence) of permanent magnetic materials on the basis of idealized microstructures, which are supposed to represent the final result of microstructures produced by CRS. For this purpose, boundary value problems with different kinds of imperfections are investigated, such that a subsequent prognosis regarding ideal microstructures can be formulated. The analyzed material is $Nd_2Fe_{14}B$, a hard magnetic material with particularly strong magnetic uniaxial anisotropy. The corresponding material parameters are given in Tab. 6.1. In the following, magnetic single grains, but also polygrain structures are considered, that are all surrounded by a free space to incorporate the influence of magnetic stray fields. Within the free space, only the magnetic Gauss law is considered. On the outer boundary of the free space the scalar potential $\varphi_0 = 0$ is prescribed, so that the external magnetic field $\overline{\boldsymbol{H}}$ can be assumed to be constant over the whole discrete domain. The applied load path for all simulations of this section is defined in Fig. 6.1. Note that the intensity of the external magnetic field is not yet defined as a numerical value in Fig. 6.1, but only plotted as a function of $\overline{\boldsymbol{H}}$ at the y-axis. This is due to the fact that although the time intervals in all subsequent simulations are identical to each other, the field strengths may differ. All simulations within this section are done using quadrilateral bi-linear interpolation functions and the condensed perturbed Lagrange multiplier.

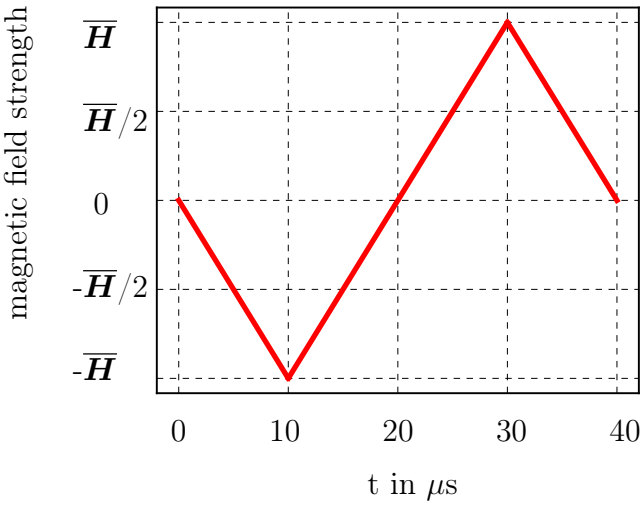

Figure 6.1: Load path of the externally applied magnetic field $\overline{\boldsymbol{H}}$.

6.1.1 Influence of varying grain sizes

The size of the magnetic grains can have a significant influence on the magnetic properties of the magnetic material under consideration. In the defined boundary value problem, a single hexagonal magnetic grain is considered with varying size of diameter. Starting from a diameter of d=25 nm at the first conducted simulation, it is increased up to a diameter of d=3000 nm in the last simulation.

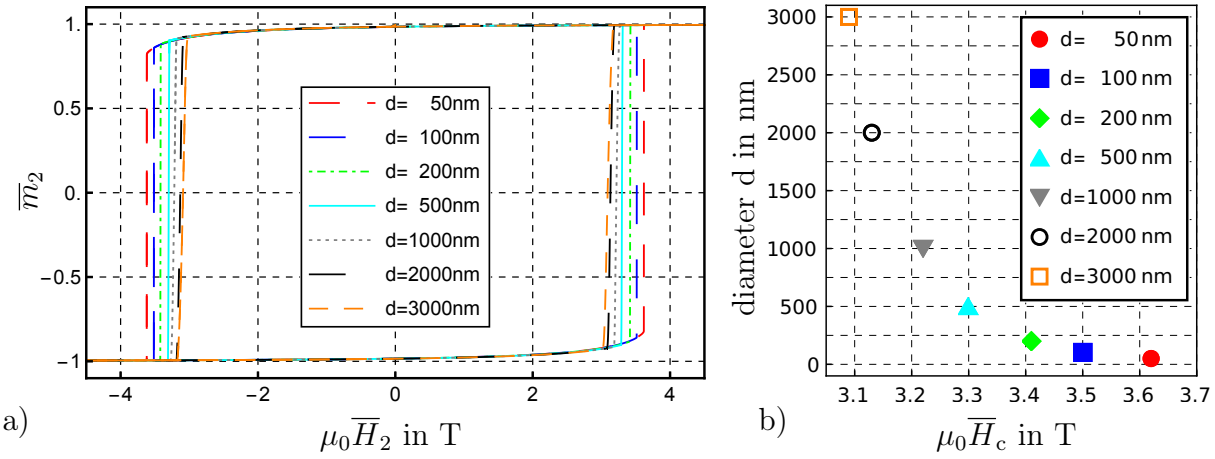

Figure 6.2: a) the simulated hysteresis curves of the different grain diameters and b) the resulting coercive field strengths H_c as a function of the grain diameter d.

Each of the simulations provides a complete hysteresis loop, enabling the comparison of all results in Fig. 6.2a). The external magnetic field $\mu_0\overline{\boldsymbol{H}} = [0, 5, 0]^{\mathrm{T}}$ T is applied in an alternating form, as shown in Fig. 6.1. Applying spherical coordinates, the initial magnetization can be defined in terms of angles as $\theta_1 = 0.45\pi$ and $\theta_2 = 0.5\pi$ for all cycles to be captured, assuming a single domain state within each grain. The hysteresis loops shown in Fig. 6.2a) exhibit a pronounced squareness. There are various possible reasons for this characteristic. The orientation of the magneto-crystalline anisotropy is exactly antiparallel to the external magnetic field and thus generates the greatest resistance to initiate a magnetic reversal. Additionally, neighboring grains and defect structures, such as inclusions, are missing, which can induce either a premature nucleation or the pinning of a reversal. This implies that the simulation considered here has been strongly idealized. However, the core statements of the simulations are still valid. The largest values in coercivity can be obtained for the smallest grains. An increase in the size of the grains results in a decrease in coercivity, as can be seen in Fig. 6.2b). It can be concluded that smaller grains are of crucial importance in the synthesis of high performance magnets.

6.1.2 Magnetization reversal in heterogeneous microstructures

In this section, two different scenarios for microstructural compositions of $Nd_2Fe_{14}B$ magnets are considered. Thereby, the special focus of this scenarios is on the influence of α-Fe impurities on the effective hysteresis properties of permanent magnetic materials. α-Fe is a soft phase material that typically forms during the casting process in the form of large dendritic grains within the $Nd_2Fe_{14}B$ matrix grains and an excess of Nd-rich phases (the latter are paramagnetic). Upon homogenization these phases recombine to form more $Nd_2Fe_{14}B$ matrix grains under elimination of Fe.

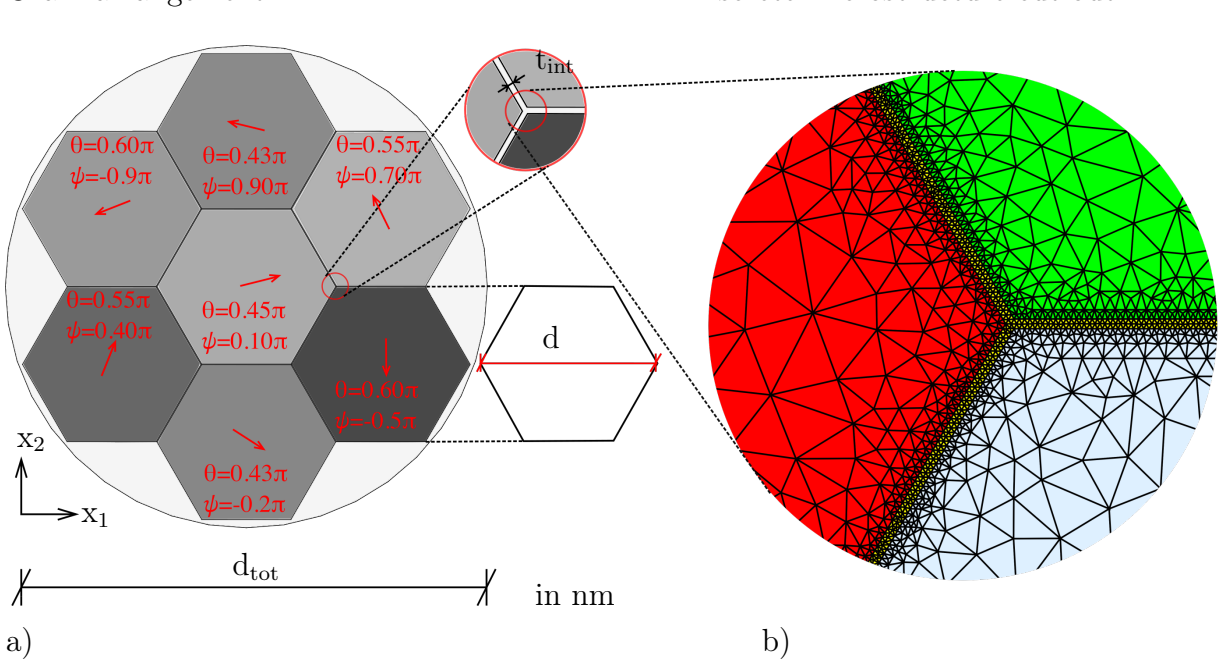

Figure 6.3: a) the microstructure of the ferromagnetic $Nd_2Fe_{14}B$ grains within the decoupling paramagnetic interphase layer of thickness t_{int}. The easy-axes of the individual grains follow the orientation of the red vectors. b) a discrete cut out of the grain boundary phase of the microstructure. Taken from Reichel et al. [2023a].

Soft magnetic materials have significantly lower resistance to external magnetic fields compared to permanent magnetic materials, resulting in significantly lower coercivity. Since the α-Fe is in direct contact with the hard magnetic $Nd_2Fe_{14}B$ phase (no separation of both materials by a paramagnetic grain boundary phase) it initiates a premature reversal within the magnetically harder part of the magnet. The result is a significantly lower coercivity of this magnet, compared to a magnet with no impurities. In the following, a grain composition without α-Fe impurities is considered, see Fig. 6.3. It consists of seven ferromagnetic grains with the material properties of $Nd_2Fe_{14}B$, cf. Tab. 6.1. The grains are assumed to have a diameter of 500 nm (doubles the single domain particle size of $Nd_2Fe_{14}B$ ~200-300 nm, cf. Gutfleisch [2000]) and are assumed to be magnetically decoupled from each other by a 5 nm thick paramagnetic Nd-rich grain boundary. The whole microstructure corresponds to the diameter d_{tot}=1350 nm. The discrete microstructure involves 57,239 finite elements and 203,592 degrees of freedom. To obtain a typical hysteresis loop and evaluate the effective magnetic behavior, an alternating external magnetic field $\mu_0 \overline{\boldsymbol{H}} = [0, 6, 0]^T$ T is applied, following the load path defined in Fig. 6.1. In the simulated hysteresis loop (Fig. 6.4f)) several kinks can be seen. These result from the different switching times due to different anisotropy orientations of the individual decoupled grains. The grain boundary prevents reversal from one switching grain to another and thus premature nucleation. The resulting coercivity of the considered microstructure is obtained from the hysteresis in Fig. 6.4f) as ~2.5 T. An improvement of this property can be achieved mainly by a better alignment of the easy-axes of the grains. A fabrication such that the easy-axes of the individual grains are oriented in one direction can lead to a more rectangular hysteresis due to a later nucleation within the grains. Of course it is a non-trivial task to obtain an perfect alignment. Hence, the latter statement implies an alignment with slight variations. The reversal process given in Fig. 6.4a)–e) shows the separate switching of the individual grains. The magnetization within each grain nucle-

ates within the corners of the corresponding grain. Subsequently, the reversal propagates cascade-like through the grain, leading to the characteristic kinks in the hysteresis.

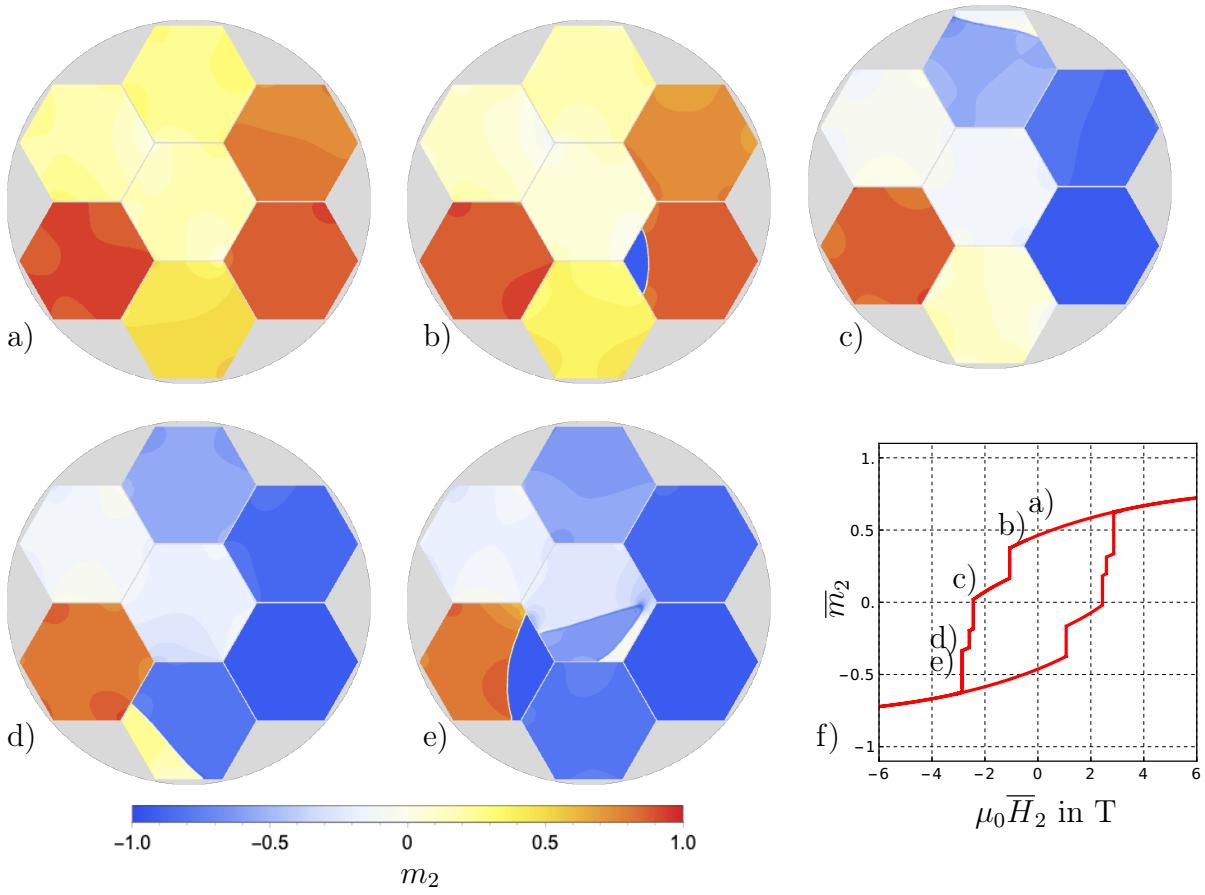

Figure 6.4: Evolution of the magnetization reversal a) – e) and its corresponding hysteresis loop f). a) the magnetization vectors are aligned parallel to the easy-axes of the individual grains, b) the nucleation starts within the corners of the grains, and c) the grains reverse. Taken from Reichel et al. [2023a].

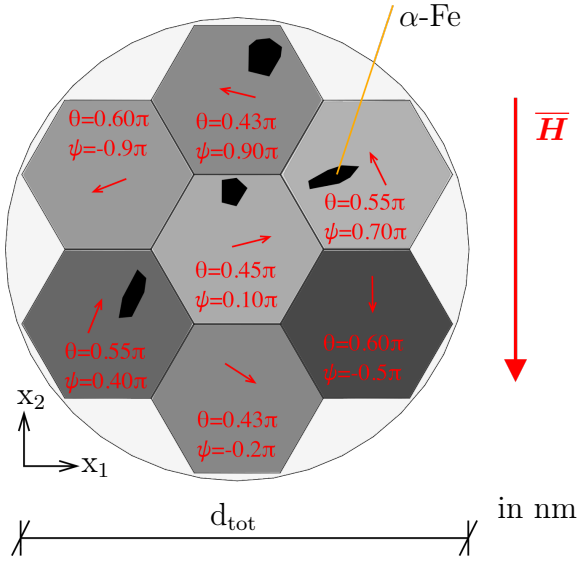

Figure 6.5: Microstructure with seven hexagonal $Nd_2Fe_{14}B$ grains and α-Fe impurities. Taken from Reichel et al. [2023a].

In the case of impurified microstructures the behavior may be different. To investigate this in more detail, the boundary value problem introduced in Fig. 6.3 is extended to contain α-Fe impurities in the following example. The modified boundary value problem with soft magnetic inclusions can be found in Fig. 6.5. Here, local impurities are taken into account by defining additional regions within the permanent magnetic grains and assigning soft magnetic properties such that the material response of α-Fe can be simulated. The following material properties of α-Fe are taken from Sridhar et al. [2016]: exchange constant $A_{\mathrm{exc}} = 1.0 \cdot 10^{-12}$ J/m, saturation magnetization $M_{\mathrm{s}} = 5 \cdot 10^{6}$ A/m and magneto-crystalline anisotropy $K_1 = 4 \cdot 10^{4}$ J/m^3, and $K_2 = 6 \cdot 10^{3}$ J/m^3.

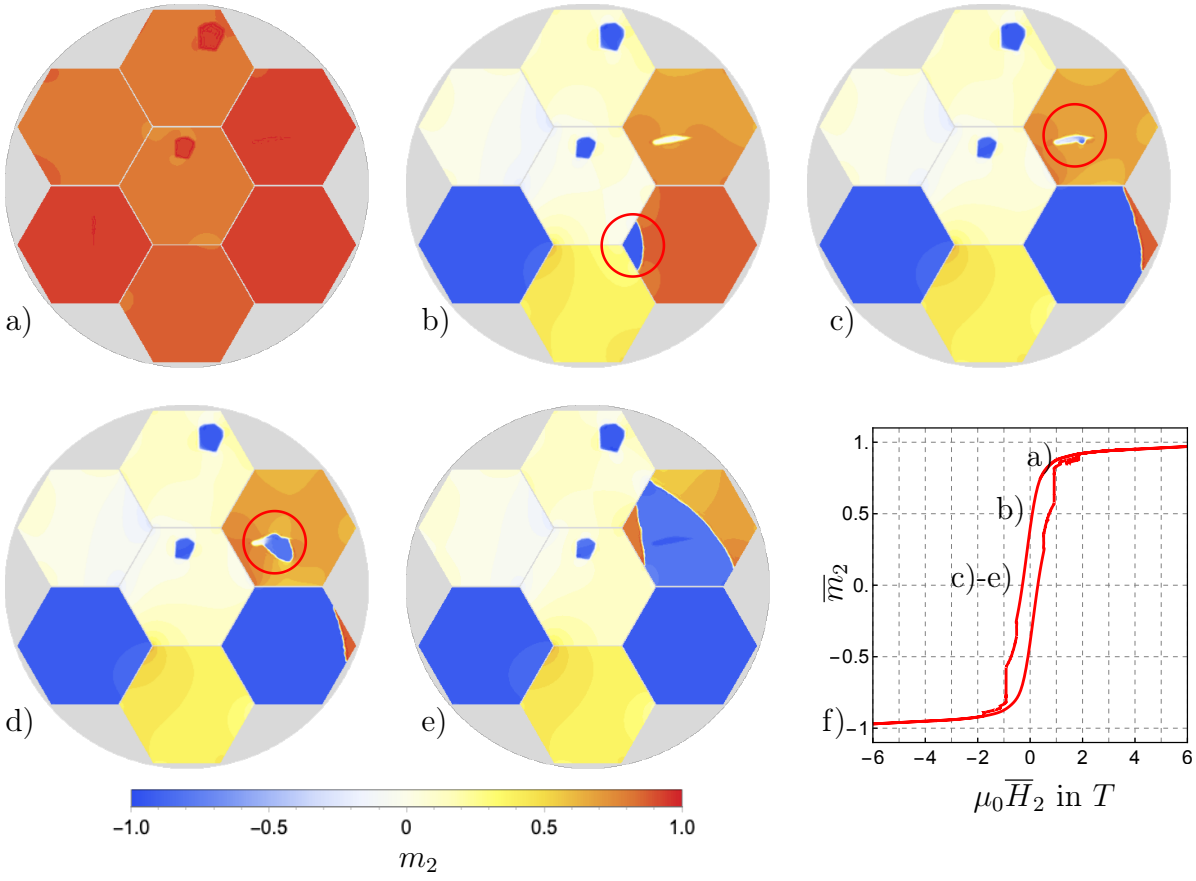

Figure 6.6: Evolution of the magnetization reversal a) – e) and its corresponding hysteresis loop f). a) the magnetization vectors are aligned parallel to the easy-axes of the individual grains, b) the nucleation starts within the corner of the homogeneous grains at triple junctions, and in c) within the α-Fe impurities. d) propagation of reversal into the grain.

The hysteresis loop is obtained by applying the alternating external magnetic field $\mu_0 \overline{\boldsymbol{H}} = [0, 6, 0]^{\mathrm{T}}$ T following the load path given in Fig. 6.1 to the microstructure presented in Fig. 6.5. The resulting hysteresis loop is about 10 times more slender compared to the previously simulated loop (Fig. 6.4f)). The reason for this behavior can be identified as the direct contact of the soft magnetic material with the permanent magnetic grain. Since the α-Fe impurities have a significantly lower resistance (coercivity) to opposing external magnetic fields, nucleation starts at these spots. Due to the fact that impurities

collect at random locations within the grain matrix during the manufacturing process, grain boundaries between the inclusions and the actual grain are missing. As a result, soft and permanent magnetic materials are in direct contact with each other, i.e. they are not exchange decoupled. After the reversal of the soft magnetic region (Fig. 6.6b)), this leads to a fast transition of the reversal to the permanent magnetic material (Fig. 6.6c)) and thus to a premature switching of the entire grain (Fig. 6.6e)). A comparison of the simulation results with the findings from Sepehri-Amin et al. [2019] gives rise to further analysis, since here α-Fe phase inclusions about 100 nm in size appear to couple effectively. However, the microstructures are different.

6.1.3 Impact of anisotropy orientations in polycrystalline microstructures

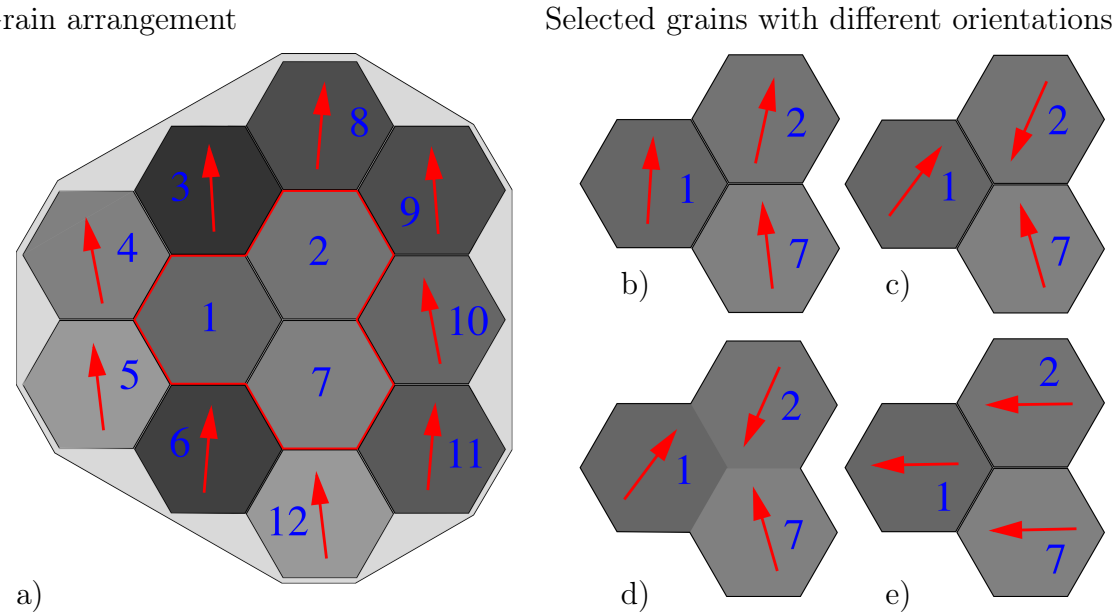

Figure 6.7: a) a microstructure consisting of 12 ferromagnetic $Nd_2Fe_{14}B$ grains. The red arrows indicate the easy-axis of the respective grains. b) - e) different easy-axes orientations within the middle grains (1,2 and 7). The difference between c) and d) is a separating Nd-rich grain boundary between the ferromagnetic grains in c), while d) assumes direct contact of the grains (no grain boundary).

The effective properties of a magnet can be strongly influenced by a wide variety of local defect structures such as large single grains within a finer grain matrix, in general defect structures such as cracks, but also misoriented grains, cf. Kronmüller [1987]. This section is primarily focused on the analysis of misoriented grains and the lack of separating grain boundaries within the microstructure. In order to analyze the local influence of a few misoriented grains on the overall behavior of the magnet, the considered microstructure must be slightly larger than the previously considered structures in Fig. 6.3 and Fig. 6.5. Thus, the microstructure given in Fig. 6.7 consists of 12 ferromagnetic grains. All considered grains have a diameter of d = 500 nm, while the thickness of the grain boundary is idealized as t_{int} = 5 nm. The grain boundary mimics the behavior of an Nd-rich layer that prevents exchange interactions between individual ferromagnetic grains. Therefore, the grains can be considered as magnetically decoupled. In the following, the microstructure $\mathcal{B}$ shown in Fig. 6.7a) is subdivided into an outer rim consisting of the outer grains $\mathcal{B}^{out}$ (3,4,5,6,8,9,10,11,12) and the inner grains $\mathcal{B}^{int}$ (1,2,7) as $\mathcal{B} = \mathcal{B}^{out} \bigcup \mathcal{B}^{int}$. On the one hand,

the orientations of the outer grains $\mathcal{B}^{\text{out}}$ are almost perfectly parallel to the x_2-axis with a deviation of $\pm 1°$ and remain unchanged in all subsequent considerations. The grains $\mathcal{B}^{\text{int}}$, on the other hand, are given different easy-axes orientations in the following simulations, as described in the items below:

Case 1: An almost perfect orientation of the easy-axes is assumed. This also implies a deviation of only $\pm 1°$ from the x_2-axis. This case represents an ideally textured microstructure and is obtained from Figs. 6.7a) and b). This assumption yields the black hysteresis loop in Fig. 6.8.

Case 2: A randomly oriented easy-axes distributions in $\mathcal{B}^{\text{int}}$ that deviates strongly from the x_2-axis is assumed in Fig. 6.7c). This assumption yields the red hysteresis loop in Fig. 6.8.

Case 3: No distinction is made between grain and grain boundary within $\mathcal{B}^{\text{int}}$. This means that $\mathcal{B}^{\text{int}}$ consists of three grains, which are in direct contact with each other and thus cannot be considered as exchange decoupled. The corresponding easy-axes orientations are sketched in Fig. 6.7d). This assumption yields the green hysteresis loop in Fig. 6.8.

Case 4: $\mathcal{B}^{\text{int}}$ is considered to be decoupled by the Nd-rich grain boundary but with only one easy-axis for all grains, i.e. the x_1-axis, as shown in Fig. 6.7e). This assumption yields the blue hysteresis loop in Fig. 6.8.

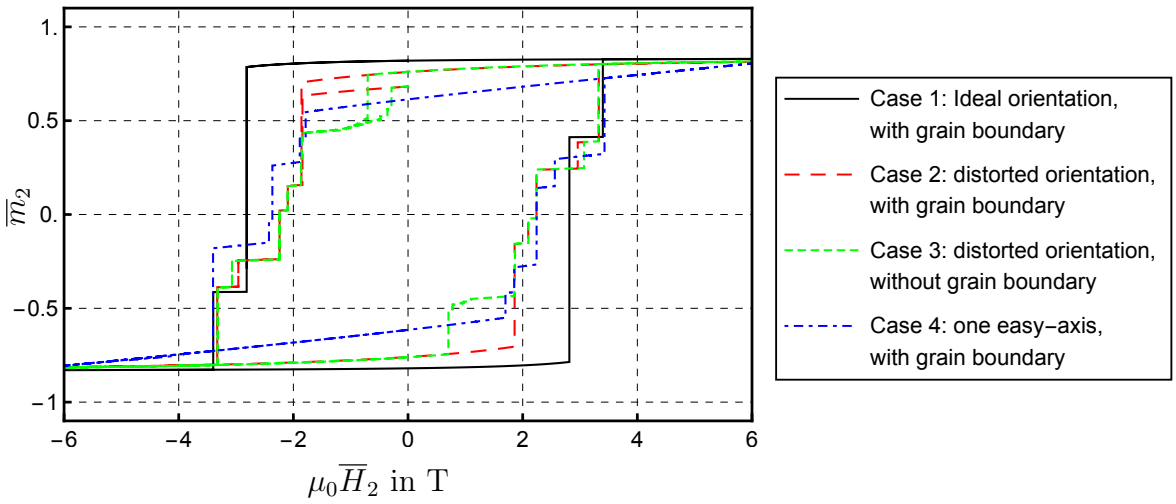

Figure 6.8: The hysteresis loops of the ideal and distorted grain compositions.

The subsequent simulations involve $\sim 110,000$ quadrilateral finite elements with ~350,000 degrees of freedom. Their resulting hystereses loops are shown in Fig. 6.8. For Case 1, i.e. the case of almost perfect alignment of the anisotropy to the x_2-axis, the hysteresis depicted in black in Fig. 6.8 appears to be very square. Due to the almost identical orientations of the anisotropy in all grains, the reversal starts simultaneously in most grains leading to the highest value of coercivity, of all here considered cases. Another advantage are the paramagnetic grain boundaries, which decouple the individual grain's switching process magnetically from the other grains. This hysteresis can thus be regarded

as a kind of upper limit of this microstructure with respect to coercivity. Case 2 considers arbitrarily defined easy-axes orientations of the inner grains $\mathcal{B}^{\text{int}}$, leading to a clearly deviating behavior compared to Case 1. The nucleation of the magnetization reversal within the grains starts much earlier, which results in a lower coercivity. Likewise, many grains switch separately, which for the middle grains can be explained in any case by their strong deviations of the anisotropy-axis from the x_2-axis. The surrounding grains switch gradually, but much earlier compared to Case 1, leading to a distinct deviating coercivity of the magnet, see Fig. 6.9a). Although the grains are separated from each other by a paramagnetic Nd-rich layer, so that an early nucleation of the grains by direct contact between reversed and non-reversed grains can be excluded, the reversed grains cause a change in the demagnetization fields, which also affect the magnetization behavior of the neighboring (non-reversed) grains.

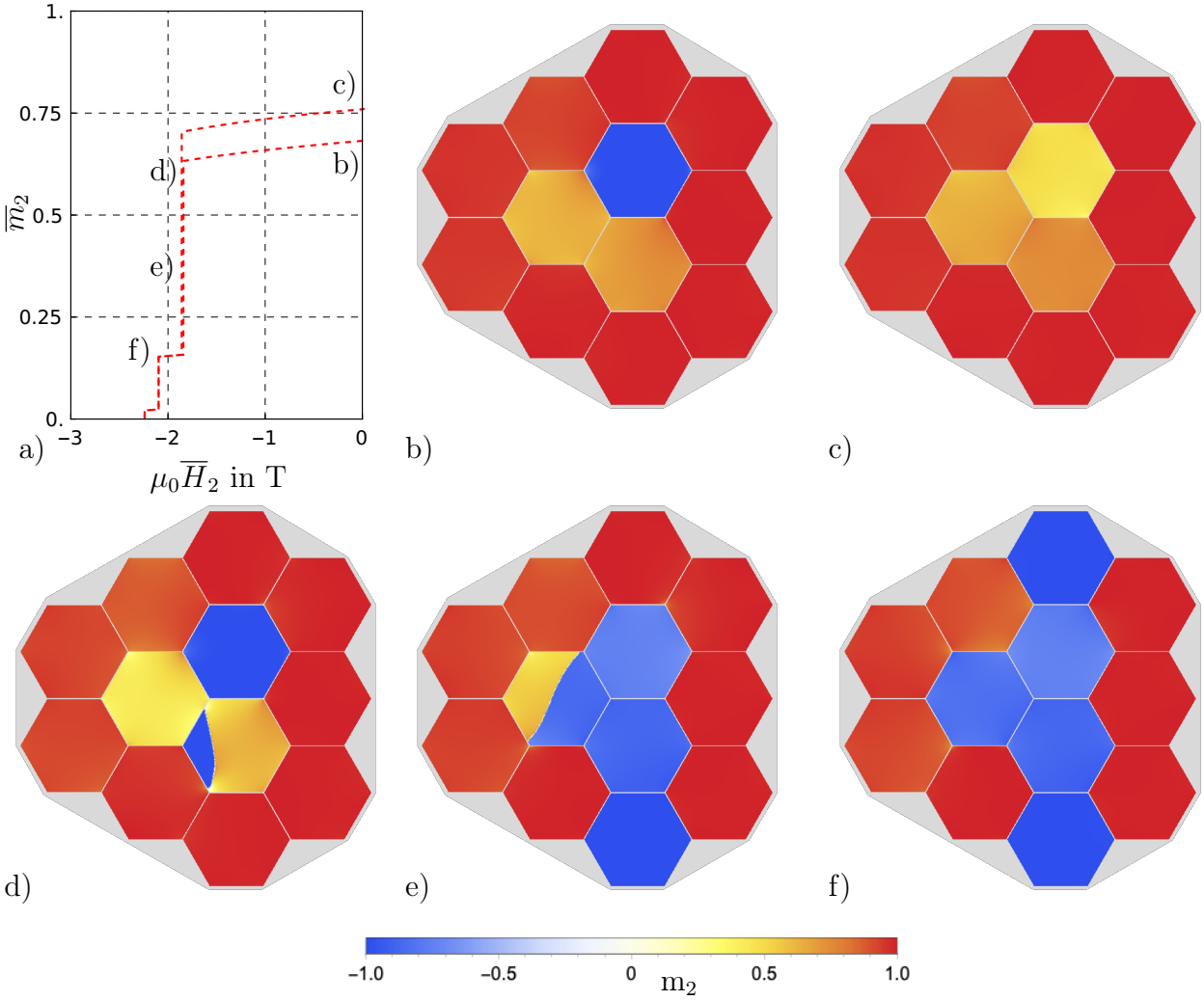

Figure 6.9: Case 2 delivers the demagnetizing branches given in a). The initial magnetization distribution is given in b), while c) shows the remanent distribution after a full magnetization along the x_2-axis. The demagnetization process is given in d)-f). The reversal starts with a nucleation at the triple junction between grain 1, 6 and 7, shown in d).

Due to the initial magnetization of the microstructure (cf. Fig. 6.7c)) the volume average of the magnetization at the beginning of the simulation is clearly below the remanence

of the magnet obtained after a complete parallel alignment of the magnetization to the external field. The remanent distribution of the magnetization, in particular of grain 2, does not correspond to the initial distribution as indicated in Fig. 6.7c), but is antiparallel to it and the easy-axis of the grain. This behavior is evident in the second quadrant of the hysteresis loop in Fig. 6.9a). Both, the initial and the remanent magnetization, are shown in Fig. 6.9b) and c). Case 3 considers no separating Nd-rich layer between the grains $\mathcal{B}^{\text{int}}$ (cf. Fig. 6.7d)). It follows that the ferromagnetic grains are in direct contact with each other and an already switching grain leads to nucleation, or premature magnetization reversal of the adjacent grain. Since no boundary hinders the propagation, a cascade-like reversal of the magnetization within the adjacent grain is the outcome, as depicted in Fig. 6.10d). After the magnetization reversal of the grains $\mathcal{B}^{\text{int}}$, the magnetization shows the same behavior as in Case 2 described above. For the difference between initial magnetization and remanence the same explanation applies as for Case 2.

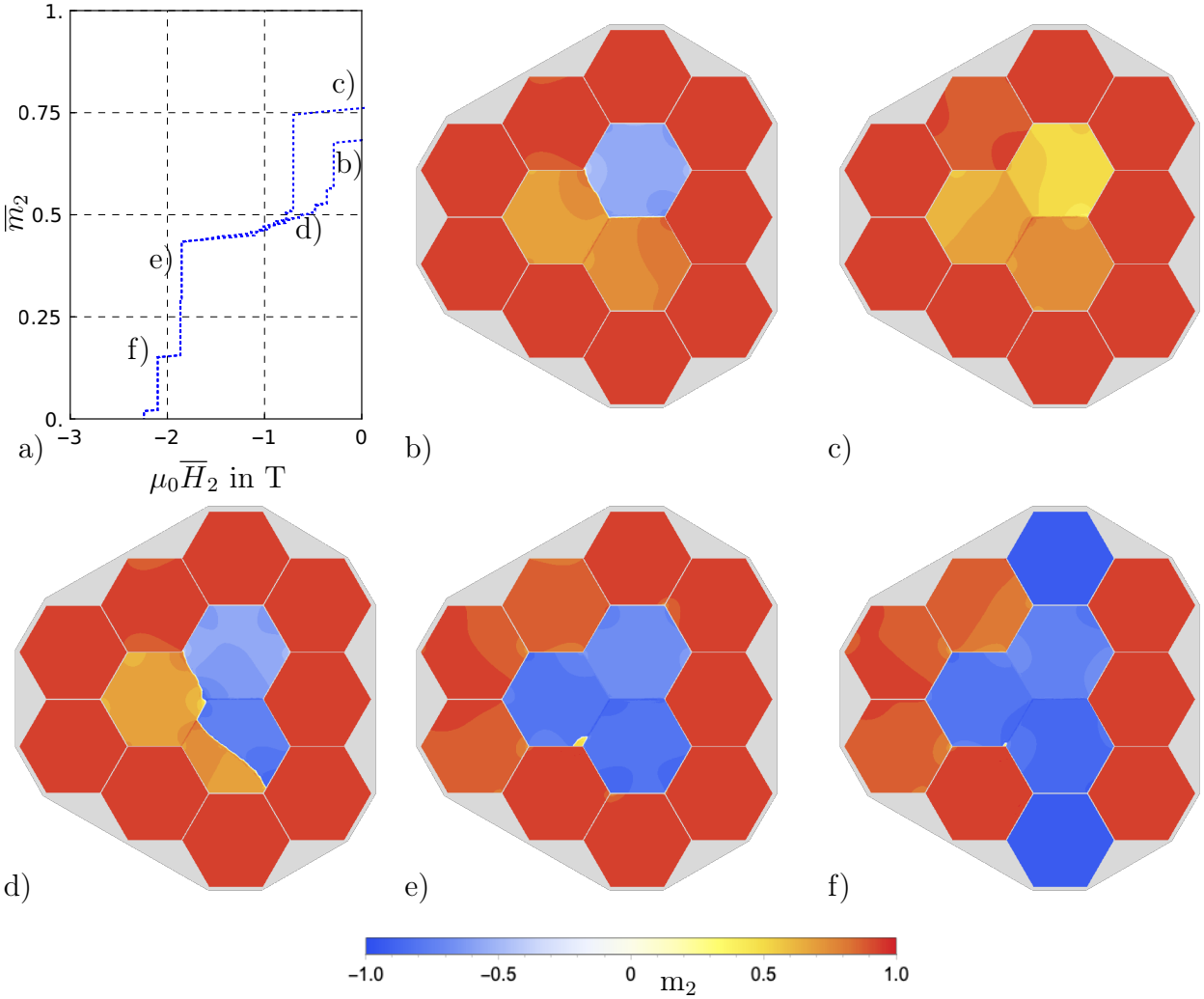

Figure 6.10: Case 3 delivers the demagnetizing branches given in a). The initial magnetization distribution is given in b), while c) shows the remanent distribution after magnetizing along the x_2-axis. The demagnetization process is depicted in d)-f). The reversal starts with a nucleation at the triple junction between the grains 2, 7 and 10 and propagates through d) grain 7 and e) grain 1. The distribution in f) is similar to Case 2.

Case 4 assumes an orientation parallel to the x_1-axis within the internal grains $\mathcal{B}^{\text{int}}$. As

evident from the blue hysteresis, this is the orientation pattern of the anisotropy that exhibits the least remanence. Since the magnetization is preferentially oriented along the easy-axis, no contribution of the inner grains $\mathcal{B}^{\text{int}}$ can be considered for the volume average calculation at time t=0 s of the simulation and also after full saturation (remanence), accordingly. Thus, the contributions to the remanence of three grains are omitted. Nevertheless, the coercivity is more pronounced than that of Case 2 and Case 3. An explanation for this behavior is that the external field tends to magnetize the inner grains $\mathcal{B}^{\text{int}}$ along their hard-axes, which is significantly more challenging than aligning the magnetization along its easy-axes. Accordingly, this process occurs very slowly, the locally generated demagnetization fields are smaller compared to the two previously considered cases, and therefore have less influence on the reversal of the grains $\mathcal{B}^{\text{ext}}$.

6.1.4 Surface defects influencing the effective performance of magnets

Stresses, cracks or other defects induced by the manufacturing process can have a strong negative influence on the magnetic properties of the entire magnet. These imperfections often appear within the region of the grain surfaces and have a locally reducing effect on the anisotropy, cf. Hrkac et al. [2014a], Hrkac et al. [2014b], and Hrkac et al. [2010]. To investigate this influence in more detail, a defect layer of some few nm thickness is defined on the surface of the individual $Nd_2Fe_{14}B$ grains, following the approaches of Süss et al. [2000] and Helbig et al. [2017]. In the considered case the defect layer is set to be 10 nm thick. Within this layer, a so-called surface anisotropy is defined as $K^{\text{sur}} = \eta\, K^{\text{ani}} \,|\, \eta \in (0,1)$, where η is a defect factor relating the defect intensity to the crystalline anisotropy. In the performed numerical analysis, defect parameters of $\eta = \{1,\ 0.9,\ 0.8,\ 0.7,\ 0.6,\ 0.1\}$ are considered. To obtain a comparison of the resulting coercivities and remanences, an alternating magnetic field of $\mu_0 \overline{\boldsymbol{H}} = [0, 6, 0]^{\text{T}}$ T, that follows the load path presented in Fig. 6.1, is applied. The discretization of the microstructure involves $\sim 57,000$ finite elements and $\sim 200,000$ degrees of freedom. The resulting hysteresis loops are shown in Fig. 6.11 and reveal a clear reduction in coercivity and remanence for decreasing defect parameters.

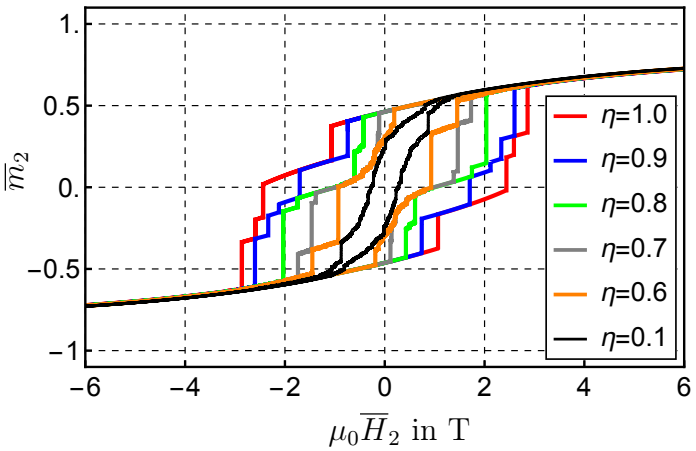

Figure 6.11: The hysteresis loops of the microstructure seen, taking into account surface anisotropy in the surfaces of the grains.

The defect parameter $\eta = 1$ corresponds to no surface defect. Thus, the resulting hysteresis matches the hysteresis presented in Fig. 6.4 with a coercivity of $H_{\text{c}} = -2.44$ T. However,

already a small reduction of this parameter to $\eta = 0.9$ causes a significant decrease in coercivity to $H_c = -1.70$ T. An even stronger reduction of the defect parameter to $\eta = 0.1$, considered to be associated with a severe damage at the surface of the grains, leads to a reduction in coercivity of $H_c = -0.28$ T and in general a very slender curve. Besides the reduction in coercivity, a reduction of remanence is obtained for defect parameters $\eta < 0.7$. Above this defect level the remanence of the magnet is not effected. Nevertheless, below this level the grains begin to posses multi domain states as shown in Fig. 6.12. While the grains with a defect parameter above $\eta = 0.7$ correspond to single domain states (e.g. cf. Fig. 6.12a)), grains with an increasing amount of defects, which implies a decreasing of the defect parameter, can posses multiple domains within a grain. Those domains can be two or more differently oriented areas within a grain, opposing at least some of each other as depicted in Fig. 6.12b) and c). Hence, those opposing domains cancel each other out and do not contribute to the remanence. These multi-domains within the grains cannot only be associated to the strong decrease in remanence, but also to the poor performance in values of coercivity associated to the parameter $\eta = 0.1$. To fully reverse the magnetization of a multi-domain grain, a complete reversal, compared to the single domain grains, of the entire grain magnetization is no longer necessary, since parts are already oriented in different directions.

Remanent magnetization depending on η

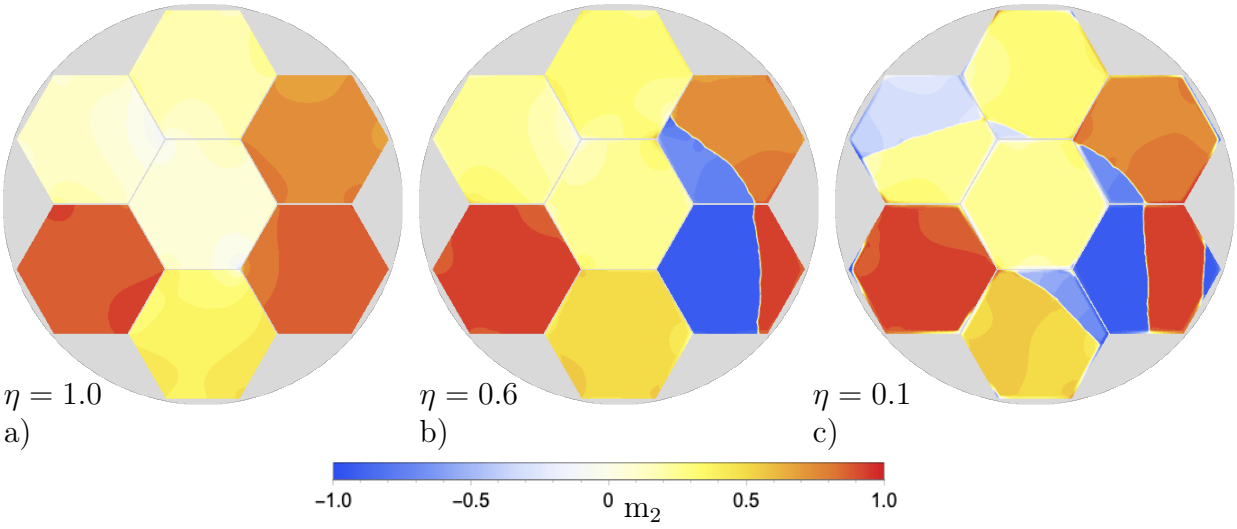

Figure 6.12: The remanent magnetization distribution of the microstructure for varying defect parameters a) $\eta = 1.0$, b) $\eta = 0.6$, and c) $\eta = 0.1$ within the surface edges.

6.2 Grain boundary analysis based on a realistic NdFeB microstructure

In this section, a sensitivity analysis of the effective magnetic properties of microstructures with respect to different types of grain boundaries is performed. This analysis involves the subsequent procedure. A distinction is made between:

Case A: a purely Nd-rich grain boundary phase, that behaves only paramagnetic (magnetostatic) representing an ideally decoupled magnetic system,

Case B: a slightly ferromagnetic grain boundary phase material, that does not completely decouple but still slightly inhibits coupling, and

Case C: a direct contact of the grains with each other, which corresponds to a full coupling.

The underlying simulation in this section is based on the microstructure[11.)] shown in Fig 6.13a). The image of the microstructure was generated using a scanning electron microscope (SEM). The dark areas represent magnetic grains, while the lighter (white) lines indicate the grain boundary layers. These grain boundary layers range between 3 to 8 nm thickness. The two white triangular spots, each wedged between three ferromagnetic grains are so-called triple junctions. Within the context of this work, a triple junction is an accumulation of mostly paramagnetic Nd-rich interphase material, which also forms the grain boundary phase. The grains consist of ferromagnetic $Nd_2Fe_{14}B$. The mostly paramagnetic grain boundaries have a magnetically decoupling effect and, depending on the thickness of the layer, can inhibit and even prevent the exchange interactions between the grains. This can lead to an overall increase in the effective performance of the magnet.

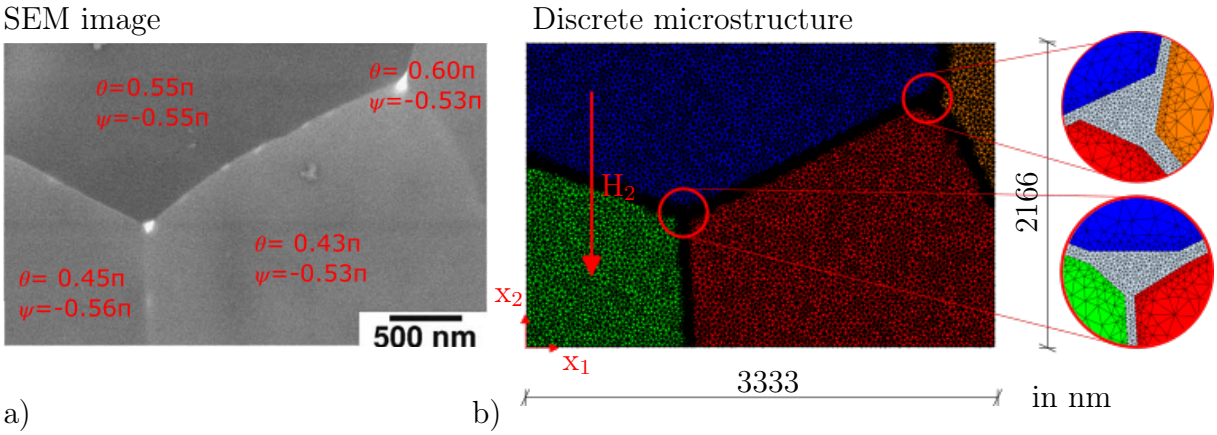

Figure 6.13: a) an SEM image of the $Nd_2Fe_{14}B$ microstructure with the separating grain boundaries and the corresponding triple junctions, taken with permission of Elsevier from Khlopkov et al. [2004]. b) the discrete microstructure approximated with finite elements and different mesh densities in the grains, the grain boundaries, and the triple junctions.

In the following, a numerical study is performed on the effects of different interphases between the grains of the magnetic microstructure. Therefore, the microstructure in Fig 6.13a) is transformed into its discrete counterpart, presented in Fig 6.13b). The microstructure, covering 3333×2166 nm in total, is discretized with 17,788 quadratic triangles, resulting in 179,045 degrees of freedom. In all simulations presented within this

[11.)] Fig 6.13a) is taken with permission of Elsevier from the publication Khlopkov et al. [2004].

section, the magnetization magnitude is constrained via a perturbed Lagrange multiplier and the magnetic field is generated by a magnetic scalar potential prescribed on the top and bottom edges of the discrete microstructure. The resulting external magnetic field $\mu_0\overline{\boldsymbol{H}} = [0, 6, 0]^{\mathrm{T}}$ T follows the load curve described in Fig. 6.16a). The material parameters of $Nd_2Fe_{14}B$ can be found in Tab. 6.1. Furthermore, an external space is omitted, so that no stray fields in the external space are considered. The orientation of the crystalline anisotropy follows the direction of the vector $\boldsymbol{a} = [\sin\theta\cos\psi, \sin\theta\sin\psi, \cos\theta]^T$, where the polar angle θ and the azimuth angle ψ can be taken from the corresponding grains in Fig 6.13a). The initial magnetization distribution follows the direction of $\boldsymbol{a}$, which approximately corresponds to the x_2-axis. For perfectly decoupled ferromagnetic grains (Case A) resulting from an Nd-rich grain boundary of 8 nm behaving purely magnetostatic (i.e., M_s^{GB}=0, A_{exc}^{GB}=0, and K_1^{GB}=0), a magnetization reversal is observed as shown in Fig. 6.14a)–c). The superscript GB indicates that the material parameters belong to the region of the grain boundaries and triple junctions.

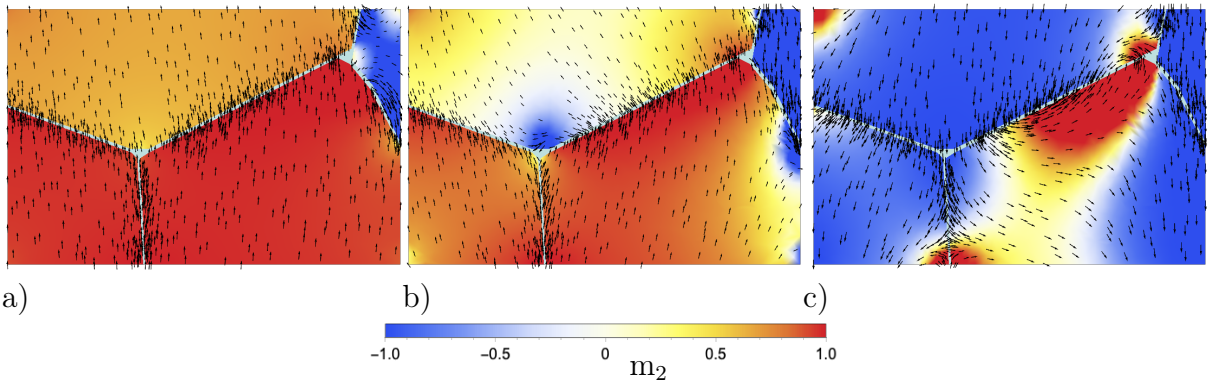

Figure 6.14: Magnetization reversal of the exchange decoupled microstructure with a) the nucleation within the corner of the smallest grain, b) the nucleation at the center triple point, and c) the almost fully reversed magnetization distribution within the microstructure.

The nucleation of the magnetization reversal starts in the area of the triple junctions, which represent a weak spot, and propagates from there through the entire grain. This cascade-like magnetization reversal is only stopped by the nearest grain boundaries, such that a jump to another grain can be prevented. The corresponding hysteresis loop (Case A: red, 8 nm) can be found in Fig. 6.16b).

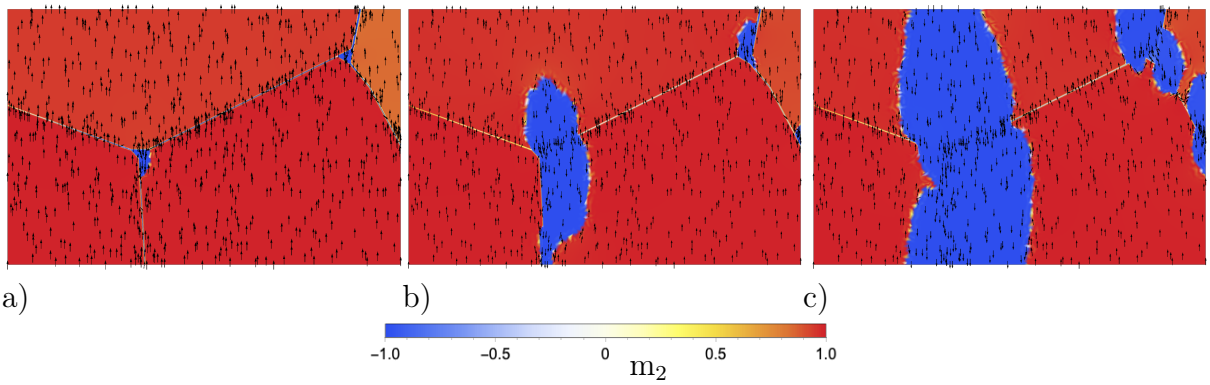

Figure 6.15: Magnetization reversal of the exchange coupled microstructure with a) the nucleation within the triple points and b)-c) the propagation into the surrounding grains.

Nevertheless, if no perfect decoupling is assumed (Case B), but a thinner interphase of 3 nm, which additionally does not consist of pure paramagnetic material, but is slightly ferromagnetic the propagation of the magnetization reversal cannot be stopped at the grain boundaries as presented in Fig. 6.15. Thus, the demagnetization process deviates strongly from Case A presented before in Fig. 6.14. The procedure is applied analogously to SODERŽNIK ET AL. [2017]; the slightly ferromagnetic grain boundary phase is assigned a significantly weakened saturation magnetization $M_s^{GB} = 0.64 \times 10^6$ A/m and an exchange coefficient $A_{exc}^{GB} = 0.4 \times 10^{-11}$ J/m. Moreover, it can be assumed that there is no pronounced orientation dependence of the material in the interphase region, which is equivalent to K_1^{GB}=0.

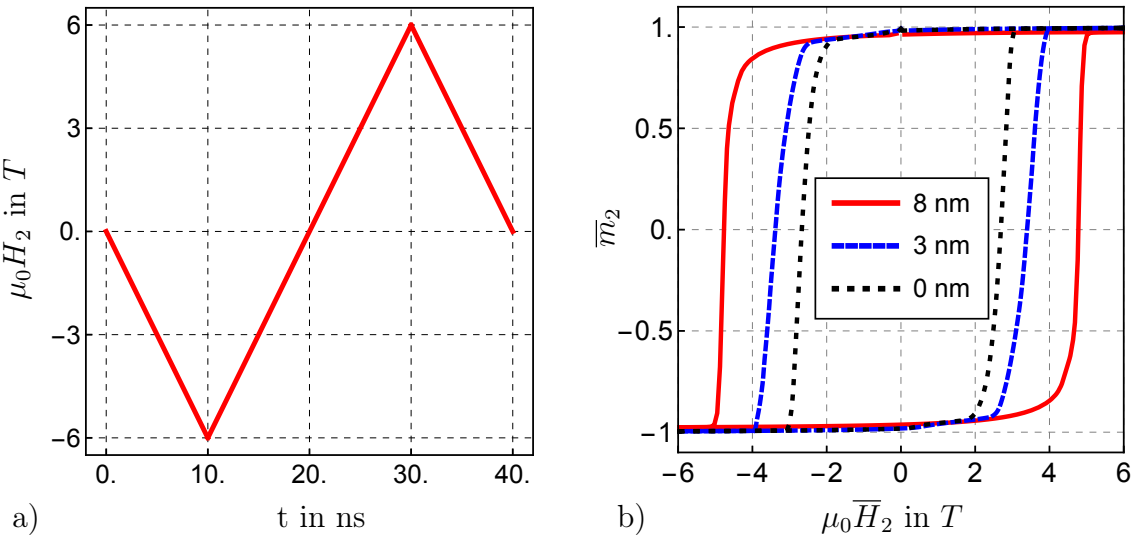

Figure 6.16: a) loading path of the magnetic field and b) the hysteresis loops for different grain boundaries.

Similar to the decoupled Case A, i.e. the red hysteresis loop in Fig. 6.16b), the nucleation starts in the region of the triple points, see Fig. 6.15a). However, the crucial difference in Case B is that the triple points reverse first and subsequently continue to propagate into the ferromagnetic grains. This implies that, compared to the previous Case A, the reversal spreads into all directions and thus leads to a significantly faster demagnetization of the entire magnet. This can also be seen in the corresponding hysteresis in Fig. 6.16b) (Case B: blue, 3 nm). A clear difference between the hysteresis of the decoupled and the coupled system is apparent. This difference eventually illustrates the loss in performance of the weakly ferromagneticaly coupled system compared to that of the perfectly decoupled system. If a microstructure without any grain boundaries is considered (Case C), which means direct contact of the grains with each other, it is evident that even the weak ferromagnetic coupling interphase of Case B can be useful in limiting magnetization reversal. This is shown by comparing the hysteresis of this last case Fig. 6.16b) (Case C: black, 0 nm) with the previous cases in Fig. 6.16b).

6.3 Simulation of a 3D heterogeneous polycrystalline $Nd_2Fe_{14}B$ microstructure

This example is devoted to the analysis of a polycrystalline $Nd_2Fe_{14}B$ microstructure consisting of 10 ferromagnetic grains that are magnetically decoupled from each other by a 3 nm thick paramagnetic Nd-rich layer. Similar to the sections above, the paramagnetic interphase indicates purely magnetostatic behavior. The material parameters of $Nd_2Fe_{14}B$ can be taken from Tab. 6.1. The easy-axes of the grains are almost parallel to the x_3-axis with a deviation of up to $\pm 10°$. The initial magnetization distribution follows the direction of the individual easy-axes within the grains. To analyze the magnetic properties of the microstructure given in Fig. 6.17, a magnetic scalar potential is prescribed on the upper and lower boundary (x_3=0 and x_3=200 nm) of the microstructure that induces a magnetic field $\mu_0 \overline{\boldsymbol{H}} = [0, 0, 6]^{\mathrm{T}}$ T. This field cycles over time, following the load path presented in Fig. 6.1, to generate the hysteresis loop presented in Fig. 6.18. For the generation of the microstructure the software tool Neper was applied in combination with a script written by C. Böhm[12.)] to generate the grain boundaries, cf. Quey et al. [2011] and Quey and Renversade [2018].

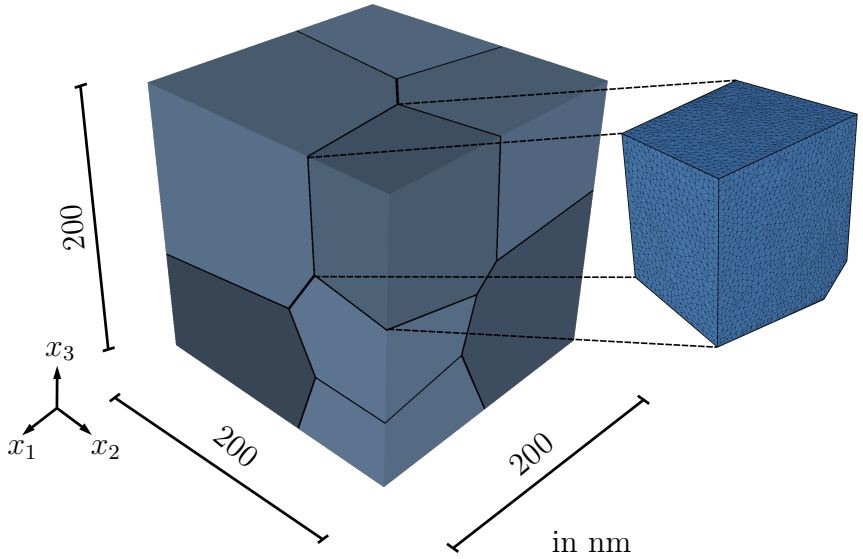

Figure 6.17: A polycrystalline microstructure consisting of hard magnetic $Nd_2Fe_{14}B$ grains and paramagnetic Nd-rich grain boundaries. The zoomed grain highlights the discrete form of the grain to give an impression of the applied mesh density.

The primary variables are interpolated using $\sim 100,000$ linear tetrahedron elements with $\sim 200,000$ degrees of freedom. The initial magnetization distribution is shown in Fig. 6.18a). As the external magnetic field increases, the magnetization vectors turn aside until a critical field is eventually reached, initiating the nucleation of the magnetization reversal. The result of this process can be seen in Fig. 6.18b). The first ferromagnetic grain changes the direction of magnetization. For now, the paramagnetic Nd-rich layer between the individual grains prevents this process from continuing in the adjacent grains. After the upper grain is almost completely switched, the neighboring grain of the first reversed grain also begins to nucleate. The utility of the Nd-rich layer becomes evident in Fig. 6.18c). Half of the magnetization of the polycrystal already points into the negative

[12.)] C. Böhm, Institute of Continuum Mechanics, Leibniz University Hannover.

x_3-direction, while the other still points into the positive x_3-direction. Finally, the signs of magnetization in all grains turn, as can be seen in Fig. 6.18d), such that the microstructure in Fig. 6.18e) is completely demagnetized. When the magnetic field increases again, the process described above is repeated, but in reverse orientation of the magnetization vectors. Thus, a complete hysteresis loop can be described.

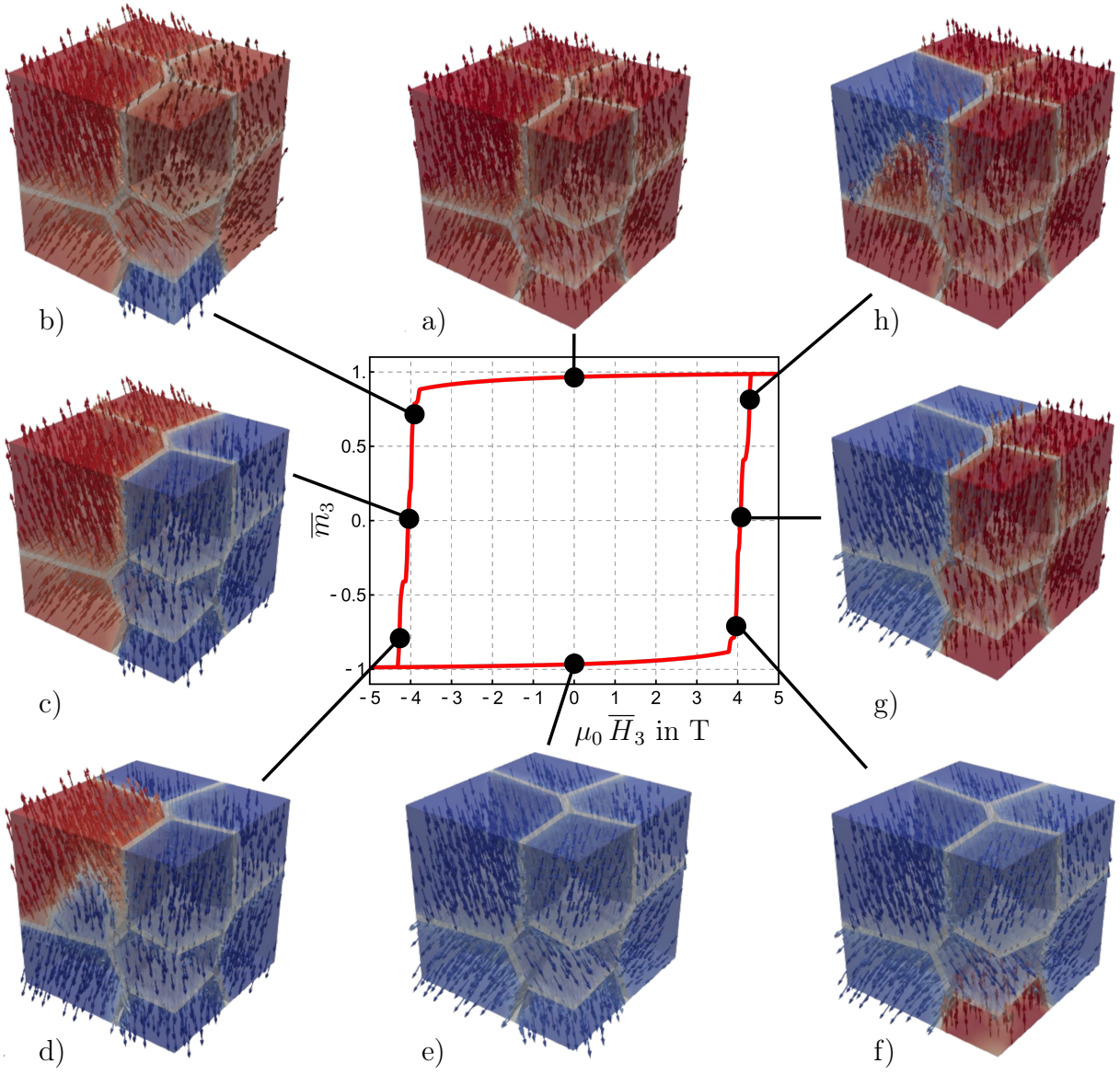

Figure 6.18: The hysteresis loop of the considered polycrystalline microstructure with its corresponding switching states a)-h).

The stepwise reversal of the magnetization in the individual grains can also be seen in the demagnetization branch of the hysteresis in Fig. 6.19. The switching of one grain proceeds very fast, but to generate further switching magnetization within subsequent grains an increase of the magnetic field is necessary. This leads to the kinks in the demagnetizing branch presented in Fig. 6.19. Since these kinks can be associated with inhibition of

reversal, they are indicators of well-decoupled magnetic grains.

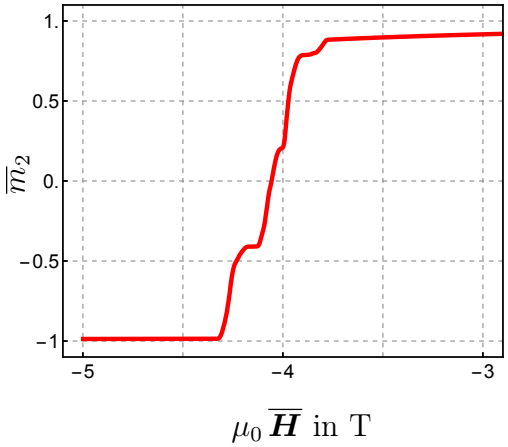

Figure 6.19: The demagnetization branch of the considered polycrystalline microstructure with several kinks.

7 Summary, conclusion, and outlook

Magnetic materials enhance the efficiency of conversion devices such as transformers, power generators like wind turbines, sensors, and electric motors used in electromobility. Due to their importance in optimizing performance in industrial applications, magnetic materials are attracting increasing interest. Hence, this work deals with the numerical characterization of magneto-mechanically coupled material behavior in the framework of the continuum mechanical theory. Fundamental topics, such as the origin of collective magnetism, but also an introduction to continuum mechanics are given first for a better understanding of the subject. Subsequently, two novel numerical methods are developed to omit the direct discretization of the external space in terms of finite elements, surrounding the magnet and allowing for efficient simulations of magnetic stray fields.
The first method is based on static condensation of the exterior space discretized by finite elements onto the surface of the interior space to be analyzed. This approach allows even the consideration of inhomogeneities within the outer space, but is limited to very large but still finite outer regions. The advantage of this method is to select the area to be condensed large enough so that errors due to too small outer spaces do not occur. Due to the static condensation in the form of a preliminary calculation, the size of the outer area does not influence the simulation time. The second method bases on the scaled boundary finite element method and provides a semi-analytical solution for the magnetostatic problem within the outer domain on the surface of the inner domain. Therefore, an SBFEM-FEM-based coupling allows better simulation results with smaller systems of equations compared to fully discretized and non-condensed exterior domains. In contrast to fully discretized geometries both methods provide a significant speedup in computational time by a factor of $\approx$5.0.
Based on the constitutive equations, i.e. the magnetic Gauss law, the Landau-Lifshitz-Gilbert equation, and the balance of momentum, a fully coupled micromagnetic-mechanically system of equations is derived. Since the magnetization vectors within micromagnetic simulations have to be restricted onto the unit sphere, what is not a priori fulfilled, constraining methods are required. The considered system of equations, applying several constraining methods, is eventually implemented and those methods are evaluated for performance, with each other. Finally it can be stated that all methods have their advantages and disadvantages, but the perturbed and condensed Lagrange multiplier has proven to be very robust and time efficient compared to all other implemented methods. Consequently, all subsequent micromagnetic simulations are performed using this formulation. Subsequently, micromagnetic simulations of more realistic structures are performed. The first subsequent series of simulations is focused on the analysis of defect structures in heterogeneous microstructures and their influence on the effective magnetic behavior. These defect structures can be assigned to microstructures produced by continuous rotary swaging. A clear correlation between a strong intensity of defect structures and decreasing effective performance of the magnets is shown. Subsequently, the influence of different grain boundaries on the efficiency of magnetic materials is investigated. Here, a clear dependence between the composition of the grain boundary interphases, which have a magnetic coupling or decoupling effect depending on the composition and coercivity is shown. Finally, a 3D polycrystalline microstructure with the individual grains separated by a grain boundary layer is investigated in this work. This example should rather serve as a motivation for further simulations and demonstrate the workability of the presented method also for large systems, i.e. large systems of equations as well as microstructures.

The functionality of the formulations presented in this work has been demonstrated in detail using representative examples. Consequently, these formulations serve as a starting point for improvements and extensions. Some possible future topics are listed below:

- The perturbed and condensed Lagrange multiplier has proven to be quite robust and performant. Nevertheless, further investigations concerning a priori length-preserving methods without singular points should be carried out to obtain a numerically even more robust formulation.
- The micromagnetic formulation of this work is based on the Landau-Lifshitz-Gilbert equation, which contains a precession term in addition to the damping term. The latter plays a negligible role in the analysis of hard magnetic materials. For this reason, comparative studies between formulations on the bases of the Landau-Lifshitz-Gilbert equation with strong damping and formulations based on the Allen-Cahn (time dependent Ginsburg-Landau equation) should be performed. The Allen-Cahn equation misses of a precession part and has the advantage of yielding symmetrical system matrices which can be advantageous within the numerical solution procedure.
- Extending the formulation with a more efficient time integration method can lead to a significant gain in accuracy and a speedup in computational time.
- Currently, a significant gap exists between the theoretically calculated and the experimentally obtained magnetic properties. This can be caused by over-ideal microstructures, which take too few of the real defects into account. For this reason, a direct comparison between experiment and simulation is necessary. This also requires a real 3D microstructure as a basis for the simulation.

A Computation of the system matrix $\mathbf{K}_{bb}^{\infty}$ of an unbounded domain by SBFEM

To solve boundary value problems within the context of the FEM and SBFEM (among others), second-order ordinary differential equations (ODE) have to be transformed into first-order ODEs. Within this framework, the system of first-order ODEs that is able to describe the evolving magnetic fields can be stated as

$$\xi \underline{\mathbf{X}}_{,\xi} = -\underline{\mathbf{Z}}\underline{\mathbf{X}} - \left\{ \begin{array}{c} \mathbf{0} \\ \underline{\mathbf{F}}(\xi) \end{array} \right\}, \tag{A.1}$$

where the variable $\underline{\mathbf{X}}$ in Eq. A.1 is defined as

$$\underline{\mathbf{X}}(\xi) = \left\{ \begin{array}{c} \xi^{0.5} \underline{\boldsymbol{\varphi}_d}(\xi) \\ \xi^{-0.5} \left(\underline{\mathbf{Q}}(\xi) - \underline{\mathbf{Q}}_0(\xi) \right) \end{array} \right\}. \tag{A.2}$$

Here, the first entry corresponds to N nodal scalar potential degrees of freedom $\underline{\boldsymbol{\varphi}_d}$ and the second entry to N contributions of the nodal flux at an interface ξ. $\underline{\mathbf{Q}}$ is the internal nodal flux and $\underline{\mathbf{Q}}_0$ the initially prescribed nodal flux due to the externally applied magnetic field. Hence, $\underline{\mathbf{X}}$ results in a total length of $2N$. The coefficient matrix

$$\underline{\mathbf{Z}} = \left[\begin{array}{cc} \left[\underline{\mathbf{E}}^0\right]^{-1} \underline{\mathbf{E}}^{1T} - 0.5\underline{\mathbf{I}} & -\left[\underline{\mathbf{E}}^0\right]^{-1} \\ -\underline{\mathbf{E}}^2 + \underline{\mathbf{E}}^1 \left[\underline{\mathbf{E}}^0\right]^{-1} \underline{\mathbf{E}}^{1T} & -(\underline{\mathbf{E}}^1 \left[\underline{\mathbf{E}}^0\right]^{-1} - 0.5\underline{\mathbf{I}}) \end{array} \right] \tag{A.3}$$

is a Hamiltonian matrix with the coefficients $\underline{\mathbf{E}}^0$, $\underline{\mathbf{E}}^1$ and $\underline{\mathbf{E}}^2$ following the derivations given in Birk et al. [2022]. A distinctive characteristic of this formulation is the additional term on the right-hand side of the Eq. A.1. It contains the contribution of the externally applied magnetic field $\underline{\mathbf{F}}$ to the system of equations. In general, all necessary definitions are now introduced to solve the scaled boundary finite element equation Eq. A.1 by means of the eigenvalue method. Here, however, numerical difficulties can occur sinceeigenvectors associated with multiple eigenvalues cannot be decoupled straightforwardly. According to Song [2004], this problem can be avoided if instead of the eigenvalue method, a combination of matrix exponential functions and a real-valued Schur decomposition of the Hamiltonian matrix $\underline{\mathbf{Z}}$ is performed. For more information on this method, it is referred to Song [2004] and Birk et al. [2022]. The transformation matrix $\underline{\boldsymbol{\Psi}}$ given in Eq. 4.69 is a result of this method and can be used to calculate the static system matrix

$$\underline{\mathbb{K}}_{bb}^{\infty} = -\underline{\boldsymbol{\Psi}}_{22} (\underline{\boldsymbol{\Psi}}_{12})^{-1}. \tag{A.4}$$

References

Definitive feasibility study on arafura's nolans project. Technical report, Arafura Resources Ltd., 2019. URL https://www.arultd.com/images/Nolans_DFS_Summary_Report_-_Final_for_website.pdf.

C. Abert, L. Exl, G. Selke, A. Drews, and T. Schrefl. Numerical methods for the stray-field calculation: A comparison of recently developed algorithms. *Journal of Magnetism and Magnetic Materials*, 326:176–185, 2013. doi: 10.1016/j.jmmm.2012.08.041.

A. Adly, I. Mayergoyz, and A. Bergqvist. Preisach modeling of magnetostrictive hysteresis. *Journal of Applied Physics*, 69(8):5777–5779, 1991. doi: 10.1063/1.347873.

G. Aiello, S. Alfonzetti, and E. Dilettoso. Finite-element solution of eddy-current problems in unbounded domains by means of the hybrid FEM-DBCI method. *IEEE Transactions on Magnetics*, 39(3):1409–1412, 2003. doi: 10.1109/TMAG.2003.810366.

N. Akulov. Über das magnetische Quadrupolmoment des Eisenatoms. *Zeitschrift für Physik*, 57(3):249–256, 1929. doi: 10.1007/BF01339712.

N. Akulov. Zur Theorie der Feinstruktur der Magnetisierungskurven der Einkristalle. *Zeitschrift für Physik*, 69(1):78–99, 1931a. doi: 10.1007/BF01391515.

N. S. Akulov. Über den Verlauf der Magnetisierungskurve in starken Feldern. *Zeitschrift für Physik*, 69(11):822–831, 1931b. doi: 10.1007/BF01339465.

F. Alouges. A new finite element scheme for Landau-Lifchitz equations. *Discrete and Continuous Dynamical Systems Series S*, 1(2):187–196, 2008. doi: 10.3934/dcdss.2008.1.187.

Y. Alvandi-Tabrizi and J. Schwartz. Micromagnetic analysis of crystallographic texturing and substrate-induced strain effects in $NiFe_2O_4$ and $CoFe_2O_4$ thin films. *Acta Materialia*, 149:193–205, 2018. doi: doi.org/10.1016/j.actamat.2018.02.039.

S. Bartels and A. Prohl. Convergence of an implicit finite flement method for the Landau–Lifshitz–Gilbert equation. *SIAM Journal on Numerical Analysis*, 44(4):1405–1419, 2006. doi: 10.1137/050631070.

K. J. Bathe. *Finite Elemente Methoden, Matrizen und lineare Algebra, die Methode der finiten Elemente, Lösungen von Gleichgewichtsbedingungen und Bewegungsgleichungen*. Springer, 1986.

M. Baumeister. Rotor of an electroc motor, 2020. URL https://unsplash.com/de/fotos/9LeEVZ6czAU.

A. Bayliss, M. Gunzburger, and E. Turkel. Boundary conditions for the numerical solution of elliptic equations in exterior regions. *SIAM Journal of Applied Mathematics*, 42(2):430–451, 1982. doi: 10.1137/0142032.

R. Becker and W. Döring. *Ferromagnetismus*. Springer-Verlag, 1939. doi: 10.1007/978-3-642-47366-1.

J.-P. Berenger. A perfectly matched layer for the absorption of electromagnetic waves. *Journal of Computational Physics*, 114:185–200, 1994. doi: 10.1006/jcph.1994.1159.

G. Bertotti. *Hysteresis in Magnetism For Physicists, Materials Scientists, and Engineers*. Gulf Professional Publishing, San Diego, 1998. doi: 10.1016/B978-0-12-093270-2.X5048-X.

G. Bertotti and I. Mayergoyz. *The Science of Hysteresis*, volume 2. Elsevier, 2005.

C. Birk, L. Liu, and C. Song. Coupled acoustic response of two-dimensional bounded and unbounded domains using doubly-asymptotic open boundaries. *Journal of Computational Physics*, 310:252–284, 2016.

C. Birk, M. Reichel, and J. Schröder. Magnetostatic simulations with consideration of exterior domains using the scaled boundary finite element method. *Computer Methods in Applied Mechanics and Engineering*, 399:115362, 2022. doi: doi.org/10.1016/j.cma.2022.115362.

R. Bjørk, E. Poulsen, K. Nielsen, and A. Insinga. MagTense: A micromagnetic framework using the analytical demagnetization tensor. *Journal of Magnetism and Magnetic Materials*, 535:168057, 2021. doi: 10.1016/j.jmmm.2021.168057.

A. Bolyachkin, H. Sepehri-Amin, I. Suzuki, H. Tajiri, Y. Takahashi, K. Srinivasan, H. Ho, H. Yuan, T. Seki, A. Ajan, and K. Hono. Transmission electron microscopy image based micromagnetic simulations for optimizing nanostructure of FePt-X heat-assisted magnetic recording media. *Acta Materialia*, 227:117744, 2022. doi: doi.org/10.1016/j.actamat.2022.117744.

O. Bolza. *Lectures on the Calculus of Variations*, volume 14. University of Chicago Press, 1904.

W. Brown. Virtues and weaknesses of the domain concept. *Review of Modern Physics*, 17(1):15–19, 1945.

W. Brown. *Micromagnetics*. Wiley, 1963.

A. Buchau, W. Rucker, O. Rain, V. Rischmüller, S. Kurz, and S. Rjasanow. Comparison between different approaches for fast and efficient 3-D BEM computations. *IEEE Transactions on Magnetics*, 39(3):1107–1110, 2003. doi: 10.1109/TMAG.2003.810167.

A. Bur, T. Wu, J. Hockel, C.-J. Hsu, H. Kim, T.-K. Chung, K. Wong, K. Wang, and G. Carman. Strain-induced magnetization change in patterned ferromagnetic nickel nanostructures. *Journal of Applied Physics*, 109(12):123903, 2011. doi: 10.1063/1.3592344.

G. F. Carey and J. T. Oden. *Finite elements: a second course, Vol. II*, volume 2. Prentice-Hall, Engelwood Cliffs. NJ, 1982.

Q. Chen and A. Konrad. A review of finite element open boundary techniques for static and quasi-static electromagnetic field problems. *IEEE Transactions on Magnetics*, 33:663–676, 1997. doi: 10.1109/20.560095.

W. Chen, D. Fredkin, and T. Koehler. A new finite element method in micromagnetics. *IEEE Transactions on Magnetics*, 29(4):2124–2128, 1993. doi: 10.1109/20.221033.

X. Chen, C. Birk, and C. Song. Time-domain analysis of wave propagation in 3-D unbounded domains by the scaled boundary finite element method. *Soil Dynamics and Earthquake Engineering*, 75:171–182, 2015.

F. Chi, L. Wießner, T. Gröb, E. Bruder, S. Sawatzki, K. Löwe, J. Gassmann, C. Müller, K. Durst, O. Gutfleisch, and P. Groche. Towards manufacturing of Nd-Fe-B magnets by continuous rotary swaging of cast alloy. *Journal of Magnetism and Magnetic Materials*, 490:165405, 2019. doi: 10.1016/j.jmmm.2019.165405.

S. Chikazumi and S. Charap. Physics of magnetism. 1978.

I. Cimrák. A survey on the numerics and computations for the Landau-Lifshitz equation of micromagnetism. *Archives of Computational Methods in Engineering*, 15(3):1–37, 2007. doi: 10.1007/BF03024947.

J. Coey. *Magnetism and magnetic materials*. Cambridge university press, Cambridge, 2010. doi: 10.1017/CBO9780511845000.

J. Coey and S. Parkin. *Handbook of magnetism and magnetic materials*. Springer Nature Switzerland, 2021. doi: 10.1007/978-3-030-63210-6.

L. Comstock. Review modern magnetic materials in data storage. *Journal of Materials Science: Materials in Electronics*, 13(9):509–523, 2002. doi: 10.1023/A:1019642215245.

S. Constantinides. Permanent magnets in a changing world market. *Magnetics Magazine*, 2016. URL `https://magneticsmag.com/permanent-magnets-in-a-changing-world-market/`.

R. Cowburn, D. Koltsov, A. Adeyeye, M. Welland, and D. Tricker. Single-domain circular nanomagnets. *Physical Review Letters*, 83(5):1042, 1999. doi: 10.1103/PhysRevLett.83.1042.

B. Cullity and C. Graham. *Introduction to magnetic materials*. John Wiley and Sons, 2 edition, 2009.

M. d'Aquino, C. Serpico, and G. Miano. Geometrical integration of Landau-Lifshitz-Gilbert equation based on the mid-point rule. *Journal of Computational Physics*, 209 (2):730–753, 2005. doi: 10.1016/j.jcp.2005.04.001.

A. DeSimone, R. Kohn, S. Müller, and F. Otto. Recent analytical developments in micromagnetics. In G. Bertotti and I. Mayergoyz, editors, *The science of hysteresis*, volume 2, pages 269–381. Elsevier, 2006.

M. Donahue and R. McMichael. Exchange energy representations in computational micromagnetics. *Physica B: Condensed Matter*, 233(4):272–278, 1997. doi: doi.org/10.1016/S0921-4526(97)00310-4.

W. Döring. Point singularities in micromagnetism. *Journal of Applied Physics*, 39(2): 1006–1007, 1968. doi: 10.1063/1.1656144.

W. Dornisch, D. Schrade, B.-X. Xu, M.-A. Keip, and R. Müller. Coupled phase field simulations of ferroelectric and ferromagnetic layers in multiferroic heterostructures. *Archive of Applied Mechanics*, 89(6):1031–1056, 2018. doi: doi.org/10.1007/s00419-018-1480-9.

L. Euler. Methodus inveniendi lineas curvas maximi minimive proprietate gaudentes, sive solutio problematis isoperimetrici lattissimo sensu accept. 1744. URL `https://scholarlycommons.pacific.edu/euler-works/65`.

L. Euler. Elementa calculi variationum. 1766. URL `https://scholarlycommons.pacific.edu/euler-works/296`.

J. Fidler and T. Schrefl. Micromagnetic modelling-the current state of the art. *Journal of Physics D: Applied Physics*, 33:R135–R156, 2000. doi: 10.1088/0022-3727/33/15/201.

J. Fidler, T. Schrefl, W. Scholz, D. Suess, R. Dittrich, and M. Kirschner. Micromagnetic modelling and magnetization processes. *Journal of Magnetism and Magnetic Materials*, 272-276:641–646, 2004. doi: doi.org/10.1016/j.jmmm.2003.12.1007. Proceedings of the International Conference on Magnetism (ICM 2003).

J. Fischbacher, A. Kovacs, M. Gusenbauer, H. Oezelt, L. Exl, S. Bance, and T. Schrefl. Micromagnetics of rare-earth efficient permanent magnets. *Journal of Physics D: Applied Physics*, 51(19):193002, 2018. doi: 10.1088/1361-6463/aab7d1.

H. Forster, T. Schrefl, W. Scholz, D. Suess, V. Tsiantos, and J. Fidler. Micromagnetic simulation of domain wall motion in magnetic nano-wires. *Journal of Magnetism and Magnetic Materials*, 249(1):181–186, 2002. doi: doi.org/10.1016/S0304-8853(02)00528-0.

C. Fox. *An introduction to the calculus of variations*. Courier Corporation, 1987.

D. Fredkin and T. Koehler. Numerical micromagnetics by the finite element method. *IEEE Transactions on Magnetics*, 23(5):3385–3387, 1987. doi: 10.1109/TMAG.1987.1065578.

D. Fredkin and T. Koehler. Numerical micromagnetics of small particles. *IEEE Transactions on Magnetics*, 24(6):2362–2367, 1988. doi: 10.1109/20.92110.

R. Gauß, C. Burkhardt, R. Carencotte, M. Gasparon, O. Gutfleisch, I. Higgins, M. Karajić, A. Klossek, M. Mäkinen, B. Schäfer, R. Schindler, and B. Veluri. Rare earth magnets and motors: A European call for action. *A report by the Rare Earth Magnets and Motors Cluster of the European Raw Materials Alliance, Berlin*, 2021.

M. Getzlaff. *Fundamentals of magnetism*. Springer Science & Business Media, 2008.

T. Gilbert. Formulation, foundations and applications of the phenomenological theory of ferromagnetism. *Ph. D. Thesis*, 1956.

T. Gilbert. A phenomenological theory of damping in ferromagnetic materials. *IEEE transactions on magnetics*, 40(6):3443–3449, 2004.

D. Givoli. Non–reflecting boundary conditions. *Journal of Computational Physics*, 94: 1–29, 1991. doi: 10.1016/0021-9991(91)90135-8.

O. Gutfleisch. Controlling the properties of high energy density permanent magnetic materials by different processing routes. *Journal of Physics C: Applied Physics*, 33: R157–R172, 2000. doi: 10.1088/0022-3727/33/17/201.

O. Gutfleisch, M. Willard, E. Brück, C. Chen, S. Sankar, and J. P. Liu. Magnetic materials and devices for the 21st century: Stronger, lighter, and more energy efficient. *Advanced Materials*, 23(7):821–842, 2011. doi: 10.1002/adma.201002180.

T. Helbig, K. Loewe, S. Sawatzki, M. Yi, B.-X. Xu, and O. Gutfleisch. Experimental and computational analysis of magnetization reversal in (Nd,Dy)-Fe-B core shell sintered magnets. *Acta Materialia*, 127:498–504, 2017. doi: 10.1016/j.actamat.2017.01.055.

J. Herbst and J. Croat. Neodymium-iron-boron permanent magnets. *Journal of Magnetism and Magnetic Materials*, 100(1):57–78, 1991. doi: doi.org/10.1016/0304-8853(91)90812-O.

R. Hertel and H. Kronmuller. Adaptive finite element mesh refinement techniques in three-dimensional micromagnetic modeling. *IEEE Transactions on Magnetics*, 34(6): 3922–3930, 1998. doi: 10.1109/20.728305.

R. Hertel, S. Christophersen, and S. Börm. Large-scale magnetostatic field calculation in finite element micromagnetics with $\mathcal{H}^2$-matrices. *Journal of Magnetism and Magnetic Materials*, 477:118–123, 2019. doi: 10.1016/j.jmmm.2018.12.103.

G. Holzapfel. *Nonlinear solid mechanics - A continuum approach for engineering*. John Wiley & Sons, 2000.

G. Hrkac, T. Woodcock, C. Freeman, A. Goncharov, J. Dean, T. Schrefl, and O. Gutfleisch. The role of local anisotropy profiles at grain boundaries on the coercivity of $Nd_2Fe_{14}B$ magnets. *Applied Physics Letters*, 97(23):232511, 2010. doi: 10.1063/1.3519906.

G. Hrkac, K. Butler, T. Woodcock, L. Saharan, T. Schrefl, and O. Gutfleisch. Modeling of Nd-oxide grain boundary phases in Nd-Fe-B sintered magnets. *JOM*, 66(7):1138–1143, 2014a. doi: 10.1007/s11837-014-0980-5.

G. Hrkac, T. Woodcock, K. Butler, L. Saharan, M. Bryan, T. Schrefl, and O. Gutfleisch. Impact of different Nd-rich crystal-phases on the coercivity of Nd-Fe-B grain ensembles. *Scripta Materialia*, 70:35–38, 2014b. ISSN 1359-6462. doi: 10.1016/j.scriptamat.2013.08.029.

A. Hubert and R. Schäfer. *Magnetic domains: The analysis of magnetic microstructures*, volume 3. Springer Science & Business Media, Berlin, 1998. doi: doi.org/10.1007/978-3-540-85054-0.

A. Inoue and F. Kong. Soft magnetic materials. *Encyclopedia of Smart Materials*, 5: 10–23, 2020. doi: 10.1016/B978-0-12-803581-8.11725-4.

A. Insinga, E. Poulsen, K. Nielsen, and R. Bjørk. A direct method to solve quasistatic micromagnetic problems. *Journal of Magnetism and Magnetic Materials*, 510:166900, 2020. doi: 10.1016/j.jmmm.2020.166900.

D. Jiles. *Introduction to Magnetism and Magnetic Materials*, volume 3. CRC Press, London, 2015. doi: 10.1007/978-1-4615-3868-4.

D. Jiles and D. Atherton. Ferromagnetic hysteresis. *IEEE Transactions on Magnetics*, 19 (5):2183–2185, 1983. doi: 10.1109/TMAG.1983.1062594.

D. Jiles and D. Atherton. Theory of ferromagnetic hysteresis. *Journal of Magnetism and Magnetic Materials*, 61(1):48–60, 1986. doi: doi.org/10.1016/0304-8853(86)90066-1.

M.-A. Keip and M. Rambausek. A multiscale approach to the computational characterization of magnetorheological elastomers. *International Journal for Numerical Methods in Engineering*, 107(4):338–360, 2016. doi: 10.1002/nme.5178.

M.-A. Keip and M. Rambausek. Computational and analytical investigations of shape effects in the experimental characterization of magnetorheological elastomers. *International Journal of Solids and Structures*, 121:1–20, 2017. doi: 10.1016/j.ijsolstr.2017.04.012.

M. Kemp. Porsche taycan parked at the roadside, 2021. URL `https://unsplash.com/de/fotos/2w_Nxti8iKE`.

M. Khan, J. Sun, B. Li, A. Przybysz, and J. Kosel. Magnetic sensors-A review and recent technologies. *Engineering Research Express*, 3(2):022005, 2021. doi: 10.1088/2631-8695/ac0838.

K. Khlopkov, O. Gutfleisch, D. Eckert, D. Hinz, B. Wall, W. Rodewald, K.-H. Müller, and L. Schultz. Local texture in Nd-Fe-B sintered magnets with maximised energy density. *Journal of Alloys and Compounds*, 365(1):259–265, 2004. doi: 10.1016/S0925-8388(03)00636-4.

C. Kittel. Physical theory of ferromagnetic domains. *Reviews of modern Physics*, 21(4):541, 1949. doi: 10.1103/RevModPhys.21.541.

E. Kneller, A. Seeger, and H. Kronmüller. *Magnetisierungskurve von Einkristallen*, pages 472–498. Springer Berlin Heidelberg, Berlin, Heidelberg, 1962. doi: 10.1007/978-3-642-86695-1_28.

A. Knittel, M. Franchin, G. Bordignon, T. Fischbacher, S. Bending, and H. Fangohr. Compression of boundary element matrix in micromagnetic simulations. *Journal of Applied Physics*, 105(7):07D542, 2009. doi: 10.1063/1.3072032.

J. Korelc. Automatic generation of finite-element code by simultaneous optimization of expressions. *Theoretical Computer Science*, 187(1):231–248, 1997.

J. Korelc. Multi-language and multi-environment generation of nonlinear finite element codes. *Engineering with Computers*, 18:312–327, 2002.

J. Korelc and P. Wriggers. *Automation of finite element methods*. Springer, 2016.

A. Kovacs, J. Fischbacher, M. Gusenbauer, H. Oezelt, H. Herper, O. Vekilova, P. Nieves, S. Arapan, and T. Schrefl. Computational design of rare-earth reduced permanent magnets. *Engineering*, 6(2):148–153, 2020. doi: doi.org/10.1016/j.eng.2019.11.006.

H. Kronmüller. Microstructure and micromagnetism. *AIP Conference Proceedings*, 10(1): 1006–1025, 1973. doi: 10.1063/1.2946732.

H. Kronmüller. Theory of nucleation fields in inhomogeneous ferromagnets. *physica status solidi (b)*, 144:385–396, 1987. doi: 10.1002/pssb.2221440134.

H. Kronmüller, R. Fischer, M. Seeger, and A. Zern. Micromagnetism and microstructure of hard magnetic materials. *Journal of Physics D: Applied Physics*, 29(9):2274, 1996. doi: 10.1088/0022-3727/29/9/008.

M. Kružík and A. Prohl. Recent developments in the modeling, analysis, and numerics of ferromagnetism. *SIAM Review*, 48(3):439–483, 2006. doi: 10.1137/S0036144504446187.

M. Kuchibhotla, A. Talapatra, A. Haldar, and A. Adeyeye. Magnetization dynamics of single and trilayer Permalloy nanodots. *Journal of Applied Physics*, 130(8):083906, 2021. doi: 10.1063/5.0060689.

M. Labusch. *A two-scale homogenization scheme for the prediction of magneto-electric product properties*. PhD thesis, Duisburg ; Essen, 2018.

M. Labusch, J. Schröder, and M. Keip. *An FE^2-Scheme for Magneto-Electro-Mechanically Coupled Boundary Value Problems*, pages 227–262. Springer International Publishing, 2018. doi: 10.1007/978-3-319-68883-1_5.

M. Labusch, J. Schröder, and D. Lupascu. 3D magnetostrictive Preisach model for the analysis of magneto-electric composites. *Archive of Applied Mechanics*, 89(6):1011–1030, 2019.

V. Lacovacci, G. Lucarini, L. Ricotti, and A. Menciassi. Magnetic field-based technologies for lab-on-a-chip applications. In M. Stoytcheva and R. Zlatev, editors, *Lab-on-a-Chip Fabrication and Application*, chapter 3. IntechOpen, 2016. doi: 10.5772/62865.

L. Landau and E. Lifshitz. On the theory of the dispersion of magnetic permeability in ferromagnetic bodies. In *Perspectives in Theoretical Physics*, pages 51–65. Elsevier, 1935. doi: 10.1016/B978-0-08-036364-6.50008-9.

C. Landis. A continuum thermodynamics formulation for micro-magneto-mechanics with applications to ferromagnetic shape memory alloys. *Journal of the Mechanics and Physics of Solids*, 56(10):3059–3076, 2008. doi: 10.1016/j.jmps.2008.05.004.

D. Lewis and N. Nigam. Geometric integration on spheres and some interesting applications. *Journal of Computational and Applied Mathematics*, 151(1):141–170, 2003. doi: doi.org/10.1016/S0377-0427(02)00743-4.

C.-Y. Liang, S. M. Keller, A. E. Sepulveda, A. Bur, W.-Y. Sun, K. Wetzlar, and G. P. Carman. Modeling of magnetoelastic nanostructures with a fully coupled mechanical-micromagnetic model. *Nanotechnology*, 25(43):435701, 2014. doi: 10.1088/0957-4484/25/43/435701.

J. Liu and G. Lin. A scaled boundary finite element method applied to electrostatic problems. *Engineering Analysis with Boundary Elements*, 36:1721–1732, 2012. doi: 10.1016/j.enganabound.2012.06.010.

J. Liu, P. Zhang, G. Lin, W. Wang, and S. Lu. Solutions for the magneto-electro-elastic plate using the scaled boundary finite element method. *Engineering Analysis with Boundary Elements*, 68:103–114, 2016. doi: 10.1016/j.enganabound.2016.04.005.

D. Lupascu, I. Anusca, M. Etier, Y. Gao, G. Lackner, A. Nazrabi, M. Sanlialp, H. Trivedi, N. Ul-Haq, and J. Schröder. *Semiconductor Effects in Ferroelectrics*, pages 97–178. Springer International Publishing, 2018. doi: 10.1007/978-3-319-68883-1_3.

B. Mahato, S. Choudhury, R. Mandal, S. Barman, Y. Otani, and A. Barman. Tunable configurational anisotropy in collective magnetization dynamics of $Ni_{80}Fe_{20}$ nanodot arrays with varying dot shapes. *Journal of Applied Physics*, 117(21):213909, 2015. doi: 10.1063/1.4921976.

P. Mariano. *Variational Views in Mechanics*. Springer, 2021. doi: 10.1007/978-3-030-90051-9.

T. Marr, J. Freudenberger, K. D. D. Seifert, H. Klauß, J. Romberg, I. Okulov, J. Scharnweber, A. Eschke, C. Oertel, W. Skrotzki, U. Kühn, J. Eckert, and L. Schultz. Ti-Al composite wires with high specific strength. *Metals*, 1(1):79–97, 2011. doi: 10.3390/met1010079.

P. Mcguiness, O. Akdogan, A. Asali, S. Bance, F. Bittner, J. Coey, N. Dempsey, J. Fidler, D. Givord, O. Gutfleisch, M. Katter, D. L. Roy, S. Sanvito, T. Schrefl, L. Schultz, C. Schwöbl, M. Soderžnik, S. Šturm, P. Tozman, K. Üstüner, M. Venkatesan, T. G. Woodcock, K. Žagar, and S. Kobe. Replacement and original magnet engineering options (ROMEOs): A european seventh framework project to develop advanced permanent magnets without, or with reduced use of, critical raw materials. *JOM*, 67(6):1306–1317, 2015. doi: 10.1007/s11837-015-1412-x.

R. McMichael, M. Donahue, D. Porter, and J. Eicke. Switching dynamics and critical behavior of standard problem No. 4. *Journal of Applied Physics*, 89(11):7603–7605, 2001. doi: 10.1063/1.1355356.

C. Miehe and G. Ethiraj. A geometrically consistent incremental variational formulation for phase field models in micromagnetics. *Computer Methods in Applied Mechanics and Engineering*, 245-246:331–347, 2012. doi: doi.org/10.1016/j.cma.2012.03.021.

J. Miltat and M. Donahue. Numerical micromagnetics: Finite difference methods. *Handbook of magnetism and advanced magnetic materials*, 2:742–764, 2007.

μMag, 1995. URL `https://www.ctcms.nist.gov/mumag/mumag.org.html`.

G. Muscas, P. Jönsson, I. Serrano, Ö. Vallin, and M. Kamalakar. Ultralow magnetostrictive flexible ferromagnetic nanowires. *Nanoscale*, 13(12):6043–6052, 2021. doi: 10.1039/d0nr08355k.

D. T. D. Nguyen, F. Javidan, M. Attar, S. Natarajan, Z. Yang, E. H. Ooi, C. Song, and E. T. Ooi. Fracture analysis of cracked magneto-electro-elastic functionally graded materials using scaled boundary finite element method. *Theoretical and Applied Fracture Mechanics*, 118:103228, 2022. doi: doi.org/10.1016/j.tafmec.2021.103228.

D. Ohmer. *Multi-physics phase-field modeling of magnetic materials*. PhD thesis, Technische Universität, Darmstadt, 2022. URL http://tubiblio.ulb.tu-darmstadt.de/131597/.

D. Ohmer, M. Yi, O. Gutfleisch, and B. X. Xu. Phase-field modelling of paramagnetic austenite–ferromagnetic martensite transformation coupled with mechanics and micromagnetics. *International Journal of Solids and Structures*, 238:111365, 2022. doi: 10.1016/j.ijsolstr.2021.111365.

F. Preisach. Über die magnetische nachwirkung. *Zeitschrift für Physik*, 94(5):277–302, 1935. doi: 10.1007/BF01349418.

A. Prohl. *Computational micromagnetism*. Springer, 1 edition, 2001. doi: 10.1007/978-3-663-09498-2.

R. Quey and L. Renversade. Optimal polyhedral description of 3D polycrystals: Method and application to statistical and synchrotron X-ray diffraction data. *Computer Methods in Applied Mechanics and Engineering*, 330:308–333, 2018. doi: doi.org/10.1016/j.cma.2017.10.029.

R. Quey, P. Dawson, and F. Barbe. Large-scale 3D random polycrystals for the finite element method: Generation, meshing and remeshing. *Computer Methods in Applied Mechanics and Engineering*, 200(17):1729–1745, 2011. doi: doi.org/10.1016/j.cma.2011.01.002.

M. Reichel, B.-X. Xu, and J. Schröder. A comparative study of finite element schemes for micromagnetic mechanically coupled simulations. *Journal of Applied Physics*, 132 (18):183903, 2022. doi: 10.1063/5.0105613.

M. Reichel, P. Groche, O. Gutfleisch, and J. Schröder. Impact of soft magnetic α-Fe in hard $Nd_2Fe_{14}B$ magnetic materials: A micromagnetic study. *Proceedings in Applied Mathematics and Mechanics*, page e202300104, 2023a. doi: 10.1002/pamm.202300104.

M. Reichel, R. Niekamp, and J. Schröder. Efficient micromagnetic simulations based on a perturbed Lagrangian function. *Journal of Applied Physics*, 134(10):103901, 2023b. doi: 10.1063/5.0159273.

M. Reichel, J. Schröder, and B.-X. Xu. Efficient micromagnetic finite element simulations using a perturbed Lagrange multiplier method. *Proceedings in Applied Mathematics and Mechanics*, 22(1):e202200016, 2023c. doi: doi.org/10.1002/pamm.202200016.

A. Rostek-Buetti. Wenn Seltene Erden zur "Waffe" werden. *Deutsche Welle*, 2019. URL https://p.dw.com/p/3Jweq.

P. Sarker, Y. Guo, H. Lu, and J. Zhu. A generalized inverse preisach dynamic hysteresis model of fe-based amorphous magnetic materials. *Journal of Magnetism and Magnetic Materials*, 514:167290, 2020. doi: https://doi.org/10.1016/j.jmmm.2020.167290.

L. Schäfer, K. Skokov, J. Liu, F. Maccari, T. Braun, S. Riegga, I. Radulov, J. Gassmann, H. Merschroth, J. Harbig, M. Weigold, and O. Gutfleisch. Design and qualification of Pr-Fe-Cu-B alloys for the additive manufacturing of permanent magnets. *Advanced Functional Materials*, 31(33):2102148, 2021. doi: 10.1002/adfm.202102148.

C. Schmitz-Antoniak. Grundlagen des Magnetismus (lecture notes). 2012/2013.

W. Scholz, J. Fidler, T. Schrefl, D. Süss, H. Forster, and V. Tsiantos. Scalable parallel micromagnetic solvers for magnetic nanostructures. *Computational Materials Science*, 28(2):366–383, 2003. doi: 10.1016/S0927-0256(03)00119-8.

J. Schröder. A numerical two-scale homogenization scheme: the FE^2–method. In J. Schröder and K. Hackl, editors, *Plasticity and Beyond - Microstructures, Crystal-Plasticity and Phase Transitions*, volume 550 of *CISM Courses and Lectures*, pages 1–64. Springer, 2014.

J. Schröder, M. Labusch, and M.-A. Keip. Algorithmic two-scale transition for magneto-electro-mechanically coupled problems; FE^2-scheme: Localization and homogenization. *Computer Methods in Applied Mechanics and Engineering*, 302:253–280, 2016. doi: https://doi.org/10.1016/j.cma.2015.10.005.

J. Schröder, M. Reichel, and C. Birk. An efficient numerical scheme for the FE-approximation of magnetic stray fields in infinite domains. *Computational Mechanics*, 70(1):141–153, 2022. doi: 10.1007/s00466-022-02162-1.

J. Schröder, R. de Boer, and J. Bluhm. *Tensor calculus for engineers with applications to continuum and computational mechanics*. Springer, Berlin, Heidelberg, New York, 2023. to appear.

H. Sepehri-Amin, I. Dirba, X. Tang, T. Ohkubo, T. Schrefl, O. Gutfleisch, and K. Hono. Development of high coercivity anisotropic Nd-Fe-B/Fe nanocomposite powder using hydrogenation disproportionation desorption recombination process. *Acta Materialia*, 175:276–285, 2019. doi: 10.1016/j.actamat.2019.06.017.

D. Shepherd, J. Miles, M. Heil, and M. Mihajlović. An adaptive step implicit midpoint rule for the time integration of newton's linearisations of non-linear problems with applications in micromagnetics. *Journal of Scientific Computing*, 80(2):1058–1082, 2019. doi: 10.1007/s10915-019-00965-8.

J. Simo, P. Wriggers, and R. L. Taylor. A perturbed Lagrangian formulation for the finite element solution of contact problems. *Computer Methods in Applied Mechanics and Engineering*, 50(2):163–180, 1985. doi: 10.1016/0045-7825(85)90088-X.

J. Sladek, V. Sladek, S. Krahulec, and C. Song. Micromechanics determination of effective properties of voided magnetoelectroelastic materials. *Computational Materials Science*, 116:103–112, 2016. doi: doi.org/10.1016/j.commatsci.2015.05.015.

M. Soderžnik, M. Korent, K. Soderžnik, M. Katter, K. Üstüner, and S. Kobe. High-coercivity Nd-Fe-B magnets obtained with the electrophoretic deposition of submicron TbF3 followed by the grain-boundary diffusion process. *Acta Materialia*, 115:278–284, 2016. doi: doi.org/10.1016/j.actamat.2016.06.003.

M. Soderžnik, H. Sepehri-Amin, T. Sasaki, T. Ohkubo, Y. Takada, T. Sato, Y. Kaneko, A. Kato, T. Schrefl, and K. Hono. Magnetization reversal of exchange-coupled and exchange-decoupled Nd-Fe-B magnets observed by magneto-optical Kerr effect microscopy. *Acta Materialia*, 135:68–76, 2017. doi: 10.1016/j.actamat.2017.05.006.

C. Song. A matrix function solution for the scaled boundary finite-element equation in statics. *Computer Methods in Applied Mechanics and Engineering*, 193:2325–2356, 2004. doi: doi.org/10.1016/j.cma.2004.01.017.

C. Song. *The Scaled Boundary Finite Element Method: Introduction to Theory and Implementation*. Wiley, 2018. doi: 10.1002/9781119388487.

C. Song and J. P. Wolf. The scaled boundary finite-element method – alias consistent infinitesimal finite-element cell method – for elastodynamics. *Computer Methods in Applied Mechanics and Engineering*, 147:329–355, 1997. doi: 10.1016/S0045-7825(97)00021-2.

A. Sridhar, M. Keip, and C. Miehe. Computational homogenization in micro-magneto-elasticity. *Proceedings in Applied Mathematics and Mechanics*, 15(1):363–364, 2015. doi: 10.1002/pamm.201510172.

A. Sridhar, M.-A. Keip, and C. Miehe. Homogenization in micro-magneto-mechanics. *Computational Mechanics*, 58:151–169, 2016. doi: 10.1007/s00466-016-1286-y.

F. Staab, Y. Yang, E. Foya, E. Bruder, B. Zingsem, E. Adabifiroozjaei, K. Skokov, M. Farle, R. Dunin-Borkowski, L. Molina-Luna, O. Gutfleisch, B. Xu, and K. Durst. Influence of amorphous phase on coercivity in SmCo5-Cu nanocomposites, 2023.

E. Stein and F.-J. Barthold. Elastizitätstheorie. In *Der Ingenieurbau, Grundwissen: Werkstoffe, Elastizitätstheorie*. 1996.

E. Stoner and E. P. Wohlfarth. A mechanism of magnetic hysteresis in heterogeneous alloys. *Philosophical Transactions of the Royal Society of London. Series A, Mathematical and Physical Sciences*, 240(826):599–642, 1948. doi: 10.1098/rsta.1948.0007.

D. Sudsom, I. Junger, C. Döpke, T. Blachowicz, L. Hahn, and A. Ehrmann. Micromagnetic simulation of vortex development in magnetic bi-material bow-tie structures. *Condensed Matter*, 5(1):5, 2020. doi: 10.3390/condmat5010005.

D. Süss, T. Schrefl, and J. Fidler. Micromagnetics simulation of high energy density permanent magnets. *IEEE transactions on magnetics*, 36(5):3282–3284, 2000. doi: 10.1109/20.908770.

I. Szabó and R. Sauer. *Mathematische Hilfsmittel des Ingenieurs: Teil 2*. 1967.

H. Szambolics, L. Buda-Prejbeanu, J. Toussaint, and O. Fruchart. A constrained finite element formulation for the Landau-Lifshitz-Gilbert equations. *Computational material science*, 44(2):253–258, 2008. doi: 10.1016/j.commatsci.2008.03.01.

R. Szewczyk. Technical BH saturation magnetization curve models for SPICE, FEM and MoM simulations. *Journal of Automation Mobile Robotics and Intelligent Systems*, 10 (2):3–7, 2016. doi: 10.14313/JAMRIS_2-2016/10.

J. Takács. A phenomenological mathematical model of hysteresis. *Compel*, 20(4):1002–1015, 2001. doi: 10.1108/EUM0000000005771.

C. Trusdell and W. Noll. *The non-linear field theories of mechanics*. third edition, 2004.

V. Tsiantos, D. Suess, T. Schrefl, and J. Fidler. Stiffness analysis for the micromagnetic standard problem No. 4. *Journal of Applied Physics*, 89(11):7600–7602, 2001. doi: 10.1063/1.1355355.

A. Vansteenkiste, J. Leliaert, M. Dvornik, M. Helsen, F. Garcia-Sanchez, and B. V. Waeyenberge. The design and verification of mumax3. *AIP Advances*, 4(10):107133, 2014. doi: 10.1063/1.4899186.

A. Vorwerk. Windrad in Dolberg. 2023.

A. Wachowiak, J. Wiebe, M. Bode, O. Pietzsch, M. Morgenstern, and R. Wiesendanger. Direct observation of internal spin structure of magnetic vortex cores. *Science*, 298 (5593):577–580, 2002. doi: 10.1126/science.1075302.

J. Wang and J. Zhang. A real-space phase field model for the domain evolution of ferromagnetic materials. *International Journal of Solids and Structures*, 50(22-23):3597–3609, 2013. doi: doi.org/10.1016/j.ijsolstr.2013.07.001.

L. Weissitsch, F. Staab, K. Durst, and A. Bachmaier. Magnetic materials via high-pressure torsion of powders. *Materials Transactions*, 64(7):1537–1550, 2023. doi: 10.2320/matertrans.MT-MF2022026.

H. Williams. Magnetic properties of single crystals of silicon iron. *Physical Review*, 52: 747–751, 1937. doi: 10.1103/PhysRev.52.747.

J. Wolf and C. Song. Dynamic-stiffness matrix in time domain of unbounded medium by infinitesimal finite element cell method. *Earthquake Engineering and Structural Dynamics*, 23:1181–1198, 1994. doi: doi.org/10.1002/eqe.4290231103.

J. Wolf and C. Song. The scaled boundary finite–element method – a primer: derivations. *Computers and Structures*, 78:191–210, 2000. doi: 10.1016/S0045-7949(00)00099-7.

P. Wriggers. *Nichtlineare Finite-Element-Methoden*. Springer-Verlag, Berlin, 2001.

P. Wriggers. *Nonlinear finite element methods*. Springer Science & Business Media, 2008. doi: 10.1007/978-3-540-71001-1.

Y. Yang, T. Oyedeji, X. Zhou, K. Albe, and B. Xu. Tailoring magnetic hysteresis of additive manufactured Fe-Ni permalloy via multiphysics-multiscale simulations of process-property relationships. *npj Computational Materials*, 9(1):103, 2023. doi: 10.1038/s41524-023-01058-9.

W. Ye, J. Liu, Q. Zang, and G. Lin. Magneto-electro-elastic semi-analytical models for free vibration and transient dynamic responses of composite cylindrical shell structures. *Mechanics of Materials*, 148:103495, 2020. doi: 10.1016/j.mechmat.2020.103495.

M. Yi and B.-X. Xu. A constraint-free phase field model for ferromagnetic domain evolution. *Proceedings of the Royal Society A*, 470(2171):20140517, 2014. doi: doi.org/10.1098/rspa.2014.0517.

H. Zhang, X. Zhang, and Y. Pei. A finite element based real-space phase field model for domain evolution of ferromagnetic materials. *Computational Materials Science*, 118: 214–223, 2016. doi: 10.1016/j.commatsci.2016.03.020.

O. Zienkiewicz and R. Taylor. *The finite element method - for solid and structural mechanics*. Elsevier, 6 edition, 2005.

Der Lebenslauf ist in der Online-Version
aus Gründen des Datenschutzes nicht enthalten.

In dieser Schriftenreihe bisher erschienene Berichte:

Nr. 1 (2004) *Ein Modell zur Beschreibung finiter anisotroper elastoplastischer Deformationen unter Berücksichtigung diskreter Rissausbreitung*, J. Löblein, Dissertation, 2004.

Nr. 2 (2006) *Polyconvex Anisotropic Energies and Modeling of Damage applied to Arterial Walls*, D. Balzani, Dissertation, 2006.

Nr. 3 (2006) *Kontinuumsmechanische Modellierung ferroelektrischer Materialien im Rahmen der Invariatentheorie*, H. Romanowski, Dissertation, 2006.

Nr. 4 (2007) *Mehrskalen-Modellierung polykristalliner Ferroelektrika basierend auf diskreten Orientierungsverteilungsfunktionen*, I. Kurzhöfer, Dissertation, 2007.

Nr. 5 (2007) *Proceedings of the First Seminar on the Mechanics of Multifunctional Materials*, J. Schröder, D.C. Lupascu, D. Balzani (Ed.), Tagungsband, 2007.

Nr. 6 (2008) *Zur Modellierung und Simulation diskreter Rissausbreitungsvorgänge*, O. Hilgert, Dissertation, 2008.

Nr. 7 (2009) *Least-Squares Mixed Finite Elements for Solid Mechanics*, A. Schwarz, Dissertation, 2009.

Nr. 8 (2010) *Design of Polyconvex Energy Functions for All Anisotropy Classes*, V. Ebbing, Dissertation, 2010.

Nr. 9 (2012) *Modeling of Electro-Mechanically Coupled Materials on Multiple Scales*, M.-A. Keip, Dissertation, 2012.

Nr. 10 (2012) *Geometrical Modeling and Numerical Simulation of Heterogeneous Materials*, D. Brands, Dissertation, 2012.

Nr. 11 (2012) *Modeling and simulation of arterial walls with focus on damage and residual stresses*, S. Brinkhues, Dissertation, 2012.

Nr. 12 (2014) *Proceedings of the Second Seminar on the Mechanics of Multifunctional Materials*, J. Schröder, D.C. Lupascu, M.-A. Keip, D. Brands (Ed.), Tagungsband, 2014.

Nr. 13 (2016) *Mixed least squares finite element methods based on inverse stress-strain relations in hyperelasticity*, B. Müller, Dissertation, 2016.

Nr. 14 (2016) *Electromechanical Modeling and Simulation of Thin Cardiac Tissue Constructs*, R. Frotscher, Dissertation, 2016.

Nr. 15 (2017) *Least-squares mixed finite elements for geometrically nonlinear solid mechanics*, K. Steeger, Dissertation, 2017.

Nr. 16 (2017) *Scale-Bridging of Elasto-Plastic Microstructures using Statistically Similar Representative Volume Elements*, L. Scheunemann, Dissertation, 2017.

Nr. 17 (2018) *Modeling of Self-healing Polymers and Polymeric Composite Systems*, S. Specht, Dissertation, 2017.

Nr. 18 (2018) *Proceedings of the Third Seminar on the Mechanics of Multifunctional Materials*, J. Schröder, D.C. Lupascu, H. Wende, D. Brands (Ed.), Tagungsband, 2018.

Nr. 19 (2018) *Least-squares finite element methods with applications in fluid and solid mechanics*, C. Nisters, Dissertation, 2018.

Nr. 20 (2018) *A two-scale homogenization scheme for the prediction of magneto-electric product properties*, M. Labusch, Dissertation, 2018.

Nr. 21 (2019) *Modeling the passive mechanical response of soft tissues: constitutive modeling approaches, efficient parameter selection and subsequent adjustments due to residual stresses*, M. von Hoegen, Dissertation, 2019.

Nr. 22 (2019) *Constitutive modeling of female pelvic floor dysfunctions and reconstructive surgeries using prosthetic mesh implants*, A. Bhattarai, Dissertation, 2019.

Nr. 23 (2019) *A contribution to stress-displacement based mixed galerkin finite elements for hyperelasticity*, N. Viebahn, Dissertation, 2019.

Nr. 24 (2020) *Gefrier- und Auftauprozesse in gesättigten porösen Materialien - ein Modellierungskonzept im Rahmen der Theorie poröser Medien*, W.M. Bloßfeld, Dissertation, 2020.

Nr. 25 (2021) *Electromechanical modelling and simulation of hiPSC-derived cardiac cell cultures*, A. Jung, Dissertation, 2021.

Nr. 26 (2021) *Mixed and Hybrid Least-Squares FEM in Nonlinear Solid Mechanics*, M. Igelbüscher, Dissertation, 2021.

Nr. 27 (2023) *The Material Point Method for dynamic Metal Processing*, S. Maassen, Dissertation, 2023.

Nr. 28 (2023) *Modeling of Fluid-Structure Interactions with the Least-Squares FEM*, S. Averweg, Dissertation, 2023.

Nr. 29 (2023) *Numerical simulation of microstructural residual stresses of hot bulk forming parts with targeted cooling*, S. Hellebrand, Dissertation, 2023.

Nr. 30 (2023) *The Theory of Porous Media in the Framework of the Mesh-in-Element Method*, S. Maike, Dissertation, 2023.